2017

POTENTIAL CONTRASTS IN CO2 AND CH4 FLUX RESPONSE UNDER CHANGING CLIMATE CONDITIONS: A SATELLITE REMOTE SENSING DRIVEN ANALYSIS OF THE NET ECOSYSTEM CARBON BUDGET FOR ARCTIC AND BOREAL REGIONS

Jennifer D. Watts
University of Montana - Missoula

POTENTIAL CONTRASTS IN CO_2 AND CH_4 FLUX RESPONSE UNDER CHANGING CLIMATE CONDITIONS: A SATELLITE REMOTE SENSING DRIVEN ANALYSIS OF THE NET ECOSYSTEM CARBON BUDGET FOR ARCTIC AND BOREAL REGIONS

By

JENNIFER DAWN WATTS

M.S. Land Resources and Environmental Sciences (Land Reclamation),
Montana State University, Bozeman, MT, 2008

B.S. Land Resources and Environmental Sciences (Geospatial Analysis),
Montana State University, Bozeman, MT, 2006

Dissertation
presented in partial fulfillment of the requirements
for the degree of

Doctor of Philosophy
in Systems Ecology

The University of Montana
Missoula, MT

May 2017

Approved by:

Scott Whittenburg, Dean of The Graduate School
Graduate School

Dr. John S. Kimball, Chair
Department of Ecosystem and Conservation Sciences

Dr. Steven W. Running
Department of Ecosystem and Conservation Sciences

Dr. Cory S. Cleveland
Department of Ecosystem and Conservation Sciences

Dr. Anna E. Klene
Department of Geography

Dr. Marco P. Maneta
Department of Geosciences

ABSTRACT

Watts, Jennifer, D., Ph.D., January 2017 *Systems Ecology*

Potential Contrasts in CO_2 and CH_4 Flux Response under Changing Climate Conditions: A Satellite Remote Sensing Driven Analysis of the Net Ecosystem Carbon Budget for Arctic and Boreal Regions

Chairperson: John S. Kimball

The impact of warming on the net ecosystem carbon budget (NECB) in Arctic-boreal regions remains highly uncertain. Heightened CH_4 emissions from Arctic-boreal ecosystems could shift the northern NECB from an annual carbon sink further towards net carbon source. Northern wetland CH_4 fluxes may be particularly sensitive to climate warming, increased soil temperatures and duration of the soil non-frozen period. Changes in northern high latitude surface hydrology will also impact the NECB, with surface and soil wetting resulting from thawing permafrost landscapes and shifts in precipitation patterns; summer drought conditions can potentially reduce vegetation productivity and land sink of atmospheric CO_2 but also moderate the magnitude of CH_4 increase.

The first component of this work develops methods to assess seasonal variability and longer term trends in Arctic-boreal surface water inundation from satellite microwave observations, and quantifies estimate uncertainty. The second component of this work uses this information to improve understanding of impacts associated with changing environmental conditions on high latitude wetland CH_4 emissions. The third component focuses on the development of a satellite remote sensing data informed Terrestrial Carbon Flux (TCF) model for northern wetland regions to quantify daily CH_4 emissions and the NECB, in addition to vegetation productivity and landscape CO_2 respiration loss. Finally, the fourth component of this work features further enhancement of the TCF model by improving representation of diverse tundra and boreal wetland ecosystem land cover types. A comprehensive database for tower eddy covariance CO_2 and CH_4 flux observations for the Arctic-boreal region was developed to support these efforts, providing an assessment of the TCF model ability to accurately quantify contemporary changes in regional terrestrial carbon sink/source strength.

ACKNOWLEDGMENT

I thank my committee: Dr. John Kimball for the support, computing resources and scientific brainstorming that made this research possible; Dr. Steve Running for the encouragement to think “outside the box” and venture into the realm of science policy and activism; Dr. Cory Cleveland for your dedication to teaching, graduate advising and advancing the state of science in academia; Dr. Marco Maneta for your advice and enthusiasm towards environmental modeling; Dr. Anna Klene for your ongoing mentorship and shared love of the Arctic (“keep CALM and carry on”). I also thank family, friends and the Numerical Terradynamic Simulation Group for continued support and encouragement. Special thanks to Dr. Lucas Jones for sharing your knowledge of microwave remote sensing and the highs/lows of PhD life. Tikanni, my faithful canine companion, thanks for tolerating me over the years. Finally, thanks to John B. for your support and comradery; cheers to the many adventures ahead!

TABLE OF CONTENTS

Chapter 1: Introduction and overview

Arctic-boreal ecosystems have been strongly affected by recent climate warming (Kaufman *et al*. 2009), an intensifying freshwater cycle (Rawlins *et al*. 2010, Kopec *et al*. 2015) and shifts in the terrestrial carbon balance (McGuire *et al*. 2012, Schuur *et al*. 2015). Over 50% of the global soil organic carbon (SOC) pool remains held within the northern high latitude regions (Hugelius *et al*. 2012, Olefeldt *et al*. 2016). Yet soil warming, a deepening permafrost active layer and a lengthening of the annual non-frozen period (Romanovsky *et al*. 2010, Schuur & Abbott 2011, Kim *et al*. 2014) could heighten the microbial mineralization of stored SOC and associated greenhouse gas release (Schuur *et al*. 2009, Sistla *et al*. 2013). Although warming generally increases SOC decomposition, the magnitude of CO_2 production is constrained by wet conditions that favor CH_4 emissions and decrease methantrophy (Turetsky *et al*. 2008, Olivas *et al.* 2010, Watts *et al.* 2014b, Treat *et al*. 2015). Regional wetting has been observed throughout the Arctic and sub-Arctic zones (Mekis & Vincent 2011, Watts *et al*. 2012, Zhang *et al*. 2013, Watts *et al*. 2014a), influenced by permafrost thaw, sub-surface ice melt, and the enhanced transport of atmospheric moisture (Kopec *et al*. 2015). These changes could increase wetland CH_4 emissions (Kirschke *et al*. 2013, Meng *et al*. 2016) which have a radiative warming potential at least 25 times more potent than CO_2 over a 100 year time period (Boucher *et al*. 2009).

Ecosystem greening in the Arctic (Zhang *et al*. 2008, Hudson & Henry 2009, Macias-Fauria *et al*. 2012, Berner *et al*. 2013, Myers-Smith *et al*. 2015) following lessening cold temperature constraints could potentially increase the northern carbon sink. In contrast, boreal regions have suffered severe drought stress and lower annual uptake of CO_2 (Zhang *et al*. 2008, Beck & Goetz 2011, Bond-Lamberty *et al*. 2012). Vegetation browning is also being observed in tundra, attributed to extreme winter and summer warming events, ground disturbances, and changes in soil hydrology and winter snowpack characteristics (Phoenix & Bjerke 2016).

Recent net CO_2 exchange in the northern high latitudes varies from a carbon sink of 291 TgC yr^{-1} to a source of 80 TgC yr^{-1}, and largely depends on the balance between carbon uptake by vegetation and losses from soil mineralization and respiration in plants (MacDougall *et al*. 2012, McGuire *et al*. 2012). Soil warming accelerates carbon losses due to the exponential effects of temperature on soil respiration (Kutzbach *et al*. 2007) whereas wet and inundated

conditions shift microbial activity towards anaerobic consumption pathways that are relatively slow, but can result in substantial CH_4 production (Moosavi & Crill 1997, Treat *et al*. 2015). Northern wetland CH_4 fluxes may be particularly sensitive to climate warming, increased soil temperatures and duration of the soil non-frozen period (Olefeldt *et al*. 2013, Zona *et al*. 2016). The northern latitudes already contain over 50% of the global wetlands (Matthews & Fung 1987), with an abundance of vegetation communities capable of direct soil-to-atmosphere CH_4 transport (Davidson *et al*. 2016). Even more concerning is that recent increases in atmospheric CH_4 concentrations have been attributed to heightened gas emissions in these northern areas during periods of intense summer warming (Dlugokencky *et al*. 2009).

Satellite and long term flask sampling networks have improved the monitoring of atmospheric CO_2 and CH_4 concentrations (Butz *et al*. 2011, Karion *et al*. 2013). However, it remains difficult to quantify the regional variability in northern carbon fluxes using top-down inversion modeling (McGuire *et al*. 2012, Bergamaschi *et al*. 2013) given the geographic sparsity of atmospheric sampling by tall towers, airborne measurements, and the sensitivity of optical/near-infrared carbon observing satellites (e.g. GOSAT) to cloud cover and minimal or absent sunlight during long Arctic winters (Parazoo *et al*. 2016).

In consequence, regional studies of terrestrial carbon budgets rely heavily on chamber and eddy covariance methods to assess ecosystem fluxes (Baldocchi *et al*. 2012, Mastepanov *et al*. 2013). Extrapolating local CH_4 fluxes to regional scales has proven difficult and is severely constrained by sparse in-situ monitoring networks and the large spatial heterogeneity in surface vegetation, soil temperatures and wetness across northern ecosystems (Tagesson *et al*. 2013, Sturtevant & Oechel 2013, Davidson *et al*. 2016). Terrestrial CH_4 studies continue to rely on biogeochemical models to assess the magnitude and spatiotemporal variability of regional carbon emissions. Model based bottom-up emission estimates of CH_4 from northern peatland and tundra range between 8 and 79 TgC yr^{-1} (Spahni *et al*. 2011, McGuire *et al*. 2012, Watts *et al*. 2014a, 2014b) and have been difficult to constrain due to uncertainty in model parameterization and the regional characterization of wetland extent and seasonal to daily variability in soil wetness (Petrescu *et al*. 2010, Riley *et al*. 2011, Wania *et al*. 2013). The impact of warming and changing surface and soil wetness on the net ecosystem carbon budget (NECB) in the Arctic-boreal regions remains highly uncertain (McGuire *et al*. 2012). Heightened CH_4 emissions from Arctic-boreal ecosystems could shift the northern NECB closer towards net carbon source

(Merbold *et al*. 2009, Huemmrich *et al*. 2010, Yu *et al*. 2012, Dolman *et al*. 2012, Sturtevant & Oechel 2013, Watts *et al*. 2014a & 2014b).

Hypotheses and objectives

This study considers the following science questions:

(i) How are recent changes in temperature, surface water inundation and soil moisture, and the annual non-frozen period affecting the Arctic-boreal net ecosystem carbon budget (NECB)? (ii) How well can a remote sensing based model approach quantify seasonal and daily terrestrial CO_2 and CH_4 exchange within the Arctic and boreal regions relative to tower eddy covariance flux observations? (iii) Where are changes in the NECB most pronounced within northern high latitude ecosystems, and to what extent are CH_4 fluxes from wetlands driving these changes relative to shifts in GPP and CO_2 emissions?

These questions coincide with the following objectives:

(i) Validate the use of satellite passive microwave retrievals of fractional terrestrial surface water inundation to detect seasonal and inter-annual changes in surface hydrology and impacts to wetland CH_4 emissions. (ii) Develop a satellite remote sensing informed Terrestrial Carbon Flux (TCF) model with enhanced vegetation functional type characterizations for boreal and tundra communities, improved thermal and moisture regulation of vegetation productivity and soil carbon mineralization in permafrost affected ecosystems, and a new wetland CH_4 production and emissions module to provide more complete estimates of NECB. (iii) Use the enhanced TCF model to provide longer-term (yrs. 2003-2015) estimates of daily CO_2 and CH_4 flux activity for the Arctic-boreal region at a 1-km spatial resolution. Use these model records, in conjunction with a compiled database of tower eddy covariance records, to inform the state of regional terrestrial NECB (carbon sink vs. carbon source).

The above objectives address the overarching goal:

To provide the Arctic-boreal research community with new datasets for surface water inundation and TCF model estimates of daily changes in vegetation primary productivity (atmospheric CO_2 assimilation), ecosystem CO_2 respiration, wetland CH_4 emissions and near surface ($\leq$ 10 cm depth) SOC stocks. This research advances carbon cycle science applications

for clarifying the northern NECB and impacts of changing environmental conditions, including ecosystem moisture and thermal constraints, on terrestrial carbon sink or source activity.

Summary overview

The six chapters of this dissertation address the above objectives and are the subject of several peer-reviewed papers and manuscripts in preparation.

Chapter 1 introduces the research topic and the primary hypotheses and objectives of this work, that are presented in detail in Chapters 2 through 5. An overall summary, conclusions and recommendations for future study is provided in Chapter 6.

In Chapter 2, I introduce the land fractional open water (Fw) database developed using satellite microwave observations from the Advanced Scanning Microwave Radiometer on the NASA Earth Observing System (AMSR-E). This work is described in Watts *et al*. (2011) and reports on recent (yrs. 2003–2010) surface inundation patterns across the Arctic-boreal region (≥ 50°N). This chapter provides a validation of the 25-km AMSR-E Fw dataset using alternative, higher spatial resolution observations from Landsat, MODIS and SRTM radar data. A regional trend analysis finds widespread surface Fw wetting occurring within continuous and discontinuous permafrost zones, and Fw drying in the more degraded sporadic/isolated permafrost areas.

In Chapter 3, I present a satellite data driven model investigation of the combined effects of surface warming and moisture variability on high northern latitude ($\geq$ 45° N) wetland CH_4 emissions, by considering sub-grid scale changes in Fw and the impact of recent (2003-2011) wetting/drying on northern CH_4 emissions (Watts *et al*. 2014a). The satellite Fw record reveals continued widespread wetting across the Arctic continuous permafrost zone, contrasting with surface drying in boreal Canada, Alaska and western Eurasia. Arctic wetting and summer warming increased wetland emissions by 0.48 Tg CH_4 yr^{-1}, but this was mainly offset by decreasing emissions (-0.32 Tg CH_4 yr^{-1}) in sub-Arctic areas experiencing surface drying or cooling.

In Chapter 4, I introduce a modified Terrestrial Carbon Flux (TCF) model developed for satellite remote sensing applications to evaluate wetland CO_2 and CH_4 fluxes over six pan-Arctic region eddy covariance flux tower sites (Watts *et al*. 2014b). The TCF model response is

investigated using in-situ data and coarser 250-m satellite (MODIS) and 0.5° reanalysis (MERRA) records. This investigation find that although the estimated annual CH_4 emissions were small (< 18 g C m^{-2} yr^{-1}) relative to R_{eco} (> 180 g C m^{-2} yr^{-1}) they reduced the across-site NECB by 23% and contributed to a global warming potential of approximately 165 $\pm$ 128 g CO_2 eq m^{-2} yr^{-1}. The model evaluation indicates a strong potential for using the TCF model approach to document landscape scale variability in CO_2 and CH_4 fluxes for northern peatland and tundra ecosystems.

In Chapter 5, I present an analysis of CO_2 and CH_4 fluxes across an extended Arctic-boreal flux tower network featuring 36 tower sites. Here I examine recent (yrs. 2003-2015) wetland carbon budgets and corresponding changes in carbon flux components using an enhanced TCF model that represents additional tundra and boreal wetland functional types (Watts *et al*. In prep). The resulting daily 1-km TCF model simulations indicate a net ecosystem carbon sink in tundra and boreal wetlands with respective average NEE values of -4 and -96 gC m^{-2} yr^{-1}. Accounting for NECB (NEE + CH_4) reduced the overall boreal wetland carbon sink by 20% and shifted tundra from carbon sink to carbon source (NECB = 1.6 gC m^{-2} yr^{-1}). Trend analysis for the 13-yr TCF model flux records did not show significant ($\alpha = 0.05$) change in annual GPP, Reco, NEE and NECB when the tower sites were grouped according to boreal or tunda ecotype. However, boreal wetlands experienced a significant increase in CH_4 flux with higher increases occurring in non-forested boreal wetlands.

Chapter 6 summarizes the findings of each chapter in relation to the initial objectives and hypotheses presented in Chapter 1. This chapter includes discussion of research outcomes and recommendations for future research.

REFERENCES

Baldocchi, D (2008) Breathing of the terrestrial biosphere: lessons learned from a global network of carbon dioxide flux measurement systems. *Austr. J. Bot.*, 56: 1–26.

Beck, P S A, S J Goetz (2011) Satellite observations of high northern latitude vegetation productivity changes between 1982 and 2008: ecological variability and regional differences. *Environ. Res. Lett*., 6. doi:10.1088/1748-9326/6/4/045501.

Berner, L T, P S A Beck, A G Bunn, S J Goetz (2013) Plant response to climate change along the forest-tundra ecotone in northeastern Siberia. *Global Change Biol*., doi:10.1111/gcb.12304.

Bergamaschi, P, S Houweling, A Segers, M Krol, C Frankenberg, R A Scheepmaker, E Dlugokencky, S C Wofsy, E A Kort, C Sweeney, T Schuck et al. (2013) Atmospheric CH_4 in the first decade of the 21st century: Inverse modeling analysis using SCIAMACHY satellite retrievals and NOAA surface measurements. *J. Geophys. Res. Atmos.,* 118: 7350-7369.

Bond-Lamberty, B, A G Bunn, A M Thomson (2012) Multi-year lags between forest browning and soil respiration at high northern latitudes. *PLoS*,7.doi:10.1371/journal.pone.005041.

Boucher, O, P Friedlingstein, B Collins, K P Shine (2009) The indirect global warming potential and global temperature change potential due to methane oxidation. *Environ. Res. Lett*., 4. doi:10.1088/1748-9326/4/4/044007.

Butz, A, S Guerlet, O Hasekamp, D Schepers, A Galli, I Aben, C Frankenberg, J -M Hartmann, H Tran, A Kuze, G Keppel-Aleks, G Toon, *et al.* (2011) Toward accurate CO_2 and CH_4 observations from GOSAT. *Geophys. Res. Lett.,* 38. doi:10.1029/2011GL047888.

Davidson, S J, M J Santos, V L Sloan, J D Watts, G K Phoenix, W C Oechel, D Zona (2016) Remote sensing of arctic tundra vegetation communities along a latitudinal gradient in North Alaska, USA. *Remote Sensing,* 8: 1-14.

Dlugokencky, E J, L Bruhwiler, J W C White, L K Emmons, P C Novelli, S A Montzka, K A Masarie, P M Lang, A M Crotwell, J B Miller, L V Gatti (2009) Observational constraints on recent increases in the atmospheric CH_4 burden. *Geophys. Res. Lett*., 36. doi:10.1029/2009GL039780.

Dolman, A J, A Shvidenko, D Schepaschenko, P Ciais, N Tchebakova, T Chen, M K van der Molen, L Belelli Marchesini, T C Maximov, S Maksyutov, E-D Schulze (2012) An estimate of the terrestrial carbon budget of Russia using inventory-based, eddy covariance and inversion methods. *Biogeosciences,* 9: 5323-5340.

Hudson, J M G, G H R Henry (2009) Increased plant biomass in a High Arctic heath community from 1981 to 2008. *Ecology*, 90: 2657-2663.

Huemmrich, K F, G Kinoshita, A Gamon, S Houston, H Kwon, W C Oechel (2010) Tundra carbon balance under varying temperature and moisture regimes. *J. Geophys. Res*., 115. doi:10.1029/2009JGR001237.

Hugelius, G, C Tarnocai, J G Bockheim, P Camill, B Elberling, G Grosse, J W Harden, K Johnson, T Jorgenson, C D Koven, P Kuhry, G Michaelson, U Mishra, et al. (2012) The Northern Circumpolar Soil Carbon Database: spatially distributed datasets of soil coverage and soil carbon storage in the northern permafrost regions. *Earth Syst. Sci. Data Discuss*., 5: 707-733.

Karion, A, C Sweeney, S Wolter, T Newberger, H Chen, A Andrews, J Kofler, D Neff, P Tans (2013) Long-term greenhouse gas measurements from aircraft. *Atmos. Meas. Tech.*, 6: 511-526.

Kopec, B G, X Feng, F A Michel, E S Posmentier (2015) Influence of sea ice on Arctic precipitation. *PNAS*, 113: 46-51.

Kim, Y, J S Kimball, K Zhang, K Didan, I Veliconga, K C McDonald (2014) Attribution of divergent northern vegetation growth responses to lengthening non-frozen seasons using satellite optical-NIR and microwave remote sensing. *Int. J. Remote Sens.*, 45: 3700-3721.

Kaufman, D S, D P Schneider, N P McKay, C M Ammann, R S Bradley, K R Briffa, G H Miller, B L Otto-Bliesner, J T Overpeck, B M Vinther (2009) Recent warming reverses long-term Arctic cooling. *Science*, 325: 1236-1239.

Kirschke, S, P Bousquet, P Ciais, M Saunois, J G Canadell, E J Dlugokencky, P Bergamaschi, D Bergmann, D R Blake, L Bruhwiler, et al. (2013) *Nature Geosci.*, 6: 813-823.

Kutzbach, L C Wille, E –M Pfeiffer (2007) The exchange of carbon dioxide between wet Arctic tundra and the atmosphere at the Lena River Delta, Northern Siberia. *Biogeosciences*, 4: 869-890.

MacDougall, A H, C A Avis, A Weaver (2012) Significant contribution to climate warming from the permafrost carbon feedback. *Nature Geosci*., 5:712-721.

Macias-Fauria, M, B C Forbes, P Zetterberg, T Kumpula (2012) Eurasian Arctic greening reveals teleconnections and the potential for structurally novel ecosystems. *Nature Clim. Change*, 2: 613-618.

Mastepanov, M, C Sigsgaard, T Tagesson, L Ström, M P Tamstorf, M Lund, T R Christensen (2013) Revisiting factors controlling methane emissions from high-Arctic tundra. *Biogeosciences*, 10: 5139-5158.

Matthews, E, I Fung (1987) Methane emission from natural wetlands: Global distribution, area, and environmental characteristics. *Global Biogeochem. Cy*., 1: 61-86.

McGuire, A D, T R Christensen, D Hayes, A Heroult, E Euskirchen, J S Kimball, C Koven, P Lafleur, P A Miller, W Oechel, P Peylin, M Williams, Y Yi (2012) An assessment of the carbon balance of Arctic tundra: comparisons among observations, process models, and atmospheric inversions. *Biogeosciences*, 9: 4543-4594.

Mekis, E, L A Vincent (2011) An overview of the second generation adjusted daily precipitation dataset for trend analysis in Canada. *Atmos.-Ocean*, 49: 463-177.

Meng, L, N Roulet, Q Zhuang, T R Christensen, S Frolking (2016) Focus on the impact of climate on wetland ecosystems and carbon dynamics. *Env. Res. Lett*., 11: 100201.

Merbold, L, W L Kutsch, C Corradi, O Kolle, C Rebmann, P C Stoy, S A Zimov, E -D Schulze (2009) Artificial drainage and associated carbon fluxes (CO_2/CH_4) in a tundra ecosystem. *Global Change Biol*., 15: 2599-2614.

Moosavi, S C, P M Crill (1997) Controls on CH_4 and CO_2 emissions along two moisture gradients in the Canadian boreal zone. *J. Geophys. Res.-Atmos.*, 102: 261-277.

Myers-Smith, I H, S C Elmendorf, P S A Beck, et al. (2015) Climate sensitivity of shrub growth across the tundra biome. *Nat. Clim. Change*, 5: 887-891.

Olefeldt, D, S Goswami, G Grosse, D Hayes, G Hugelius, P Kuhry, A D McGuire, V E Romanovsky, A B K Sannel, E A G Schuur, M R Turetsky (2016) Circumpolar distribution and carbon storage of thermokarst landscapes. *Nat. Commun*., 7: 13043.

Olivas, P C, S F Oberbauer, C E Tweedie, W C Oechel, A Kuchy (2010) Responses of CO_2 flux components of Alaskan Coastal Plain tundra to shifts in water table. *J. Geophys. Res.-Biogeosci.*, 115. doi:1029/2009JG001254.

Parazoo, N C, R Commane, S C Wofsy, C D Koven, C Sweeney, D M Lawrence, J Lindaas, R Y-W Chang, C E Miller (2016) Detecting regional patterns of changing CO_2 flux in Alaska. *PNAS*, 113: 7733-7738.

Petrescu, A M R, L P H van Beek, J van Huissteden, C Prigent, T Sachs, C A Corradi, F J W Parmentier, A J Dolman (2010) Modeling regional to global CH_4 emissions of boreal and Arctic wetlands. *Global Biogeochem. Cy*., 24. doi: 1029/2009GB003610.

Phoenix, G K, J W Bjerke (2016) Arctic browning: extreme events and trends reversing arctic greening. *Global Change Biol*., 33: 2960-2962.

Rawlins, M A, M Steele, M M Holland, J C Adam, J E Cherry, J A Francis, P Y Groisman, L D

Hinzman, T G Huntington, D L Kane, J S Kimball, et al. (2010) Analysis of the Arctic System for freshwater cycle intensification: Observations and expectations. *Amer. Met. Soc*., 23: 5715-5735.

Riley, W J, Z M Subin, D M Lawrence, S C Swenson, M S Torn, L Meng, M N Mahowald, P Hess (2011) Barriers to predicting changes in global terrestrial methane fluxes: analyses using CLM4Me, a methane biogeochemistry model integrated in CESM. *Biogeosciences*, 8: 1925-1953.

Romanovsky, V E, S L Smith, H H Christiansen (2010) Permafrost thermal state in the polar northern hemisphere during the International Polar Year 2007-2009: A synthesis. *Permafrost Periglac. Process*., 21: 106-116.

Schuur, E A G, B Abbott (2011) Climate change: high risk of permafrost thaw. *Nature*, 480: 32-33.

Schuur, E A G, A D McGuire, C Schadel, G Grosse, J W Harden, D J Hayes, G Hugelius, C D Koven, P Kuhry, D M Lawrence, S M Natali, et al. (2015) Climate change and the permafrost carbon feedback. *Nature*, 520: 171-179.

Sistla, S A, J C Moore, R T Simpson, L Gough, G R Shaver, J P Schimel (2013) Long-term warming restructures Arctic tundra without changing net soil carbon storage. *Nature*, 497: 615-619.

Spahni, R, R Wania, L Neef, M van Weele, I Pison, P Bousquet, C Frankenberg, F Joos, I C Prentice, P van Velthoven (2011) Constraining global methane emissions and uptake by ecosystems. *Biogeosciences*, 8: 1643-1665.

Sturtevant, C S, W C Oechel (2013) Spatial variation in landscape-level CO_2 and CH_4 fluxes from Arctic coastal tundra: influence from vegetation, wetness, and the thaw lake cycle. *Global Change Biol.*, 19: 2853-5866.

Treat, C C, S M Natali, J Ernakovich, C M Iversen, M Lupascu, A D McGuire et al. (2015) A pan-Arctic synthesis of CH_4 and CO_2 production from anoxic soil incubations. *Global Change Biol*., 21: 2787-2803.

Turetsky, M R, C C Treat, M P Waldrop, J M Waddington, J W Harden, A D McGuire (2008) Short-term response of methane fluxes and methanogen activity to water table and soil warming manipulations in an Alaskan peatland. *J. Geophys. Res.*, 113. doi: 10.1029/2007JG000494.

Wania, R, J R Melton, E L Hodson, B Poulter, B Ringeval, R Spahni, T Bohn, C A Avis, G Chen, A V Eliseev, S N Denisov, P O Hopcroft, D P Lettenmaier, et al. (2013) Present state of global wetland extent and wetland methane modelling: methodology of a model inter-comparison project (WETCHIMP). *Geosci. Model Dev*., 6: 617-641.

Watts, J. D., J. S. Kimball, L. A. Jones, R. Schroeder, K. C. McDonald (2012) Satellite microwave remote sensing of contrasting surface water inundation changes within the Arctic-Boreal Region. *Rem. Sens. Environ.,* 127: 223-236.

Watts, J D, Kimball J S, Bartsch A, and McDonald K C (2014a) Surface water inundation in the boreal-Arctic: potential impacts on regional methane emissions. *Environ. Res. Lett.,* 9: 1-13.

Watts, J D, Kimball J S, Parmentier F J W, Sachs T, Rinne J, Zona D, Oechel W, Tagesson T, Jackowicz-Korczyński M, Aurela A (2014b) A satellite data driven biophysical model approach for estimating northern peatland and tundra CO_2 and CH_4 fluxes. *Biogeosciences* 11: 1961-1980.

Watts, J D, J S Kimball, R Commane, D Zona, M Helbig, D Olefeldt, F J W Parmentier, T Sachs, L Bruhwiler, O Sonnentag, E Euskirchen, J Kochendorfer, E Humphreys, D Nadeau, J Rinne, M Lund, T Tagesson, M Jackowicz-Korczynski, W C Oechel, M Aurela, M Ueyama, et al. (In Prep.) Regional and longer-term variability in the northern high latitude wetland carbon budget. For submission to *Global Change Biol*.

Yu, Z, J Loisel, D P Brosseau, D W Beilman, S J Hunt (2010) Global peatland dynamics since the Last Glacial Maximum. *Geophys. Res. Lett.,* 37: doi:10.1029/2010GL0

Zhang, K, J S Kimball, E H Hogg, M Zhao, W C Oechel, J J Cassano, S W Running (2008) Satellite-based model detection of recent climate-driven changes in northern high-latitude vegetation productivity. *J. Geophys. Res*., 113: doi:10.1029/2007JG000621.

Zhang, Y, T Sachs, C Li, J Boike (2012) Upscaling methane fluxes from closed chambers to eddy covariance based on a permafrost biogeochemistry integrated model. *Global Change Biol.* 18: 1428-1440.

Zona, D, B Gioli, R Commane, J Lindaas, S C Wofsy, C E Miller, S J Dinardo, S Dengel, C Sweeney, A Karion, R Y-W Chang, J M Henderson, P C Murphy, J P Goodrich, V Moreaux, A Liljedahl, J W Watts, J S Kimball, D A Lipson, W C Oechel (2016) Cold season emissions dominate the Arctic tundra methane budget. *Proc. Nat. Acad. Sci.,* 113: 40-45.

Chapter 2: Validation of pan-Arctic surface fractional water inundation database with high temporal frequency using satellite observations from the advanced scanning microwave radiometers (AMSR-E/AMSR-2)

Corresponding publication:

Watts J D, J S Kimball, L A Jones, R Schroeder, K C McDonald (2012) Satellite microwave remote sensing of contrasting surface water inundation changes within the Arctic-Boreal Region. *Rem. Sens. Environ.*, 127: 223-236.

2.1 Abstract

Surface water inundation in the Arctic–boreal region is dynamic and strongly influences land-atmosphere water, energy and carbon (CO_2, CH_4) fluxes, and potential feedbacks to climate change. Here we report on recent (2003–2010) surface inundation patterns across the Arctic-boreal region (≥ 50°N) and within major permafrost (PF) zones detected using satellite passive microwave remote sensing retrievals of daily fractional open water (Fw) cover from the Advanced Microwave Scanning Radiometer for EOS (AMSR-E). The AMSR-E Fw (25-km resolution) maps reflect strong microwave sensitivity to sub-grid scale open water variability and compare favorably ($0.71 \leq R2 \leq 0.84$) with alternative, static Fw maps derived from finer scale (30-m to 250-m resolution) Landsat, MODIS and SRTM radar (MOD44W) data. The AMSR-E retrievals show dynamic seasonal and annual variability in surface inundation that is unresolved in the static Fw maps. The AMSR-E Fw record also corresponds strongly ($0.71 \leq R \leq 0.87$) with regional wet/dry cycles inferred from basin discharge records. An AMSR-E algorithm sensitivity analysis shows a conservative estimate of Fw retrieval uncertainty (RMSE) within ±4.1% for effective resolution of regional inundation patterns and seasonal to annual variability. A regional trend analysis of the 8-year AMSR-E record shows no significant Arctic–boreal region wide Fw trend for the period, and instead reveals contrasting inundation changes within different PF zones. Widespread Fw wetting is detected within continuous (92% of grid cells with significant trend; $p < 0.1$) and discontinuous (82%) PF zones, while sporadic/isolated PF areas show widespread (71%) Fw drying trends. These results are consistent with previous studies showing evidence of contrasting regional inundation patterns linked to PF degradation and associated changes to surface hydrology under recent climate warming.

2.2 Introduction

Surface hydrology in the Arctic-boreal region is closely linked to permafrost and the balance between precipitation and evapotranspiration. Permafrost, soil frozen for two or more years, underlays approximately 64% (19.6×10^6 km^2) of regions above 49°N (Brown *et al.* 1998). Although permafrost is widespread at high latitudes due to low mean annual temperatures, it also occurs in the sub-Arctic where localized conditions such as poor drainage, dense vegetation and thick organic litter layers reduce surface warming (Shur & Jorgenson 2007). Extensive wetland and lake systems exist throughout the Arctic-boreal region, despite the characteristically arid climate, where permafrost or strata with low permeability impedes vertical soil infiltration and subsurface drainage (van Huissteden *et al.* 2011, Woo *et al.* 2006). However, the relative stability of permafrost within the Arctic-boreal is uncertain given continued climate warming (Graversen *et al.* 2008, Hinzman *et al.* 2005, Kaufman *et al.* 2009). Changes in precipitation and evapotranspiration (Rawlins *et al.* 2010, Zhang *et al.* 2009) will also affect surface water extent.

Permafrost thaw has been observed throughout the Arctic-boreal region (Camill 2005, Frauenfeld *et al.* 2004, Payette *et al.* 2004). Ice melt within the frozen soil layer initially increases inundation, but continued thawing is purported to reduce surface water extent through drainage pathway expansion (Smith *et al.* 2007, White *et al.* 2007). A concern in the Arctic-boreal region is the potential for large global methane (CH_4) emissions resulting from regional thaw lake and wetland expansion (Anisimov 2007, Anisimov & Reneva 2006, Avis *et al.* 2011, Walter *et al.* 2007) because permafrost affected areas hold a large portion of the global soil organic carbon pool (Tarnocai *et al.* 2009). Better information regarding permafrost thaw and the spatial extent and duration of surface inundation is needed to improve ecosystem carbon dioxide (CO_2) and CH_4 emission estimates (Avis *et al.* 2011, O'Connor *et al.* 2010).

In Siberia, lake area has reportedly increased in continuous permafrost zones (Walter *et al.* 2006) and has decreased substantially (Smith *et al.* 2005) where permafrost degradation is more advanced (i.e. discontinuous, sporadic, isolated zones). Similar trends have also been documented in Alaska (Jones *et al.* 2011a, Yoshikawa & Hinzman 2003). These regional observations provide critical insight regarding the influence of permafrost thaw on surface hydrology, but are specific to point-in-time conditions for a small portion of the Arctic-boreal landscape. Satellite remote sensing-based assessments using optical-infrared (IR) sensors are

regionally extensive but prone to signal degradation from persistent clouds, smoke and other atmosphere aerosol effects, and seasonal decreases in solar illumination at higher latitudes (Fily *et al.* 2003, Jones *et al.* 2007).

Alternatively, satellite microwave remote sensing is well-suited to monitor surface inundation owing to its strong sensitivity to surface water presence, reduced sensitivity to solar illumination and atmosphere contamination, and the deployment of microwave sensors on polar orbiting satellites that enable daily observations in northern land areas (Kaheil & Creed 2009). Satellite-based microwave radiometry has been used to analyze global inundation patterns (Papa *et al.* 2010). Arctic-specific studies have also examined regional inundation (Fily *et al.* 2003, Mialon *et al.* 2005) and associations between surface water extent and river discharge (Papa *et al.* 2008, Schroeder *et al.* 2010). However, satellite-based microwave remote sensing has yet to be utilized to examine spatiotemporal relationships between surface inundation and permafrost zones across the Arctic-boreal region.

In this study, we examine regional patterns, temporal variability and recent trends in surface inundation across the Arctic-boreal zone and within sub-regions characterized by continuous, discontinuous and sporadic/isolated permafrost. Daily fractional open water cover (*Fw*) was derived from 18.7 and 23.8 GHz frequency brightness temperature (*Tb*) series from the Advanced Microwave Scanning Radiometer for EOS (AMSR-E), where the *Fw* retrievals represent the proportional surface water cover within 25-km equal area grid cells (Jones *et al.* 2010). Fractional open water is defined as standing surface water and saturated soils that are unmasked by overlying vegetation biomass and moist organic debris, including plant litter and moss layers. Upwelling microwave radiance at 18.7 GHz frequency has a limited ability to penetrate overlying vegetation biomass and moist organic debris, so that most of the *Fw* signal originates from standing water emissions within open areas and under low density vegetation cover.

This approach differs from previous studies (Fily *et al.* 2003, Papa *et al.* 2010) because Fw and associated temperature, atmosphere and vegetation factors are determined synergistically using multi-frequency and polarization *Tb* records from a single sensor, AMSR-E (Jones *et al.* 2010, 2011). This approach allows independence from other ancillary data for determining microwave scattering effects from intervening atmosphere and vegetation layers. An algorithm

sensitivity analysis was first performed to estimate AMSR-E *Fw* retrieval uncertainty. The daily AMSR-E *Fw* record was then temporally composited to mean monthly and maximum annual values; these data were compared against available static open water maps derived from the UMD Global 250-m Land Water Mask (MOD44W) for the Arctic-boreal domain and regional Landsat-based (30-m res.) land cover classifications. The AMSR-E *Fw* data were also compared against dynamic river discharge records for major Arctic river basins to evaluate *Fw* response to climate variability and periodic wet/dry cycles inferred from the basin discharge records. The *Fw* results were evaluated both regionally and on a per grid-cell basis to document recent (2003–2010) inundation changes across the Arctic-boreal domain and within the major permafrost zones.

2.3 Methods

2.3.1 AMSR-E Fw estimates

The daily *Fw* retrievals were derived from AMSR-E *Tb* records using the algorithm described by Jones *et al.* (2010). The AMSR-E microwave radiometer was launched in December 2002 on the polar orbiting (1:30 AM/PM equatorial crossings) EOS Aqua satellite, which has orbital swath convergence and sub-daily temporal sampling for northern (≥ 50°N) regions. The AMSR-E sensor measures horizontal (H) and vertical (V) polarized *Tb* values at six (6.9, 10.7, 18.7, 23.8, 36.5, 89.0 GHz) frequencies (Kawanishi *et al.* 2003). The AMSR-E instrument ceased effective operations in October 2011, but a follow-on mission (AMSR-2; Oki *et al.* 2010) was launched in May 2012 aboard the Global Change Observation Mission-Water (GCOM-W1) satellite. The retrieval algorithm uses AMSR-E 18.7 and 23.8 GHz H- and V polarized *Tb* values to estimate *Fw*, which is the effective open water fraction in the sensor field of view, surface (~2 m height) air temperature (*Ta*), vegetation optical depth (τ), and atmosphere (total column water vapor; *Vp*) parameters simultaneously (Jones *et al.* 2010). The nomenclature associated with these algorithms and the corresponding *Fw* analysis is presented in Table 1.

While the algorithm is applicable for surface inundation it was not designed to detect soil moisture conditions (where surface water is not present) because only higher (18.7 and 23.8 GHz) frequency *Tb* data are used for the *Fw* retrieval. Prior to algorithm input, the *Tb* data are screened for precipitation, radio frequency interference (18.7 GHz only), and frozen or snow-covered conditions (Jones & Kimball 2011, Kim *et al.* 2011). However, ice and wet snow can

persist well above the freezing point during spring onset and winter warm periods, which sometimes co-occur with the rapid expansion of inundated area from ice and snowmelt. Additionally, lake ice can persist for many days after thaw has occurred in surrounding landscape and lake edges. These mixed-phased situations, where liquid water, ice and wet snow co-occur, tend to be classified as non-frozen conditions by the screening algorithm and result in strong *Fw* seasonality coinciding with annual freeze-thaw cycles. Grid cells with ≥ 50% (~314 km^2) permanent ice or open water cover were identified and screened (masked from further analysis) using the 0.25° gridded UMD MODIS land cover product obtained from the Global Land Data Assimilation System (GLDAS; Jones *et al.* 2010). This screening removes 2% (~4.2×10^5 km^2) of non-ocean open water cells associated with larger inland water bodies within the Arctic-boreal region and is consistent with the terrestrial focus of the AMSR-E global land parameter database (Jones *et al.* 2010); the remaining Arctic-boreal domain spans roughly 2.29×10^7 km^2, post-screening.

The retrieval algorithm uses a simplified forward radiometric *Tb* model to estimate *Fw*, *Ta*, and τ. The forward model is a set of simultaneous equations expressed in terms of *Tb* ratios to reduce their dependence on temperature (Jones *et al.* 2010, Njoku & Li 1999), leaving quantities that are influenced primarily by *Vp* and emissivity (ε). Surface emissivity (εs) in turn depends upon *Fw* and τ. The resulting system of ratio equations (Jones *et al.* 2010) is then iteratively solved for *Vp*, *Fw*, and τ. Jones *et al.* (2010) report a 3.5 K root mean square error (RMSE) uncertainty across time and space for the temperature retrievals relative to surface station network air temperature measurements, a statistic which incorporates biases from one station to another. The amount of *Fw* in the landscape is the primary factor influencing estimated εs and *Tb* sensitivity to *Vp*, which in turn impact *Ta* retrieval accuracy. Favorable *Ta* retrieval accuracies therefore provide indirect verification of *Fw* retrieval accuracy. The error sensitivity analysis presented in the following section quantifies the relationship between *Ta* and *Fw* retrieval accuracy, and examines algorithm sensitivity to surface soil moisture variability on the *Tb* ratios, which is assumed to have negligible impact on the *Fw* calculations.

2.3.2 Error sensitivity analysis

An algorithm error sensitivity analysis was conducted to determine *Fw* retrieval uncertainty by performing *Fw* retrievals on a simulated *Tb* dataset. The analysis is based on

forward and inverse models for 18.7 and 23.8 GHz, H and V polarization *Tb* data (Jones *et al.* 2010) provides a detailed description of the algorithms). The inverse model summarized below (Eqs. 1–2) uses polarization and frequency (*p, f*) dependent *Tb* values received by a space borne sensor to estimate landscape surface characteristics (Section III C in Jones *et al.* 2010), where Tb_u and Tb_d are the respective upwelling and downwelling atmospheric brightness temperatures and Tb_s is the upwelling surface brightness temperature. Atmospheric attenuation of the microwave signal by *Vp* is characterized by its transmissivity (*ta*); Ω is a surface roughness parameter that is assumed to be unity at the AMSR-E incidence angle (55° from nadir) and frequencies considered by the algorithm (Matzler 2005).

$$Tb_{(p,f)} = Tb_{u(f)} + t_{a(f)}\left[Tb_{s(f,p)} + \Omega\,(1 - e_{s(f,p)})Tb_{d(f)}\right] \quad \text{Eq. 1}$$

Atmospheric absorption and emission are temperature dependent and primarily occur in the lower atmosphere for the 18.7 and 23.8 GHz channels, allowing the approximation that $Tb_{u(f)} \cong Tb_{d(f)} \cong \left(1 - t_{a(f)}\right)T_a$ (Weng & Grody 1998). The sensor observed Tb_s (Eq. 2) is assumed to represent a mixture of *Tb* emissions from land (Tb_l) and surface water body (Tb_w) components; Tb_l from a vegetated surface is described as a layer of semi-transparent vegetation over smooth, bare soil. The calculation of canopy τ in terms of vegetation water content is described elsewhere (Jones *et al.* 2010 Section III; Jones *et al.* 2011b). The characteristically high dielectric constant of water strongly impacts Tb_s and allows for significant microwave sensitivity to even relatively low *Fw* levels.

$$Tb_{s(f,p)} = FwTb_{w(f,p)} + (1 - Fw)Tb_{l(f,p)} \quad \text{Eq. 2}$$

The forward model (Section III A in Jones *et al.* 2010) simulates the land surface as a mixture of open water and single scattering vegetation overlain by a plane-parallel non-scattering atmosphere. The forward model is summarized below (Eqs. 3–5) and describes *Tb* emission by land surface components and its upward propagation and interaction with intervening vegetation canopy and atmosphere layers, whereas the inverse model (Eqs. 1–2) uses *Tb* values received by a space borne sensor to estimate landscape surface characteristics (Section III C in Jones *et al.* 2010). The simplified forward model describes *Tb* as a linear function of t_a and a t_c parameter that represent the attenuation of upwelling soil emissions by the intervening vegetation canopy and litter layer. This simplified linear function ignores the surface reflection terms included in the inverse model by assuming that reflection is low for land surfaces with relatively

high emissivity and that the sub-grid scale emissions are averaged by antenna gain (Jones *et al.* 2010).

$$Tb_{(p,f)} = T_s \left[t_{a(f)} \varepsilon_{(p,f)} + (1 - t_{a(f)}) \delta \right] \quad \delta \approx \frac{T_a}{T_s} \qquad \text{Eq. 3}$$

$$\varepsilon_{s(p,f)} = Fw \varepsilon_{w(p,f)} + (1 - Fw) \varepsilon_{l(p,f)} \qquad \text{Eq. 4}$$

$$\varepsilon_{l(p,f)} = \varepsilon_{os(p,f)} t_c + (1 - \omega)(1 - t_c) \qquad \text{Eq. 5}$$

Surface emissivity is a function of both land (ε_l) and open water (ε_w) components; δ is the ratio of T_a to surface temperature (T_s), which compensates for a vertical gradient between the two temperature components. Vegetation single scattering albedo (ω) and emissivity for open water, bare soil (ε_{os}) are parameter constants (Table II in Jones *et al*. 2010). The *Fw*, t_c, andV_p (which influences t_a) parameters are estimated iteratively using temperature insensitive T_b ratios and are described elsewhere (Jones *et al*. 2010; Section III C).

For the Monte-Carlo error analysis, T_b values were first simulated with the forward model using specified geophysical input parameters. Monte Carlo forward simulations were used to generate the resulting T_b dataset. Geophysical parameter space was sampled by drawing from uniform distributions of each of the following input parameters over specified ranges: >0–0.5 for volumetric (m^3 m^{-3}) soil moisture; 273-303 K for T_a; > 0-60 mm for V_p; and vegetation opacity corresponding to canopy water content of 0–10 kg m^{-2}. The impact of cloud liquid water for the considered frequencies is assumed to be small relative to other sources of uncertainty for high-latitude regions and subsequently was not considered. Water ε is treated as a constant because the algorithm was developed for land-dominated scenes and does not consider in detail the effect of waves, foam and salinity, which can be substantial for large water bodies (Jones *et al.* 2010, 2011b).

The simulated T_b data were used as inputs to the inverse algorithm to estimate *Fw* and errors were calculated by comparing the intermediate geophysical parameter estimates with those initially specified. The potential error contributions from three primary sources were evaluated including: (1) systematic bias from the simplified emission model, (2) random radiometer noise, assumed to follow a Gaussian distribution with standard deviation of 0.5 K and uncorrelated across T_b channels, and (3) parameter uncertainty. Parameter uncertainty originates primarily from ω and δ. To represent parameter uncertainty in the forward model, the two parameters are perturbed with Gaussian noise (standard deviation=0.02) about their respective nominal values of

0.05 and 0.95. Additionally, δ is intended as a calibration parameter to adjust the overall temperature retrieval bias of the inverse model relative to the forward model, and was therefore assigned a slightly higher value of 0.96 for the inverse algorithm (Jones *et al.* 2010).

Simulations were conducted first with all random error sources evaluated separately to examine the effects of each individual source. The individual error sources were then combined to estimate the total overall *Fw* retrieval error. For each combination of errors, we performed 30 simulation sets each with 1000 realizations of *Fw* varying from 0 to 0.5 in 0.05 increments for a total of 3.3×10^5 simulations. The accuracy for each *Fw* increment was determined by averaging across the RMSE differences obtained in each of the 30 sets of realizations. The standard deviation of the RMSE across each set is < 0.0015, indicating that the Monte Carlo sampling density was sufficient to produce stable, repeatable results. To partition the relative contribution of error from each source, four combinations of error sources were considered, including systematic bias from the simplified emission model, random error from radiometer noise (termed "T_b noise"), random error from ω, random error from δ, and total error from all sources. Each random error source term necessarily includes the bias source from the simplified emission model, but the terms are otherwise independent of one another. The surface T_a retrievals serve as an important indirect check on surface emissivity retrievals, and hence *Fw* accuracy. Therefore, estimated T_a and *Fw* retrieval uncertainties are reported together (Figure 1).

2.3.3 Fw verification

The daily AMSR-E *Fw* retrievals from the AM (descending) overpass were used to generate monthly mean (Fw_{avg}) and maximum (Fw_{mx}) inundation records for the 2003-2010 period. Image composites were derived from the AMSR-E Fw_{avg} and Fw_{mx} records by taking the period mean from 2003 to 2010. The Fw_{avg} and Fw_{mx} composites were verified against alternative static *Fw* (Fw_s) classification maps, including those derived from the 250-m resolution UMD Global Land Water Mask (MOD44W) for the Arctic–boreal domain, and finer (30-m) resolution Landsat-based maps for Alaska, North Central Canada and Northern European sub-regions. The AMSR-E record for 2010 was not included in the comparison against the Fw_s maps because it was still being processed. The MOD44Wproduct is derived from a compilation of the Shuttle Radar Topography Mission (SRTM) Water Body dataset for regions < 60°N,

which was created using SRTM radar and digital terrain data with Landsat-based Geocover data. The SRTM data is unavailable for land areas ≥ 60°N and the MOD44W product was derived solely from the MODIS (MOD44C) Collection 5 (2000-2008) open water classification product in these regions (Carroll *et al.* 2009). The MOD44W product effectively replaces the Global Lakes and Wetlands Database, which only incorporates data prior to the mid-1990s (Lehner & Doell 2004). Although the MOD44C data were used to gap-fill some regions < 60°N in the MOD44W product, the extent of this substitution is minimal.

Finer (30-m) resolution data were obtained from the Landsat-based 2001 National Land Cover Dataset (Homer *et al.* 2004) for Alaska, which used Landsat Enhanced Thematic Mapper Plus (ETM+) imagery collected during the 2001 growing season. Similar Landsat-based open water data were provided by a subset (~1×10^6 km^2) of the Circa-2000 Land Cover of Canada Database (Geobase Canada 2009) for the Canada sub-region and a regional land cover classification (Potapov *et al.* 2011) of the Northern European sub-region. The Geobase land cover map used cloud/snow-free Landsat Thematic Mapper (TM) and ETM+ imagery from 1996 to 2005 (80% of imagery was collected between 1999 and 2001). Land cover data obtained from Potapov *et al.* (2011) were derived from cloud-free ETM+ imagery collected during the 2003–2007 growing season.

The Fw_s maps were aggregated to the coarser spatial scale of the AMSR-E *Fw* record by determining proportional open water cover within overlying 25-km equal area scalable earth grid cells (EASE-grid) consistent with the approximate spatial resolution of the AMSR-E *Fw* retrievals. The Fw_s map grid cells corresponding to ≥ 50% permanent ice or open water within the GLDAS land cover map were excluded from the analysis for consistency with the AMSR-E *Fw* retrievals. Vegetated wetland classes in the Alaska and Canada land cover maps were excluded from the Fw_s calculations due to relative greater susceptibility of these areas for open water misclassification (omission and commission) and inconsistencies in wetland class types between different land cover products (Ozesmi & Bauer 2002, Selkowitz & Stehman 2011). The Landsat-based maps also had a “Snow/Ice” class; frozen water bodies within this class were not incorporated into Fw_s calculations due to difficulty separating these areas from other frozen surfaces.

A 3×3 cell (AMSR-E grid) weighted box-car filter was applied for spatial aggregation of the Fw_s data to represent the effective AMSR-E footprint, whereby antenna side lobe gain and variability of the sensor orbital track cause spatial smearing of the AMSR-E ellipsoidal swath T_b footprints (Amarin *et al.* 2010). The resulting MOD44W and Landsat-based Fw_s datasets were compared against AMSR-E Fw_{avg} and Fw_{mx} composites over a 7 year (2003–2009) period to determine the correspondence between the AMSR-E results and Fw_s estimates. Metrics included the coefficient of determination (R^2) to evaluate the percent of variability in the Fw_s maps explained by the AMSR-E Fw_{avg} and Fw_{mx} composites, and regional wet or dry biases as compared to the Fw_s maps. The *Fw* monthly minimums (Fw_{mn}) were also evaluated but are not presented, as they did not show improved correspondence with Fw_s relative to the Fw_{avg} and Fw_{mx} results.

The AMSR-E *Fw* data were compared with monthly mean river discharge (Q; $m^3\ s^{-1}$) measurement records for the major Arctic-boreal basins to evaluate Fw inundation sensitivity to seasonal and inter-annual climate variability, and periodic wet/dry cycles indicated by the discharge records. Available monthly Q records from 2003 to 2010 were obtained from downstream stations (indicated in parentheses) for the Yukon (Pilot Station; 61° 55′ N, 162° 52′ W), Mackenzie (Arctic Red River; 67° 27′ N, 133° 44′ W), Ob (Salehard; 66° 37′ N, 66° 35′ E), Yenisei (Igarka; 67° 25′ N, 86° 28′ E) and Lena (Polyarnaya; 72° 24′ N, 126° 20′ E) river basins (http://rims/unh.edu). Correlation between Q and basin-averaged AMSR-E Fw_{avg} results were examined using bi-monthly non-frozen season anomalies for April–May (AM), June–July (JJ) and August–September (AS) periods. Tri-monthly (MAM, JJA, SON) parameter anomalies were compared for the Ob to account for a longer characteristic lag between basin inundation and river discharge for this region (Schroeder *et al.* 2010).

2.3.4 Fw trend analysis

Regional AMSR-E *Fw* trends were examined for the Arctic-boreal domain (≥ 50°N) and within three major permafrost zones defined by the International Permafrost Association (IPA) Circum-Arctic Map of Permafrost and Ground Ice Conditions (Brown *et al.* 1998). The continuous permafrost zone includes regions where permafrost covers > 90% of the landscape; the discontinuous permafrost zone is characterized by 50-90% permafrost coverage within the landscape; the sporadic/isolated permafrost zone represents areas with high spatial patchiness (<

50% permafrost coverage) and greater seasonal soil thaw depth.

Inundation trends were examined by applying the Mann–Kendall trend test (Kendall rank correlation to the annual scale data; a value of 1 (0) indicates perfect (no) correlation with time) to AMSR-E annual means for Fw_{avg} and Fw_{mx} records from 2003 to 2010. Mann–Kendall (MK) is a non-parametric statistical test that determines trend direction and significance, and is often used for hydrological applications because it does not assume a specific population distribution (Chandler & Scott 2011). Normal approximations are used to determine test significance (p-value) with larger sample sizes, whereas exact tests are used when the sample size is small (Hipel & McLeod 2005, Sheskin 2004). Mann–Kendall analysis can be influenced by serial correlation, unless the magnitude of trend is large (Zhang *et al.* 2006). As a precaution against serial correlation, the Yue–Pilon method was used prior to applying the trend test (Yue *et al.* 2002). The Yue–Pilon method first applies the non-parametric Theil–Sen estimator that determines the median slope of all possible paired sample points; the slope and lag-1 autocorrelation are removed if autocorrelation is detected (Yue *et al.* 2002). The slope and resulting uncorrelated residuals are then merged to create a blended series to which the MK test is applied.

The total AMSR-E *Fw* inundation extent (km^2) was obtained for the Arctic-boreal domain and North American and Eurasian sub-regions (not limited to permafrost regions) daily and aggregated to monthly and annual intervals. We expect these area estimates (km^2) to be scale dependent, reflecting observations originally obtained at a 22-km native resolution; consequently, those obtained from finer scale satellite retrievals might differ from these estimates. Annual *Fw* extent was also determined regionally for continuous, discontinuous, and sporadic/isolated permafrost zones. The annual number of grid cells with *Fw* present ($Fw > 0$) was obtained for each region, as was the mean annual *Fw* duration (the number of days per year that *Fw* was detected). These records were examined for trends using the MK analysis and trend significance was assessed at a minimum 90% ($p < 0.1$) probability level. The Fw trends were evaluated on a per-grid cell basis across the Arctic-boreal domain because of spatial heterogeneity in climate, permafrost condition, and surface characteristics. The relative proportions of significant ($p < 0.1$) cells with positive and negative trends were determined for each permafrost zone. Trends in *Fw* duration were also examined on a per-grid cell basis to

ascertain the potential influence of changes in non-frozen season length and the corresponding period of *Fw* retrievals on surface inundation trends. Areas with significant ($p < 0.1$) trends in *Fw* inundation and *Fw* duration were also compared against regions identified as having significant changes in non-frozen period length (Kim *et al.* 2012). Trends in Fw_{mn}, which may reflect relatively stable lake bodies, are not statistically significant and are not presented in the study results.

Evaluating trends on a per grid-cell basis can substantially increase the false discovery rate (Wilks 2006), which is the expected proportion of Type I error (false positives) among all significant hypotheses. For example, $\alpha = 0.1$ indicates that there is a 10% chance that a trend will be falsely detected per test or that 10% of all tests will be false positives. Adjusting p-values for false discovery can substantially reduce the number of expected Type I errors because α will instead correspond to tests showing significant results, rather than the total number of tests considered. In addition to per-cell p-values (indicating local significance) we also estimated q-values (adjusted p-values) for each grid cell using the False Discovery Rate (FDR) approach which evaluates characteristics of the p-value distribution. This conservative approach can be used to address multiple hypothesis testing and is more robust to spatial dependence (Wilks 2006).

2.4 Results

2.4.1 Error sensitivity analysis

The Monte Carlo error sensitivity analysis indicates total *Fw* uncertainty within ±0.041 (RMSE) with a positive dependence on *Fw* (Figure 1). The positive dependence between retrieval uncertainty and Fw extent indicates that the simplified emission (forward) model biases become more prevalent as ε_S decreases with higher *Fw*. As ε_S decreases, the emission model becomes more sensitive to atmospheric factors because the intervening atmosphere contrasts more with a radiometrically dark water background than it does against relatively bright land (Chang & Milan 1982). In addition, the land fraction decreases as *Fw* increases and the emission model becomes proportionally less sensitive to ε_l factors. Minimal *Fw* retrieval error at lower inundation levels indicates that surface soil moisture variability does not significantly degrade results relative to other T_b model error sources.

In contrast to *Fw*, the T_a retrieval is more sensitive to ε_S error, which flattens the T_a retrieval uncertainty response at higher *Fw* levels. For T_a, the error contributions of ω and δ show opposing trends with *Fw*, resulting from the previous trade-off between ε_l and atmospheric sensitivities at higher *Fw* levels. This tradeoff is more evident for the ω and δ components because model bias is relatively low (b | ± 1| K) for T_a as a result of algorithm calibration (discussed in Section 2.2). The overall T_a errors from the sensitivity analysis range from 3.7 to 4.1 K, compared to the observed 3.5 K T_a error relative to Northern Hemisphere weather station records (Jones *et al.* 2010). This discrepancy indicates that ω and δ are not as variable as specified and that the simplified emission model adequately represents surface T_a and T_b observations; these results also indicate that the reported overall *Fw* error is a conservative estimate.

2.4.2 Fw verification and regional analysis

The AMSR-E *Fw* results compare favorably with the MOD44W and Landsat-based Fw_S maps for the respective Arctic-boreal and regional domains. The Fw_{avg} map composite (AMSR-E Fw_{avg} averaged over the 2003-2009 period) accounts for 71-84% (R^2) of variability in the Fw_S maps, while the Fw_{mx} composites account for a lower 39-80% (R^2) of Fw_S variability (Table 1). The mean RMSE difference between the AMSR-E Fw_{avg} and Fw_{mx} products, and Fw_S is ≤ 5%. The strongest regional correspondence (R^2 = 0.84) is observed between AMSR-E Fw_{avg} and lower latitude (< 60°N) Fw_S regions where the MOD44W product is partially derived from radar (SRTM) imagery. The lowest correspondence (R^2 = 0.39) occurs in western Russia where the Fw_{mx} retrievals are higher than corresponding Landsat-based Fw_S levels in the largely agricultural and wetland dominated areas. A small negative (dry) bias (i.e. - 8.21% ≤ MRE ≤ - 0.56%) is observed for AMSR-E Fw_{avg} relative to Fw_S (Table 2; Figure 2), whereas the Fw_{mx} results show a small positive (wet) bias (- 0.96 ≤ MRE ≤ 5.48%) (Table 2; Figure 3). Regionally, Fw_{avg} and Fw_{mx} are lower than Fw_S along major rivers and in glaciated areas characterized by lakes surrounded by shallow, rocky substrate (e.g. portions of the Northwest Territories and North Central Canada). In contrast, Fw_{avg} and Fw_{mx} are predominately higher than the Fw_S results in wetland-dominated regions (e.g. Canadian Shield, Yenisey and Lena river

basins).

The summer Fw_{avg} and Q anomalies for the five Arctic river basins show favorable correlations ($R \geq 0.71$; Figure 4) despite other hydrological influences on Q, including direct runoff contributions from snowmelt and groundwater (Papa *et al.* 2008, Syed *et al.* 2007). Relatively strong correlations ($R \geq 0.82$) are observed for basins with lower mean summer Fw_{avg} extent, including the Yukon (Fw_{avg} represents 2.07% of the basin area or 1.72×10^4 km^2), Lena (1.77% or 4.44×10^4 km^2), and Yenisey (1.85% or 4.51×10^4 km^2).

Lower correlations are observed for the Ob and Mackenzie ($R = 0.71$ and 0.76, respectively) basins where the proportional Fw_{avg} extent is relatively larger (3.16% or 7.87×10^4 km^2; 11.26% or 1.89×10^5 km^2). This lower correspondence is likely due to extensive Q regulation by basin reservoirs along the Ob and Mackenzie rivers (McClelland *et al.* 2004, Yang *et al.* 2004). Similarities in relative dry (negative) and wet (positive) year anomalies between Fw_{avg} and Q indicate that the *Fw* retrievals capture regional wet and dry cycles reflected in the discharge observations (Figure 4). Negative *Fw* and Q anomalies in 2004 for the Yukon, Mackenzie and Yenisey basins coincide with regional drought (Alkama *et al.* 2010, Zhang *et al.* 2009), while strong positive anomalies in 2007 for the Ob and in 2009 for the Yukon, Mackenzie, Lena and Yenisey basins coincide with documented wet periods (Arndt *et al.* 2010, Rowland *et al.* 2009).

The *Fw* inundation extent in the Arctic-boreal region is highest within large wetland complexes of the major watersheds, including the Canadian Shield, Yukon River Delta, the Kolyma, Indigirka, Lena, Ob-Yenisey, Volga lowlands and Scandinavia (Figure 5). Seasonal *Fw* variability is also greatest within these regions, and in the agricultural areas of southwestern Russia, southern Alberta and Saskatchewan CN relative to other areas in the domain (Figure 5). On a seasonal basis region-wide *Fw* inundation (Fig. 6) is lowest in January–February (2.9×10^5 km^2 Fw_{avg}; 4.16×10^5 km^2 Fw_{mx}) and highest in July (2.78×10^6 km^2 Fw_{mx}) and August (1.94×10^6 km^2 Fw_{avg}).

Maximum inundation extent in Eurasia occurs in June–July and precedes the August maximum in North America (Figure 6). On an annual basis, the largest *Fw* inundation year

(based on total annual inundation extent) for the Arctic-boreal domain during the 2003-2010 observation period coincides with above-average precipitation in North America and Eurasia in 2005 (Shein *et al.* 2007), whereas the lowest inundation year (2004) coincides with relatively warm summer conditions in North America and a multi-year (2001-2003) drought in the Arctic–Boreal region (Parker *et al.* 2006, WMO 2005, Zhang *et al.* 2008). Similarly, the wettest *Fw* years for Eurasia (2007) and North America (2010) coincide with relatively warm winters and wet summers (Kennedy *et al.* 2008, WMO 2011). The lowest *Fw* years observed for North America (2004) and Eurasia (2010) reflect anomalous dry summer conditions in Alaska and western Canada (Kochtubajda *et al.* 2011,Wendler *et al.* 2010) and a severe summer drought in Russia (Wegren 2011, WMO 2011). The comparison be- tween AMSR-E *Fw* and MOD44W Fw_S inundation extent for the Arctic-boreal, Eurasia and North America regions indicates that the MOD44W estimates are considerably larger than the Fw_{avg} retrievals and closer to the summer Fw_{mx} retrievals (Figure 6). This difference occurs because *Fw* seasonal variability is not resolved in the static open water product.

2.4.3 Fw trends

A strong positive (increasing) trend in the annual number of grid cells with *Fw* present (*Fw* count) is observed for all permafrost zones (Table 3), at a rate of roughly 140 cells yr^{-1} (~73,910 km^2 or roughly 0.67% per year; Table 3) when considering Fw_{mx}. This trend is influenced primarily by *Fw* changes within Eurasian continuous and sporadic/isolated permafrost zones, and discontinuous permafrost areas in North America as these areas show larger (and significant; $p < 0.1$) increases in *Fw* counts relative to other regions. An increase in *Fw* presence is observed for all three permafrost zones, with the rate of expansion ranging from roughly 33 cells yr^{-1} (discontinuous zone) to 65 cells yr^{-1} (continuous zone) (Table 4). The strong positive trend in *Fw* duration observed for the Arctic-boreal region is primarily driven by the continuous and discontinuous permafrost zones in North America (Table 3). Changes in *Fw* duration within these areas (increasing at 0.76 days yr^{-1} for the Arctic-boreal zone; Table 4) may reflect an overall increase in precipitation and lengthening of the non-frozen season (Kim *et al.* 2012, McClelland *et al.* 2006). A positive, moderate trend in total *Fw* inundation (*Fw* area) is observed only in Fw_{mx} and is primarily influenced by the Eurasian continuous and North American

discontinuous permafrost zones. Although not significant, a weak (p ~ 0.13) positive Fw_{avg} trend is observed for the continuous permafrost zone and for North American discontinuous permafrost areas. Overall, significant regional trends in the *Fw* count and *Fw* area metrics are not observed when the Arctic-boreal, North American and Eurasian sub-regions are considered (Table 3). Significant decreasing trends in *Fw* count, *Fw* duration and *Fw* area are not observed in the regional analyses.

Areas of widespread *Fw* inundation increase are observed through- out the continuous permafrost zone when the MK trend test is applied on a per grid-cell basis (Figure 7). The continuous permafrost zone has the highest proportion (92%; 91-94% is the 95% confidence interval for proportions) of grid cells with locally significant Fw_{avg} wetting trends, followed by 82% (79-86%) of cells in discontinuous permafrost regions. Conversely, sporadic/isolated permafrost regions show widespread *Fw* inundation decrease (71%; 66-74%). The overall contrast between inundation patterns within the three permafrost zones is similar for Fw_{mx}, but the overall trend extent is weaker compared to the Fw_{avg} results, with 63% (61-65%) and 59% (55-63%) of grid cells showing Fw_{mx} wetting trends within respective continuous and discontinuous permafrost zones. In the sporadic/isolated permafrost zone, 48% (44–52%) of Fw_{mx} grid cells having significant trends show drying. Although widespread wetting occurs within the continuous permafrost zone, large regions of drying are also observed in northern Québec and Newfoundland, the Canadian Baffin and Banks islands, north of the Seward Peninsula in Alaska, and the Panteleikha River wetlands in Siberia (Figure 7).

In the discontinuous permafrost zone the largest regions of drying occur directly south of the Alaska Seward Peninsula and in northern Saskatchewan CN. Although 71% of grid cells with significant Fw_{mx} trends within the sporadic/isolated permafrost zone show drying, areas of wetting are observed in northern British Columbia, northern Saskatchewan and Manitoba, east of James Bay in Québec CN, in the Scandinavian Lapland and southern Siberia (Figure 7). These grid cells are not significant ($q < 0.1$) when controlled for false discovery rate, which is not surprising given the small percentage of grid cells within permafrost zones that show local trend significance ($p < 0.1$) and the large number of grid cells to which the trend test was applied. Furthermore, the resulting q-values (~0.45–0.58) are relatively lower in areas that are locally significant ($p < 0.1$) compared to those that are not (~ 0.68–0.90). Given the conservative nature

of the FDR correction, the relatively lower q-values in areas with local significance ($p < 0.1$), and indication of area-wide changes in the regional trend analysis it appears that areas having locally significant MK trend reflect physical changes in surface inundation characteristics.

Only a small portion of grid cells having locally significant wetting trends coincide with an increase in *Fw* duration. Approximately 9% (2,831 grid cells) of the Arctic-boreal permafrost zone shows a significant increase in AMSR-E Fw_{avg} over the 8 year period (Figure 7), with a mean inundation increase of 0.16% (0.98 km^2) per cell yr^{-1}. Approximately 2.6% (74 grid cells) also show a significant ($p < 0.10$) increasing trend in annual *Fw* duration (within the Eurasian continuous permafrost zone). Only 19 of the 74 grid cells with positive *Fw* duration trends correspond with a significant increase in non-frozen season length (Kim *et al*. 2012) and are located mainly in southeastern Russia. Similarly, 2.2% (712 grid cells) of the Arctic-boreal permafrost zone shows a significant decrease in Fw_{avg} inundation (Figure 7) and corresponds to an average *Fw* decline of 0.17% (1.05 km^2 per cell yr^{-1}); 2.5% of these (18 grid cells, within the sporadic/isolated zone in Québec) are associated with a significant decrease in *Fw* duration but do not correspond to documented trends in non-frozen period length (Kim *et al.* 2012).

2.5 Discussion

2.5.1 Fw verification and surface water patterns

The regional inundation patterns derived from the AMSR-E *Fw* retrievals are similar to alternative open water maps derived from the finer scale MOD44W and Landsat products despite the inherent coarser spatial resolution of the AMSR-E footprint. The favorable accuracy of AMSR-E *Fw* retrievals is attributed to the strong sensitivity of micro- wave emissivity to landscape variations in surface dielectric constant caused by the presence of even a small fraction of surface water relative to a non-inundated land surface. Differences between the static open water maps (Fw_S) and dynamic *Fw* retrievals are primarily due to differences in the seasonal timing and duration of the sensor retrievals. Stronger similarities between AMSR-E Fw_{avg} and MOD44W Fw_S results occurred at lower (< 60°N) latitudes where the MOD44W results are largely derived from SRTM, which has microwave characteristics like AMSR-E, including relative insensitivity to atmosphere effects (e.g. clouds), enhanced sensitivity to surface water cover and insensitivity to surface water signal contamination by vegetation (Pietroniro &

Leconte 2005). The stronger regional similarity may also be influenced by differences in wetland type and characteristic inundation patterns between lower and higher latitude regions.

The general Fw_{avg} dry bias reflects the tendency for higher Fw_S in temporally dynamic inundation regions due to limited (e.g. summer-only) satellite optical-IR image collection periods. The AMSR-E *Fw* results indicate large seasonal and inter-annual variability in Arctic–Boreal zone inundation, with respective Fw_{avg} variability (SD) on the order of ±60% (± 6.4 × 10^5 km^2) and ± 3% (± 3.1 × 10^4 km^2); this dynamic variability is not adequately represented by the static open water maps. The AMSR-E Fw_{avg} retrievals are also lower than the Fw_S results in characteristically dynamic inundation areas along major river corridors and in other areas where inundation is largely absent during dry periods but abundant following seasonal snowmelt or rain events (Brown & Young 2006).

Although the AMSR-E *Fw* dry bias is effectively eliminated or reversed (wet bias) for the Fw_{mx} results, it remains evident along river systems and seasonally varying lakes and wetlands. In contrast, the AMSR-E Fw_{avg} and Fw_{mx} results are predominately wetter than the Fw_S results in wetland dominated landscapes (e.g. Canadian Shield, Yenisey and Lena river basins). The lower Fw_S inundation levels within these regions may be due to reduced open water detection by optical-IR satellite sensors in areas with higher vegetation density (Kaheil & Creed 2009, Ozesmi & Bauer 2002). Excluding vegetated wetland and frozen lake bodies from the Landsat-based Fw_S calculations may have contributed to differences between the AMSR-E *Fw* and Fw_S results in the Alaska and North Central Canada sub-regions. However, similar areas of relatively higher AMSR-E *Fw* inundation, including the Ob-Yenisey lowlands and Canadian Shield, are evident in the MOD44W comparison where the exclusion of wetland and frozen classes is not an issue.

The AMSR-E *Fw* sensitivity to seasonal and annual surface water variability is also demonstrated in the comparison against river Q. Severe, multi-year (2001-2003) boreal drought conditions (Alkama *et al.* 2010, Zhang *et al.* 2008) are manifested as large negative *Fw* and Q anomalies for the Yukon, Mackenzie and Yenisey rivers in 2004. Large positive *Fw* and Q anomalies coincide with major flooding events in 2007 for the Ob (Schroeder *et al.* 2010), and 2009 for the Yukon, Mackenzie, Lena and Yenisey due to a combination of river ice jams, rapid snowmelt and precipitation (Arndt *et al.* 2010, Rowland *et al.* 2009). These findings are like

prior studies reporting strong correlations between satellite microwave *Fw* retrievals and Q over Arctic river systems (Papa *et al.* 2010, Schroeder *et al.* 2010). Linkages between basin *Fw* and Q response can be complex and do not always show direct correspondence (Papa *et al.* 2008), as is observed for the Mackenzie basin in 2004 and 2010. These differences are driven by the timing and duration of spring snowmelt and groundwater contributions, river ice jams, precipitation events, reservoir outflow and other changes in hydrological connectivity and Q that may not correspond directly to *Fw* changes (McClelland *et al.* 2011). Furthermore, the *Fw* parameter corresponds directly to surface water area, whereas Q can vary independently in response to additional water storage (e.g. soil, snow, and groundwater) fluctuations (Landerer *et al.* 2010).

The AMSR-E *Fw* patterns for the Arctic–boreal (≥ 50°N) domain are consistent with previous regional observations (Schroeder *et al.* 2010, Smith *et al.* 2007). In North America, the AMSR-E Fw_{avg} results reveal widespread inundation within the Canadian Shield region, a landscape characterized by expansive peatlands, lake systems and large soil organic carbon pools (Tarnocai 2006). In Eurasia, *Fw* inundation is relatively extensive within the major Arctic river basins (particularly along the Yenisey and in the Okrug-Yugra Ob river region), southern Finland and the Russian Republic of Karelia. More extensive inundation occurs along the Volga river system and in peatlands of the southern West Siberian lowlands (Kremenetski *et al.* 2003). Inundation extent is lowest in the January-February period when much of the landscape is frozen, and is highest in July (Fw_{mx}) and August (Fw_{avg}) following seasonal thawing and summer precipitation.

The earlier seasonal maximum observed in Fw_{mx} likely reflects extensive overland flow following snowmelt and rain events on still-frozen surfaces (Woo *et al.* 2006). The seasonal inundation variability observed in the AMSR-E *Fw* retrievals reflects strong correspondence between surface inundation and regional temperature and precipitation patterns in northern landscapes (Rouse 2000). This is particularly evident in Eurasia where a sharp decline in inundation extent following the summer *Fw* maximum coincides with characteristic high evaporation rates and low precipitation in late summer and fall (Landerer *et al.* 2010, Serreze & Etringer 2003). The temporal *Fw* variability observed in the major wetland and agricultural regions is also consistent with similar seasonal changes in precipitation and evaporation for these areas (Rouse 2000).

2.5.2 Fw trends

The per-grid cell analysis indicates widespread Fw_{avg} increase within continuous permafrost areas and overall decline within the sporadic/ isolated permafrost zone. These inundation trends concur with reports from localized field studies throughout the Arctic-boreal region (Jones *et al.* 2011a, Smith *et al.* 2005, Walter *et al.* 2006, Yoshikawa & Hinzman 2003). The high proportion of grid cells showing positive *Fw* inundation trends in the discontinuous permafrost zone appears to contradict previous reports of declining lake numbers within discontinuous permafrost areas in Siberia and Alaska (Smith *et al.* 2005, Yoshikawa & Hinzman 2003). A few key differences account for this apparent discrepancy. First, our study evaluated a continuous daily *Fw* record in permafrost zones across the entire Arctic-boreal domain over an eight-year period, which enabled a relatively precise assessment of dynamic inundation changes, whereas previous studies were constrained by a limited number of observation days and involved relatively small spatial domains.

Additionally, the AMSR-E *Fw* retrievals provide a measure of the proportional surface water cover within a relatively coarse (25-km) resolution grid cell, rather than specific lake number counts. The *Fw* retrievals do not resolve individual water bodies, but are insensitive to signal degradation from low solar illumination and atmosphere (clouds, smoke) contamination, and have enhanced microwave sensitivity to surface inundation in vegetated areas. These attributes are particularly relevant in Arctic-boreal landscapes, which have characteristically low solar illumination, short non-frozen seasons and frequent cloud cover, and in the continuous permafrost zone where lateral drainage from primary lakes can increase the number of smaller water bodies without an overall change in surface water extent (Jones *et al.* 2011a, White *et al.* 2007).

The re-distribution of surface water through lateral drainage could have contributed to the observed expansion in the annual number of grid cells with *Fw* present within permafrost regions. Satellite optical-IR remote sensing analyses might detect an overall decrease in total water body area where lateral drainage is occurring if smaller water bodies (e.g. ponds, small streams, wetlands) are obscured by vegetation, or if only primary lakes are examined. This may account for an apparent discrepancy between a recent MODIS-based study indicating an extensive reduction in surface lake area over northern Canada (Carroll *et al.* 2011), and this

study which shows a general *Fw* increase in many of the same regions, particularly in the northwestern Canadian Shield. The timing of the MODIS retrievals used by Carroll *et al.* (2011) may have also influenced the resulting lake trends as bedrock-underlain water bodies within this region depend on precipitation recharge and therefore show strong seasonal and annual variability (Spence & Woo 2008). Because our evaluations incorporate daily AMSR-E *Fw* observations during the non-frozen period, some of the observed increase in *Fw* inundation may be artifacts of a lengthening non-frozen season trend (Kim *et al.* 2012). However, only a small proportion (2.6%) of grid cells with significant *Fw* inundation increase also show a significant in-crease in annual *Fw* duration, and less than 0.7% of these cells coincide with an increase in the non-frozen season. Likewise, only 2.5% of grid cells having a significant decreasing *Fw* inundation trend also show a significant change in *Fw* duration, and none of these cells indicate a significant trend in non-frozen season length.

Although the per-grid cell analysis shows areas of significant *Fw* wetting and drying trends within Arctic-boreal permafrost zones, results from the regional analysis are less clear but indicate that *Fw* presence and annual duration are increasing. Only the regional Fw_{mx} (monthly maximum) results indicate increasing trends in inundation area, although a weak ($p = 0.13$) positive Fw_{avg} trend is detected for continuous permafrost areas. The overall lack of significant inundation trends in the regional Fw_{avg} results is likely due to the large spatial variability in *Fw* patterns where areas with positive *Fw* trends are offset by regions with declining inundation, and the characteristically large temporal variability in inundation and relatively short (8 year) AMSR-E *Fw* record. The Fw_{mx} trend is likely more sensitive to surface inundation extremes following spring thaw, snowmelt and precipitation related wetting events, whereas Fw_{avg} is temporally smoothed and provides a better measure of overall mean inundation state. Smaller, palustrine wetlands are especially affected by changes in wetting events. Water bodies are also influenced by changes in precipitation (Rawlins *et al.* 2010), in addition to recharge from localized ice melt or lateral drainage (Jones *et al.* 2011a, White *et al.* 2007), human-related activities and erosional processes (Hinkel *et al.* 2007), changes in water table position and disturbance from wildfires (Riordan *et al.* 2006).

The significant increase in regional *Fw* duration, primarily for the continuous and North American discontinuous permafrost zones, indicates an expanding non-frozen season and

corresponding longer inundation period influenced by rainfall (Woo *et al.* 2006). Increased evapotranspiration could also affect *Fw* duration in regions where lakes and wetlands are influenced by the seasonal water balance (Adam & Lettenmaier 2008, Riordan *et al.* 2006). However, the overall water balance in the Arctic-boreal remains largely positive, as indicated by generally increasing trends in regional river discharge (McClelland *et al.* 2006, Peterson *et al.* 2002, Rawlins *et al.* 2010) and the increase in *Fw* area reported in this study.

The variability in *Fw* trends throughout the Arctic-boreal region reflects large spatial heterogeneity in climate, surface conditions and permafrost state. The continuous permafrost zone is particularly susceptible to degradation due to rapid warming following sub-surface ice melt (Romanovsky *et al.* 2010). Spatial differences in surface temperature and snow thickness also influence variability in permafrost thaw (Rigor *et al.* 2000, Stieglitz *et al.* 2003).

Ecosystem characteristics have allowed permafrost to persist under climatic conditions no longer conducive to its formation (Shur & Jorgenson 2007). Plant canopies reduce understory snow accumulation (winter ground insulation) and summer radiative warming; surface organic layers maintain cool, moist conditions that provide additional thermal buffering (Smith & Riseborough 2002). These environmental factors allow relatively less degraded permafrost to persist within discontinuous and sporadic/isolated permafrost zones. Thaw within these regional pockets influences inundation expansion, as was observed in Québec CN near Hudson Bay where an abundance of thaw lakes has been documented (Watanabe *et al.* 2011). In some areas, climate warming may overwhelm ecosystem buffering, as was observed in Québec and Labrador CN where surface drying has resulted from increased summer warming trends (Mekis & Vincent 2011) in addition to thaw depth and sub-surface drainage expansion. Extensive peat accumulation on thawed surfaces and thermokarst ponds can also decrease open water inundation area and may be responsible for the observed *Fw* decrease in northeastern Canada (Filion & Begin 1998, Minayeva & Sirin 2010).

2.6 Conclusions

We conducted an analysis of fractional surface water (*Fw*) inundation for the Arctic-boreal region using daily satellite passive microwave remote sensing retrievals from the AMSR-E sensor record. The daily *Fw* retrievals were temporally aggregated to monthly mean (Fw_{avg})

and maximum (Fw_{MX}) temporal intervals and represent the proportion of surface water inundation within an approximate 25-km resolution footprint. Our results indicate large seasonal and inter-annual variability in Arctic-boreal regional inundation, with respective *Fw* variability (SD) on the order of ± 60% (± 6.4×10^5 km^2) and ± 3% (± 3.1×10^4 km^2). The total annual inundation extent (km^2) for the domain was largely stable over the 2003-2010 observation period; this finding concurs with an earlier assessment covering the 1993-2000 period (Papa *et al.* 2010). However, our results also indicate locally significant, contrasting *Fw* wetting and drying trends in permafrost affected areas.

Regions of widespread inundation increase are observed throughout the continuous permafrost zone, while *Fw* drying is predominant within sporadic/isolated permafrost areas. Methane emission levels are strongly influenced by open water extent (Walter *et al.* 2007). Areas showing increased Fw wetting are of concern as atmospheric CH_4 is a potent greenhouse gas and recent increases from Arctic wetlands have been reported (Bloom *et al.* 2010). In lieu of climatic conditions favorable to permafrost development and continued surface wetting, an overall decline in *Fw* inundation area appears likely (Avis *et al.* 2011, van Huissteden *et al.* 2011). Nevertheless, total Arctic-boreal zone inundation will remain stable if *Fw* expansion continues to offset regions of inundation decline.

Surface water inundation changes captured by the AMSR-E *Fw* retrievals provide an indicator of recent climate variability within northern landscapes, though the spatiotemporal distribution and underlying drivers of open water change need to be better understood to adequately separate longer term inundation trends from characteristically large seasonal and inter-annual *Fw* variability (Prowse & Brown 2010). A forward model sensitivity analysis indicated that the AMSR-E *Fw* retrievals are relatively accurate (conservative RMSE uncertainty within ± 4.1%), and that the *Fw* results effectively detect sub-grid surface inundation relative to finer scale (30-m to 250-m resolution) static open water maps. The relative consistency in resolving regional patterns and enhanced microwave sensor capabilities for continuous monitoring provide for improved resolution of characteristic dynamic seasonality and periodic wet/dry cycles in surface inundation across the Arctic-boreal domain.

The combination of frequent *Fw* monitoring from satellite passive microwave sensor records and finer scale open water maps available from satellite optical-IR and radar sensor

records may enable improved resolution of spatial patterns and seasonal to annual variability in regional water bodies that can be used in context with available climate data to improve understanding of regional climate change impacts to surface hydrology, energy and carbon cycles in Arctic-boreal regions. More detailed information concerning the temporal variability in inundation extent and the separation of *Fw* into wetland and lake area components will benefit carbon modeling efforts, especially for CH_4 emissions, which are strongly influenced by the extent and duration of surface inundation.

2.7 References

Adam, J C, D P Lettenmaier (2008) Application of new precipitation and reconstructed streamflow products to streamflow trend attribution in northern Eurasia. *J. Clim.*, 21: 1807–1828.

Alkama, R, B Decharme, H Douville, M Becker, A Cazenave, J Sheffield, et al. (2010) Global evaluation of the ISBA-TRIP continental hydrological system. Part 1: Comparison to GRACE terrestrial water storage estimates and in situ river discharges. *American Met.Soc.*, 11: 583–600.

Amarin, R, C Ruf, L Jones (2010) Impact of spatial resolution on wind field derived estimates of air pressure depression in the hurricane eye. *Remote Sens.*, 2: 665–672.

Anisimov, O A (2007) Potential feedback of thawing permafrost to the global climate system through methane emission. *Environ. Res. Lett.*, 2 (7 pp.).

Anisimov, O A, S Reneva (2006) Permafrost and changing climate: The Russian perspective. *Ambio*, 35: 169–175.

Arndt, D S, M O Baringer, M R Johnson (Eds.) (2010) State of the climate in 2009. *Bull. American Met. Soc.*, 91 (224 pp.).

Avis, C A, A J Weaver, K J Meissner (2011) Reduction in areal extent of high-latitude wetlands in response to permafrost thaw. *Nature Geosci. Lett.*, 4: 444–448.

Bloom, A A, P I Palmer, A Fraser, D S Reay, C Frankenberg (2010) Large-scale controls of Methanogenesis inferred from methane and gravity spaceborne data. *Science*, 327: 322–325.

Brown, J, O J Ferrians, J A Heginbottom, E S Melnikov (1998) Circum-Arctic map of permafrost and ground-ice conditions. Boulder, CO: National Snow and Ice Data

Center/World Data Center for Glaciology. Digital Media.

Brown, L, K L Young (2006) Assessment of three mapping techniques to delineate lakes and ponds in a Canadian High Arctic wetland complex. *Arctic*, 59: 283–293.

Camill, P (2005) Permafrost thaw accelerates in boreal peatlands during late 20th century climate warming. *Climatic Change*, 68: 135–152.

Carroll, M L, J R G Townshend, C M DiMiceli, T Loboda, R A Sohlberg, R A (2011) Shrinking lakes of the Arctic: Spatial relationships and trajectory of change. *Geophys. Res. Lett.*, 38 (5 pp.).

Carroll, M, J Townshend, C DiMiceli, P Noojipady, R Sohlberg (2009) A new global raster water mask at 250 meter resolution. *Int. J. Digital Earth*, 2: 291–308.

Chandler, R E, E M Scott (2011) Statistical methods for trend detection and analysis in the environmental sciences. West Sussex, UK: Wiley & Sons, Ltd. 368 pp.

Chang, A T, A S Milan (1982) Retrieval of ocean surface and atmospheric parameters from multichannel microwave radiometric measurements. *IEEE Trans. Geosci. Remote Sens.*, 2: 217–224.

Filion, L, Y Begin (1998) Recent paludification of kettle holes on the central islands of Lake Bienville, northern Quebec, Canada. *The Holocene*, 8: 91–96.

Fily, M, A Royer, K Goita, C Prigent (2003) A simple retrieval method for land surface temperature and fraction of water surface determination from satellite microwave brightness temperatures in sub-arctic areas. *Remote Sens. Environ.*, 85: 328–338.

Frauenfeld, O W, T Zhang, R G Barry, D Gilichinsky (2004) Interdecadal changes in seasonal freeze and thaw depths in Russia. *J. Geophys. Res.*, 109 (12 pp.).

Geobase Canada (2009) Land Cover, Circa 2000 Vector. Vector Digital Data. Government of Canada, Natural Resources Canada, Earth Sciences Sector, Centre for Topographic Information-Sherbrooke.

Graversen, R G, T Mauritsen, M Tjernstrom, E Källén, G Svensson (2008) Vertical structure of recent Arctic warming. *Nature*, 541: 53–56.

Hinkel, K M, B M Jones, W R Eisner, C J Cuomo, R A Beck, R Frohn (2007) Methods to assess natural and anthropogenic thaw lake drainage on the western Arctic coastal plain of northern Alaska. *J. Geophys. Res.*, 112 (9 pp.).

Hinzman, L D, N D Bettez, W R Bolton, F S Chapin, M B Dyurgerov, C L Fastie, et al. (2005) Evidence and implications of recent climate change in northern Alaska and other Arctic

regions. *Climatic Change*, 72: 251–298.

Hipel, K W, A I McLeod (2005) Time series modeling of water resources and environmental systems. Electronic reprint of book (http://www.stats.uwo.ca/faculty/aim/ 1994Book/) originally published in 1994 by Elsevier, Amsterdam, The Netherlands (1013 pp.).

Homer, C, C Huang, L Yang, B Wylie, M Coan (2004) Development of a 2001 national land cover database for the United States. *Photogrammetric Eng. Remote Sens.*, 70: 829–840.

Jones, B, M G Grosse, C D Arp, M C Jones, K M Walter Anthony, V E Romanovsky (2011a) Modern thermokarst lake dynamics in the continuous permafrost zone, northern Seward Peninsula, Alaska. *J. Geophys. Res.*, 116 (13 pp.).

Jones, L A, C R Ferguson, J S Kimball, K Zhang, S T K Chan, K C McDonald, et al. (2010) Satellite microwave remote sensing of daily land surface air temperature minima and maxima from AMSR-E. *IEEE J. Selected Topics Applied Earth Obs. Remote Sens.*, 3: 111–123.

Jones, L A, J S Kimball (2011c) Daily global land surface parameters derived from AMSR-E. Boulder Colorado USA: National Snow and Ice Data Center. Digital media http://nsidc.org/data/nsidc-0451.html

Jones, L A, J S Kimball, K C McDonald, S T K Chan, E G Njoku, W C Oechel (2007) Satellite microwave remote sensing of boreal and Arctic soil temperatures from AMSR-E. IEEE Trans. *Geosci. Remote Sens.*, 45 (15 pp.).

Jones, M O, L A Jones, J S Kimball, K C McDonald (2011b) Satellite passive microwave remote sensing for monitoring global land surface phenology. *Remote Sens. Environ.*, 115: 1102–1114.

Kaheil, Y H, I F Creed (2009) Detecting and downscaling wet areas on Boreal landscapes. *IEEE Geosci. Remote Sens. Lett.*, 6: 179–183.

Kaufman, D S, D P Schneider, N P McKay, C M Ammann, R S Bradley, K R Briffa, et al. (2009) Recent warming reverses long-term Arctic cooling. *Science*, 325: 1236–1239.

Kawanishi, T, T Sezai, Y Ito, K Imaoka, T Takeshima, Y Ishido, et al. (2003) The Advanced Microwave Scanning Radiometer for the Earth Observing System (AMSR-E), NASDA's contribution to the EOS for global energy and water cycle studies. *IEEE Trans. Geosci. Remote Sens.*, 41: 184–194.

Kennedy, J, H Titchner, D Parker, M Beswick, J Hardwick, P Thorne (2008) Global and regional climate in 2007. *Weather*, 63: 296–304.

Kim, Y, J S Kimball, K C McDonald, J Glassy (2011) Developing a global data record of daily landscape freeze/thaw status using satellite passive microwave remote sensing. *IEEE*

Trans. Geosci. Remote Sens., 49: 949–960.

Kim, Y, J S Kimball, K Zhang, K C McDonald (2012) Satellite detection of increasing Northern Hemisphere non-frozen seasons from 1979 to 2008: Implications for regional vegetation growth. *Remote Sens. Environ.*, 121: 472–487.

Kochtubajda, B, W R Burrows, D Green, A Liu, K R Anderson, D McLennan (2011) Exceptional cloud-to-ground lightning during an unusually warm summer in Yukon, Canada. *J. Geophys. Res.*, 116 (20 pp.).

Kremenetski, K V, A A Velichko, O K Borisova, G M MacDonald, L C Smith, K E Frey, et al. (2003) Peatlands of the western Siberian lowlands: current knowledge on zonation, carbon content and late Quaternary history. *Quaternary Sci. Rev.*, 22: 703–723.

Landerer, F W, J O Dickey, A Güntner (2010) Terrestrial water budget of the Eurasian pan-Arctic from GRACE satellite measurements during 2003–2009. *J. Geophys. Res.*, 115 (14 pp.).

Lehner, B, P Doell (2004) Development and validation of a global database of lakes, reservoirs and wetlands. *J. Hydro.*, 296: 1–22.

Matzler, C (2005) On the determination of surface emissivity from satellite observations. *IEEE Geosci. Remote Sens. Lett.*, 2: 160–163.

McClelland, J W, S J Dery, B J Peterson, R M Holmes, E F Wood (2006) A pan-arctic evaluation of changes in river discharge during the latter half of the 20th century. *Geophys. Res. Lett.* 33 (4 pp.).

McClelland, J W, R M Holmes, K H Dunton, R Macdonald (2011) The Arctic Ocean estuary. *Estuaries and Coasts*, 34 (16 pp.).

McClelland, J W, R M Holmes, B J Peterson, M Stieglitz (2004) Increasing river discharge in the Eurasian Arctic: Consideration of dams, permafrost thaw, and fires as potential agents of change. *J. Geophys. Res.*, 109 (12 pp.).

Mekis, É, L A Vincent (2011) An overview of the second generation adjusted daily precipitation dataset for trend analysis in Canada. *Atmosphere-Ocean*, 49: 163–177.

Mialon, A, A Royer, M Fily (2005) Wetland seasonal dynamics and interannual variability over northern high latitudes, derived from microwave satellite data. *J. Geophys. Res.* 110 (9 pp.).

Minayeva, T, A Sirin (2010) Arctic peatlands. Arctic biodiversity trends report 2010: Selected indicators of change (pp. 71–74).

Njoku, E G, L Li (1999) Retrieval of land surface parameters using passive microwave

measurements at 6–18 GHz. *IEEE Trans. Geosci. Remote Sens.*, 37: 79–93.

O'Connor, F M, O Boucher, N Gedney, C D Jones, G A Folberth, R Coppell, et al. (2010) Possible role of wetlands, permafrost, and methane hydrates in the methane cycle under future climate change: A review. *Reviews Geophys.*, 48 (33 pp.).

Oki, T, K Imaoka, M Kachi (2010) AMSR instruments on GCOM-W1/2: Concepts and applications. Geosciences and Remote Sensing Symposium (IGARSS), 2010 IEEE International. 25–30 July, 2010, Honolulu, HI (pp. 1363–1366).

Ozesmi, S L, M E Bauer (2002) Satellite remote sensing of wetlands. *Wetlands Ecol. Manage.*, 10: 381–402.

Papa, F, C Prigent, F Aires, C Jimenez, W B Rossow, E Matthews (2010) Interannual variability of surface water extent at the global scale, 1993–2004. *J. Geophy. Res.*, 115 (17 pp.).

Papa, F, C Prigent, W B Rossow (2008) Monitoring flood and discharge variations in the large Siberian rivers from a multi-satellite technique. *Surveys Geophys.*, 29: 297–317.

Parker, D E, J Kennedy, J Hardwick (2006) Global and regional climate in 2004. *Weather*, 60: 197–205.

Payette, S, A Delwaide, M Caccianiga, M Beauchemin (2004) Accelerated thawing of subarctic peatland permafrost over the last 50 years. *Geophys. Res. Lett.*, 31 (4 pp.).

Peterson, B J, R M Holmes, J W McClelland, C J Vorosmarty, R B Lammers, A I Shiklomanov, et al. (2002) Increasing river discharge to the Arctic Ocean. *Science*, 298: 2171–2173.

Pietroniro, A, R Leconte (2005) A review of Canadian remote sensing and hydrology, 1999–2003. *Hydrol. Proc.*, 19: 285–301.

Potapov, P, S Turubanova, M C Hansen (2011) Regional-scale boreal forest cover and change mapping using Landsat data composites for European Russia. *Remote Sens. Environ.*, 115: 548–561.

Prowse, T D, K Brown (2010) Appearing and disappearing lakes in the Arctic and their impacts on biodiversity. Arctic Biodiversity Trends Report 2010: Selected indicators of change (pp. 68–70).

Rawlins, M A, M Steele, M M Holland, J C Adam, J E Cherry, J A Francis, et al. (2010) Analysis of the Arctic system for freshwater cycle intensification: observations and expectations. *J. Clim.*, 23: 5715–5737.

Rigor, I G, R L Colony, S Martin (2000) Variations in surface air temperature observations in the Arctic, 1979–97. *J. Clim.*, 13: 896–914.

Riordan, B, D Verbyla, A D McGuire (2006) Shrinking ponds in subarctic Alaska based on 1950–2002 remotely sensed images. *J. Geophys. Res.*, 111 (11 pp.).

Romanovsky, V E, S L Smith, H H Christiansen (2010) Permafrost thermal state in the Polar Northern Hemisphere during the International Polar Year 2007–2009: a synthesis. *Permafrost Periglacial Processes*, 21: 106–116.

Rouse, W R (2000) The energy and water balance of high-latitude wetlands: controls and extrapolation. *Global Change Bio.*, 6: 59–68.

Rowland, J C, C J Wilson, S P Brumby, P A Pope (2009) Arctic river mobility: A baseline assessment. American Geophysical Union, Fall Meeting 2009, abstract #H44C-05.

Schroeder, R, M A Rawlins, K C McDonald, E Podest, R Zimmermann, M Kueppers (2010) Satellite microwave remote sensing of North Eurasian inundation dynamics: Development of coarse-resolution products and comparison with high-resolution synthetic aperture radar data. *Environ. Res. Lett.*, 5 (7 pp.).

Selkowitz, D J, S V Stehman (2011) Thematic accuracy of the National Land Cover Database (NLCD) 2001 land cover for Alaska. *Remote Sens. Environ.*, 115: 1401–1407.

Serreze, M C, A J Etringer (2003) Precipitation characteristics on the Eurasian Arctic drainage system. *Int. J. Clim.*, 23: 1267–1291.

Shein, K A, A M Waple, H J Diamond, J M Levy (2007) State of the climate in 2005. World Meteorological Organization No. 1015. 114 pp.

Sheskin, D J (2004) Handbook of parametric and nonparametric statistical procedures. Boca Raton, FL: CRC Press/Chapman & Hall 719 pp.

Shur, Y L, M T Jorgenson (2007) Patterns of permafrost formation and degradation in relation to climate and ecosystems. *Permafrost Periglacial Process.*, 18: 8–19.

Smith, M W, D W Riseborough (2002) Climate and the limits of permafrost: a zonal analysis. *Permafrost and Periglacial Process.*, 13: 1–15.

Smith, L C, Y Sheng, G M MacDonald (2007) A first pan-Arctic assessment of the influence of glaciation, permafrost, topography and peatlands on Northern Hemisphere lake distribution. *Permafrost and Periglacial Process.*, 18: 201–208.

Smith, L C, Y Sheng, G M MacDonald, L D Hinzman (2005) Disappearing Arctic lakes. *Science*, 308: 1429.

Spence, C, M Woo (2008) Hydrology of the northwestern subarctic Canadian Shield. In M. Woo (Ed.), Cold Region Atmospheric and Hydrologic Studies. The Mackenzie GEWEX Experience. Hydrologic processes, Vol. 2. (pp. 235–256) Berlin: Springer-Verlag.

Stieglitz, M, S J Dery, V E Romanovsky, T E Osterkamp (2003) The role of snow cover in the warming of arctic permafrost. *Geophysical Res. Lett.*, 30 (4 pp.).

Syed, T H, J S Famiglietti, V Zlotnicki, M Rodell (2007) Contemporary estimates of Pan-Arctic freshwater discharge from GRACE and reanalysis. *Geophys. Res. Lett.*, 34 (6 pp.).

Tarnocai, C (2006) The effect of climate change on carbon in the Canadian peatlands. *Global Planetary Change*, 53: 222–232.

Tarnocai, C, J G Canadell, A G Schuur, P Kuhry, G Mazhitova, S Zimov (2009) Soil organic carbon pools in the northern circumpolar permafrost region. *Glob. Biogeochem. Cycles*, 23 (11 pp.).

van Huissteden, J, C Berrittella, F J W Parmentier, Y Mi, T C Maximov, A J Dolman (2011) Methane emission by permafrost thaw lakes limited by lake drainage. *Nature Climate Change*, 1: 119–123.

Walter, K M, L C Smith, F S Chapin III (2007) Methane bubbling from northern lakes: Present and future contributions to the global methane budget. *Phil. Trans. Royal Society A*, 365: 1657–1676.

Walter, K M, S A Zimov, J P Chanton, D Verbyla, F S Chapin, F. S., III (2006) Methane bubbling from Siberian thaw lakes as a positive feedback to climate warming. *Nature*, 443: 71–75.

Watanabe, S, I Laurion, K Chokmani, R Pienitz, W F Vincent (2011) Optical diversity of thaw ponds in discontinuous permafrost: A model system for water color analysis. *J. Geophys. Res.*, 116 (17 pp.).

Wegren, S K (2011) Food security and Russia's 2010 drought. *Eurasian Geo. Econ.*, 52: 140–156.

Wendler, G, J Conner, B Moore, M Shulski, M Stuefer (2010) Climatology of Alaskan wildfires with special emphasis on the extreme year of 2004. *Theoretical Applied Climat.*, 99: 67–74.

Weng, F, N C Grody (1998) Physical retrieval of land surface temperature using the special sensor microwave imager. *J. Geophys. Res.*, 103: 8839–8848.

White, D, L L Hinzman, L Alessa, J Cassano, M Chambers, K Falkner et al. (2007). The arctic freshwater system: Changes and impacts. *J. Geophy. Res.*, 112 (21 pp.).

Wilks, D S (2006) On “field significance” and the false discovery rate. *J. Applied Met. Clim.*, 45: 1181–1189.

WMO (2005) WMO statement on the status of the global climate in 2004. The World Meteorological Organization WMO-No. 983. (12 pp.).

WMO (2011) WMO statement on the status of the global climate in 2010. The World Meteorological Organization WMO-No. 1074. (20 pp.).

Woo, M, K L Young, L Brown (2006) High Arctic wetlands: Their occurrence, hydrological characteristics and sustainability. *J. Hydro.*, 320: 432–450.

Yang, D, B Ye, A Shiklomanov (2004) Discharge characteristics and changes over the Ob river watershed in Siberia. *American Met. Society*, 5: 595–610.

Yoshikawa, K, L D Hinzman (2003) Shrinking therokarst ponds and groundwater dynamics in discontinuous permafrost near council, Alaska. *Permafrost Periglacial Process.*, 14: 151–160.

Yue, S, P Pilon, B Phinney, G Cavadias (2002) The influence of autocorrlation on the ability to detect trend in hydrological series. *Hydrol. Process.*, 16: 1807–1829.

Zhang, K, J S Kimball, E H Hogg, M Zhao, W C Oechel, J J Cassano, et al. (2008) Satellite-based model detection of recent climate-driven changes in northern high-latitude vegetation productivity. *J. Geophys. Res.*, 113 (13 pp.).

Zhang, K, J S Kimball, Q Mu, L A Jones, S J Goetz, S W Running (2009) Satellite based analysis of northern ET trends and associated changes in the regional water balance from 1983 to 2005. *J. Hydrol.*, 379: 92–110.

Zhang, Q, C Liu, C Xu, Y Xu, T Jiang (2006) Observed trends of annual maximum water level and streamflow during past 130 years in the Yangtze River basin, China. *J. Hydrol.*, 324: 255–265.

Tables

Table 2.1 Commonly used nomenclature.

Nomenclature	
Symbol	Explanation
Fw	Fractional open water cover
Fw_{avg}	AMSR-E Fw, monthly mean
Fw_{mx}	AMSR-E Fw, monthly maximum
Fw_s	Fw derived from static classification maps
Tb	AMSR-E brightness temperature, 18.7 and 23.8 GHz
Tb_u	Upwelling atmospheric brightness temperature
Tb_d	Downwelling atmospheric brightness temperature
Tb_s	Upwelling surface brightness temperature
Tb_l	Tb emissions from land components
Tb_w	Tb emissions from water components
T_a	Air temperature (~ 2 m height)
T_s	Surface temperature
δ	Ratio of T_a to T_s
τ	Vegetation optical depth
V_p	Total column water vapor in atmosphere
ε	Emissivity
ε_s	Emissivity, surface
ε_l	Emissivity, land surface
ε_{os}	Emissivity, bare soil
ε_w	Emissivity, open water
t_a	Transmissivity
t_c	Attenuation of upwelling Tb_s by canopy and litter
Ω	Surface roughness
ω	Vegetation single scattering albedo

Table 2.2 Summary of statistical comparisons for AMSR-E monthly means (Fw_{avg}) and maximums (Fw_{mx}) against the MOD44W static open water (Fw_s) map for the pan-Arctic domain, and regional (Northern Europe, Alaska, North Central CN) Fw_s maps from Landsat. Measures of similarity include coefficient of determination (R^2), mean residual error (MRE) for AMSR-E Fw - Fw_s, and RMSE. The relationships are significant at a 0.05 probability level.

Region	R^2		% MRE		% RMSE	
	Fw_{avg}	Fw_{mx}	Fw_{avg}	Fw_{mx}	Fw_{avg}	Fw_{mx}
pan-Arctic (all)	0.77	0.72	-0.82	4.92	5.55	6.01
pan-Arctic (< 60°N)	0.84	0.75	-0.92	4.43	3.90	4.86
pan-Arctic (≥ 60 °N)	0.71	0.69	-0.70	5.48	6.90	7.01
N. Europe	0.78	0.39	-0.56	5.34	1.86	3.15
Alaska	0.81	0.80	-1.87	3.00	6.27	6.42
N. C. Canada	0.75	0.75	-8.21	-0.96	4.53	4.51

Table 2.3 Summary of statistical comparisons for AMSR-E monthly means (Fw_{avg}) and maximums (Fw_{mx}) against the MOD44W static open water (Fw_s) map for the pan-Arctic domain, and regional (Northern Europe, Alaska, North Central CN) Fw_s maps from Landsat. Measures of similarity include coefficient of determination (R^2), mean residual error (MRE) for AMSR-E Fw - Fw_s, and RMSE. The relationships are significant at a 0.05 probability level.

Region	R^2		% MRE		% RMSE	
	Fw_{avg}	Fw_{mx}	Fw_{avg}	Fw_{mx}	Fw_{avg}	Fw_{mx}
pan-Arctic (all)	0.77	0.72	-0.82	4.92	5.55	6.01
pan-Arctic (< 60°N)	0.84	0.75	-0.92	4.43	3.90	4.86
pan-Arctic (≥ 60 °N)	0.71	0.69	-0.70	5.48	6.90	7.01
N. Europe	0.78	0.39	-0.56	5.34	1.86	3.15
Alaska	0.81	0.80	-1.87	3.00	6.27	6.42
N. C. Canada	0.75	0.75	-8.21	-0.96	4.53	4.51

Table 2.4 Mann Kendall tau trend strength for AMSR-E *Fw* in the pan-Arctic domain, individual permafrost (PF) zones and associated sub-regions. Regional trends (yrs. 2003-2010) were evaluated for the total annual number of grid cells with *Fw* present (*Fw* Count), the mean annual duration of *Fw* inundation (*Fw* Duration), and percent change in mean annual inundation area (*Fw* Area) derived from *Fw* monthly means (Fw_{avg}) and maximums (Fw_{mx}). The sub-regions evaluated include North America (NA) and Eurasia (EA), continuous (C), discontinuous (D), and sporadic/isolated (S) PF zones. The possible range for tau is -1 to 1 and the sign indicates trend direction; |1| indicates a perfect rank agreement with time. Trend significance (in bold) is denoted by asterisks * and ** for respective 0.1 and 0.05 probability levels.

Region	*Fw* Count	*Fw* Duration	*Fw* Area	
			Fw_{avg}	Fw_{mx}
Pan-Arctic (≥ 50°N)	0.34	**0.71****	0.33	0.24
NA	0.24	**0.71****	0.14	0.33
EA	0.33	0.52	-0.05	0.14
All PF zones	**0.81****	**0.71****	0.43	**0.62***
C	**0.71****	**0.90****	0.53	**0.71****
D	**0.62***	**0.71****	0.24	0.43
S	**0.62***	0.52	-0.14	0.42
C-NA	0.24	**0.90****	0.42	0.52
C-EA	**0.62***	**0.90****	0.43	**0.61***
D-NA	**0.62***	**0.71****	0.52	**0.62***
D-EA	0.52	0.52	-0.33	-0.05
S-NA	0.05	0.52	-0.05	0.14
S-EA	**0.62***	0.43	0.33	-0.04

Table 2.5 Trend slope estimates for AMSR-E *Fw* in the pan-Arctic domain, individual permafrost (PF) zones and associated sub-regions. The slope estimates (yrs. 2003-2010) were evaluated for the total annual number of grid cells with *Fw* present (*Fw* Count), the mean annual duration of *Fw* inundation (*Fw* Duration), and percent change in mean annual inundation area (*Fw* Area) derived from *Fw* monthly means (Fw_{avg}) and maximums (Fw_{mx}). The sub-regions evaluated include North America (NA) and Eurasia (EA), continuous (C), discontinuous (D), and sporadic/isolated (S) PF zones. Trend significance (in bold) is denoted by asterisks * and ** for respective 0.1 and 0.05 probability levels.

Region	*Fw* Count (cells yr^{-1})	*Fw* Duration (days yr^{-1})	*Fw* Area (% yr^{-1})	
			Fw_{avg}	Fw_{mx}
Pan-Arctic (≥ 50°N)	218.69	**0.76****	25,000	98,293
NA	10.28	**0.80****	4,648	43,787
EA	186.78	0.61	-2,938	18,047
All PF zones	**140.52****	**0.64****	36,929	**73,910***
C	**65.34****	**0.82****	16,179	**16,907****
D	**33.65***	**0.26****	4,583	12,493
S	**53.39***	0.78	8,285	31,573
C-NA	-4.59	**0.91****	13,375	966
C-EA	**51.90***	**0.76****	-1,127	**19,772***
D-NA	**15.97***	**0.43****	4,591	**10,101***
D-EA	16.54	0.11	-3,410	494
S-NA	0.85	0.65	5,438	12,287
S-EA	**38.68***	0.71	7,992	184

Figures

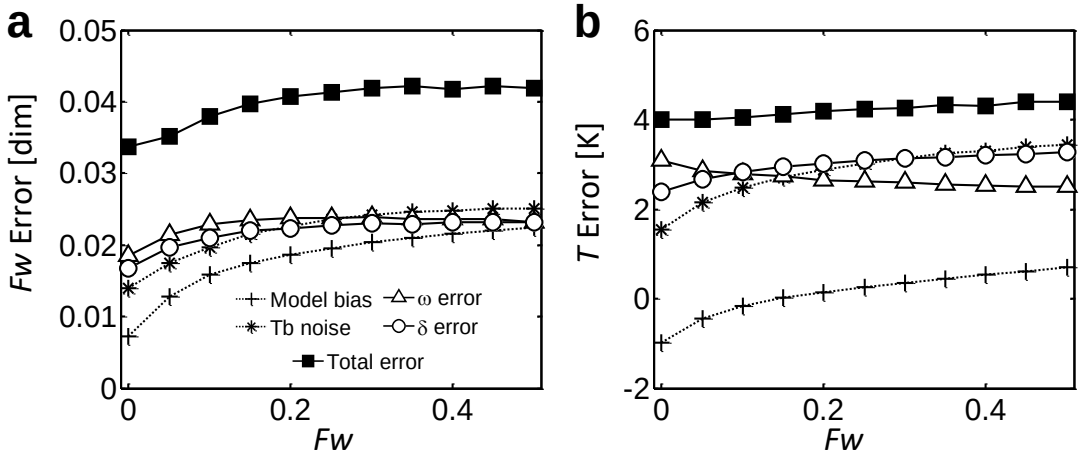

Figure 2.1 Simulated RMSE uncertainty for AMSR-E algorithm retrievals of *Fw* (**a**) and surface temperature (*T*) (**b**) expressed over a range of *Fw* variability. All data series contain both random errors from various sources denoted in the legend (See Section 2.2 for explanation) and systematic errors resulting from the simplified emission model (denoted as "Model bias" for the series without random error sources). Symbols represent mean RMSE values calculated across 30 simulation sets (1000 model runs per set) with *Fw* varying from 0 to 0.5 in 0.05 increments. The RMSE standard deviations for each group of sets are within the symbol bounds (≤ 0.0015 for *Fw* and ≤ 0.15 K for *T*).

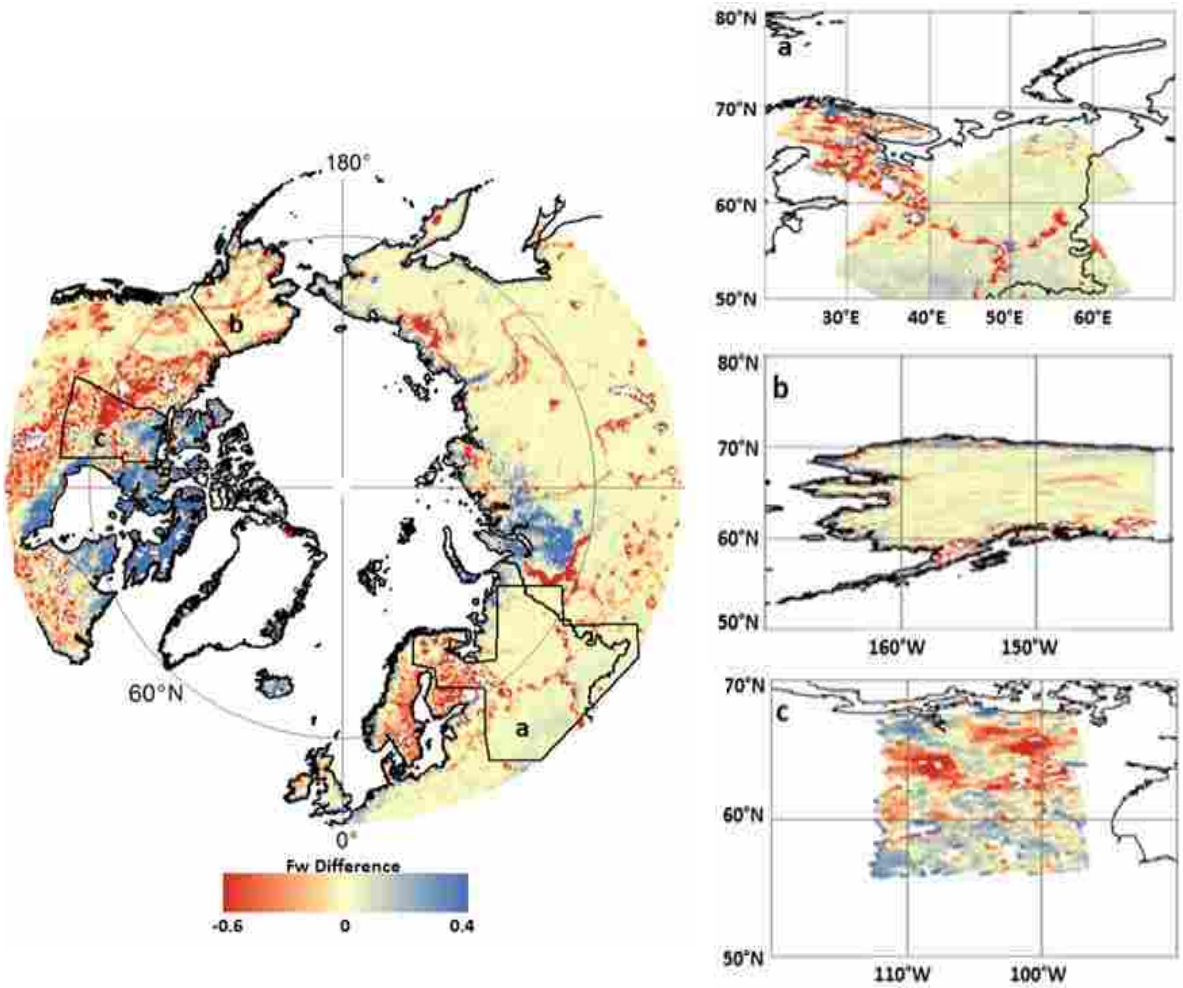

Figure 2.2 Difference maps between mean annual *Fw* determined from AMSR-E mean monthly *Fw* (Fw_{avg}) values minus corresponding static *Fw* (Fw_s) values from the MOD44W product for the pan-Arctic domain and Landsat based land cover classifications for three sub-regions: Northern Europe (**a**), Alaska (**b**) and North Central CN (**c**). Red hues show regions where MOD44W or Landsat-based Fw_s estimates are greater than AMSR-E Fw_{avg}, while blue hues indicate regions where AMSR-E Fw_{avg} values are higher than Fw_s.

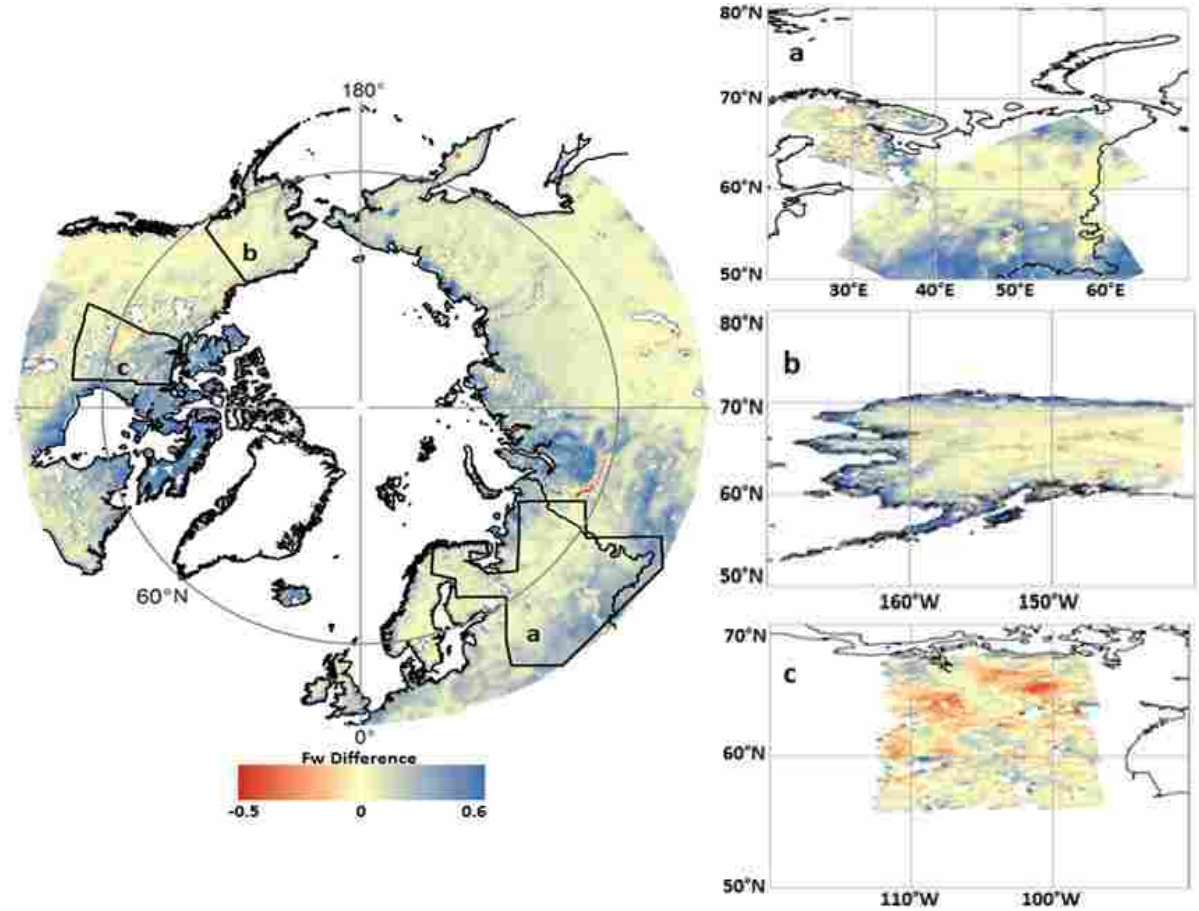

Figure 2.3 Difference maps between mean annual *Fw* determined from AMSR-E monthly maximum *Fw* values (Fw_{mx}) minus corresponding static *Fw* (Fw_s) values derived from the MOD44W product for the pan-Arctic domain and Landsat based land cover classifications for three sub-regions: Northern Europe (**a**), Alaska (**b**) and North Central CN (**c**). Red hues show regions where MOD44W or Landsat-based Fw_s estimates are greater than AMSR-E Fw_{mx}, while blue hues indicate regions where AMSR-E Fw_{mx} values are higher than Fw_s.

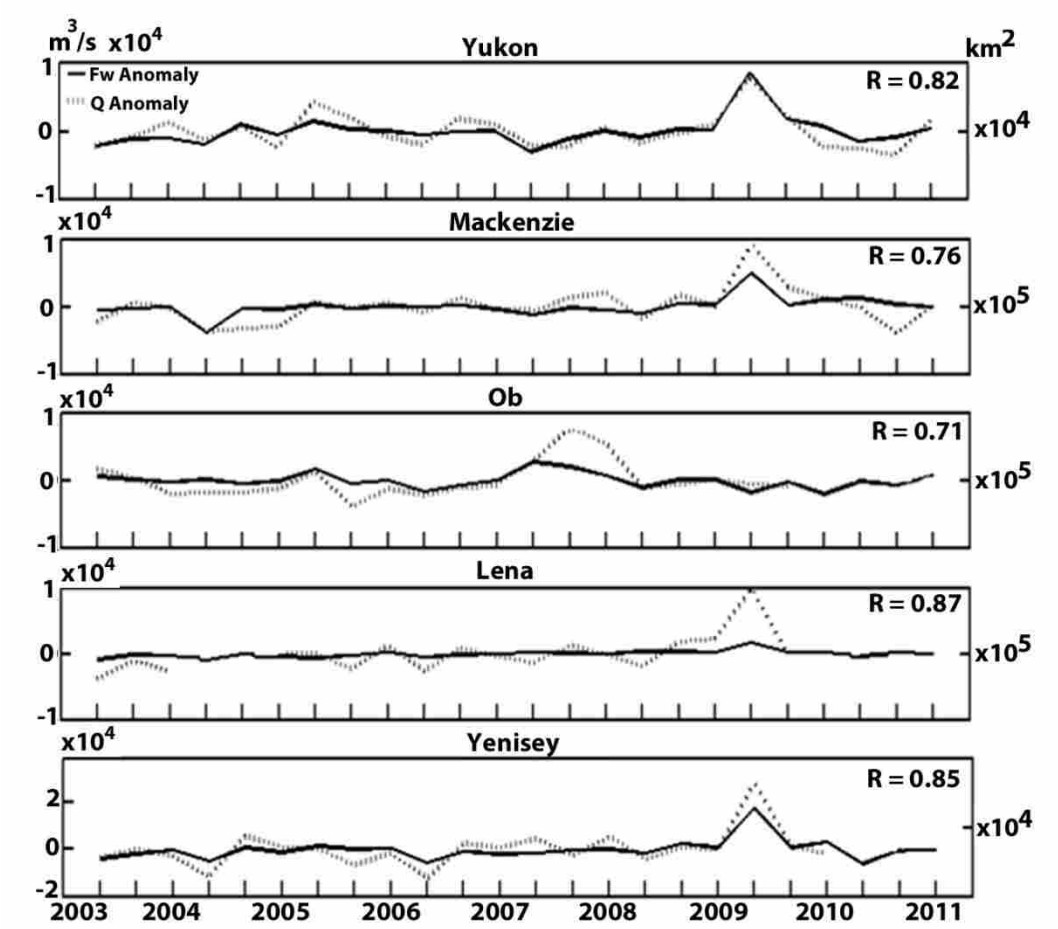

Figure 2.4 Mean river discharge (Q, m^3/s) and corresponding basin-averaged Fw_{avg} (km^2) anomalies for the Yukon, Mackenzie, Ob, Lena and Yenisey river basins over the 8 year (2003-2010) AMSR-E record. To minimize temporal lag effects between basin surface water storage and discharge, anomalies were calculated from bi-monthly means during the northern summer months (AM, JJ, AS), except for the Ob basin where the anomalies were derived from tri-monthly (MAM, JJA, SON) means. The temporal Q gaps in the Ob, Lena, and Yenisey records are due to missing station observations. Sample sizes for the correlation coefficients (R) range from 17 to 24 anomaly observations. Basin R values range from 0.71 to 0.87 and are significant at the 0.01 probability level.

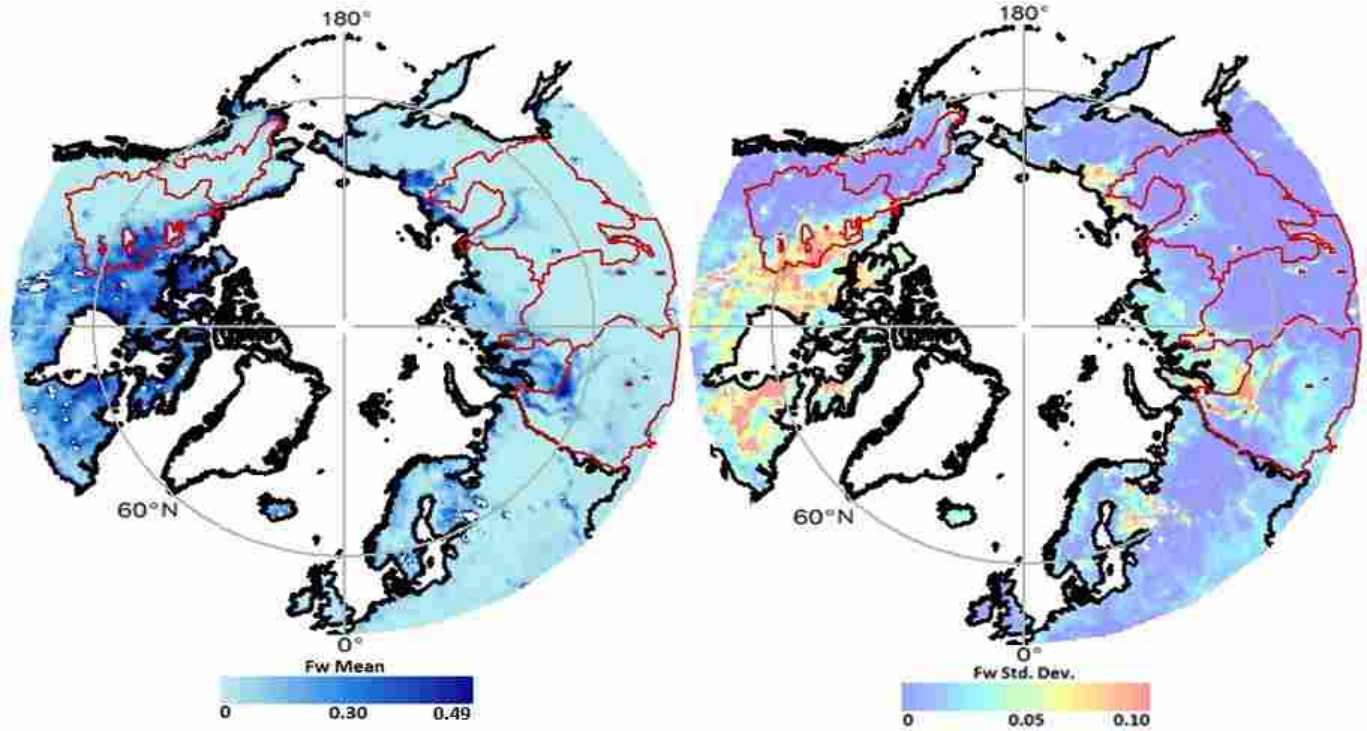

Figure 2.5 Study period (2003-2010) *Fw* means (left) and corresponding standard deviations (right) for the pan-Arctic domain ($\geq$ 50ºN) as determined from AMSR-E *Fw* monthly means (Fw_{avg}). The Yukon, Mackenzie, Ob, Lena and Yenisey river basins are outlined in red.

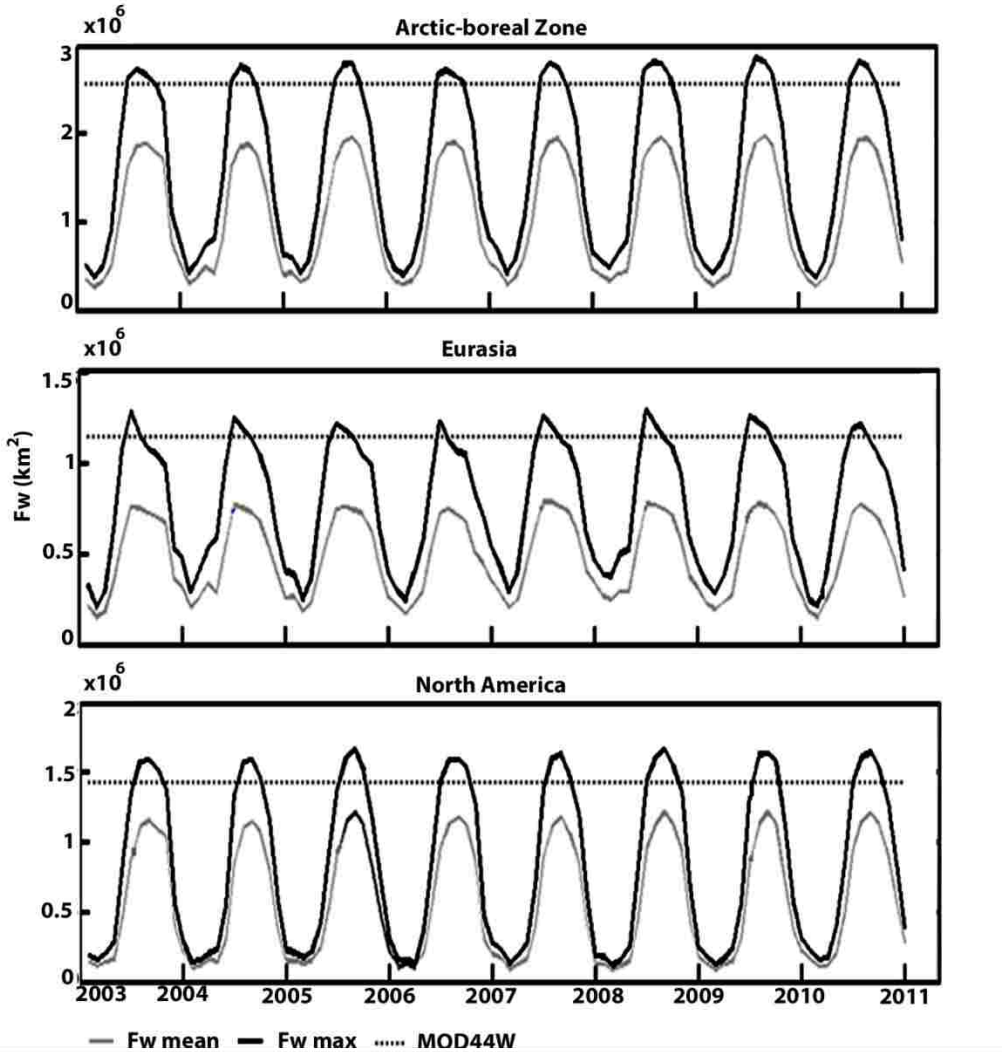

Figure 2.6 Seasonal progressions in AMSR-E *Fw* area (km^2) for selected regions within the pan-Arctic domain ($\geq$ 50 ^{o}N) as determined from *Fw* monthly means (Fw_{avg}, in gray) and monthly maximums (Fw_{mx}, in black) for the study period (2003-2010). Static *Fw* estimates (Fw_s) from the MOD44W open water map (black, dashed) are presented for the same regions.

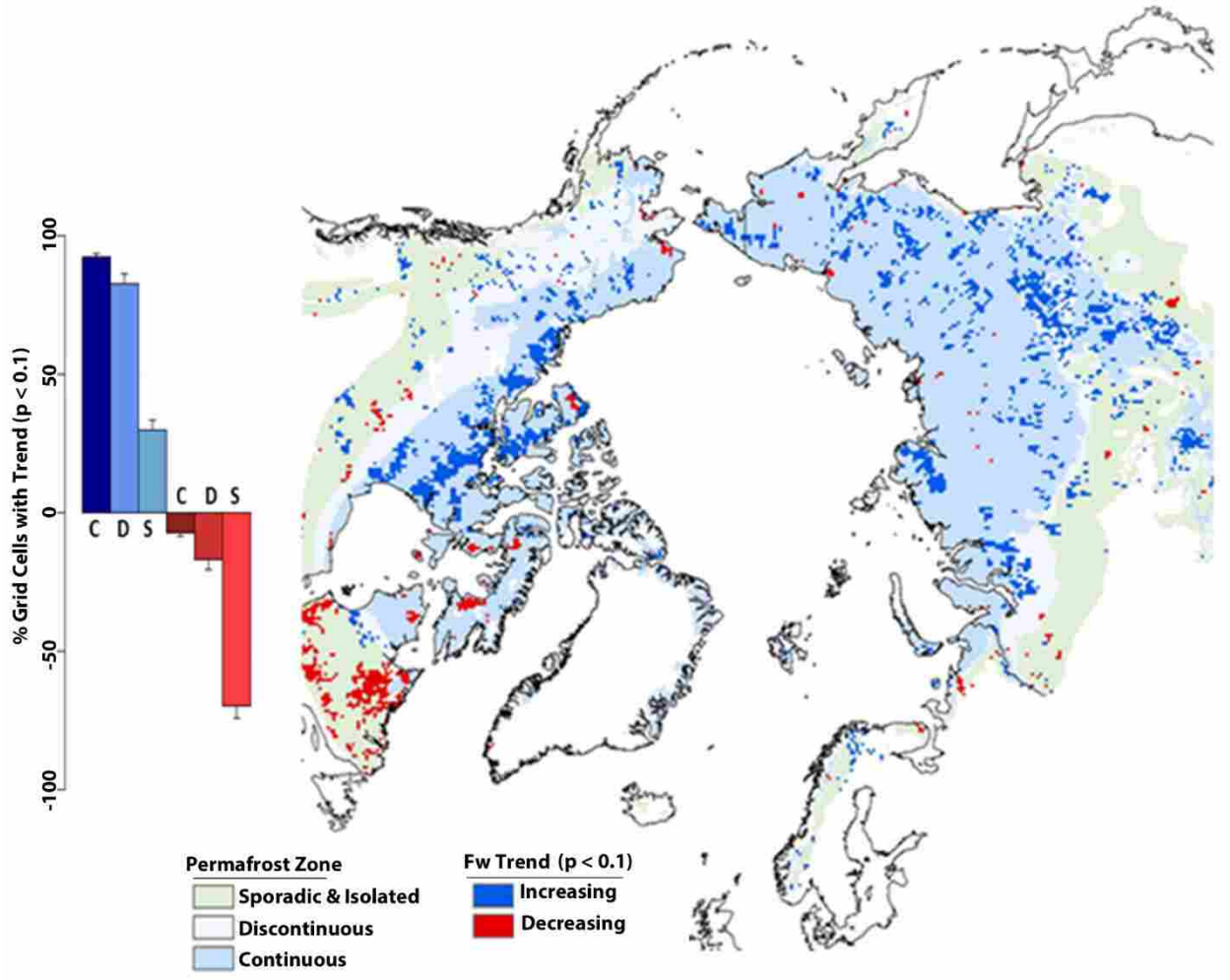

Figure 2.7 Significant ($p < 0.10$) *Fw* trend areas within permafrost (PF) regions for mean annual *Fw* (Fw_{avg}) determined from AMSR-E mean monthly *Fw* values from 2003-2010. The blue, light blue-gray and light green areas represent continuous (C), discontinuous (D) and sporadic/isolated (S) PF zones, respectively. The blue areas indicate significant positive *Fw* trends, while red areas indicate significant negative *Fw* trends. The relative proportion (%) of grid cells having significant positive or negative trends within each PF zone is summarized in the corresponding bar graph; error bars indicate 95% confidence intervals for the PF area proportions.

Chapter 3: Surface water inundation in the Arctic-boreal zone: potential impacts on regional methane emissions

Corresponding publication:

Watts J D, J S Kimball, A Bartsch, K C McDonald (2014) Surface water inundation in the boreal-Arctic: potential impacts on regional methane emissions. *Environ. Res. Lett.*, 9: 1-13

3.1 Abstract

Northern wetlands may be vulnerable to increased carbon losses from methane (CH_4), a potent greenhouse gas, under current warming trends. However, the dynamic nature of open water inundation and wetting/drying patterns may constrain regional emissions, offsetting the potential magnitude of methane release. Here we conduct a satellite data driven model investigation of the combined effects of surface warming and moisture variability on high northern latitude ($\geq$ 45° N) wetland CH_4 emissions, by considering (1) sub-grid scale changes in fractional water inundation (Fw) at 15-day, monthly and annual intervals using 25-km resolution satellite microwave retrievals, and (2) the impact of recent (2003-2011) wetting/drying on northern CH_4 emissions. The model simulations indicate mean summer emissions of 55 Tg CH_4 yr^{-1} from Arctic-boreal wetlands. Approximately 12% and 16% of the emissions originate from open water and landscapes with emergent vegetation, respectfully, determined from 15-day Fw means or maximums, and significant increases in regional CH_4 emissions were observed when incorporating inundated land fractions into the model simulations at monthly or annual time scales. The satellite Fw record reveals widespread wetting across the Arctic continuous permafrost zone, contrasting with surface drying in boreal Canada, Alaska and western Eurasia. Arctic wetting and summer warming increased wetland emissions by 0.48 Tg CH_4 yr^{-1}, but this was mainly offset by decreasing emissions (-0.32 Tg CH_4 yr^{-1}) in sub-Arctic areas experiencing surface drying or cooling. These findings underscore the importance of monitoring changes in surface moisture and temperature when assessing the vulnerability of Arctic-boreal wetlands to enhanced greenhouse gas emissions under a shifting climate.

3.2 Introduction

Wetlands and lakes cover approximately 2-8% of the Arctic-boreal region (Watts *et al.* 2012), with large fluctuations in surface water extent resulting from seasonal melt cycles, summer precipitation and drought events (Schroeder *et al.* 2010, Bartsch *et al.* 2012, Helbig *et al.* 2013). Wet surface conditions and characteristically colder temperatures greatly reduce the rate of organic carbon decomposition in northern wetland environments (Harden *et al.* 2012, Elberling *et al.* 2013). As a result, over 50% of the global soil organic carbon pool is stored in these regions (Turetsky *et al.* 2007, Hugelius *et al.* 2013). Landscapes with inundated or moist surfaces are particularly vulnerable to carbon loss as methane (CH_4) (Turetsky *et al.* 2008, Fisher *et al.* 2011, Olefeldt *et al.* 2013). Contemporary estimates of methane source contributions from northern wetlands range between 12 and 157 Tg CH_4 yr^{-1} (Petrescu *et al.* 2010, McGuire *et al.* 2012, Meng *et al.* 2012, Gao *et al.* 2013), and may double over the next century if surface temperatures continue to rise (Koven *et al.* 2011, Schneider von Deimling *et al.* 2012).

Various wetland maps have been used to define the extent of methane emitting area (Matthews & Fung 1987, Aselmann & Crutzen 1989, Reeburgh *et al* 1998, Lehner & Döll 2004, Schneider *et al.* 2009, Glagolev *et al.* 2011), but their static nature fails to capture dynamic spatiotemporal variations in surface wetness within Arctic-boreal environments. Modeling studies are increasingly using satellite based inundation data to characterize the impact of changing surface water coverage on regional methane emissions (Petrescu *et al.* 2010, Riley *et al.* 2011, Zhu *et al.* 2011, Meng *et al.* 2012, Bohn *et al.* 2013, Wania *et al.* 2013). These datasets include the GIEMS (Global Inundation Extent from Multi-Satellites) record (Prigent *et al.* 2007, Papa *et al.* 2010) that estimates monthly inundation within 0.25° resolution grid cells using microwave observations from the Special Sensor Microwave/Imager (SSM/I) and ERS Synthetic Aperture Radar (SAR). However, the GIEMS record only spans from 1993 to 2004 and relies on visible (0.58-0.68 μm) and near-infrared (0.73-1.1 μm) Advanced Very High Resolution Radiometer (AVHRR) data to account for vegetation canopy effects on microwave retrievals (Papa *et al.* 2010). An alternative method, described by Schroeder *et al.* (2010) and integrated into methane studies for western Siberia (Bohn *et al.* 2013, Wania *et al.* 2013), avoids the use of optical/infrared information by incorporating QuikSCAT scatterometer and 6.9 GHz passive

microwave data from the Advanced Microwave Scanning Radiometer for EOS (AMSR-E) to determine 25 km grid fractional water coverage at 10 day intervals.

A recent approach introduced by Jones *et al.* (2010) uses AMSR-E 18.7 and 23.8 GHz, H- and V- polarized brightness temperatures to retrieve 25-km resolution daily fractional open water (Fw) inundation, and does not require ancillary information (e.g. AVHRR optical or QuikSCAT radar) to account for microwave scattering effects from intervening atmosphere and vegetation. The Jones *et al.* (2010) AMSR-E Fw data have been used to evaluate recent seasonal and inter-annual inundation variability across the northern high latitudes and permafrost regions, with a demonstrated sensitivity to changes in the surface water balance, and a relatively low observation spatial uncertainty of approximately 4% (Watts *et al.* 2012). Although satellite optical and radar remote sensing can characterize wetland and open water distributions at finer ($\leq$ 150 m resolution) scales (Bartsch *et al.* 2012, Rover *et al.* 2012, Bohn *et al.* 2013, Muster *et al.* 2013) this information is often constrained to localized analyses with minimal repeat observations and is not yet conducive for the pan-Arctic wide monitoring of surface inundation.

This study examines the potential implications of recent (2003 to 2011) variability in surface wetness on methane efflux from northern high latitude ($\geq$ 45ºN) wetlands, and the contrasting influence of regional changes in moisture and temperature on summer (May through September) emission budgets using recent satellite remote sensing and reanalysis information. We postulate that seasonal and inter-annual fluctuations in surface inundation can greatly limit the magnitude of methane release from wetland environments, particularly if summer warming coincides with periods of drought. Conversely, northern wetlands may be more susceptible to methane emissions when the extent and duration of surface wetness is sustained or increasing. We conducted a series of carbon and climate sensitivity simulations using the Joint UK Land Environment Simulator (JULES) methane emissions model (Clark *et al.* 2011, Bartsch *et al.* 2012), with input Fw means and maximums at 15-day, monthly, and annual intervals as derived from an AMSR-E global daily land parameter record (Jones *et al.* 2010, 2011a). In this study, Fw is defined as the proportional surface water cover within 25 km equal area AMSR-E grid cells (Watts *et al.* 2012), and includes inundated soils, open water (e.g. lake bodies) and areas

with emergent vegetation. We then evaluated the impact of recent temperature variability and wetting/drying on methane emission budgets for the northern wetland regions.

3.3 Methods

3.3.1 Study region

The land area considered in this analysis was determined using Arctic-boreal peatland maps (i.e. Gunnarsson & Löfroth 2009, Yu *et al.* 2010, Franzén *et al.* 2012), and the REgional Carbon Cycle and Assessment Processes (RECCAP) tundra domain (McGuire *et al.* 2012). To coincide with the spatial extent of AMSR-E Fw coverage, we also removed 25-km grid cells having $\geq$ 50% permanent ice or open water cover using the UMD MODIS land cover product (described in Jones *et al.* 2010). The resulting study region spans approximately 2 x 10^7 km^2 (Figure 1), and contains 72% of northern continuous and discontinuous permafrost affected landscapes (Brown *et al.* 1998).

3.3.2 Model description and calibration

The JULES model approach (Clark *et al.* 2011, Bartsch *et al.* 2012) accounts for the major factors (i.e. temperature, carbon substrate availability, landscape wetness) that control global methane emissions (Bloom *et al.* 2010, Olefeldt *et al.* 2013). Albeit relatively simple and lacking in detailed physical processes, this method is useful for pan-Arctic simulations because it avoids extensive parameterization requirements that can substantially increase estimate uncertainty (Riley *et al.* 2011). The model regulates methane emissions per available carbon substrate (C, kg m^{-2}) and an efflux rate constant (k_{CH4}, d^{-1}) that is modified by a temperature dependent Q_{10} factor (Gedney *et al.* 2004, Clark *et al.* 2011). The temperature effects on methane production are controlled using daily input surface soil temperature (T_s, in kelvin) and a thermal reference state (T_0, 273.15 K):

$$F_{CH4} = \alpha \left(C \times k_{CH4} \times Q_{10}^{(T_s - T_0)/10} \times FThw \right) \quad (1)$$

For this analysis, we limit our investigation to non-frozen surface conditions defined using daily satellite passive microwave sensor derived binary (0 or 1) freeze/thaw (*FThw*) constraints (Kim *et al.* 2013). The resulting daily grid cell fluxes (F_{CH4}, tonne CH_4) were

averaged over a 15-day time step and scaled (α) using AMSR-E Fw information to regulate methane emissions according to volumetric soil moisture (θ) conditions for non-inundated surface fractions. The daily input T_s and θ (≤ 10 cm soil depth) records were obtained from the NASA GEOS-5 MERRA (Modern Era Retrospective-analysis for Research and Applications) Land reanalysis archive with native 0.5° x 0.6° resolution (Reichle *et al.* 2011) and posted to a 25 km resolution polar equal-area scalable earth (EASE) grid consistent with the AMSR-E Fw data. The MERRA Land parameters have been evaluated for high latitude regions, with favorable correspondence in relation to independent satellite microwave and in-situ observations (Yi *et al.* 2011).

Soil metabolic carbon (C_{met}) pools obtained from a Terrestrial Carbon Flux (TCF) model (Kimball *et al.* 2009, Yi *et al.* 2013) were used as the substrate for methanogenesis. The TCF carbon estimates reflect daily changes in labile plant residues and root exudates, and have been evaluated against existing soil organic carbon inventory records for the high latitude regions (described in Yi *et al.* 2013). The C_{met} inputs (kg C m^{-2} d^{-1}) were generated for the study region by a 1000 year spin-up of the model using a ten year (2000-2009) record of Moderate Resolution Imaging Spectroradiometer (MODIS) 1 km resolution NDVI (Normalized Difference Vegetation Index) and MERRA daily surface meteorology and soil moisture inputs.

The JULES model k_{CH4} and Q_{10} parameters were calibrated using mean monthly eddy covariance methane fluxes (mg CH_4 m^{-1} d^{-1}) from five northern wetland tower sites (Figure 1) that are described in the published literature (i.e. Rinne *et al.* 2007, Sachs *et al.* 2008, Wille *et al.* 2008, Zona *et al.* 2009, Long *et al.* 2010, Parmentier *et al.* 2011), in conjunction with mean MERRA reanalysis C_{met} and T_s climatology over the 2003-2011 summer (May through September) period. A resulting Q_{10} value of 3.7 and a k_{CH4} rate of 3.7 x 10^{-5} d^{-1} minimized the root-mean-square-error (RMSE) differences between the model and flux tower observations at 17.62 mg CH_4 m^{-2} d^{-1}. A Q_{10} of 3.7 was also used by Clark *et al.* (2010) and is similar to those reported in other studies (Ringeval *et al.* 2010, Waldrop *et al.* 2010, Lupascu *et al.* 2012). Further model verification was also obtained by evaluating summer flux chamber measurements (see Supplementary Table S3.1) from tundra (n = 15 site records), boreal wetland (n = 11) and lake (n = 17) locations.

3.3.3 Regional simulations

Grid-scale (25 km) wetland methane emissions were obtained using dynamic 15-day, monthly and annual summer AMSR-E Fw means or maximums from 2003 to 2011. Methane simulations were also examined using a static mean summer Fw map derived from the 2003-2011 record. The regional simulations were evaluated against NOAA ESRL atmospheric methane flask measurements (Dlugokencky *et al.* 2013) from Barrow, AK, Lac LaBiche, CAN, and Pallas Sammaltunturi, FI, to assess the ability of the model to capture between-year changes in methane concentrations that may correspond with fluctuations in wetland methane emissions (Lelieveld *et al.* 1998). For Barrow and Sammaltunturi, the dry air mole fractions were available from 2003 through 2011; the Lac LaBiche data were available from 2008 onward.

A Hybrid Single Particle Lagrangian Integrated Trajectory (HYSPLIT; Draxler & Rolph 2013, Rolph 2013) model, with a 100 m receptor point altitude and input GDAS-1 meteorology (Rodell *et al.* 2004), was used to obtain backward (30 day) atmospheric trajectories for each flask site, and showed the dominant source contributions at Barrow to originate primarily from northern Alaska, the Yukon, and eastern Siberia. For the respective Lac LaBiche and Sammaltunturi locations, the major source regions were from northern Canada, or extending from Scandinavia eastward into western Russia. To determine the relative correspondence between modeled annual methane emission contributions and observed mean summer dry air mole fractions, Pearson product-moment correlation coefficients (r) were derived using spatial means from a 3 x 3 grid cell window centered on each flask location. Regional point correlation maps (Ding & Wang 2005) were also obtained by evaluating $r\ (e_j, a_k)$ for each grid cell within the methane source regions, where e_j is the modeled mean summer emissions time series at a given cell location and a_k is the atmospheric methane concentration time series at a flask sampling site.

Regional changes in surface water coverage, soil moisture and temperature were evaluated using a non-parametric Mann-Kendall trend analysis that accounts for serial correlation prior to determining trend significance (Yue *et al.* 2002, Watts *et al.* 2012). The Kendall rank correlations were applied to the mean summer AMSR-E Fw, and MERRA T_s and θ records on a per-grid cell basis from 2003 to 2011. Trend significance was determined at a

minimum 95% ($p < 0.05$) probability level. The Kendall trend analysis was also applied to the modeled cumulative annual methane emissions to identify regions that may be vulnerable to increasing anaerobic carbon losses.

3.4 Results and discussion

3.4.1 Model evaluation against in situ methane flux observations

The model simulations captured overall temporal variability ($r^2 = 0.65$, $p < 0.05$) observed in the monthly tower eddy covariance records, with a RMSE value of 17.6 mg CH_4 m^{-2} d^{-1} that is similar to other regional studies (Meng *et al.* 2012, Zhu *et al.* 2013). Significant differences ($\alpha = 0.05$; two-sample t-test with unequal variance) were not observed (figure S1) between the model estimates and mean monthly tower eddy covariance ($t = 1.45$, $p = 0.15$), boreal chamber ($t = 0.05$, $p = 0.96$), and northern lake ($t = 0.79$, $p = 0.45$) fluxes. However, the modeled fluxes were significantly smaller ($t = 3.67$, $p < 0.01$) than the tundra chamber observations and did not adequately capture larger (> 140 mg CH_4 m^{-2} d^{-1}) eddy covariance fluxes from a peatland site in northern Sweden (Jackowicz-Korczyński *et al.* 2010). These discrepancies may reflect the presence of tall sedges (e.g. *E. angustifolium*), which can substantially increase emission rates through aerenchymateous tissue pathways (Joabsson *et al.* 1999), or the limited representation of landscape scale emissions by chamber measurements given the potentially large contrasts in methane fluxes from dry and wet vegetation communities (Parmentier *et al.* 2011) and functional groups (Kao-Kniffin *et al.* 2010).

The modeled methane fluxes were within the 5-140 mg CH_4 m^{-2} d^{-1} range observed in the lake measurements (Zimov *et al.* 1997, Laurion *et al.* 2010, Desyatkin *et al.* 2009, Sabrekov *et al.* 2012), although these observations primarily reflect diffusive gas release and background bubbling instead of episodic ebullition events. As a result, the model simulations may underestimate ebullition release from open water bodies, particularly in carbon-rich thermokarst regions characterized by methane seeps (Walter *et al.* 2006). However, the fraction of lake bodies exhibiting this seep behavior is not well quantified, and a recent analysis of sub-Arctic

lakes reported that summer ebullition events averaged only 13 mg CH_4 m^{-2} d^{-1}, with a low probability of bubble fluxes exceeding 200 mg m^{-2} d^{-1} (Wik *et al.* 2013).

3.4.2 Regulatory effects of surface water and temperature on regional methane emissions

3.4.2.1 Wetland inundation characteristics

Approximately 7% (1.4 x 10^6 km^2 $\pm$ 3%) of the Arctic-boreal domain was inundated with surface water during the non-frozen summer season, as indicated by the 2003-2011 AMSR-E Fw retrieval means. Over 60% of the wetlands were located in North America, primarily within the Canadian Shield region, and the majority of inundation occurred above 59° N within major wetland complexes, including the Ob-Yenisei and Kolyma Lowlands in Siberia (Figure 2). A strong seasonal pattern in surface water was observed across the high latitudes, with an abrupt increase in May or early June following surface ice and snow melt, and the onset of spring precipitation (Figure 3). In Eurasia, peak inundation occurred in June, followed by a gradual decline with summer drought and increased evaporative demand (Rawlins *et al.* 2009, Schroeder *et al.* 2010, Bartsch *et al.* 2012, Watts *et al.* 2012). In North America, the seasonal expansion of surface water continued through July, before beginning to subside with the onset of surface freezing.

The influence of wet/dry cycles on surface water extent was evident throughout the Arctic-boreal region. The summer of 2004 was the driest observed over the AMSR-E Fw record, with a 6% decrease in inundation from the long-term mean that coincided with drought conditions across the Arctic Basin and Alaska (Rinsland *et al.* 2007, Zhang *et al.* 2008, Jones *et al.* 2013). In North America, 2005 and 2006 were the wettest summers, with a 7% increase in water coverage. These positive anomalies were also reflected in the high river discharge observed in the Yukon basin (Watts *et al.* 2012) and Hudson Bay lowlands (Déry *et al.* 2011) following high spring snow melt and summer precipitation. The wettest summer in Eurasia occurred in 2010, with a 5% increase in surface water that was primarily associated with a strong La Niña event that brought cooler air and precipitation to central Siberia despite an anomalous heat wave and drier conditions in western Russia (Schneidereit *et al.* 2012, Trenberth & Fasullo 2012).

3.4.2.2 Regional summer methane simulations

Summer methane emissions estimated for non-inundated land fractions averaged 47.9 ± 1.8 Tg CH_4 yr^{-1} over the northern wetlands. This increased to 54.6 ± 1.8 Tg CH_4 yr^{-1} when also considering contributions from inundated landscapes based on the 15-day AMSR-E Fw means. These results are within the range of emissions (39 to 89 Tg CH_4 yr^{-1}) reported from previous modeling studies using other satellite-based Fw retrievals (Table 1; Petrescu *et al.* 2010, Ringeval *et al.* 2010, Riley *et al.* 2011, Spahni *et al.* 2011, Wania *et al.* 2013), but are higher than those from atmospheric inversion analyses of northern peatlands (approximately 30 Tg CH_4 yr^{-1}, Spahni *et al.* 2011). The coarse resolution (0.5° x 0.6°) reanalysis meteorology used in the model simulations do not well represent sub-grid variability in soil wetness and temperature controls (von Fischer *et al.* 2010, Sachs *et al.* 2010, Sturtevant & Oechel 2013), which may lead to systematic biases when evaluating methane emissions at larger scales (Bohn & Lettenmaier 2010). However, top-down inversion analyses are also prone to uncertainties from atmospheric transport conditions and the limited number of observation sites within high latitude regions (Berchet *et al.* 2013, Nisbet *et al.* 2014).

In northern wetlands, 80-98% of annual methane emissions occur during the summer (Alm *et al.* 1999, Jackowicz-Korczyński *et al.* 2010, Song *et al.* 2012) due to strong thermal controls on methane production, carbon substrate and water availability (Strom *et al.* 2003, Christensen *et al.* 2003, Wagner *et al.* 2009). The influence of summer warming on regional methane emissions was apparent in the model simulations, with peak efflux occurring in June and July (Figure S3.2). This seasonal pattern has been observed in atmospheric methane mixing ratios across the Arctic (Aalto *et al.* 2007, Pickett-Heaps *et al.* 2010, Fisher *et al.* 2011). Also evident was the impact of wet/dry cycles on regional methane contributions, with annual summer emission budgets fluctuating by ± 4%, relative to the 2003-2011 mean. The modeled emissions were lowest in 2004 despite anomalously high temperatures throughout the Arctic-boreal region (Chapin *et al.* 2005), due to drought conditions in Alaska and northern Canada. In contrast, higher emissions in 2005 resulted from warm and wet weather in North America.

Surface moisture variability also influenced the correspondence between the modeled emissions and summer atmosphere methane concentrations from the regional flask

measurements. Regions showing a positive correspondence between modeled methane emissions and atmosphere concentrations largely reflected atmospheric transport trajectories indicated in the HYSPLIT simulations (Figure S3.3), with stronger agreement ($r > 0.7$, $p \leq 0.05$) occurring in areas characterized by open water or prone to periodic inundation (Figure 4). Immediate to the flask sites, mean summer inundation varied from 2 to 10%, with moist soil fractions accounting for > 85% of simulated emissions. At Lac LaBiche, annual emissions variability corresponding to wet soil fractions agreed well ($r = 0.96$, $p = 0.02$) with the flask observations.

In contrast, relatively poor agreement was observed at Barrow and Sammaltunturi where emission patterns for inundated portions of the landscape corresponded more closely with atmospheric methane concentrations (Table 2). At Barrow, the correspondence was similar ($r > 0.43$, $p \leq 0.12$) for model simulations using dynamic 15-day or annual Fw inputs, reflecting methane source contributions from thermokarst lakes and inundated tundra in the surrounding landscape (Dlugokencky *et al.* 1995). In contrast, the modeled emissions at Sammaltunturi corresponded closely ($r = 0.86$, $p < 0.01$) with flask observations when accounting for 15-day variability in Fw extent, but showed minimal agreement when using annual Fw inputs. This discrepancy may be attributed to less open water cover in the surrounding region and a tendency for summer precipitation events to produce intermittent flooding due to shallow soil layers and limited drainage (Aalto *et al.* 2007). These results differ from the Lac LaBiche site, where nearby peatlands are characterized by deeper layers of surface litter and moss (Dlugokencky *et al.* 2011) that can substantially reduce surface water coverage.

3.4.3 Fw temporal scaling effects on summer methane budgets

Wetland studies have increasingly used satellite microwave remote sensing to quantify the extent of methane emitting area, given the strong microwave sensitivity to surface moisture and relative insensitivity to solar illumination constraints and atmospheric signal attenuation. Regional inundation information has been incorporated into model simulations using monthly, annual, or static multi-year Fw means (Ringeval *et al.* 2010, Petrescu *et al.* 2010, Hodson *et al.* 2011, Riley *et al.* 2011, Spahni *et al.* 2011, Meng *et al.* 2012, Wania *et al.* 2013). However, our

simulation results show that temporal Fw scaling can lead to substantial differences in methane emission estimates (Table 1).

In this analysis, inundation extent within the Arctic-boreal wetland regions increased by 4-7% and 20-30% when using respective mean monthly or annual AMSR-E Fw inputs instead of finer (15-day) temporal intervals. The coarser Fw temporal inputs resulted in respective increases in estimated methane emission budgets by 3% ($t = 1.6$, $p = 0.05$) and 17% ($t = 6.7$, $p < 0.01$) in Eurasia, relative to simulations using finer 15-day Fw temporal inputs. The impacts of Fw temporal scaling in North America were not significant ($t \leq 0.7$, $p > 0.24$), with corresponding increases of 0.5% (Fw monthly) and 2% (Fw annual) in estimated annual methane emissions. The observed emissions sensitivity to Fw scaling in Eurasia primarily results from precipitation and flooding events in early summer, followed by mid-summer drying (Serreze & Etringer 2003). As a result, Fw means considered over longer time intervals in these regions may be biased towards spring inundation conditions, and may not reflect regional decreases in surface wetness occurring during the warmer mid-summer months. Directly incorporating Fw maximums, sometimes used to quantify multi-year surface hydrology trends (Bartsch *et al.* 2012, Watts *et al.* 2012), also led to substantial increases ($t > 7.5$, $p < 0.01$) in estimated methane emissions by > 40% in North America and 62% in Eurasia relative to simulations using static Fw means.

3.4.4 Potential impact of regional wetting and drying trends on methane emission budgets

Significant ($p < 0.05$) increases in surface inundation were observed over 5% (1×10^6 km^2) of the high latitude wetlands domain from 2003 to 2011, with substantial Fw wetting occurring within northern tundra and permafrost affected landscapes (Figure 5). While the regional wetting patterns may correspond with shifts in northward atmospheric moisture transport (Rawlins *et al.* 2009, Skific *et al.* 2009, Dorigo *et al.* 2012, Screen 2013), trends within the Arctic Rim may be more closely influenced by thermokarst expansion, reductions in seasonal ice cover (Smith *et al.* 2005, Rowland *et al.* 2010, Watts *et al.* 2012), and summer warming (Figure 6a). In portions of western Siberia, localized cooling and residual winter snow melt (Cohen *et al.* 2012) may also contribute to surface wetting. Regional drying was also observed across 3% (6×10^5 km^2) of the northern wetland domain, particularly in northern boreal Alaska,

eastern Canada and Siberia (Figure 5). These declines in surface water extent may result from an increase in summer evaporative demand (Arp *et al.* 2011) and the terrestrialization of open water environments following lake drainage (Payette *et al.* 2004, Jones *et al.* 2011b, Roach *et al.* 2011, Helbig *et al.* 2013).

The combined influence of warming and wetting in the AMSR-E Fw and reanalysis surface meteorology records contributed to an increase in methane emissions across 16% of the Arctic-boreal domain (Figure 6b), at a mean rate of 43 tonne CH_4 yr^{-1} from 2003 to 2011. These increases occurred primarily in Canada and eastern Siberia, where summer warming has been observed in both in-situ measurements and reanalysis records (Figure S3.4, Screen *et al.* 2010, Smith *et al.* 2010, Walsh *et al.* 2011). This finding agrees with a projected 15% increase in methane emitting area with continued climate change in the northern wetland regions (Gao *et al.* 2013). A significant ($p < 0.05$) decrease in modeled methane emissions, associated with regional surface drying and cooling patterns, was also observed across 11% of the region (Figure 6b, 40 tonne CH_4 yr^{-1}) and offset gains in overall methane emissions over the 2003-2011 period.

3.5 Conclusions

Northern Arctic-boreal ecosystems may be especially vulnerable to methane emissions given climate warming, abundant soil carbon stocks, and a predominately wet landscape (Isaksen *et al.* 2011, van Huissteden *et al.* 2011, Olefeldt *et al.* 2013). We found that 7% of northern wetlands were characterized by open water or emergent vegetation, with the majority of inundation occurring in the Canadian Shield lowlands and Ob-Yenisei river basins. Areas of significant ($p < 0.05$) increase in surface water extent were more prevalent within the Arctic Rim and may coincide with heightened summer precipitation (Landerer *et al.* 2010, Screen 2013) or high latitude permafrost thaw (Rowland *et al.* 2010, Watts *et al.* 2012). The combined effect of surface wetting and warming contributed to regional increases of 0.48 Tg CH_4 yr^{-1} in estimated methane emissions. Our analysis also revealed surface drying throughout the boreal zones of southern Sweden, western Russia and eastern Canada, as has been anticipated with increasing summer temperatures and drought conditions in the sub-Arctic (Frolking *et al.* 2006, Tarnocai

2006). This landscape drying contributed to a 0.32 Tg CH_4 yr^{-1} decrease in summer emissions, and largely offset any increases in region-wide methane release.

Regional modeling studies should consider the potential impacts of Fw scaling when prescribing the extent of methane emitting area in northern wetland regions, given the dynamic nature of surface water in northern landscapes (Schroeder *et al.* 2010, Bartsch *et al.* 2012, Watts *et al.* 2012). Our model sensitivity analysis shows significant differences in estimated annual emissions determined from coarse monthly or annual Fw relative to finer scale (15-day) inundation inputs. Although the estimated emissions rate of 55 Tg CH_4 yr^{-1} is similar to the results from previous studies, it may overestimate the magnitude of methane release from pan-boreal and Arctic wetland regions, given difficulties accounting for finer scale soil temperature and moisture heterogeneity (Sachs *et al.* 2008, Parmentier *et al.* 2011, Muster *et al.* 2013) using coarse $\geq$ 0.5° reanalysis information. The NASA Soil Moisture Active Passive (SMAP) mission (Entekhabi *et al.* 2014) launched early 2015 and provides new global satellite L-band passive microwave observations of the land surface, with regular monitoring of northern soil thermal and moisture dynamics at 1-2 day intervals and moderate (9 km) spatial scales. These new observations may provide for the improved quantification of regional patterns and temporal dynamics in surface environmental conditions, which is needed to reduce uncertainty in regional and global methane emissions.

3.6 References

Aalto, T, J Hatakka, M Lallo (2007) Topospheric methane in northern Finland: seasonal variations, transport patterns and correlations with other trace gases. *Tellus B,* 59: 251-59.

Alm, J, L Schulman, J Walden, H Nykänen, P J Martiknainen, J Silvola (1999) Carbon balance of a boreal bog during a year with an exceptionally dry summer. *Ecology,* 80: 161-74.

Arp, C D, B M Jones, F E Urban, G Grosse (2011) Hydrogeomorphic processes of thermokarst lakes with grounded-ice and floating-ice regimes on the Arctic coastal plain, Alaska. *Hydrol. Process.,* 25: 2422-38.

Aselmann, I, P J Crutzen (1989) Global distribution of natural freshwater wetlands and rice paddies, their net primary productivity, seasonality and possible methane emissions. *J. Atmos. Chem.,* 8: 307-58.

Bartsch, A, A M Trofaier, G Hayman, D Sabel, S Schlaffer, D B Clark, E Blyth (2012) Detection of open water dynamics with ENVISAT ASAR in support of land surface modeling at high latitudes. *Biogeosciences* 9: 703-14.

Berchet, A, I Pison, F Chevallier, P Bousquet, S Conil, M Geever, T Laurila, J Lavrič, M Lopez, J Moncrieff, J Necki, M Ramonet, M Schmidt, M Steinbacher, J Tarniewicz (2013) Towards better error statistics for atmospheric inversions of methane surface fluxes. *Atmos. Chem. Phys.*, 13: 7115-32.

Blodau, C, T R Moore (2002) Micro-scale CO_2 and CH_4 dynamics in a peat soil during a water fluctuation and sulfate pulse. *Soil Bio. Biogeochem.,* 35: 335-47.

Bloom, A A, P I Palmer, A Fraser, D S Reay, C Frankenberg (2010) Large-scale controls of methanogenesis inferred from methane and gravity spaceborne data. *Science,* 327: 322-25.

Bohn, T J, D P Lettenmaier (2010) Systematic biases in large-scale estimates of wetland methane emissions arising from water table formulations. *Geophys. Res. Lett.,* 37 L22401 doi:10.1029/2010GL045450.

Bohn, T J, E Podest, R Schroeder, N Pinto, K C McDonald, M Glagolev, I Filippov, S Maksyutov, M Heimann, X Chen, D P Lettenmaier (2013) Modeling the large-scale effects of surface moisture heterogenieity on wetland carbon fluxes in the West Siberian Lowland. *Biogeosciences,* 10: 6559-76.

Brown, J, O J Ferrians Jr., J A Heginbottom, E S Melnikov (1998) Circum-Arctic Map of permafrost and ground-ice conditions. Boulder, CO: National Snow and Ice Data Center/World Data Center for Glaciology. Digital Media.

Bruhwiler, L M, E Dlugokencky, K Masarie, M Ishizawa, A Andrews, J Miller, C Sweeney, P Tans, D Worthy (2014) CarbonTracker-CH_4: an assimilation system for estimating emissions of atmospheric methane. *Atmos. Chem. Phys. Discuss.*, 14: 2175-233.

Chapin, III F S, M Sturm, M C Serreze, J P McFadden, J R Key, A H Lloyd, A D McGuire, T S Rupp, A H Lynch, J P Schimel, J Beringer, W L Chapman, H E Epstein, E S Euskirchen, L D Hinzman, G Jia, C L Ping, K D Tape, C D C Thompson, D A Walker, J M Welker (2005) Role of land-surface changes in Arctic summer warming. *Science*, 310: 657-60.

Christensen, T R, A Ekberg, L Ström, M Mastepanov, N Panikov, M Öquist, B H Svensson, H Nykänen, P J Martikainen, H Oskarsson (2003) Factors controlling large scale variations in methane emissions from wetlands. *Geophys. Res. Lett.*, 30: 1414.

Clark, D B, L M Mercado, S Sitch, D C Jones, N Gedney, M J Best, M Pryor, G G Rooney, R L H Essery, E Blyth, O Boucher, R J Harding, C Huntingford, P M Cox (2011) The Joint UK Land Environmental Simulator (JULES), model description-Part 2: carbon fluxes and vegetation dynamics. *Geosci. Model Dev.*, 4: 701-22.

Cohen, J L, J C Furtado, M A Barlow, V A Alexeev, J E Cherry J E (2012) Arctic warming, increasing snow cover and widespread boreal winter cooling. *Environ. Res. Lett.*, 7 014007. doi:10.1088/1748-9326/7/1/014007.

Desyatkin, A R, F Takakai, P P Fedorov, M C Nikolaeva, R V Desyatkin, R Hatano (2009) CH_4 emission from different stages of thermokarst formation in Central Yakutia, East Siberia. *Soil Sci. Plant Nutr.*, 55: 558-70.

Ding, Q, B Wang (2005) Circumglobal teleconnection in the Northern Hemisphere Summer. *J. Climate*, 18: 3483-505.

Dlugokencky, E J, L P Steel, P M Lang, K A Masarie (1995) Atmospheric methane at Mauna Loa and Barrow observatories: Presentation and analysis of in situ measurements. *J. Geophys. Res.*, 100: 103-13.

Dlugokencky E J, L Bruhwiler, J W C White, L K Emmons, P C Novelli, S A Montzka, K A Masarie, P M Lang, A M Crotwell, J B Miller, L V Gatti (2009) Observational constraints on recent increases in the atmospheric CH_4 burden. *Geophys. Res. Lett.* 36: L18803 doi:10.1029/2009GL039780.

Dlugokencky, E J, E G Nisbet, R Fisher, D Lowry (2011) Global atmospheric methane:

budget, changes and dangers. *Phil. Trans. R. Soc. A*, 369: 2058-72.

Dlugokencky, E J, P M Lang, A M Crotwell, K A Masarie, M J Crotwell (2013) Atmospheric Methane Dry Air Mole Fractions from the NOAA ESRL Carbon Cycle Cooperative Global Air Sampling Network, 1983-2012, Version: 2013-08-28, ftp://aftp.cmdl.noaa.gov/data/trace_gases/ch4/flask/surface/.

Dorigo, W, R de Jeu, D Chung, R Parinussa, Y Liu, W Wagner, D Fernández-Prieto (2012) Evaluating global trends (1988-2010) in harmonized multi-satellite surface moisture. *Geophys. Res. Lett.,* 39: L18405 doi:10.1029/2012GL052988.

Draxler, R R, G D Rolph (2013) HYSPLIT (HYbrid Single-Particle Lagrangian Integrated Trajectory) Model access via NOAA ARL READY Website (http://www.arl.noaa.gov/HYSPLIT.php) NOAA Air Resources Laboratory, College Park, MD.

Elberling, B, A Michelsen, C Schädel, E A Schuur, H H Christiansen, L Berg, M P Tamstorf, C Sigsgaard (2013) Long-term CO_2 production following permafrost thaw. *Nature Clim. Change,* 3: 890-94.

Entekhabi, D, S Yueh, P O'Neill, K Kellogg et al. (2014) SMAP Handbook, JPL Publication, JPL 400-1567, Jet Propulsion Laboratory, Pasadena, California, 182 pages.

Fisher, R E, S Sriskantharajah, D Lowry, M Lanoisellé, C M R Fowler, R H James, O Hermansen, C Lund, A Stohl, J Greinert, P B R Nisbet-Jones, J Mienert, E G Nisbet (2011) Arctic methane sources: Isotopic evidence for atmospheric inputs. *Geophys. Res. Lett.*, 38: L21803 doi:10.1029/2011GL049319.

Franzén, L G, F Lindberg, V Viklander, A Walther (2012) The potential peatland extent and carbon sink in Sweden, as related to the Peatland/Ice Age Hypothesis. *Mires & Peat,* 10: 1-19.

Frolking, S, N Roulet, J Fuglestvedt (2006) How northern peatlands influence the Earth's radiative budget: Sustained methane emission verses sustained carbon sequestration. *J. Geophys. Res.,* 111: G01008 doi:10.1029/2005JG000091.

Gao, X, C A Schlosser, A Sokolov, K W Anthony, Q Zhuang, D Kicklighter (2013) Permafrost degradation and methane: low risk of biogeochemical climate-warming feedback. *Environ. Res. Lett.,* 8: 035014 doi:10.1088/1748-9326/8/3/035014.

Gedney, N, P M Cox, C Huntingford (2004) Climate feedback from wetland emissions. *Geophys. Res. Lett.,* 31: L20503 doi:10.1029/2004GL020919.

Glagolev, M, I Kleptsova, I Filippov, S Maksyutov, T Machida (2011) Regional methane emission from West Siberia mire landscapes. *Environ. Res. Lett,* .6: 045214 doi:10.1088/1748-9326/6/4/045214.

Gunnarsson, U, M Löfroth (2009) Wetlands Inventory – Results from 25 Years of Inventory. National Final Report for Wetland Inventory (VMI) in Sweden). Naturvårdsverket Rapport 5925, (120 pp.).

Harden, J W, C D Koven, C L Ping, G Hugelius, D A McGuire, P Camill, T Jorgenson, P Kuhry, G J Michaelson, J A O'Donnell, E A G Schuur, C Tarnocai, K Johnson, G Grosse (2012) Field information links permafrost carbon to physical vulnerabilities of thawing. *Geophys. Res. Lett.,* 39: L15704 doi:1029/2012GL051958.

Helbig, M, J Boike, M Langer, P Schreiber, B R K Runkle, L Kutzbach (2013) Spatial and seasonal variability of polygonal tundra water balance: Lena River Delta, northern Siberia (Russia). *Hydrogeol. J.* 21: 133-47.

Hodson, E L, B Poulter, N E Zimmermann, C Prigent, J O Kaplan (2011) The El Niño Southern Oscillation and wetland methane interannual variability. *Geophys. Res. Lett.,* 38: L08810 doi:10.1029/2011GL046861.

Hugelius, G, C Tarnocai, G Broll, J G Canadell, P Kuhry, D K Swanson (2013) The Northern Circumpolar Soil Carbon Database: Spatially distributed datasets of soil coverage and soil carbon storage in the northern permafrost regions. *Earth Sys. Sci. Data,* 5: 3-13.

Isaksen, I S A, M Gauss, G Myhre, K M Walter Anthony, C Ruppel (2011) Strong atmospheric chemistry feedback to climate warming from Arctic methane emissions. *Glob. Change Biol.* 25: GB2002 doi:10.1029/2010GB003845.

Jackowicz-Korczyński, M, T R Christensen, K Bäckstrand, P Crill, T Friborg, M Mastepanov, L Ström (2010) Annual cycle of methane emission from a subarctic peatland. *J. Geophys. Res.* 115: G02009 doi:10.1029/2008JG000913.

Joabsson, A, T R Christensen, B Wallén (1999) Vascular plant controls on methane emissions from northern peatforming wetlands. *TREE,* 14: 385-88.

Jones, B M, G Grosse, C D Arp, M C Jones, K M Walter Anthony, V E Romanovsky (2011b) Modern thermokarst lake dynamics in the continuous permafrost zone, northern Seward Peninsula, Alaska. *J. Geophys. Res*., 116: G00M03 doi: 10.1029/2011JG001666.

Jones, L A, C R Ferguson, J S Kimball, K Zhang, S T K Chan, K C McDonald, E G Njoku, E F Wood (2010) Satellite microwave remote sensing of daily land surface air temperature minima and maxima from AMSR-E. *IEEE J-STARS* 3: 111-23.

Jones, L A, J S Kimball (2011a) Daily global land surface parameters derived from AMSR-E. Boulder Colorado USA: National Snow and Ice Data Center. Digital media. nsidc.org/data/nsidc-0451.html.

Jones, M O, J S Kimball, L A Jones (2013) Satellite microwave detection of boreal forest recovery from the extreme 2004 wildfires in Alaska and Canada. *Glob. Change Biol.,* 19 3111-22.

Kao-Kniffin, J, D S Freyre, T C Balser (2010) Methane dynamics across wetland plant species. *Aquatic Botany,* 93: 107-13.

Kim, Y, J S Kimball, J Glassy, K C McDonald (2013) MEaSUREs Global Record of Daily Landscape Freeze/Thaw Status. Version 2. Boulder, Colorado USA: NASA DAAC at the National Snow and Ice Data Center, http://nsidc.org/data/nsidc-0477.

Kimball, J S, L A Jones, K Zhang, F A Heinsch, K C McDonald, W C Oechel (2009) A satellite approach to estimate land-atmosphere CO_2 exchange for boreal and Arctic biomes using MODIS and AMSR-E. *IEEE Geosci. Remote Sens.* 47: 569-87.

Koven, C D, B Ringeval, P Friedlingstein, P Ciais, P Cadule, D Khvorostyanov, G Krinner, C Tarnocai (2011) Permafrost carbon-climate feedbacks accelerate global warming. *PNAS,* 108: 14769-74.

Landerer, F D, J O Dickey, A Güntner (2010) Terrestrial water budget of the Eurasian pan-Arctic from GRACE satellite measurements during 2003-2009. *Geophys. Res-Atmos.,* 115: D23115 doi:10.1029/2010JD014584.

Laurion, I, W F Vincent, S MacIntyre, L Retamal, C Dupont, P Francus, R Pienitz (2010) Variability in greenhouse gas emissions from permafrost thaw ponds. *Limnol. Oceanogr.* 55: 115-33.

Lehner, B, P Döll (2004) Development and validation of a global database of lakes, reservoirs and wetlands. *J. Hydrol.* 296: 1-22.

Lelieveld, J, P J Crutzen, F J Dentener (1998) Changing concentration, lifetime and climate forcing of atmospheric methane. *Tellus B,* 50: 128-50.

Long, K D, L B Flanagan, T Cai (2010) Diurnal and seasonal variation in methane emissions in a northern Canadian peatland measured by eddy covariance. *Glob. Change Biol.,* 16: 2420-35.

Lupascu, M, J L Wadham, E R C Hornibrook, R D Pancost (2012) Temperature sensitivity of methane production in the permafrost active layer at Stordalen, Sweden: A comparison with non-permafrost northern wetlands. *Arct. Antarct. Alp. Res.,* 44: 469-82.

Matthews, E, I Fung (1987) Methane emissions from natural wetlands: Global distribution, area, and environmental characteristics of sources. *Glob. Biogeochem. Cy.,* 1: 61-86.

McGuire, A D, T R Christensen, D Hayes, A Heroult, E Euskirchen, J S Kimball, C Koven, P Lafleur, P A Miller, W Oechel, P Peylin, M Williams, Y Yi (2012) An assessment of the carbon balance of Arctic tundra: comparisons among observations, process models, and atmospheric inversions. *Biogeosciences,* 9: 3185-204.

Meng, L, P G M Hess, N M Mahowald, J B Yavitt, W J Riley, Z M Subin, D M Lawrence, S C Swenson, J Jauhiainen, D R Fuka (2012) Sensitivity of wetland methane emissions to model assumptions: application and model testing against site observations. *Biogeosciences,* 9: 2793-819.

Muster, S, B Heim, A Abnizova, J Boike (2013) Water body distributions across scales: a remote sensing based comparison of three Arctic tundra wetlands. *Remote Sens*., 5: 1498-523.

Nisbet, E G, E J Dlugokencky, P Bousquet (2014) Methane on the rise — again. *Science,* 31:493-95.

Olefeldt, D, M R Turetsky, P M Crill, A D McGuire (2013) Environmental and physical controls on northern terrestrial methane emissions across permafrost zones. *Glob. Change Biol.,* 19: 589-603.

Parmentier, F J W, J van Huissteden, M K van der Molen, G Schaepman-Strub, S A Karsanaev, T C Maximov, A J Dolman (2011) Spatial and temporal dynamics in eddy covariance observations of methane fluxes at a tundra site in northeastern Siberia. *J. Geophys. Res.*, 116: G03016, doi:10.1029/2010JG001637

Papa, F, C Prigent, F Aires, C Jimenez, W B Rossow (2010) Interannual variability of surface water extent at global scale 1993-2004. *J. Geophys. Res.,* 115: D12111 doi:10.1029/2009JD012674.

Payette, S, A Delwaide, M Caccianiga, M Beauchemin (2004) Accelerated thawing of subarctic peatland permafrost over the last 50 years. *Geophys. Res. Lett.,* 31: L18208 doi:10.1029/2004GL020358.

Petrescu, A M R, L P H van Beek, J van Huissteden, C Prigent, T Sachs, C A R Corradi, F J W Parmentier, A J Dolman (2010) Modeling regional to global CH_4 emissions of boreal and arctic wetlands. *Glob. Biogeochem. Cy.,* 24: GB4009 doi:10.1029/2009GB003610.

Pickett-Heaps, C A, D J Jacob, K J Wecht, E A Kort, S C Wofsy, G S Diskin, D E J Worthy, J O Kaplan, I Bey, J Drevet (2011) Magnitude and seasonality of wetland methane emissions from the Hudson Bay Lowlands (Canada). *Atmos. Chem. Phys.,* 11: 3773-79.

Prigent, C, F Papa, F Aires, Rossow W B, E Matthews (2007) Global inundation dynamics inferred from multiple satellite observations 1993-2000. *J. Geophys. Res.,* 112: D12107 doi:10.1029/2006JD007847.

Rawlins, M A, H Ye, D Yang, A Shiklomanov, K C McDonald (2009) Divergence in seasonal hydrology across northern Eurasia: emerging trends and water cycle linkages. *J. Geophys. Res.,* 114: D18119 doi:10.1029/2009JD011747.

Reeburgh, W S, J Y King, S K Regli, G W Kling, N A Auerbach, D A Walker (1998) A CH_4 emission estimate for the Kuparuk River basin, Alaska. *J. Geophys. Res. Atmos.*, 103: 29005-13.

Reichle, R H, R D Koster, G J M De Lannoy, B A Forman, Q Liu, S P P Mahanama, A Toure (2011) Assessment and enhancement of MERRA land surface hydrology estimates. *J. Clim.,* 24: 6322-38.

Riley W J, Z M Subin, D M Lawrence, S C Swenson, M S Torn, L Meng, N M Mahowald, P Hess (2011) Barriers to predicting changes in global terrestrial methane fluxes: Analyses using CLM4Me, a methane biogeochemistry model integrated in CESM. *Biogeosciences*, 8: 1925-53.

Rinne J, T Riutta, M Pihlatie, M Aurela M, S Haapanala, J P Tuovinen, E S Tuittila (2007) Annual cycles of methane emission from a boreal fen measured by the eddy covariance Technique. *Tellus B*, 59: 449-57.

Ringeval, B, N de Noblet-Ducoudré, P Ciais, P Bousquet, C Prigent, F Papa, W B Rossow (2010) An attempt to quantify the impact of changes in wetland extent on methane emissions on the seasonal and interannual time scales. *Glob. Biogeochem. Cy.,* 24: GB2003 doi:10.1029/2008GB003354.

Rinsland, C P, G Dufour, C D Boone, P F Bernath, L Chiou, P F Coheur, S Turquety, C Clerbaux (2007) Satellite boreal measurements over Alaska and Canada during June-July 2004: simultaneous measurements of upper tropospheric CO, C_2H_6, HCN, CH_3Cl, CH_4, C_2H_2, CH_3OH, HCOOH, OCS and SF_6 mixing ratios. *Glob. Biogeochem. Cy.,* 21: GB3008 doi:10.1029/2006GB002795.

Roach, J, B Griffith, D Verbyla, J Jones (2011) Mechanisms influencing changes in lake area in Alaskan boreal forest. *Glob. Change Biol.,* 17: 2567-83.

Rodell, M, P R Houser, U Jambor, J Gottschalck, K Mitchell, C J Meng, K Arsenault, B

Cosgrove, J Radakovich, M Bosilovich, J K Entin, J P Walker, D Lohmann, D Toll (2004) The Global Land Data Assimilation System. *Bull. Amer. Meteor. Soc.,* 85: 381-94.

Rolph, G D (2013) Real-time Environmental Applications and Display sYstem (READY) Website (http://www.ready.noaa.gov) NOAA Air Resources Laboratory, College Park, MD.

Rover, J, L Ji, B K W Wylie, L L Tieszen (2012) Establishing water body areal extent trends in interior Alaska from multitemporal Landsat data. *Remote Sens. Lett.,* 3: 595-604.

Rowland, J C, C E Jones, G Altmann, R Bryan, B T Crosby, L D Hinzman, D L Kane, D M Lawrence, A Mancino, P Marsh, J P McNamara, V E Romanvosky, H Toniolo, B J, E Trochim, C J Wilson, G L Geernaert (2010) Arctic landscapes in transition: responses to thawing permafrost. *Eos Trans., AGU,* 91: 229-30.

Sabrekov, A F, M V Glagolev, I V Filippov, V S Kazantsev, E D Lapshina, T Machida, S S Maksyutov (2012) Methane emissions from North and Middle Taiga mires of Western Siberia: Bc8 Standard Model. *Moscow Soil Sci. Bulletin,* 67: 45-53.

Sachs, T, C Wille, J Boike, L Kutzbach (2008) Environmental controls on ecosystem-scale CH_4 emission from polygonal tundra in the Lena River Delta, Siberia. *J. Geophys. Res.,* 113: G00A03 doi:10.1029/2007JG000505.

Sachs, T, M Giebels, J Boike, L Kutzbach (2010) Environmental controls on CH_4 emission from polygonal tundra on the microsite scale in the Lena river delta, Siberia. *Global Change Biol.,* 11: 3096-110.

Schneider, J, G Grosse, D Wagner (2009) Land cover classification of tundra environments in the Arctic Lena Delta based on Landsat 7 ETM+ data and its application for upscaling of methane emissions. *Remote. Sens. Environ.,* 113: 380-91.

Schneider von Deimling, T, M Meinshausen, A Levermann, V Huber, K Frieler, D M Lawrence, V Brovkin (2012) Estimating the near-surface permafrost-carbon feedback on global warming. *Biogeosciences,* 9: 649-65.

Schroeder, R, M A Rawlins, K C McDonald, E Podest, R Zimmerman, M Kueppers (2010) Satellite microwave remote sensing of North Eurasian inundation dynamics: Development of coarse-resolution products and comparison with high-resolution synthetic aperture radar data. *Environ. Res. Lett.,* 5: 015003 doi:10.1088/1748-9326/5/1/015003.

Screen, J A, I Simmonds (2010) The central role of diminishing sea ice in recent Arctic temperature amplification. *Nature,* 464: 1334-37.

Screen, J A (2013) Influence of Arctic sea ice on European summer precipitation. *Environ. Res. Lett.,* 8: 044015 doi:10.1088/1748-9326/8/4/044015.

Serreze, M C, A J Etringer (2003) Precipitation characteristics of the Eurasian arctic drainage system. *Int. J. Climatol.,* 23: 1267-91.

Skific, N, J A Francis, J J Cassano (2009) Attribution of projected changes in atmospheric moisture transport in the Arctic: a self-organizing map perspective. *J. Climate,* 22: 4135-53.

Smith, L C, Y Sheng, G MacDonald, L D Hinzman (2005) Disappearing arctic lakes. *Science,* 308: 1429.

Smith, S L, V E Romanovsky, A G Lewkowicz, C R Burn, M Allard, G D Clow, K Yoshikawa, J Throop (2010) Thermal state of permafrost in North America: a contribution to the International Polar Year. *Permafrost and Periglac. Process.,* 21: 117-35.

Song, C, X Xu, X Sun, H Tian, L Sun, Y Miao, X Wang, Y Guo (2012) Large methane emission upon spring thaw from natural wetlands in the northern permafrost region. *Environ. Res. Lett.,* 7: 034009 doi:10.1088/1748-9326/7/3/034009.

Spahni, R, R Wania, L Neef, M van Weele, I Pison, P Bousquet, C Frankenberg, P N Foster, F Joos, I C Prentice, P van Velthoven (2011) Constraining global methane emissions and uptake by ecosystems. *Biogeosciences,* 8: 1643-65.

Ström, L, A Ekberg, M Mastepanov, T R Christensen (2003) The effect of vascular plants on carbon turnover and methane emissions from a tundra wetland. *Glob. Change Biol.,* 9: 1185-92.

Sturtevant, C S, W C Oechel (2013) Spatial variation in landscape-level CO_2 and CH_4 fluxes from arctic coastal tundra: influence from vegetation, wetness, and the thaw lake cycle. *Glob. Change Biol.,* 19: 2853-66.

Tarnocai, C (2006) The effect of climate change on carbon in Canadian peatlands. *Global Planet. Change,* 53: 222-32.

Turetsky, M R, R K Wieder, D H Vitt, R J Evans, K D Scott (2007) The disappearance of relict permafrost in boreal north America: Effects on peatland carbon storage and fluxes. *Glob. Change Biol.,* 13: 1922-34.

Turetsky, M R, C C Treat, M P Waldrop, J M Waddington, J W Harden, A D McGuire (2008) Short-term response of methane fluxes and methanogen activity to water table and soil warming manipulations in an Alaskan peatland. *J. Geophys. Res. Biogeosci.,* 113: G00A10 doi:10.1029/2007JG000496.

Turetsky, M R, A Kotowska, J Bubier, N B Dise, P Crill, E R C Hornibrook, K Minkkinen, T R Moore, I H Myers-Smith, H Nykänen, D Olefeldt, J Rinne, S Saarnio, N Shurpali, E S Tuittila, J M Waddington, J R White, K P Wickland, M Wilmking (2014) A synthesis of methane emissions from 71 northern, temperate, and subtropical wetlands. *Glob. Change Biol.* doi:10.1111/gcb.12580.

van Huissteden, J, C Berrittella, F J WParmentier, Y Mi, T C Maximov, A J Dolman (2011) Methane emissions from permafrost thaw lakes limited by lake drainage. *Nature Clim. Change,* 2: 119-23.

von Fischer, J C, R C Rhew, G M Ames, B K Fosdick, P E von Fischer (2010) Vegetation height and other controls of spatial variability in methane emissions from the Arctic coastal tundra at Barrow, Alaska. *J. Geophys. Res.,* 115: G00I03 doi:10.1029/2009JG001283.

Wagner, D, S Kobabe, S Liebner (2009) Bacterial community structure and carbon turnover in permafrost-affected soils of the Lena Delta, northeastern Siberia. *Can. J. Microbiol.,* 55; 73-83.

Waldrop, M P, K P Wickland, R White III, A A Berhe, J W Harden, V E Romanovsky (2010) Molecular investigations into a globally important carbon pool: permafrost-protected carbon in Alaskan soils. *Glob. Change Biol.*, 9: 2543-54.

Walsh, J E, J E Overland, P Y Groisman, B Rudolf (2011) Ongoing climate change in the Arctic. *AMBIO,* 40: 6-16.

Walter, K M, S A Zimov, J P Chanton, D Verbyla, F S Chapin III (2006) Methane bubbling from Siberian thaw lakes as a positive feedback to climate warming. *Nature,* 443: 71-5.

Wania, R, J R Melton, E L Hodson, B Poulter, B Ringeval, R Spahni, T Bohn, C A Avis, G Chen, A V Eliseev, P O Hopcroft, W J Riley, Subin Z M, Tian H, van Bodegom P M, T Kleinen, Z C Yu, J S Singarayer, S Zurcher, D P Lettenmaier, D J Beerling, S N Denisov, C Prigent, E Papa, J O Kaplan (2013) Present state of global wetland extent and wetland methane modeling: methodology of a model inter-comparison project (WETCHIMP). *Geosci. Model Dev.,* 6: 617-41.

Watts, J D, J S Kimball, L J Jones, R Schroeder, K C McDonald (2012) Satellite microwave remote sensing of contrasting surface water inundation changes within the Arctic-Boreal region. *Remote Sens. Environ*., 127: 223-36.

Watts, J D, J S Kimball, F J W Parmentier, T Sachs, D Zona, W Oechel, T Tagesson, M Jackowicz-Korczyński, M Aurela (2014) A satellite data driven biophysical modeling approach for estimating northern peatland and tundra CO_2 and CH_4 fluxes.

Biogeosciences, 11:1961-80.

Wik, M, P M Crill, R K Varner, D Bastviken (2013) Multiyear measurements of ebullitive methane flux from three subarctic lakes. *J. Geophys. Res.,* 118: 1307-21.

Wille, C, L Kutzbach, T Sachs, D Wagner, E M Pfeiffer (2008) Methane emission from Siberian arctic polygonal tundra: eddy covariance measurements and modeling. *Glob. Change Biol.,* 14: 1395-408.

Yi, Y, J S Kimball, L A Jones, R H Reichle, K C McDonald (2011) Evaluation of MERRA land surface estimates in preparation for the soil moisture active passive mission. *J. Climate,* 24: 3797-816.

Yi, Y, J S Kimball, L A Jones, R H Reichle, R Nemani, H A Margolis (2013) Recent climate and fire disturbance impacts on boreal and arctic ecosystem productivity estimated using a satellite-based terrestrial carbon flux model. *J. Geophys. Res.,* 118: 1-17.

Yu, Z, J Loisel, D B Brosseau, D W Beilman, S J Hunt (2010) Global peatland dynamics since the Last Glacial Maximum. *Geophys. Res. Lett.,* 37: L13402 doi:1029/2010GL043584.

Yue, S, P Pilon, B Phinney, G Cavadias (2002) The influence of autocorrelation on the ability to detect trend in hydrological series. *Hydrol. Process.,* 16: 1807-29.

Zhang, K, J S Kimball, E H Hogg, M Zhao, W C Oechel, J J Cassano, S W Running (2008) Satellite-based model detection of recent climate-driven changes in northern high-latitude vegetation productivity. *J. Geophys. Res.,* 113: G03033 doi:10.1029/2007JG000621.

Zhang, X, J He, J Zhang, I Polyakov, R Gerdes, J Inoue, P Wu (2013) Enhanced poleward moisture transport and amplified northern high-latitude wetting trend. *Nature Clim. Change,* 3: 47-51.

Zimov, S A, Y V Voropaev, I P Semiletov, S P Davidov, S F Prosiannikov, F S Chapin III, M C Chapin, S Trumbore, S Tyler (1997) North Siberian lakes: A methane source fueled by Pleistocene carbon. *Science,* 277: 800-1.

Zhu, X, Q Zhuang, M Chen, A Sirin, J Melillo, D Kicklighter, A Sokolov, L Song (2011) Rising methane emissions in response to climate change in Northern Eurasia during the 21st century. *Environ. Res. Lett*., 6: 045211 doi:10.1088/1748-9326/6/4/045211.

Zhu, X, Q Zhuang, Z Qin, M Glagolev, L Song (2013) Estimating wetland methane emissions from the northern high latitudes from 1990 to 2009 using artificial neural networks. *Glob. Change Biol.,* 27: 592-604.

Zona, D, W C Oechel, J Kochendorfer, U K T Paw, A N Salyuk, P C Olivas, S F Oberbauer, D A Lipson (2009) Methane fluxes during the initiation of a large-scale water table manipulation experiment in the Alaskan Arctic. *Glob. Biogeochem. Cy.,* 23: GB2013 doi:10.1029/2009GB003487.

Tables

Table 3.1 Wetland methane (CH_4) emissions and associated surface inundation extent determined by regional modeling studies using satellite microwave based surface water (Fw) retrievals to define the spatial extent of methane producing area. The Fw inputs include those scaled using 15-day, monthly and annual Fw means and maximums, or a static multi-summer Fw mean climatology. The methane emissions determined in this study are reported for inundated and combined inundated/non-inundated wetland landscape fractions.

Study	Model	Domain	Fw Source	Fw Period	Fw Scaling	Fw Area (km^2)	Simulation Period (CH_4)	Emissions (Tg CH_4 yr^{-1}) ± Std. Dev.
Petrescu *et al* (2010)	PEATLAND-VU	55° – 70° N	Prigent *et al* (2007)	1993 – 2000	Monthly Clim. (Avg.)	1.6×10^6	2001 – 2006	
					Adjusted Area	4.4×10^6		89
Ringeval *et al* (2010)	ORCHIDEE	> 50° N	Prigent *et al* (2007)	1993 – 2000	Month Avg.	–	1993 – 2000	41
Riley *et al* (2011)	CLM4Me	45° – 70° N	Prigent *et al* (2007)	1993 – 2000	Month Avg.	$2 \text{ to } 3 \times 10^6$	1995 – 1999	70
Spahni *et al* (2011)	LPJ-WHyMe	45° – 90° N	Prigent *et al* (2007)	1993 – 2000	Month Avg.	2.1×10^6	2004	38.5 – 51.1
Wania *et al* (2013)	LPJ-WHyMe	> 45° N	Prigent *et al* (2007), Papa *et al* (2010)	1993 – 2004	Annual Clim. (Avg.)	–	1993 – 2004	40
Wania *et al* (2013), Melton *et al* (2013)	LPJ-Bern	35° – 90° N	Prigent *et al* (2007), Papa *et al* (2010)	1993 – 2004	Monthly Clim. (Avg.)	–	2004	81
This Study (All Areas)	JULES-TCF	45° – 80° N	Jones *et al* (2010), Watts *et al* (2012)	2003 – 2011	15-day Avg.	1.4×10^6	2003 – 2011	54.6 + 1.8
This Study (Inundated Only)	JULES-TCF	45° – 80° N	Jones *et al* (2010), Watts *et al* (2012)	2003 – 2011	15-day Avg.	1.4×10^6	2003 – 2011	6.6 ± 0.2
					15-day Max.	1.8×10^6		9 ± 0.3
					Month Avg.	1.5×10^6		6.7 ± 0.2
					Month Max.	2×10^6		9.8 ± 0.3
					Annual Avg.	1.7×10^6		7.1 ± 0.3
					Annual Max.	3×10^6		12.6 ± 0.4
					Annual Clim. (Avg.)	1.7×10^6		7.2 ± 0.3

Table 3.2 Mean summer fractional water (Fw) inundation and Pearson correspondence (*r*, with associated significance) between flask station dry air mole fractions (nmol CH_4 mol^{-1}) and cumulative methane emission estimates (tonne CH_4 grid $cell^{-1}$) within a 3 x 3 window centered at Barrow (BRW), Lac LaBiche (LLB) and Pallas Sammaltunturi (PAL). The model simulations incorporate dynamic 15 day or mean annual Fw; non-inundated grid cell fractions are regulated by surface soil moisture content (θ).

Location	Fw Inundation (%)	Dynamic Fw	Annual Fw	θ	Fw + θ
		R			
BRW	5 – 15%	0.46 (p = 0.11)	0.43 (p = 0.12)	-0.14 (p = 0.36)	0.05 (p = 0.45)
LLB	3 – 4%	0.65 (p = 0.24)	0.74 (p = 0.18)	0.94 (p = 0.03)	0.96 (p = 0.02)
PAL	1 – 3%	0.86 (p < 0.01)	0.02 (p = 0.48)	0.10 (p = 0.4)	0.13 (p = 0.37)

Figures

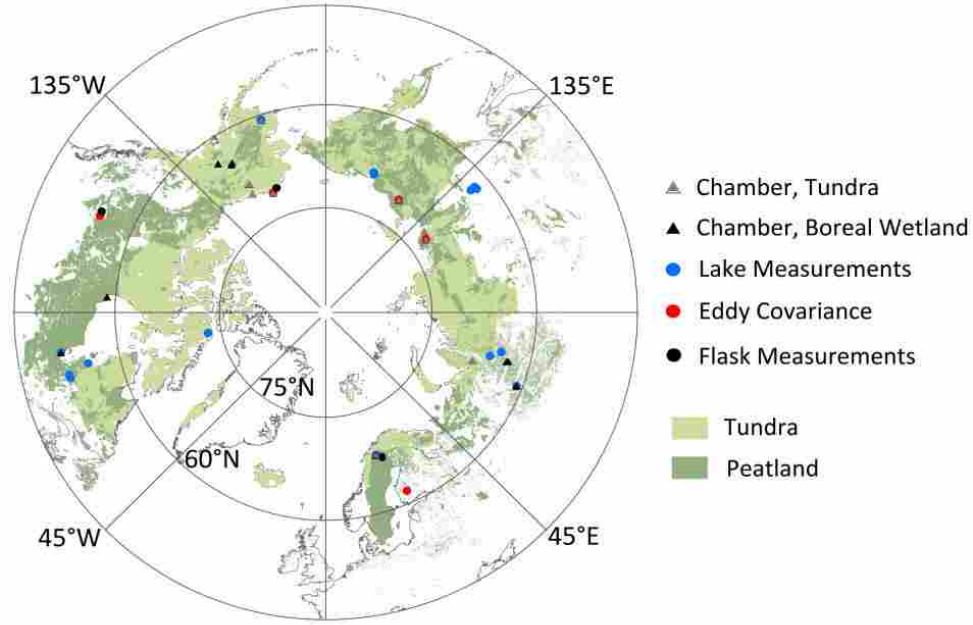

Figure 3. 1 Locations of tower eddy covariance, flux chamber, lake and flask measurement sites used to verify methane emission simulations for the Arctic-boreal (≥ 45°N) peatlands (based on data provided by Gunnarsson & Löfroth 2009, Yu *et al.* 2010, Franzén *et al.* 2012) and RECCAP tundra domain.

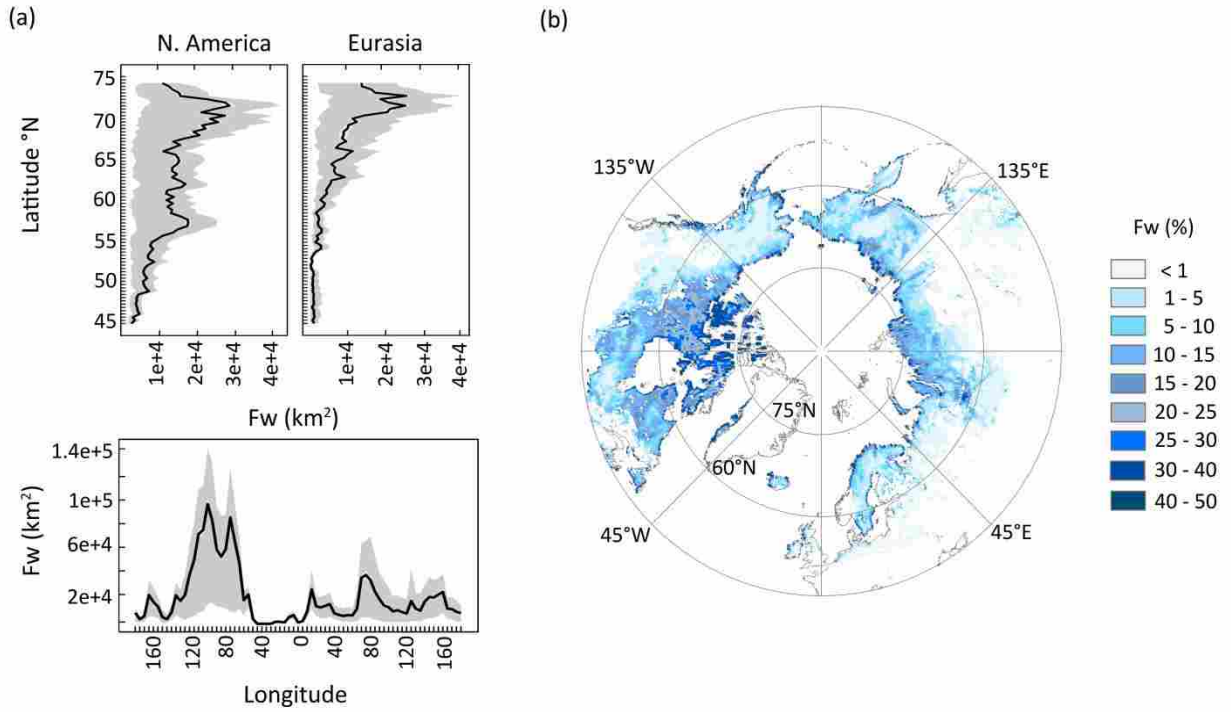

Figure 3.2 Regional variability in fractional surface water (Fw) within the northern (≥ 45°N) wetland regions by (a) latitudinal and longitudinal distribution and (b) pan-Arctic domain; black lines and grey shading in (a) denote respective Fw spatial means and standard deviations [± SD]. A multi-year (2003-2011) mean of daily summer AMSR-E Fw retrievals was used to derive the spatial extent of inundation.

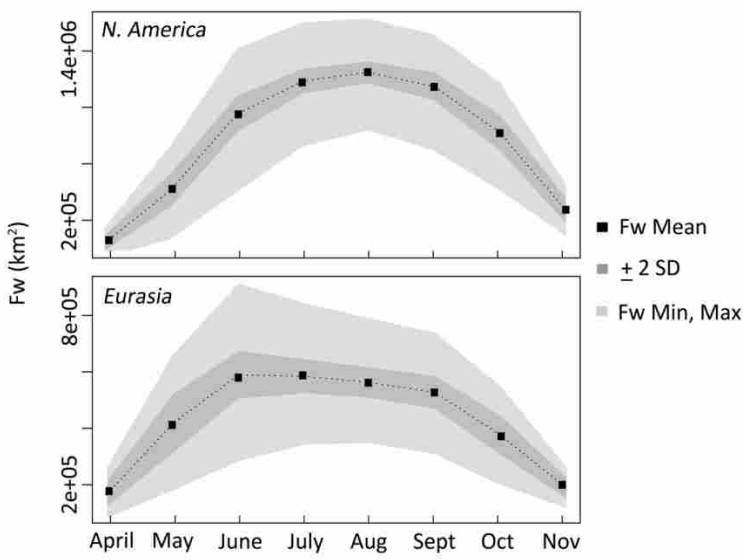

Figure 3.3 Seasonal (2003-2011) variability in AMSR-E Fw inundation (km^2) within the Arctic-boreal wetland domain. The mean monthly Fw climatology is indicated in black, and corresponding $\pm$ 2 SD (Fw minima, maxima) are denoted by dark (light) grey shading.

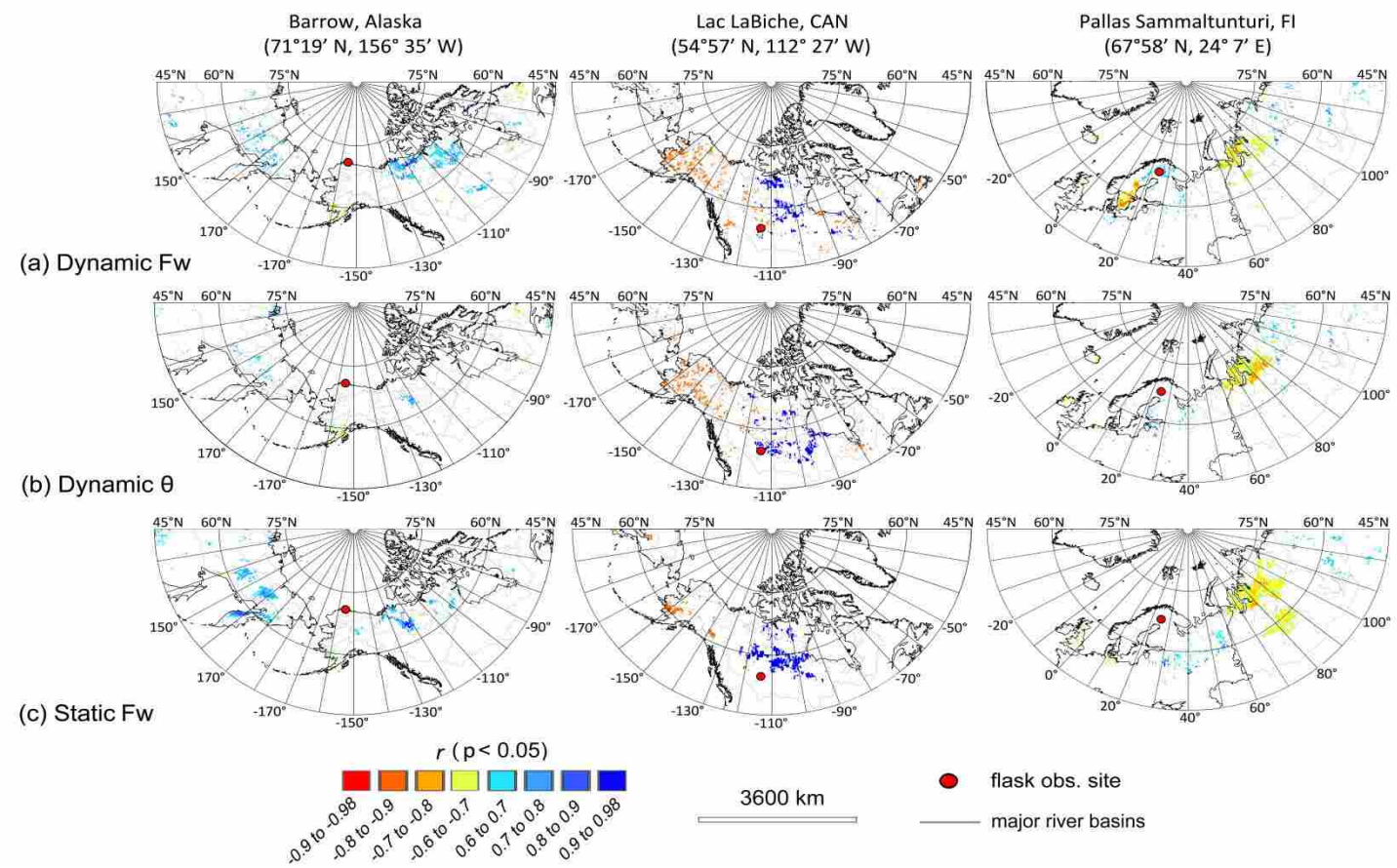

Figure 3.4 Regional Pearson correlation (*r*) between mean summer (May through September) dry air mole fractions (nmol CH_4 mol^{-1}) from NOAA ESRL flask sites in Alaska, Canada, and Finland, and modeled methane emissions (tonne CH_4 $cell^{-1}$) for sub-grid inundated (Fw) and non-inundated surface moisture (Θ) conditions. Methane emissions from inundated surfaces reflect model simulations using dynamic 15 day Fw inputs, or static Fw climatology for the 2003-2011 summer period. The correlation significance is determined at a minimum 95% probability level.

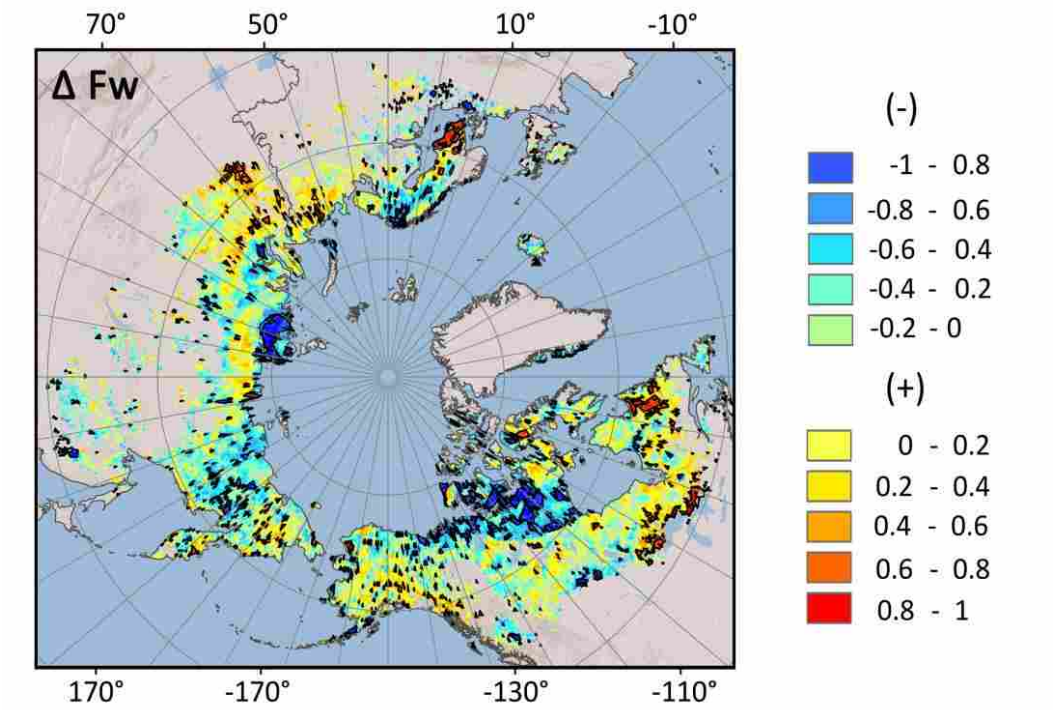

Figure 3.5 Recent summer AMSR-E Fw wetting and drying trends in the northern ($\geq$ 45°N) wetland regions, indicated by Mann-Kendall tau rank coefficients. Positive (negative) tau represents an increase (decrease) in surface water cover. Black polylines denote areas having significant ($p < 0.05$, $|tau| > 0.6$) change in surface water extent over the 2003-2011 satellite observation record.

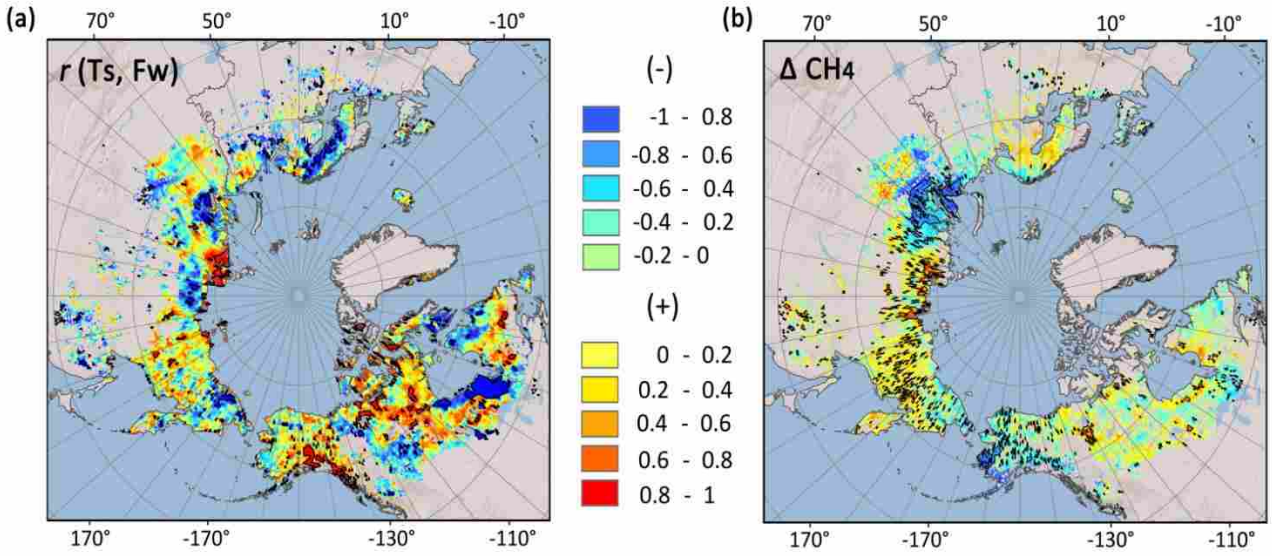

Figure 3.6 Regional (a) Pearson correlations (*r*) between summer MERRA reanalysis surface soil temperature (T_s) and AMSR-E Fw inundation extent from 2003 to 2011, and (b) trends (Mann-Kendall tau) in wetland methane (CH_4) emissions for inundated and wet soil landscapes. Areas of significant ($p < 0.05$) correlation or trend are indicated by the black polylines.

Chapter 3 Supplement

Table S3.1 Location and description of tower eddy covariance, chamber and lake flux measurement records used for methane (CH_4) model calibration and validation.

Location	Coordinates	Description	Year(s)	Month(s) of Measurement	Method	Average Flux (mg CH_4 m^{-2} d^{-1})	Reference
Barrow, Alaska	71°17’ N, 156°35’ W	wet tundra	2007	July	EC	25	Zona *et al* (2009)
Central Alberta, Canada	54°57’ N, 112°28’ W	boreal fen	2007	May-Sept.	EC	25	Long *et al* (2010)
Stordalen Mire, Sweden	68°21’ N, 19°02’ E	wet tundra	2006,2007	May-Sept.	EC	137	Jackowicz-Korczynski *et al* (2010)
Siikaneva, Finland	61°50' N, 24°12' E	boreal fen	2005	May-Sept.	EC	66	Rinne *et al* (2007)
Lena River Delta, Siberia	72°22' N, 126°30' E	wet tundra	2003,2006	July-Sept.	EC	19	Sachs *et al* (2008), Wille *et al* (2008)
Kytalyk, Siberia	69°36’ N, 161°20’ E	wet tundra	2009	June	EC	38	Parmentier *et al* (2011)
Barrow, Alaska	71°17’ N, 156°37’ W	wet tundra	2007	July	Flux chamber	50	von Fischer *et al* (2010)
Barrow, Alaska	71°17’ N, 156°37’ W	flooded tundra	2007	July	Flux chamber	84	von Fischer *et al* (2010)
North Slope, Alaska	70°03’ N, 148°34’ W	wet tundra	1984	Aug.	Flux chamber	119	Sebacher *et al* (1986)
Brooks Range, Alaska	68°26’ N, 149°22’ W	wet tundra	1984	Aug.	Flux chamber	40	Sebacher *et al* (1986)
Toolik Lake, Alaska	68°38’ N, 149°38’ W	wet tundra	1991,1992	June-Aug.	Flux chamber	57	Christensen (1993)
Toolik Lake, Alaska	68°38’ N, 149°38’ W	wet tundra	1991-1993	June-Aug.	Flux chamber	94	Schimel *et al* (1995)
Bethel, Alaska	60°45’ N, 161°45’ W	wet tundra	1988	July, Aug.	Flux chamber	73	Bartlett *et al* (1992)
Bethel, Alaska	60°45’ N, 161°45’ W	tundra lake	1988	July, Aug.	Flux chamber	65	Bartlett *et al* (1992)
Stordalen Mire, Sweden	68°21’ N, 19°02’ E	wet tundra	1998-2000	June-Sept.	Flux chamber	147	Öquist and Svensson (2002)
Stordalen Mire, Sweden	68°22’ N, 19°03’ E	wet tundra	2000-2007	July, Aug.	Flux chamber	35	Bäckstrand *et al* (2010)
Lena River Delta, Siberia	72°22' N, 126°28' E	wet tundra	1999-200	July, Aug.	Flux chamber	36	Wagner *et al* (2003)
Tiksi, Siberia	71°50’ N, 130°0’ E	tundra peatland	1993-1995	July, Aug.	Flux chamber	46	Nakano *et al* (2000)
Cherskii, Siberia	70°49’ N, 147°29’ E	wet tundra	2003	July-Oct.	Flux chamber	29	Merbold *et al* (2009)
Indigirka lowlands, Siberia	70°48’ N, 147°26’ E	wet tundra	2004	Aug.	Flux chamber	173	van Huissteden *et al* (2005)
Yamal, Siberia	68°08’ N, 71°42’ E	wet tundra	1995	June, Aug.	Flux chamber	64	Heyer *et al* (2002)
Fairbanks, Alaska	64°52’ N, 147°51’ W	boreal muskeg	1987-1990	May-Sept.	Flux chamber	35	Whalen and Reeburgh (1992)

Bonanza Creek, Alaska	64°41’ N, 148°19’ W	boreal wetland	2003	May-Sept.	Flux chamber	93	Wickland *et al* (2006)
Alaska Range	63°41’ N, 144°29’ W	boreal marsh	1984	Aug.	Flux chamber	106	Sebacher *et al* (1986)
Hudson Bay, Canada	58°45’ N, 94°09’ W	sub-arctic fen/bog	1990	June-Sept.	Flux chamber	72	Roulet *et al* (1994)
James Bay, Canada	51°35’ N, 81°16’ W	boreal fen/bog	1990	June-Oct.	Flux chamber	52	Roulet *et al* (1994)
Storflaket, Sweden	68°20’ N, 18°58’ E	subarctic mire	2007	May-Sept.	Flux chamber	21	Lund *et al* (2009)
Noyabr'sk Pyaku Pur, Siberia	63°24’ N, 74°34’ E	wet boreal hollow	2008-2010	Summer/Autumn	Flux chamber	20	Sabrekov *et al* (2012)
Noyabr'sk, Siberia	63°09’ N, 74°51’ E	boreal bog	2008-2010	Summer/Autumn	Flux chamber	29	Sabrekov *et al* (2012)
Mukhrino, Siberia	60°53’ N, 68°40’ E	boreal bog	2008-2010	Summer/Autumn	Flux chamber	7	Sabrekov *et al* (2012)
Bethel, Alaska	60°45’ N, 161°45’ W	thermokarst lake	1988	July, Aug.	Flux chamber	10	Bartlett *et al* (1992)
Nunavik, Canada	73°09’ N, 79°58’ W	thermokarst lake	2007	June, July	Dissolved. gas conc.	14	Laurion *et al* (2010)
Nunavik, Canada	55°16’ N, 77°46’ W	thermokarst lake	2007	June, July	Dissolved. gas conc.	2	Laurion *et al* (2010)
Quebec, Canada	52°09’ N, 76°10’ W	boreal lake	2006-2008	May, June	Dissolved. gas conc.	0.69	Demarty *et al* (2011)
Quebec, Canada	52°12’ N, 75°29’ W	boreal lake	2006-2008	May, June	Dissolved. gas conc.	0.3	Demarty *et al* (2011)
Hudson Bay, Canada	51°35’ N, 81°16’ W	boreal pond/lake	1990	June-Oct.	Flux chamber	126	Roulet *et al* (1994)
James Bay, Canada	51°35’ N, 81°16’ W	boreal pond	1990	June-Sept.	Static chamber	12	Roulet *et al* (1994)
Stordalen Mire, Sweden	68°21’ N, 19°03’ E	thermokarst lake	2007	Summer, Non-frozen period	Dissolved. gas conc.	31	Karlsson *et al* (2010)
Kolyma lowland, Siberia	69°N, 161° E	thermokarst lake	-	May-July	Dissolved. gas conc.	5	Zimov *et al* (1997)
Northern Siberia	68°45’ N, 161°20’ E	thermokarst lake	2003-2004	June-Sept.	Bubble traps	39	Walter *et al* (2006)
Khanty-Mansiysk, Siberia	65°52’ N, 74°58’ E	thermokarst lake	2005	July, Aug.	Floating chamber	6	Repo *et al* (2007)
Purpe, Siberia	64°27’ N, 77°04’ E	boreal pond	2008-2010	Summer/Autumn	Static chamber	5	Sabrekov *et al* (2012)
Yakutsk, Siberia	62°54’ N, 130°33’ E	thermokarst pond	2007	June, Aug.	Floating chamber	140	Desyatkin *et al* (2009)
Yakutsk, Siberia	62°11’ N, 130°33’ E	thermokarst pond	2007	June, Aug.	Floating chamber	38	Desyatkin *et al* (2009)
Yakutsk, Siberia	62°11’ N, 130°34’ E	thermokarst pond	2007	June, Aug.	Floating chamber	119	Desyatkin *et al* (2009)
Yakutia, Siberia	62°05’ N, 129°45’ E	thermokarst pond	2000-2001	June, July	Floating chamber	48	Morishita *et al* (2003)
Mukhrino, Siberia	60°53’ N, 68°38’ E	boreal mire/lake	2008-2010	Summer/Autumn	Static chamber	57	Sabrekov *et al* (2012)

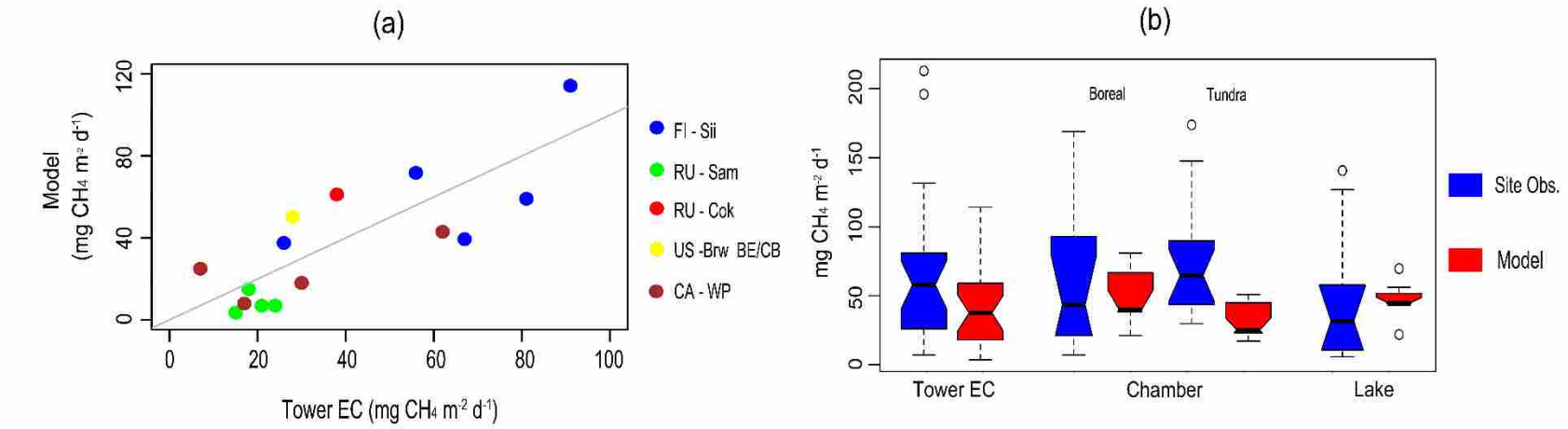

Figure S3.1 Modeled methane fluxes (mg CH_4 m^{-2} d^{-1}) evaluated against mean monthly (a) tower eddy covariance (EC) records from Alaska (US-Brw BE/CB), Canada (CA-WP), Finland (Fi-Sii), Russia (RU-Sam, RU-Cok) and (b) chamber (boreal and tundra wetlands) and lake flux observations. Boxplot notches indicate the 95% confidence interval around the median (black horizontal line); lower and upper box boundaries indicate the first and third quartiles. The methane emission estimates for tundra sites are significantly lower ($p < 0.05$, $n = 10$) than the flux chamber observations.

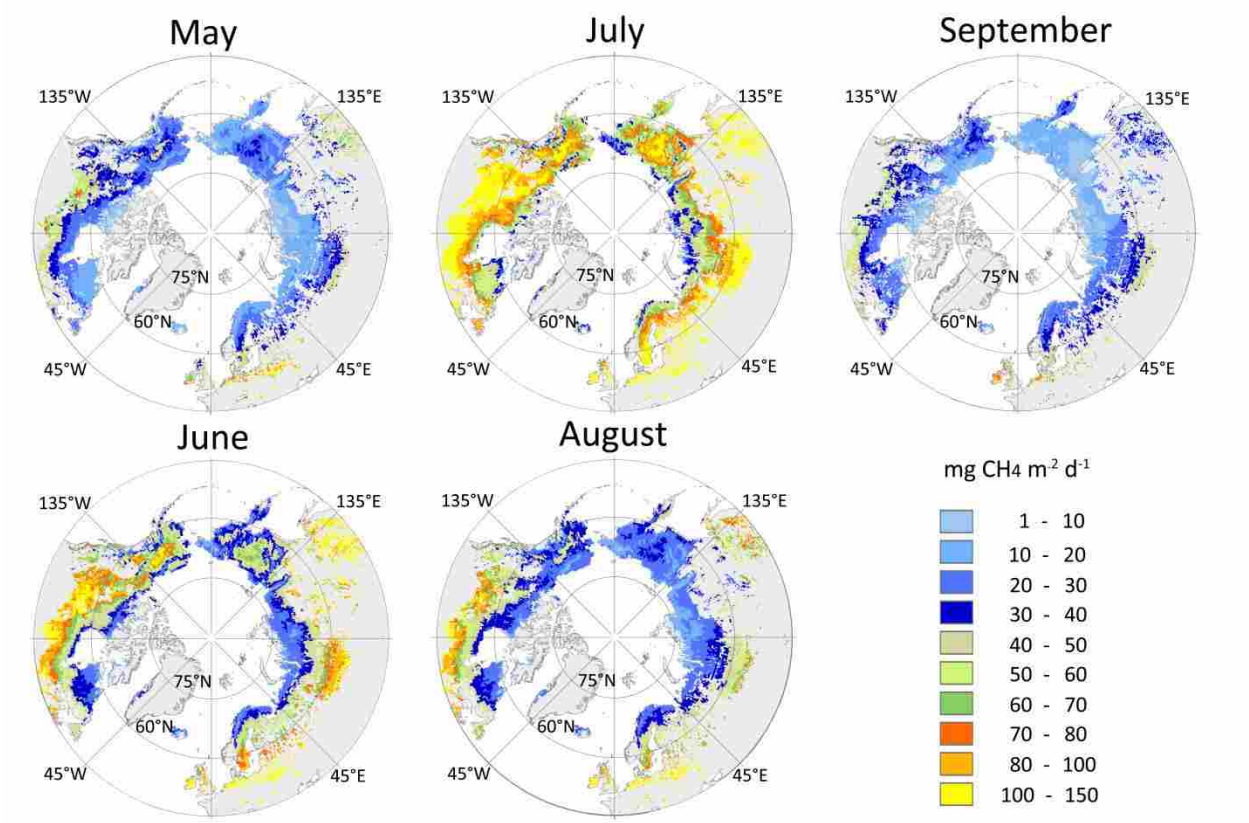

Figure S3.2 Mean summer methane fluxes (mg CH_4 m^{-2} d^{-1}) for northern tundra and peatland regions, over the 2003 to 2011 study period. The northward progression of summer emissions reflects soil warming and lessening frozen surface constraints, in addition to increases in labile carbon availability.

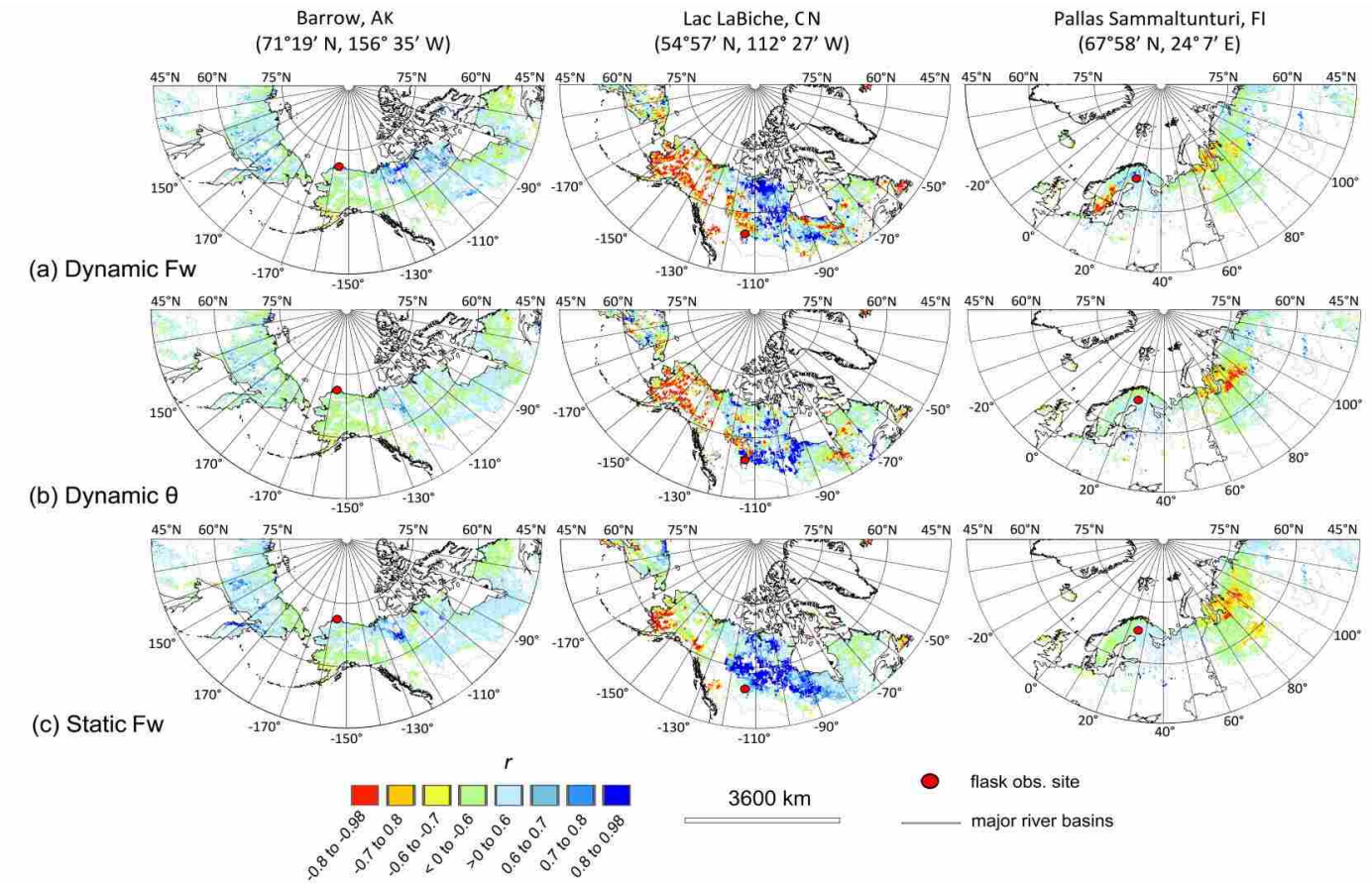

Figure S3.3 Regional correlations (*r*) between mean summer (May through September) dry air mole fractions (nmol CH_4 mol^{-1}) from NOAA ESRL flask sites in Alaska, Canada, and Finland, and modeled methane emissions (tonne CH_4 $cell^{-1}$) for sub-grid inundated (Fw) and non-inundated surface moisture conditions. The emissions from inundated surfaces reflect model simulations using dynamic 15-day Fw inputs, or static Fw climatology for the 2003-2011 summer period.

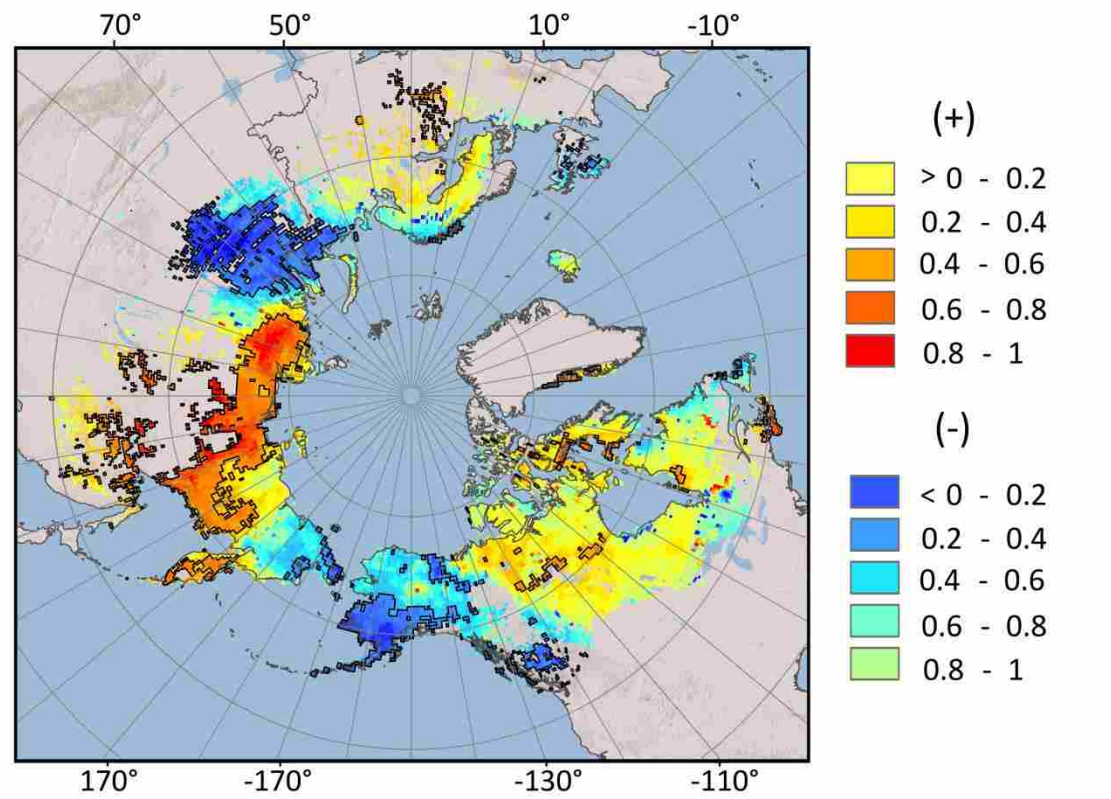

Figure S3.4 Recent trends in MERRA reanalysis summer surface soil temperature (T_s) for northern wetland regions $\geq$ 45°N, as indicated by Mann-Kendall tau rank coefficients. Positive (negative) tau indicates regional warming (cooling); black polylines denote areas with significant ($p < 0.05$) change over the 2003-2011 period.

S3 References

Bäckstrand, K, P M Crill, M Jackowicz-Korczyński, M Mastepanov, T R Christensen, D Bastviken (2010) Annual carbon gas budget for a subarctic peatland, Northern Sweden *Biogeosciences.* 7: 95-108.

Bartlett, K B, P M Crill, R L Sass, R C Harriss, N B Dise (1992) Methane emissions from tundra environments in the Yukon-Kuskokwim Delta, Alaska. *J. Geophys. Res.,* 97: 645-60.

Christensen, T R (1993) Methane emissions from Arctic tundra. *Biogeochem*. 21: 117-139.

Demarty, M, J Bastien, A Tremblay (2011) Annual follow-up of gross diffusive carbon dioxide and methane emissions from a boreal reservoir and two nearby lakes in Quebec, Canada. *Biogeosciences,* 8: 41-53.

Desyatkin, A R, F Takakai, P P Fedorov, M C Nikolaeva, R V Desyatkin, R Hatano (2009) CH_4 emission from different stages of thermokarst formation in Central Yakutia, East Siberia. *J. Soil Sci. Plant Nut.,* 55: 558-70.

Heyer, J, U Berger, I L Kuzin, O N Yakovlev (2002) Methane emissions from different ecosystem structures of the subarctic tundra in Western Siberia during midsummer and during the thaw period. *Tellus B,* 54: 231-49.

Jackowicz-Korczyński, M, T R Christensen, K Bäckstrand, P Crill, T Friborg, M Mastepanov, L Ström (2010) Annual cycle of methane emission from a subarctic peatland. *J. Geophys. Res.,* 115: G02009 doi:10.1029/2008JG00913.

Karlsson, J, T R Christensen, P Crill, J Förster, D Hammarlund, M Jackowicz-Korczynski, U Kokfelt, C Roehm, P Rosén (2010) Quantifying the relative importance of lake emissions in the carbon budget of a subarctic catchment. *J. Geophys. Res.* 115: G03006 doi:1029/2010JG001305.

Laurion, I, W F Vincent, S MacIntyre, L Retamal, C Dupont, P Francus, R Pienitz (2010) Variability in greenhouse gas emissions from permafrost thaw ponds. *Limnol. Oceanogr.,* 55: 115-33.

Long, K D, L B Flanagan, T Cai (2010) Diurnal and seasonal variation in methane emissions in a northern Canadian peatland measured by eddy covariance. *Glob. Change Biol.,* 16: 2420-35.

Lund, M, T R Christensen, M Mastepanov, A Lindroth, L Ström (2009) Effects of N and P fertilization on the greenhouse gas exchange in two northern peatlands with contrasting N deposition rates. *Biogeosciences,* 2135-44.

Merbold, L, W L Kutsch, C Corradi, O Kolle, C Rebmann, P C Stoy, S A Zimov, E D Schulze (2009) Artificial drainage and associated carbon fluxes (CO_2/CH_4) in a tundra ecosystem. *Glob. Change Biol.*, 15: 2599-614.

Morishita, T, R Hatano, R V Desyatkin (2003) CH_4 flux in an alas ecosystem formed by forest disturbance near Yakutsk, Eastern Siberia, Russia. *J. Soil Sci. Plant Nut.*, 49: 369-77.

Nakano, T, S Kuniyoshi, M Fukuda (2000) Temporal variation in methane emissions from tundra wetlands in a permafrost area, northeastern Siberia. *Atmos. Environ.*, 34: 1205-13.

Öquist, M G, B H Svensson (2002) Vascular plants as regulators of methane emissions from a subarctic mire ecosystem. *J. Geophys. Res.*, 107: 4580 doi:10.1029/2001JD001030.

Parmentier, F J W, J van Huissteden, M K van der Molen, G Schaepman-Strub, S A Karsanaev, T C Maximov, A J Dolman (2011) Spatial and temporal dynamics in eddy covariance observations of methane fluxes at a tundra site in northeastern Siberia. *J. Geophys. Res.* 116: G03016, doi:10.1029/2010JG001637.

Repo, M E, J T Huttunen, A V Naumov, A V Chichulin, E D Lapshina, W Bleuten, P J Martikainen (2007) Release of CO_2 and CH_4 from small wetland lakes in western Siberia *Tellus B*, 59: 788-96.

Rinne J, T Riutta, M Pihlatie, M Aurela M, S Haapanala, J P Tuovinen, E S Tuittila (2007) Annual cycles of methane emission from a boreal fen measured by the eddy covariance Technique. *Tellus B*, 59: 449-57.

Roulet, N T, A Jano, C A Kelly, L F Klinger, T R Moore, R Protz, J A Ritter, W R Rouse (1994) *J. Geophys. Res.*, 99: 1439-54.

Sabrekov, A F, M V Glagolev, I V Filippov, V S Kazantsev, E D Lapshina, T Machida, S S Maksyutov (2012) Methane emissions from North and Middle Taiga mires of Western Siberia: Bc8 Standard Model. *Moscow Soil Sci. Bulletin*, 67: 45-53.

Sachs, T, C Wille, J Boike, L Kutzbach (2008) Environmental controls on ecosystem-scale CH_4 emission from polygonal tundra in the Lena River Delta, Siberia. *J. Geophys. Res.*, 113: 3096-110.

Schimel, J P (1995) Plant transport and methane production as controls on methane flux from arctic wet meadow tundra *Biogeochem.*, 28: 183-200.

Sebacher, D I, R C Harriss, K B Bartlett, S M Sebacher, S S Grice (1986) Atmospheric methane sources: Alaskan tundra bogs, an alpine fen, and a subarctic boreal marsh. *Tellus B*, 38: 1-10.

Wagner, D, S Kobabe, E M Pfeiffer, H W Hubberten (2003) *Permafrost Periglac. Process*., 14: 173-85.

Walter, K M, S A Zimov, J P Chanton, D Verbyla, F S Chapin III (2006) Methane bubbling from Siberian thaw lakes as a positive feedback to climate warming. *Nature,* 443: 71-5.

Whalen, S C, W S Reeburgh (1992) Interannual variations in tundra methane emissions: A 4-year time series at fixed sites. *Global Biogeochem. Cy.*, 6: 139-59.

Wickland, K P, R G Striegl, J C Neff, T Sachs (2006) Effects of permafrost melting on CO_2 and CH_4 exchange of a poorly drained black spruce lowland. *J. Geophys. Res*., 111: G02011 doi:10.1029/2005JG000099.

Wille C, L Kutzbach, T Sachs, D Wagner, E M Pfeiffer (2008) Methane emission from Siberian arctic polygonal tundra: eddy covariance measurements and modeling. *Glob. Change Biol*.14 1395-408.

van Huissteden, J, T C Maximov, A J Dolman (2005) High methane flux from an arctic floodplain (Indigirka lowlands, eastern Siberia). *J. Geophys. Res.*, 110: G02002 doi:10.1029/2005JG000010.

von Fischer, J C, R C Rhew, G M Ames, B K Fosdick, P E von Fischer (2010) Vegetation height and other controls of spatial variability in methane emissions from the Arctic coastal tundra at Barrow, Alaska. *J. Geophys. Res.*, 115: G00I03 doi:10.1029/2009JG001283.

Zimov, S A, Y V Voropaev, I P Semiletov, S P Davidov, S F Prosiannikov, F S Chapin III, M C Chapin, S Trumbore, S Tyler (1997) North Siberian lakes: a methane source fueled by Pleistocene carbon. *Science*, 277: 800-1.

Zona, D, W C Oechel, J Kochendorfer, U K T Paw, A N Salyuk, P C Olivas, S F Oberbauer, D A Lipson (2009) Methane fluxes during the initiation of a large-scale water table manipulation experiment in the Alaskan Arctic. *Glob. Biogeochem. Cy.* 23: GB2013 doi:10.1029/2009GB003487.

Chapter 4: A satellite data driven biophysical modeling approach for estimating northern wetland peatland and tundra CO_2 and CH_4 fluxes

Corresponding publication:

Watts J D, J S Kimball, F J W Parmentier, T Sachs, J Rinne, D Zona, W Oechel, T Tagesson, M Jackowicz-Korczyński, A Aurela (2014) A satellite data driven biophysical modeling approach for estimating northern peatland and tundra CO_2 and CH_4 fluxes. *Biogeosciences,*11: 1961-1980

4.1 Abstract

The northern terrestrial net ecosystem carbon balance (NECB) is contingent on inputs from vegetation gross primary productivity (GPP) to offset the ecosystem respiration (R_{eco}) of carbon dioxide (CO_2) and methane (CH_4) emissions, but an effective framework to monitor the regional Arctic NECB is lacking. We modified a Terrestrial Carbon Flux (TCF) model developed for satellite remote sensing applications to evaluate wetland CO_2 and CH_4 fluxes over pan-Arctic eddy covariance (EC) flux tower sites. The TCF model estimates GPP, CO_2 and CH_4 emissions using in-situ or remote sensing and reanalysis based climate data as inputs. The TCF model simulations using in-situ data explained > 70% of the r^2 variability in the 8 day cumulative EC measured fluxes. Model simulations using coarser satellite (MODIS) and reanalysis (MERRA) records accounted for approximately 69% and 75% of the respective r^2 variability in the tower CO_2 and CH_4 records, with corresponding RMSE uncertainties of $\leq$ 1.3 g C m^{-2} d^{-1} (CO_2) and 18.2 mg C m^{-2} d^{-1} (CH_4). Although the estimated annual CH_4 emissions were small (< 18 g C m^{-2} yr^{-1}) relative to R_{eco} (> 180 g C m^{-2} yr^{-1}), they reduced the across-site NECB by 23% and contributed to a global warming potential of approximately 165 $\pm$ 128 g CO_2 eq m^{-2} yr^{-1} when considered over a 100-year time span. This model evaluation indicates a strong potential for using the TCF model approach to document landscape scale variability in CO_2 and CH_4 fluxes, and to estimate the NECB for northern peatland and tundra ecosystems.

4.2 Introduction

Northern peatland and tundra ecosystems are important components of the terrestrial carbon cycle and store over half of the global soil organic carbon reservoir in seasonally frozen and permafrost soils (Hugelius *et al*. 2013). However, these systems are becoming increasingly vulnerable to carbon losses as CO_2 and CH_4 emissions, resulting from climate warming and changes in the terrestrial water balance (Kane *et al*. 2012, Kim *et al*. 2012) that can increase soil carbon decomposition. Recent net CO_2 exchange in northern tundra and peatland ecosystems varies from a sink of 291 Tg C yr^{-1} to a source of 80 Tg C yr^{-1}, when considering the substantial uncertainty in regional estimates using scaled flux observations, atmospheric inversions, and ecosystem process models (McGuire *et al*. 2012). The magnitude of carbon sink largely depends on the balance between carbon uptake by vegetation productivity and losses from soil mineralization and respiration processes. High latitude warming can increase ecosystem carbon uptake by reducing cold-temperature constraints on plant carbon assimilation and growth (Hudson *et al*. 2011, Elmendorf *et al*. 2012). Soil warming also accelerates carbon losses due to the exponential effects of temperature on soil respiration, whereas wet and inundated conditions shift microbial activity towards anaerobic consumption pathways that are relatively slow but can result in substantial CH_4 production (Moosavi & Crill, 1997, Merbold *et al*. 2009).

Regional wetting across the Arctic (Watts *et al*. 2012, Zhang *et al*. 2012a) may increase CH_4 emissions, which have a radiative warming potential at least 25 times more potent than CO_2 per unit mass over a 100-year time horizon (Boucher *et al.* 2009). The northern latitudes already contain over 50 % of global wetlands and recent increases in atmospheric CH_4 concentrations have been attributed to heightened gas emissions in these areas during periods of warming (Dlugokencky *et al*. 2009, Dolman *et al*. 2010). Northern peatland and tundra ($\geq$ 50°N) reportedly contribute between 8-79 Tg C in CH_4 emissions each year, but these fluxes have been difficult to constrain due to uncertainty in the parameterization of biogeochemical models, the regional characterization of wetland extent and water table depth, and a scarcity of ecosystem scale CH_4 emission observations (Petrescu *et al*. 2010, Riley *et al*. 2011, Spahni *et al*. 2011, McGuire *et al*. 2012, Meng *et al*. 2012).

Ecosystem studies using chamber and tower eddy covariance (EC) methods continue to provide direct measurements of CO_2 and CH_4 fluxes and add valuable insight into the environmental constraints on these processes. However, extrapolating localized carbon fluxes to regional scales has proven difficult and is severely constrained by the limited number of in-situ observations and the large spatial extent and heterogeneity of peatland and tundra ecosystems. Recent approaches have used satellite-based land cover classifications, photosynthetic leaf area maps, or wetness indices to "up-scale" CO_2 (Forbrich *et al*. 2011, Marushchak *et al*. 2013) and CH_4 (Tagesson *et al*. 2013, Sturtevant & Oechel 2013) flux measurements. Remote sensing inputs have also been used in conjunction with biophysical process modeling to estimate landscape-level changes in plant carbon assimilation and soil CO_2 emissions (Yuan *et al*. 2011, Tagesson *et al*. 2012a, Yi *et al*. 2013). Previous analyses of regional CH_4 contributions have ranged from the relatively simple modification of CH_4 emission rate estimates for wetland fractions per temperature and carbon substrate constraints (Potter *et al*. 2006, Clark *et al*. 2011) to the use of more complex multi-layer wetland CH_4 models with integrated hydrological components (McGuire *et al*. 2012, Wania *et al.* 2013). Yet, most investigations have not examined the potential for simultaneously assessing CO_2 and CH_4 fluxes, and the corresponding net ecosystem carbon balance (Sitch *et al.* 2007, Olefeldt *et al.* 2012, McGuire *et al*. 2012) for peatland and tundra using a satellite remote sensing based model approach.

It is well recognized that sub-surface conditions influence the land-atmosphere exchange of CO_2 and CH_4 production. However, near-surface soil temperature, moisture and carbon substrate availability play a crucial role in regulating ecosystem carbon emissions. Strong associations between surface soil temperature ($\leq$ 10 cm depth) and CO_2 respiration have been observed in Arctic peatland and tundra permafrost systems (Kutzbach *et al*. 2007). Significant relationships between CH_4 emissions and temperature have also been reported (Hargreaves *et al*. 2001, Zona *et al.* 2009, Sachs *et al*. 2010). Although warming generally increases the decomposition of organic carbon, the magnitude of CO_2 production is constrained by wet soil conditions (Olivas *et al*. 2010) which instead favor CH_4 emissions and decrease methantrophy in soil and litter layers (Turetsky *et al*. 2008, Olefeldt *et al.* 2012). Oxidation by methanotrophic communities in surface soils can reduce CH_4 emissions by over 90 % when gas transport occurs

through diffusion (Preuss *et al*. 2013), but this constraint is often minimized when pore water content rises above 55-65 % (von Fischer & Hedin, 2007, Sjögersten & Wookey 2009).

Despite increases in the availability of organic carbon and accelerated CO_2 release due to soil warming and thickening of the active layer in permafrost soils (Dorrepaal *et al*. 2009), anaerobic communities have shown a preference for light-carbon fractions (e.g. amines, carbonic acids) that are more abundant in the upper soil horizons (Wagner *et al*. 2009). Similarly, labile carbon substrates from recent photosynthates and root exudates have been observed to increase CH_4 production relative to heavier organic carbon fractions (Ström *et al*. 2003, Dijkstra *et al*. 2012, Olefeldt *et al*. 2013) that require longer decomposition pathways to break down complex molecules into the simple compounds (i.e. acetate, $H_2 + CO_2$) used in methanogenesis (Le Mer & Roger 2001).

The objective of this study was to evaluate the feasibility of using a satellite remote sensing data driven modeling approach to assess the daily and seasonal variability in CO_2 and CH_4 fluxes from northern peatland and tundra ecosystems, according to near-surface environmental controls including soil temperature, moisture and available soil organic carbon. In this paper, we incorporate a newly developed CH_4 emissions algorithm within an existing Terrestrial Carbon Flux (TCF) CO_2 model framework (Kimball *et al*. 2012; Yi *et al*. 2013). The CH_4 emissions algorithm simulates gas production using near-surface temperature, anaerobic soil fractions and labile organic carbon as inputs. Plant CH_4 transport is determined by vegetation growth characteristics derived from gross primary production (GPP), plant functional traits and canopy/surface turbulence. Methane diffusion is determined based on temperature and moisture constraints to gas movement through the soil column, and oxidation potential. Ebullition of CH_4 is assessed using a simple gradient method (van Huissteden *et al*. 2006).

The integrated TCF model allows for satellite remote sensing information to be used as primary inputs, requires minimal parameterization relative to more complex ecosystem process models, and provides a framework to monitor the terrestrial net ecosystem carbon balance (NECB). Although the NECB also encompasses other mechanisms of carbon transport, including dissolved and volatile organic carbon emissions and fire-based particulates, the NECB

is limited in this study to CO_2 and CH_4 fluxes, which often are primary contributors in high latitude tundra and peatland ecosystems (McGuire *et al*. 2010).

To evaluate the combined CO_2 and CH_4 algorithm approach, we compared TCF model simulations to tower EC records from six northern peatland and tundra sites within North America and Eurasia. For this study, baseline simulations driven with tower EC based GPP and in-situ meteorology data were first used to assess the capability of the TCF model approach to quantify temporal changes in landscape scale carbon (CH_4 and CO_2) fluxes. Secondly, CO_2 and CH_4 simulations using internal TCF model GPP estimates (Yi *et al*. 2013) and inputs from satellite and global model reanalysis records were used to evaluate the relative uncertainty introduced when using coarser scale information in place of in-situ data. These satellite and reanalysis driven simulations were then used to determine the annual CO_2 and CH_4 fluxes at the six tower sites, and the relative impact of CH_4 emissions on the NECB.

4.3 Methods

4.3.1 TCF model description

The combined TCF model CO_2 and CH_4 framework regulates carbon gas exchange using soil surface temperature, moisture and soil organic carbon availability as inputs, and has the flexibility to run simulations at local and regional scales. TCF model estimates of ecosystem respiration (R_{eco}) and net ecosystem CO_2 exchange (NEE) have been evaluated against tower EC datasets from boreal and tundra systems using GPP, surface ($\leq$ 10 cm depth) soil temperature (T_s) and volumetric moisture content (θ) inputs available from global model reanalysis and satellite remote sensing records (Kimball *et al*. 2009, McGuire *et al*. 2012). A recent adjustment to the TCF model (Kimball *et al*. 2012, Yi *et al*. 2013) incorporates a light-use efficiency (LUE) algorithm that provides internally derived GPP calculations to determine R_{eco} and NEE fluxes at a daily time step. The adjusted TCF CO_2 model also allows for better user control over parameter settings and surface meteorological inputs (Kimball *et al.* 2012). The CO_2 and newly added CH_4 flux model components are described in the following sections. A summary of the

TCF model inputs, parameters, and the associated parameter values used in this study are provided in the Supplement (Tables S4.1 and S4.2; Figure S4.1).

4.3.1.1 CO_2 flux component

The internal TCF model GPP algorithm estimates daily fluxes based on a biome-dependent vegetation maximum LUE coefficient ($\varepsilon_{max;}$ mg C MJ^{-1}) which represents the optimal conversion of absorbed solar energy and CO_2 to plant organic carbon through photosynthesis (Kimball *et al*. 2012). To account for daily minimum air temperature (T_{min}) and atmospheric vapor pressure deficit (*VPD*) constraints on photosynthesis (Running *et al*. 2004), ε_{max} is reduced (ε) using dimensionless linear rate scalars ranging from 0 (total inhibition) to 1 (no inhibition) that are described elsewhere (i.e. Kimball *et al*. 2012, Yi *et al*. 2013). In this study, we also account for the sensitivity of shallow rooted vegetation and bryophytes, which lack vascular tissues for water transport, to changes in surface volumetric soil water (Wu *et al*. 2013), where θ_{min} and θ_{max} are the specified minimum and maximum parameter values:

$$\varepsilon = \varepsilon_{\max} \times f(VPD) \times f(T_{\min}) \times f(\theta)$$

$$\text{where } f(\theta) = (\theta - \theta_{\min}) / (\theta_{\max} - \theta_{\min}). \quad (1)$$

Simulated GPP (g C m^{-2} d^{-1}) is obtained as:

$$GPP = \varepsilon \times 0.45\, SW_{rad} \times FPAR \quad (2)$$

where SW_{rad} (W m^{-2}) is incoming shortwave radiation and FPAR is the fraction of daily photosynthetically active solar radiation (PAR; MJ m^{-2}) absorbed by plants during photosynthesis. For this approach, PAR is assumed to be 45 % of SW_{rad} (Zhao *et al*. 2005). Remotely sensed normalized difference vegetation index (NDVI) records have been used to estimate vegetation productivity (Schubert *et al*. 2010a, Parmentier *et al*. 2013) and changes in growing season length (Beck & Goetz 2011) across northern peatland and tundra environments. Daily FPAR is derived using the approach of Badawy *et al*. (2013) to mitigate potential biases in low biomass landscapes (Peng *et al*. 2012):

$$FPAR = \frac{0.94(Index - Index_{\min})}{Index_{range}} \quad (3)$$

This approach uses NDVI or simple ratio (SR; i.e. (1+NDVI)/(1-NDVI)) indices as input *Index* values. The results are then averaged to obtain FPAR. $Index_{\text{range}}$ corresponds to the difference between the 2nd and 98th percentiles in the NDVI and SR distributions (Badawry *et al*. 2012).

Biome-specific autotrophic respiration (R_a) is estimated using a carbon use efficiency (CUE) approach that considers the ratio of net primary production (NPP) to GPP (Choudhury 2000). Carbon loss from heterotrophic respiration (R_h) is determined using a 3-pool soil litter decomposition scheme consisting of metabolic (C_{met}), structural (C_{str}) and recalcitrant (C_{rec}) organic carbon pools with variable decomposition rates. The C_{met} pool represents easily decomposable plant residue and root exudates including amino acids, sugars and simple polysaccharides, whereas the C_{str} pool consists of litter residues such as hemi-cellulose and lignin (Ise *et al*. 2008, Porter *et al*. 2010). The C_{rec} pool includes physically and chemically stabilized carbon derived from the C_{met} and C_{str} pools and corresponds to humified peat. A fraction of daily NPP (F_{met}) is first allocated as readily decomposable litterfall to C_{met} and the remaining portion (1-F_{met}) is transferred to C_{str} (Ise & Moorcroft 2006, Kimball *et al*. 2009). To account for reduced mineralization in tundra and peatland environments, approximately 70 % of C_{str} (F_{str}) is reallocated to C_{rec} (Ise & Moorcroft 2006, Ise *et al*. 2008):

$$dC_{met} / dt = NPP \times F_{met} - R_{h,met} \quad (4)$$

$$dC_{str} / dt = NPP\,(1 - F_{met}) - (F_{str} \times C_{str}) - R_{h,str} \quad (5)$$

$$dC_{rec} / dt = (F_{str} \times C_{str}) - R_{h,rec} \quad (6)$$

Daily CO_2 loss from the C_{met} pool (i.e. $R_{h,met}$) is determined as the product of C_{met} and an optimal decomposition rate parameter (K_p). The realized decomposition rate (K_{met}) results from the attenuation of K_p by dimensionless T_s and θ multipliers (T_{mult} and W_{mult}, respectively), that vary between 0 (fully constrained) and 1 (no constraint):

$$K_{met} = K_p \times T_{mult} \times W_{mult} \quad (7)$$

$$T_{mult} = \exp[\,308.56\,(66.02^{-1} - (T_s + T_{ref} - 66.17)^{-1})\,] \quad (8)$$

$$W_{mult} = 1 - 2.2\,(\theta - \theta_{opt})^2 \quad (9)$$

The temperature constraints are imposed using an Arrhenius-type function (Lloyd & Taylor, 1994, Kimball *et al.* 2009) where decomposition is no longer limited when average daily T_s exceeds a user-specified reference temperature (T_{ref}; in K) which can vary with carbon substrate complexity, physical protection, oxygen availability and water stress (Davidson & Janssens 2006). The W_{mult} modifier accounts for the inhibitory effect of dry and near-saturated soil moisture conditions on heterotrophic decomposition (Oberbauer *et al*. 1996). For this study, θ_{opt} is set to 80 % of pore saturation to account for ecosystem adaptations to wet soil conditions (Ise *et al*. 2008, Zona *et al*. 2012) and near-surface oxygen availability provided by plant root transport (Elberling *et al*. 2011). Decomposition rates for C_{str} and C_{rec} (K_{str}, K_{rec}) are determined as 40 % and 1 % of K_{met}, respectively (Kimball *et al*. 2009), and R_h is the total CO_2 loss from the three soil organic carbon pools:

$$R_h = K_{met} \times C_{met} + K_{str} \times C_{str} + K_{rec} \times C_{rec} \quad (10)$$

Finally, the TCF model estimates NEE (g C m^{-2} d^{-1}) as the residual difference between R_{eco}, which includes R_a and R_h respiration components, and GPP. Negative (-) and positive (+) NEE fluxes denote respective terrestrial CO_2 sink and source activity:

$$NEE = (R_a + R_h) - GPP \quad (11)$$

4.3.1.2 CH_4 flux component

A CH_4 emissions algorithm was incorporated within the TCF model to estimate CH_4 fluxes for peatland and tundra landscapes. The model estimates CH_4 production according to T_s, θ, and labile carbon availability. Plant CH_4 transport is modified by vegetation growth and production, plant functional traits, and canopy aerodynamic conductance which takes into account the influence of wind turbulence on moisture/gas flux between vegetation and the atmosphere. The CH_4 module is similar to other process models (e.g. Walter & Heimann 2000, van Huissteden *et al*. 2006) but reduces to a one-dimensional near-surface soil profile following Tian *et al*. (2010) to simplify model parameterization amenable to remote sensing applications. For the purposes of this study, the soil profile is defined for near-surface soil layers as most temperature and moisture retrievals from satellite remote sensing do not characterize deeper soil conditions. Although this approach may not account for variability in carbon fluxes associated

with deeper soil constraints, field studies from high latitude ecosystems have reported strong associations between CH_4 emissions and near-surface conditions including T_s and soil moisture (Hargreaves *et al*. 2001, Sachs *et al*. 2010, von Fischer *et al*. 2010, Sturtevant *et al*. 2012, Tagesson *et al*. 2012b).

Soil moisture in the upper rhizosphere is a fundamental control on CH_4 production and emissions to the atmosphere. Methanogenesis (R_{CH4}) within the saturated soil pore volume (φ_s; m^{-3}; the aerated pore volume is denoted as φ_a) is determined according to an optimal CH_4 production rate (R_o; μM CH_4 d^{-1}) and labile photosynthates:

$$R_{CH4} = (R_o \times \varphi_s) \times C_{met} \times Q_{10p}^{(Ts - Tp)/10} \quad (12)$$

For this study, CH_4 production was driven using the soil C_{met} pool to reflect contributions by lower weight carbon substrates (Reiche *et al*. 2010, Corbett *et al*. 2012) in labile organic carbon-rich environments. Carbon from the C_{str} pathway may also be allocated for CH_4 production in ecosystems with lower labile organic carbon inputs and higher contributions by hydrogenotrophic methanogenesis (Alstad & Whiticar 2011). The Q_{10p} temperature modifier is used as an approximation to the Arrhenius equation and describes the temperature dependence of biological processes (Gedney & Cox 2003, van Huissteden *et al*. 2006). The reference temperature (T_p) typically reflects mean annual or non-frozen season climatology. Both Q_{10p} and T_p can be adjusted, in addition to R_o, to accommodate varying temperature sensitivities in response to ecosystem differences in substrate quality and other environmental conditions (van Hulzen *et al*. 1999, Inglett *et al*. 2012). Methane additions from R_{CH4} are first allocated to a temporary soil storage pool (C_{CH4}) prior to determining the CH_4 emissions for each 24-h time step; C_{met} is also updated to account for carbon losses due to CH_4 production.

The magnitude of daily CH_4 emissions (F_{CH4}) from the soil profile is determined through plant transport (F_{plant}), soil diffusion (F_{diff}) and ebullition (F_{ebull}) pathways:

$$F_{CH4} = F_{plant} + F_{diff} + F_{ebull} \quad (13)$$

Vegetation plays an important role in terrestrial CH_4 emissions by allowing for gas transport through the plant structure, avoiding slower diffusion through the soil column and often reducing the degree of CH_4 oxidation (Joabsson *et al*. 1999). Daily F_{plant} is determined using a rate

constant (C_p) modified by vegetation growth and production (f_{grow}), an aerodynamic term (λ) and a rate scalar (P_{trans}) that account for differences in CH_4 transport ability according to plant functional type:

$$F_{plant} = (C_{CH4} \times C_p \times f_{grow} \times \lambda \times P_{trans})\,(1 - P_{ox}) \quad (14)$$

A fraction of F_{plant} is oxidized (P_{ox}) prior to reaching the atmosphere and can be modified according to plant functional characteristics (Frenzel & Rudolph 1998; Ström *et al*. 2005, Kip *et al*. 2010). Plant transport is further reduced under frozen surface conditions to account for pathway obstruction by ice and snow or bending of the plant stem following senescence (Hargreaves *et al*. 2001, Sun *et al*. 2012). The magnitude of f_{grow} is determined as the ratio of daily GPP to its annual maximum and is used to account for seasonal differences in root and above-ground biomass (Chanton 2005).

Aerodynamic conductance (g_a) represents the influence of near-surface turbulence on energy/moisture fluxes between vegetation and the atmosphere (Roberts 2000, Yan *et al.* 2012) and gas transport within the plant body (Sachs *et al*. 2008, Wegner *et al*. 2010, Sturtevant *et al*. 2012):

$$g_a = \frac{k^2 \mu_m}{\ln[(z_m - d)/z_{om}]\ln[(z_m - d)/z_{ov}]} \quad (15)$$

Values for z_m and d are the respective anemometer and zero plane displacement heights (m); z_{om} and z_{ov} are the corresponding roughness lengths (m) for momentum, heat and vapor transfer. The von Karman constant (k; 0.40) is a dimensionless constant in the logarithmic wind velocity profile (Högström 1988), μ_m is average daily wind velocity (m s^{-1}), d is calculated as 2/3 of the vegetation canopy height, z_{om} is roughly 1/8th of canopy height (Yang & Friedl 2002), and z_{ov} is $0.1 z_{om}$ (Yan *et al.* 2012). The estimated g_a is then scaled between 0 and 1 to obtain λ using a linear function for sites with a lower observed sensitivity to surface turbulence; for environments with a higher sensitivity to surface turbulence, a quadratic approach is used when μ_m exceeds 4 m s^{-1}:

$$\lambda = 0.0246 + 0.5091 g_a, \quad \mu_m \leq 4 \text{ m s}^{-1}$$

$$\lambda = 0.0885 - (3.28 g_a) + (44.51 g_a^{\,2}), \quad \mu_m > 4 \text{ m s}^{-1} \quad (16)$$

Although this approach focuses on the influence of wind turbulence on plant gas transport within vegetated wetlands, it is also applicable for inundated microsites where increases in surface water mixing can stimulate CH_4 degassing (Sachs *et al*. 2010). In addition, Eq. 15 reflects near-neutral atmospheric stability and adjustments may be necessary to accommodate unstable or stable atmospheric conditions (Raupach 1998).

The upward diffusion of CH_4 within the soil profile is determined using a one-layer approach similar to Tian *et al*. (2010). The rate of CH_4 transport (D_e; m^{-2} d^{-1}) is considered for both saturated (D_{water}; 1.73×10^{-4} μM CH_4 d^{-1}) and aerated (D_{air}; 1.73 μM CH_4 d^{-1}) soil fractions:

$$D_e = (D_{water} \times \varphi_s)(D_{air} \times \varphi_a) \tag{17}$$

Potential daily transport through diffusion (P_{diff}) is estimated as the product of D_e and the gradient between C_{CH4} and the concentration of CH_4 in the atmosphere (Air_{CH4}). This is further modified by soil tortuosity (τ; 0.66), which increases exponentially for $T_s < 274$ K to account for slower gas movement at colder temperatures and barriers to diffusion resulting from near-surface ice formation (Walter & Heimann 2000, Zhuang *et al*. 2004) and pathway constraints within the saturated pore fraction ($1 - \theta$):

$$\begin{aligned} P_{diff} &= \tau \times D_e \left(C_{CH4} - Air_{CH4}\right)(1-\theta) \\ T_s \geq 274, &\quad \tau = 0.66 \\ T_s < 274, &\quad \tau = 0.05 + 10^{-238} \times T_s^{97.2} \end{aligned} \tag{18}$$

A portion of diffused CH_4 is oxidized (R_{ox}) before reaching the soil surface, using a Michaelis-Menten kinetics approach that is scaled by φ_a:

$$R_{ox} = \frac{(V_{max} \times \varphi_a) P_{diff}}{(K_m + \varphi_a) P_{diff}} \times Q_{10d}^{(Ts - Td)/10} \tag{19}$$

where V_{max} is the maximum reaction rate and K_m is the substrate concentration at $0.5V_{max}$ (van Huissteden *et al*. 2006). Oxidation during soil diffusion is modified by soil temperature Q_{10} constraints (Q_{10d}); T_d is the reference temperature and can be defined using site-specific mean annual T_s (Le Mer & Roger 2001). Total daily CH_4 emission (F_{diff}) from the soil diffusion pathway is determined by substracting R_{ox} from P_{diff}.

The CH_4 algorithm uses a gradient-based approach to account for slow or "steady-rate" ebullition from inundated micro-sites in the landscape (Rosenberry *et al*. 2006, Wania *et al*. 2010), whereas episodic events originating deeper within the soil require more complex modeling techniques and input data requirements (Kettridge *et al*. 2011) that are beyond the scope of this study. Emission contributions due to ebullition occur when C_{CH4} exceeds a threshold value (v_e) of 500 μM (van Huissteden *et al*. 2006). The magnitude of gas release is determined by steady-rate bubbling (C_e) applied within the saturated soil pore space (φ_s):

$$F_{ebull} = (C_e \times \varphi_s)(C_{CH4} - \upsilon_e), \qquad C_{CH4} > v_e \tag{20}$$

4.3.2 Study sites and in situ data records

Tower EC records from six pan-Arctic peatland and tundra sites in Finland, Sweden, Russia, Greenland and Alaska were used to assess the integrated TCF model CO_2 and CH_4 simulations (Figure 1; Table 1). The Scandinavian tower sites include Siikaneva (SK) in southern Finland and Stordalen Mire (SM) in northern Sweden near the Abisko Scientific Research Station. The Lena River Delta (LR) site is located on Samoylov Island in northern Siberia and EC measurements from the Kytalyk (KY) flux tower were collected near Chokurdakh in northeastern Siberia. The Zackenberg (ZK) flux tower is located within Northeast Greenland National Park, and tower data records for Alaska were obtained from a water table manipulation experiment (Zona *et al*. 2009; 2012, Sturtevant *et al*. 2012) approximately 6 km east of Barrow (BA). With exception of Siikaneva, the EC tower footprints represent wet permafrost ecosystems with complex, heterogeneous terrain that includes moist depressions, drier, elevated hummocks and inundated microsites. Vegetation within the tower footprints (Rinne *et al*. 2007; Riutta *et al*. 2007, Sachs *et al*. 2008, Jackowicz-Korczyński *et al.* 2010, Parmentier *et al.* 2011a, Zona *et al*. 2011, Tagesson *et al*. 2012b) consists of *Carex* and other sedges, dwarf shrubs (e.g. *Dryas* and *Salix*), grasses (e.g. *Arctagrostis*) and *Sphagnum* moss (with exception of Zackenberg).

Mean daily T_s and θ site measurements corresponding to near-surface ($\leq$ 10 cm) soil depths were selected when possible (Table 1), to better coincide with the soil penetration depths anticipated for upcoming satellite-based microwave remote sensing missions (Kimball *et al*.

2012). For Siikaneva, reanalysis θ was used in place of in-situ measurements as only water table depth information was available to describe soil wetness (Rinne *et al*. 2007). At the Lena River site T_s and θ ($\leq$ 12 cm) observations were obtained from the nearby Samoylov meteorological station and represent tundra polygon wet center, dry rim and slope conditions (Boike *et al*. 2008; Sachs *et al*. 2008). Although θ was also measured during summer 2006, the in-situ records are limited to the wet polygon center location (Boike, personal communication, 2012) and were not used in this study due to the potential for overestimating saturated site conditions. For Zackenberg, site T_s measurements were obtained at a 2 cm depth (Tagesson *et al*. 2012a, b) within the tower footprint, while near-surface θ (< 20 cm) and $\geq$ 5 cm T_s measurements were collected adjacent to the site (Sigsgaard *et al*. 2011). At Stordalen, site θ measurements were not available at the time of this study (Jackowicz-Korczyński *et al*. 2010). Barrow (Zona *et al*. 2009, Sturtevant *et al*. 2012) includes southern (S), central (C) and northern (N) tower locations; in 2007 only CO_2 and CH_4 EC measurements from the northern tower were used in the analysis, due to minimal EC data availability for the other tower sites following data processing (Zona *et al*. 2009). Many of the Barrow CO_2 measurements were also rejected for the 2009 period; as a result NEE was not partitioned into R_{eco} and GPP (Sturtevant *et al*. 2012).

4.3.3 Remote sensing and reanalysis inputs

Daily input meteorology was obtained from the Goddard Earth Observing System Data Assimilation Version 5 (GEOS-5) MERRA archive (Rienecker *et al.* 2011) with 1/2 x 2/3° spatial resolution. The MERRA records were recently verified for terrestrial CO_2 applications in high latitude systems (Yi *et al*. 2011; 2013, Yuan *et al*. 2011), and provide model enhanced T_s and surface θ information similar to the products planned for the NASA Soil Moisture Active Passive (SMAP) mission (Kimball *et al*. 2012). In addition to near surface ($\leq$ 10 cm) T_s and θ information from the MERRA-Land reanalysis (Reichle *et al*. 2011) required for the R_{eco} and CH_4 simulations, daily MERRA SW_{rad}, T_{min} and VPD records were used to drive the internal GPP calculations. The MERRA near-surface (2 m) wind parameters were also used to obtain mean daily μ_m for the CH_4 simulations. The MERRA-Land records for Greenland are spatially limited due to land cover/ice masking inherent in the reanalysis product, and MERRA T_s and θ were not available for the Zackenberg tower site. As a proxy, T_s was derived from reanalysis

surface skin temperatures by applying a simple Crank-Nicholson heat diffusion scheme which accounts for energy attenuation with increasing soil depth (Wania *et al*. 2010); for θ, records from a nearby grid cell were used to represent moisture conditions at Zackenberg.

For the daily LUE-based GPP simulations, quality screened cloud-filtered 16-day 250 m NDVI values from MODIS Terra (MOD13A1) and Aqua (MYD13Q1) data records (Solano *et al.* 2010) were used as model inputs. Differences between the MOD13A1 and MYD13Q1 retrievals were minimal at the tower locations, and the combination of Terra and Aqua MODIS records reduced the retrieval gaps to approximate 8 day intervals. The NDVI retrievals correspond to the center coordinate locations for each flux tower site, and temporal linear interpolation was used to scale the 8-day NDVI records to daily inputs. Coarser (500-1000 m resolution) NDVI records were not used in this study due to the close proximity of water bodies at the tower sites, which can substantially reduce associated FPAR retrievals. In addition, 250 m MODIS vegetation indices have been reported to better capture the overall seasonal variability in tower EC flux records (Schubert *et al*. 2012).

4.3.4 TCF model parameterization

A summary of the site specific TCF model parameters is provided in the Supplement (Table S4.2). Parameter values associated with grassland biomes were selected for the LUE model VPD and T_{min} modifiers used to estimate GPP (Yi *et al*. 2013), as more specific values for tundra and moss-dominated wetlands were not available. Parameter values for θ_{max} were obtained using growing-season maximum θ measurements for each site and θ_{min} was set to 0.15 for scaling purposes. Model ε_{max} was specified as 0.82 mg C $MJ^{-1}$for the duration of the growing season, although actual LUE can vary throughout the summer due to differences in vegetation growth phenology and nutrient availability (Connolly *et al*. 2009, King *et al*. 2011). The tundra CUE ranged from 0.45 to 0.55 (Choudhury 2000); a lower CUE value of 0.35 was used for the moss-dominated Siikaneva site due to a more moderate degree of carbon assimilation occurring in bryophytes that has been observed in other sub-Arctic communities (Street *et al*. 2012). For the TCF model F_{met} parameter, the percentage of NPP allocated to C_{met} varied between 70 % and 72 % for tower tundra sites (Kimball *et al*. 2009) compared to 50 % and 65 % for Siikaneva and Stordalen where moss cover is more abundant. The TCF model R_o parameter ranged from 4.5

and 22.4 μM CH_4 d^{-1} (Walter & Heimann 2000, van Huissteden *et al*. 2006). Values for Q_{10p} varied between 3.5 and 4 due to an enhanced microbial response to temperature variability under colder climate conditions (Gedney & Cox 2003, Inglett *et al*. 2012). A Q_{10d} of 2 was assigned for CH_4 oxidation (Zhuang *et al*. 2004, van Huissteden *et al*. 2006). Parameter values for P_{trans}, which indicates relative plant transport ability, ranged from 7 to 9 (dimensionless); lower values were assigned to tower locations with a higher proportion of shrub and moss cover, whereas higher P_{trans} corresponds to sites where sedges are more prevalent (Ström *et al*. 2005, Rinne *et al*. 2007). For λ, the scaled conductance for lower site wind sensitivity was used in the CH_4 model simulations, except for Lena River which showed higher sensitivity to surface turbulence. Values for P_{ox} ranged from 0.7 in tundra to 0.8 in *Sphagnum*-dominated systems to account for higher CH_4 oxidation by peat mosses (Parmentier *et al*. 2011c). Due to a lack of detailed soil profile descriptions and heterogeneous tower footprints, soil porosity was assigned at 75 % for sites with more abundant fibrous surface layer peat (i.e. Siikaneva and Stordalen) and 70 % elsewhere to reflect more humified or mixed organic and mineral surface soils (Elberling *et al*. 2008, Verry *et al*. 2011).

4.3.5 TCF model simulations

The TCF model was first evaluated against tower EC records using simulations driven with in-situ environmental data including EC based GPP, T_s, θ and μ_m. This step allowed for baseline TCF model R_{eco} and CH_4 flux estimates to be assessed without introducing additional uncertainties from input reanalysis meteorology and LUE model derived GPP calculations. Four additional TCF model simulations were conducted using reanalysis θ, T_s, μ_m (in the CH_4 module), or internal model GPP in place of the in-situ data. A final TCF model run included only satellite and reanalysis based data, and was used to establish annual GPP, R_{eco} and CH_4 carbon budgets for each site. Baseline carbon pools were initialized by continuously cycling ("spinning-up") the model for the tower years of record (described in Table 1) to reach a dynamic steady-state between estimated NPP and surface soil organic carbon stocks (Kimball *et al.* 2009). In-situ data records were used during the model spin-up to establish baseline organic carbon conditions for the first five TCF model simulations, although it was often necessary to

supplement these data with reanalysis information to obtain a continuous annual time series. The final model simulation did not include in-situ data in the spin-up process.

The temporal agreement between the tower EC records and TCF model simulations was assessed using Pearson correlation coefficients (r; $\pm$ one standard deviation) for the daily, 8 day, and total-period (EC length of record) cumulative carbon fluxes and corresponding tests of significance at a 0.05 probability level. The 8 day and total-period cumulative fluxes were evaluated, in addition to the daily fluxes, to account for differences between the model estimates and tower EC records stemming from temporal lags between changing environmental conditions and resulting carbon (CO_2, CH_4) emissions (Lund *et al*. 2010, Levy *et al*. 2012). The mean residual error (MRE) between the tower EC records and TCF modeled CO_2 and CH_4 fluxes was used to identify potential positive (underestimation) and negative (overestimation) biases in the simulations; root-mean-square-error (RMSE) differences were used as a measure of model estimate uncertainty in relation to the tower EC records.

4.4 Results

4.4.1 Surface organic carbon pools

The TCF model generated surface soil organic carbon pools represent steady-state conditions obtained through the continuous cycling of in-situ or satellite and reanalysis environmental data for the years of record associated with each tower site (described in Table 1). Approximately 600 and 1000 years of model spin-up were required for C_{rec} to reach dynamic steady state conditions. Over 95 % of the resulting total carbon pool was allocated to C_{rec} by the TCF model, with 2-3 % stored as C_{met} and the remainder partitioned to C_{str}. The estimated carbon pools from the in-situ (reanalysis-based) model spin-up ranged from approximately 3.3 kg C m^{-2} (2.3 kg C m^{-2}) for Zackenberg and Stordalen to 1.3 kg C m^{-2} (2.1 kg C m^{-2}) for the other tower sites.

Differences in carbon stocks, resulting from the use of satellite remote sensing and reanalysis information in the TCF model, reflect warm or cold biases in the input T_s records relative to the in-situ data that modified the rate of CO_2 loss during model initialization. The

larger carbon stocks at Zackenberg, compared to the other tundra sites, resulted from higher tower EC based GPP inputs that often exceeded 5 g C m^{-2} d^{-1} in mid-summer, and a short (< 50 day) peak growing season (Tagesson *et al*. 2012a) that minimized TCF modeled R_h losses. Although it was necessary to use internal LUE based GPP calculations for Stordalen in the absence of available CO_2 records, the resulting C_{met} and C_{rec} carbon stocks were similar in magnitude to surface litter measurements at this site (Olsrud & Christensen 2011). The TCF model simulated carbon stock for Lena River was less than a 2.9 kg C m^{-2} average determined from in-situ (≤ 10 cm depth) measurements of nearby river terrace soils (Zubrzycki *et al*. 2013), but this could have resulted from site spatial heterogeneity and the use of recent climate records in the model spin-up that may not reflect past conditions.

4.4.2 LUE based GPP

The GPP simulations using reanalysis and satellite based inputs captured the overall seasonality observed in the tower records (Figure 2; Table 2) and explained 76% (r^2; $p < 0.05$, $N = 7$) of variability in the total EC period-of-record fluxes (Figure 3). The across-site RMSE and MRE were 1.3 ± 0.51 and -0.1 ± 0.7 g C m^{-2} d^{-1}, respectfully. Although the 8 day cumulative flux correspondence between the tower EC and TCF model GPP estimates was strong (r^2 = 75 ± 16 %), the model-tower agreement decreased considerably for daily GPP (r^2 = 57 ± 22%). These differences may reflect a delayed response in vegetation productivity following changes in atmospheric and soil conditions (Lund *et al*. 2010), and short term fluctuations in the reanalysis SW_{rad} inputs. For Kytalyk, the large RMSE (2.2 g C m^{-2} d^{-1}) observed for the TCF model GPP simulations resulted from warm spring air temperatures that reduced T_{min} constraints on carbon assimilation, although a similar increase in GPP did not occur in the EC based records. This lack of response likely resulted from a shallow (< 14 cm) early season thaw depth at this site, that limited bud break activity in deeper rooted shrubs (e.g. *Betula nana* and *Salix pulchra*). To address this, an additional simulation was conducted using a temperature driven phenology model described in Parmentier *et al*. (2011a) to better inform the start of growing season in the TCF model. This step reduced the corresponding RMSE difference for Kytalyk by 56% (to 1 g C m^{-2} d^{-1}) with an associated r^2 of 67%.

Although previous LUE models (e.g. Running *et al*. 2004, Yi *et al*. 2013) have relied solely on VPD to represent water related constraints to GPP, our approach also considers soil moisture to better account for the sensitivity of bryophytes and shallow rooted vegetation to surface drying (Wu *et al.* 2013). Including this additional moisture constraint reduced the overall TCF model and tower GPP RMSE and MRE differences by approximately 14% and 92%. However, the model simulations continued to overestimate GPP fluxes for Siikaneva, Lena River (2003), and Kytalyk (MRE = -0.6 $\pm$ 0.8 g C m^{-2} d^{-1}). This residual GPP bias could be influenced by inconsistencies between the coarse scale MERRA reanalysis inputs and local tower meteorology, as reported elsewhere (e.g. Yi *et al*. 2013), although systematic biases for the high latitude regions have not been identified. For instance, periods of warmer (3 to 4 °C) reanalysis T_{min} inputs relative to in-situ measurements at Lena River in 2003 led to seasonally higher TCF modeled GPP fluxes. In contrast, the reanalysis T_{min} at Barrow was 2 to 7 °C cooler in mid-summer than the local meteorology; this resulted in significantly lower ($p < 0.05$) TCF model GPP estimates relative to the tower EC records (Table 2). It is also possible that differences in the light response curve and respiration models, used when partitioning the site EC NEE fluxes into GPP and R_{eco} (i.e. Aurela *et al*. 2007, Kutzbach *et al*. 2007; Parmentier *et al*. 2011a, Tagesson *et al*. 2012, Zona *et al*. 2012), may have contributed to differences between the TCF model simulations and tower CO_2 records. However, further investigation is needed to determine the expected range of GPP and R_{eco} that might result from variability in the flux partitioning routines.

4.4.3 R_{eco} and NEE

The in-situ TCF model R_{eco} simulations accounted for 59 $\pm$ 28% and 76 $\pm$ 24% (r^2) of the observed variability in the respective daily and 8 day cumulative tower EC fluxes (Figure 4; Table 2). As with GPP, the r^2 agreement increased to 89% ($p < 0.05$, $N = 6$) when considering the total-period cumulative fluxes (Figure 3). The overall RMSE difference for the in-situ based TCF model R_{eco} and NEE simulations was 0.74 $\pm$ 0.45 g C m^{-2} d^{-1} when using 5 cm depth T_s inputs. A corresponding across-site MRE of -2.1 $\pm$ 5.7 g C m^{-2} d^{-1} indicated that the TCF model simulations overestimated R_{eco} relative to the tower records, and slightly underestimated NEE (MRE = 0.1 $\pm$ 0.4 g C m^{-2} d^{-1}). We also conducted TCF model simulations using 8-10 cm depth

in-situ T_s inputs, instead of those from $\leq$ 5 cm (as reported in Table 2), to investigate the influence of deeper soil thermal controls on site R_{eco} response; this step reduced the overall RMSE by approximately 12%.

Incorporating the TCF internal LUE model GPP estimates increased the overall RMSE for R_{eco} and NEE by 23% relative to the in-situ based simulations, compared to a respective 3% and 14% increase when using reanalysis θ or T_s inputs (Figure 5). The model-tower daily and 8 day cumulative correspondence was also lower (r^2 = 32 and 56%, respectively) for CO_2 simulations driven using internally derived GPP, relative to those using reanalysis θ or T_s inputs (r^2 = 57 and 72%) in place of the in-situ records. Without the in-situ inputs, the respective RMSE and MRE difference between the reanalysis based R_{eco} (NEE) simulations and the tower EC records averaged 0.9 $\pm$ 0.4 and -0.2 $\pm$ 0.9 g C m^{-2} d^{-1} (1 $\pm$ 0.5 and 0.3 $\pm$ 0.05 g C m^{-2} d^{-1}).

The reanalysis and remote sensing based TCF model R_{eco} (NEE) simulations accounted for 51 $\pm$ 29 (45 $\pm$ 34) % and 71 $\pm$ 17 (62 $\pm$ 34) % of the observed r^2 variability in the respective daily and 8 day tower EC records. The mean r^2 values exclude TCF model results for Barrow and Kytalyk, which did not show significant ($r \leq 0.20$; $p \geq 0.16$) agreement with the site EC records (Table 2). For Barrow, it is likely that the water table manipulations at this site led to local temperature and moisture variability that was not reflected in the coarse reanalysis and remote sensing inputs. The minimal agreement at Kytalyk is attributed to higher R_h losses driven by warmer reanalysis T_s inputs, and increased R_a contributions due to the overestimation of GPP relative to the tower EC records.

4.4.4 CH_4 fluxes

The in-situ TCF model CH_4 simulations explained 64 $\pm$ 11 % and 80 $\pm$ 12 % (r^2) of the respective daily and 8 day cumulative variability observed in the tower EC records (Figure 6; Table 3), when excluding Kytalyk ($p = 0.1$). The r^2 correspondence increased to 98 % when considering the total period-of-record emissions across the six sites (Fig. 3; $p < 0.05$, $N = 9$). At Kytalyk, Parmentier *et al*. (2011b) reported large differences in measured half-hourly CH_4 fluxes following shifts in wind direction, and larger emissions from portions of the tower footprint containing *Carex* sp., *E. angustifolium* and inundated microsites. Although this may have

contributed to the observed discrepancy between the TCF model estimates and tower EC record, attempts to systematically screen the CH_4 observations based on wind direction, or to use daily EC medians instead of mean values, did not substantially improve the model results.

On average, the in-situ TCF model simulations overestimated CH_4 fluxes relative to the tower EC records (MRE = -2.2 mg C m^{-2} d^{-1}), with RMSE differences varying from 6.7 to 42.5 mg C m^{-2} d^{-1}. Without including μ_m in the TCF model, the resulting RMSE increased by > 10 % and the mean daily correspondence decreased to r^2 < 40%. The most substantial difference was observed for Lena River, where excluding μ_m reduced the daily and 8 day emission correspondence by over 60 %. Unlike the TCF model R_{eco} results, deeper (10 cm depth) T_s measurement inputs did not improve the RMSE values, except for Barrow (2007N) where the RMSE decreased by 35%. This sensitivity to deeper T_s conditions may reflect changes in active layer depth following water table manipulations at this site (Zona *et al*. 2009, 2012), and associated changes in carbon substrate availability. In contrast, the RMSE for Lena River was 15 % higher when using in-situ 10 cm T_s records in the TCF model simulations instead of 5 cm depth measurements. A 6 % decrease in the RMSE occurred for Zackenberg (2008) when using the warmer (3 to 5 °C) 2 cm depth T_s records, relative to model simulations using 5 cm T_s inputs. Contrary to expectations, the 2 cm depth T_s inputs did not improve RMSE differences for Zackenberg in 2009 when site moisture conditions were drier (Tagesson *et al*. 2012a).

The reanalysis driven TCF model CH_4 simulations (Figure 6; Table 3) accounted for 48 $\pm$ 16 % and 79 $\pm$ 8% (r^2) of the respective daily and 8 day variability in the tower EC records when excluding the less favorable results for Kytalyk (r^2 = 8 and 44%, respectively). Although slightly lower than the in-situ TCF model CH_4 estimates, the coarser reanalysis and remote sensing driven simulations explained 96% (r^2) of the total period-of-record emissions at these sites (Figure 3). The corresponding model RMSE was 18.2 $\pm$ 13.6 mg C m^{-2} d^{-1}, with an associated MRE difference of 1.8 $\pm$ 7.3 mg C m^{-2} d^{-1} that indicated the slight model underestimation of daily CH_4 emissions. The model RMSE differences increased by approximately 15% when using reanalysis μ_m records or internal GPP estimates in place of the in-situ inputs, and by 10% when incorporating reanalysis T_s and θ inputs (Figure 7).

4.4.5 Estimates of annual carbon budgets

The reanalysis and remote sensing driven TCF model simulations indicated a net CO_2 sink (NEE = -34.5 $\pm$ 18.5 g C m^{-2} yr^{-1}) for the tower sites, excluding Barrow in 2009 (NEE = 7.3 g C m^{-2} yr^{-1}) where the estimated R_{eco} emissions exceeded annual GPP (Figure 8). Other studies near Barrow have also reported NEE losses from wet tundra communities, resulting from drier micro-scale surface conditions and warming within the hummocky landscape (Huemmrich *et al*. 2010b, Sturtevant & Oechel 2013) which can strongly influence R_{eco}. The corresponding TCF model R_{eco} estimates ranged from 133 (Zackenberg in 2009) to 494 g C m^{-2} yr^{-1} (Stordalen in 2006) with lower CO_2 emissions occurring in the colder, more northern tundra sites. The strongest NEE carbon sink indicated by the model simulations was observed for the peat-rich Siikaneva site (-70.3 g C m^{-2} yr^{-1}) due to high annual GPP (462.5 g C m^{-2} yr^{-1}) relative to the other tower locations. Although tower EC CO_2 records were not available for Stordalen to verify the TCF model NEE results (-50.8 and -65.8 g C m^{-2} yr^{-1} respectively), the estimates are slightly smaller (~ 30 g C m^{-2} d^{-1}) than other NEE approximations over the same time period (Christensen *et al*. 2012) but are similar to observations reported for other years at this site (Olefeldt *et al*. 2012; Marushchak *et al*. 2013).

The annual TCF model CH_4 estimates determined using the reanalysis inputs averaged 6.9 ($\pm$ 5.5) g C m^{-2} yr^{-1} for the six tower sites. The highest CH_4 emissions were observed for Stordalen and Siikaneva ($\geq$ 11.8 g C m^{-2} yr^{-1}) due to higher model-defined CH_4 production rates and summer reanalysis T_s records that were often 5 °C warmer than the other sites. In contrast, model CH_4 emissions were lowest for Barrow (1.8 g C m^{-2} yr^{-1}) due to smaller GPP estimates and colder summer reanalysis T_s records that did not reflect the unusually warm site conditions in 2007 (Shiklomanov *et al*. 2010). The annual TCF model CH_4 emissions for Lena River were relatively small (2.3 g C m^{-2} yr^{-1}, on average), but are similar in magnitude to site CH_4 estimates determined using more complex coupled biogeochemical and permafrost models (i.e. Zhang *et al.* 2012b). Although the TCF modeled CH_4 fluxes contributed only 1-5% of annual carbon emissions (R_{eco} + CH_4) at the tower sites, which is similar to previous reports (Schneider von Deimling *et al.* 2012), these CH_4 emissions reduced the NECB (-23.3 $\pm$ 19.6 g C m^{-2} yr^{-1}) by approximately 23 % relative to NEE. The annual model estimates indicated that the site CO_2 and

CH_4 fluxes, excluding Barrow and Lena River, contributed to a net global warming potential (GWP) of 188 $\pm$ 68 g CO_2eq m^{-2} yr^{-1} over a 100 year time horizon (Boucher *et al*. 2009) with total GWP influences by CH_4 at approximately 9% to 44% that of R_{eco}. Similarly the Lena River and Barrow sites mitigated GWP at a mean rate of -40 g CO_2eq m^{-2} yr^{-1} in 2006 and 2007, but were net GWP contributors in 2003 and 2009 (25 and 160 g CO_2eq m^{-2} yr^{-1}, respectfully). Although site CO_2 contributions from methantrophy during plant transport and soil diffusion were estimated to range from 3.8 to 58.3 g C m^{-2} yr^{-1}, these contributions represented < 14% of total TCF model derived R_{eco}.

4.5 Discussion and conclusions

The level of complexity in biophysical process models has increased considerably in recent years but there remain large differences in carbon flux estimates for northern high latitude ecosystems (McGuire *et al*. 2012, Wania *et al*. 2013). An integrated TCF model CO_2 and CH_4 framework was developed to improve carbon model compatibility with remote sensing retrievals that can be used to inform changes in surface conditions across northern peatland and tundra regions. Although the TCF model lacks the biophysical and hydrologic complexity found in more sophisticated process models (e.g. Zhuang *et al*. 2004, Wania *et al*. 2010), it avoids the need for extensive parameterization by instead employing generalized surface vegetation growth, temperature, and moisture constraints on ecosystem CO_2 and CH_4 fluxes.

Despite the relatively simple model approach and landscape heterogeneity at the tower sites, the TCF model simulations derived from local tower inputs captured the overall seasonality and magnitude of R_{eco} and CH_4 fluxes observed in the tower EC records. Overall the R_{eco}, NEE and CH_4 emission simulations determined using local site inputs showed strong mean correspondence (8 day $r > 0.80$; $p < 0.05$) with tower EC records, but the strength of agreement varied considerably for the daily fluxes due to temporal lags between changing environmental conditions and carbon emissions (Zhang *et al*. 2012b), and larger EC measurement uncertainty at the daily time step (Baldocchi *et al*. 2008, Yi *et al*. 2013). The respective RMSE differences from the in-situ TCF model CO_2 and CH_4 simulations averaged 0.7 $\pm$ 0.4 g C m^{-2} d^{-1} and 17.9 $\pm$

11.5 mg C m^{-2} d^{-1} which is comparable to other site based model results (e.g. Marushchak *et al*. 2013, Sturtevant & Oechel 2013).

In this study, we used near-surface T_s records in the model simulations to better coincide with the soil depths represented by upcoming satellite remote sensing missions, but acknowledge that deeper T_s controls are also important for regulating high latitude carbon emissions. This was evident in TCF model R_{eco} results where RMSE differences between the in-situ based simulations and tower EC fluxes generally improved when using deeper 10 cm T_s inputs instead of those from shallower ($\leq$ 5 cm) soil depths. However, the TCF model CH_4 simulations were more favorable when using near-surface (2 to 5 cm) T_s inputs. The observed CH_4 emission sensitivity to surface soil warming may be influenced by cold temperature constraints on CH_4 production in the carbon-rich root zone where organic acids are more abundant (Turetsky *et al*. 2008, Olefeldt *et al*. 2013). Light-weight carbon fractions have been shown to be more susceptible to mineralization following soil thaw and temperature changes than heavier, more recalcitrant soil organic carbon pools in high latitude environments (Glanville *et al*. 2012). However, the depletion of older organic carbon stocks may also become more prevalent in permafrost soils subject to thawing and physiochemical destabilization (Schuur *et al*. 2009, Hicks Pries *et al*. 2013a) in the absence of wet, anoxic conditions (Hugelius *et al*. 2012, Hicks Pries *et al*. 2013b). Seasonal changes in T_s constraints were also evident in this study, especially in the Zackenberg records where the TCF model underestimated tower R_{eco} and CH_4 emissions in autumn by not accounting for warmer temperatures deeper in the active layer that can sustain microbial activity following surface freezing (Aurela *et al*. 2002).

Allowing the TCF model vegetation CUE parameter to change over the growing season instead of allocating R_a as a static fraction of GPP may also improve model and tower R_{eco} agreement. In Arctic tundra, R_a can contribute anywhere from 40% to 70% of $R_{eco,}$ with higher maintenance and growth respiration occurring later in the growing season when root systems expand deeper into the soil active layer (Hicks Pries *et al*. 2013a). Representing R_a as a fixed proportion of daily GPP in the TCF model, and not accounting for the use of stored plant carbon reserves, may also have contributed to the lower R_{eco} estimates during spring and autumn transitional periods when photosynthesis is reduced.

Our estimates of peatland and tundra CO_2 fluxes using TCF model simulations driven by MERRA reanalysis and satellite (MODIS) remote sensing inputs showed favorable agreement relative to the tower EC observations, with relatively moderate RMSE uncertainties of 1.3 $\pm$ 0.5 (GPP), 0.9 $\pm$ 0.4 (R_{eco}) and 1 $\pm$ 0.5 (NEE) g C m^{-2} d^{-1}. These model accuracies are similar to those reported in a previous TCF model analysis for the northern regions (Yi *et al*. 2013), and other Arctic LUE based GPP studies (Tagesson *et al*. 2012a, McCallum *et al*. 2013). The associated model-tower RMSE for CH_4 was 18.2 $\pm$ 13.6 mg C m^{-2} d^{-1}, and is comparable to results from previous remote sensing driven CH_4 analyses (Meng *et al*. 2012, Tagesson *et al*. 2013). The larger observed differences between TCF model and tower EC based GPP results may reflect seasonal changes in nutrient availability (Lund *et al*. 2010), although one peatland study reported that nutrient limitations to plant productivity could be detected indirectly by MODIS NDVI retrievals (Schubert *et al*. 2010b). It is more likely that this reduced correspondence resulted from fluctuations in the reanalysis SW_{rad} inputs (Yi *et al*. 2011) and uncertainty associated with satellite NDVI and resulting FPAR inputs stemming from residual snow cover and surface water effects on optical-IR reflectance (Delbert *et al.* 2005).

High latitude studies have reported difficulty in using satellite NDVI to determine the start of spring bud burst and seasonal variability in leaf development (Huemmrich *et al.* 2010a). Evaluating other portions of the visible spectrum, including blue and green reflectances, in addition to NDVI has helped to alleviate this problem in remote sensing applications (Marushchak *et al*. 2013) and should be considered in subsequent studies. Incorporating phenological constraints into the TCF LUE model may also better characterize early season GPP, especially for plant communities such as *E. vaginatum* that are sensitive to changes in active layer depth (Parmentier *et al*. 2011a, Natali *et al*. 2012). Considering T_s as an additional constraint in the TCF LUE model may also better account for autumn GPP activity under frozen air temperatures if plant-available moisture is still available within the root zone (Christiansen *et al*. 2012). Yi *et al*. (2013) attempted to address this condition by incorporating satellite passive microwave-based freeze/thaw records (37 GHz) to constrain GPP according to frozen, transitional, or non-frozen surface moisture states but did not report a significant improvement, likely due to the coarse (25 km) resolution freeze/thaw retrievals.

The TCF model assessment of annual NECB for the six northern tower EC sites indicate that CH_4 emissions reduced the terrestrial net carbon sink by 23% relative to NEE. Although GPP at the Lena River and Barrow sites mitigated GWP additions from R_{eco} and CH_4 in two of the years examined, in most years the tower sites were GWP contributors by approximately 165 $\pm$ 128 g CO_2eq m^{-2} yr^{-1} when considering the impact of CH_4 on atmospheric forcing over a 100-year time span. These results are consistent with other model based analyses of Arctic carbon fluxes (McGuire *et al*. 2010) and emphasize the importance of evaluating CO_2 and CH_4 emissions simultaneously when quantifying the terrestrial carbon balance and GWP for northern peatland and tundra ecosystems (Christensen *et al*. 2012, Olefeldt *et al*. 2012). However, on-going efforts are needed to better inform landscape scale spatial/temporal variability in soil moisture, temperature and vegetation controls on CO_2 and CH_4 fluxes for future model assessments using a combined network of in-situ soil measurements and strategically placed EC tower sites (Sturtevant & Oechel 2013), and regional airborne surveys. The new SMAP mission (launched early 2015) may also help to determine landscape soil moisture and thermal constraints on northern carbon fluxes through relatively fine scale (9 km resolution) and lower frequency ($\leq$ 1.4 GHz) microwave retrievals with enhanced soil sensitivity (Entekhabi *et al*. 2010, Kimball *et al*. 2012), complimented by recent improvements in Arctic-specific reanalysis data (Bromwich *et al*. 2010, Henderson *et al*. 2015). These advances, in conjunction with a suitable model framework to quantify ecosystem NEE and CH_4 emissions, provide the means for regional carbon assessments and monitoring of the net ecosystem carbon budget and underlying environmental constraints.

4.6 References

Alstad, K P, M J Whiticar (2011) Carbon and hydrogen isotope ratio characterization of methane dynamics for Fluxnet Peatland Ecosystems. *Org. Geochem.*, 42: 548-558.

Aurela, M, T Laurila, J Tuovinen (2002) Annual CO_2 balance of a subarctic fen in northern Europe: importance of wintertime efflux. *J. Geophys. Res.*, 107: ACH 17-1-17-12, doi:10.1029/2002JD002055.

Aurela, M, T Riutta, T Laurila, J P Tuovinen, T Vesala, E S Tuittila, J Rinne, S Haapanala, J Laine (2007) CO_2 exchange of a sedge fen in southern Finland-the impact of a drought period. *Tellus B*, 59: 826-837.

Badawy, B, C Rödenbeck, M Reichstein, N Carvalhais, M Heiman (2013) Technical Note: The simple diagnostic photosynthesis and respiration model (SDPRM). *Biogeosciences*, 10: 6485-6508.

Baldocchi, D (2008) "Breathing" of the terrestrial biosphere: lessons learned from a global network of carbon dioxide flux measurement systems. *Aust. J. Bot.*, 56: 1-26.

Beck, P S A, S J Goetz (2011) Satellite observations of high northern latitude vegetation productivity changes between 1982-2008: ecological variability and regional differences, *Environ. Res. Lett.*, 6: 045501.

Boike, J, C Wille, A Abnizova (2008) Climatology and summer energy and water balance of polygonal tundra in the Lena River Delta, Siberia. *J. Geophys. Res.*, 113: G03025.

Boucher, O, P Friedlingstein, B Collins, K P Shine (2009) The indirect global warming potential and global temperature change potential due to methane oxidation. *Environ. Res. Lett.*, 4: 044007.

Bromwich, D, Y H Kuo, M Serreze, J Walsh, L S Bai, M Barlage, K Hines, A Slater (2010) Arctic system reanalysis: call for community involvement. *EOS T. Am. Geophys. Un.*, 91: 13-14.

Chanton, J P (2005) The effect of gas transport on the isotope signature of methane in wetlands. *Org. Geochem.*, 36: 753-768.

Choudhury, B J (2000) Carbon use efficiency, and net primary productivity of terrestrial vegetation. *Adv. Space Res.*, 26: 1105-1108.

Christensen, T R, M Jackowicz-Korczyński, M Aurela, P Crill, M Heliasz, M Mastepanov, T Friborg (2012) Monitoring the multi-year carbon balance of a subarctic palsa mire with micrometeorological techniques. *AMBIO*, 41: 207-217.

Christiansen, C T, N M Schmidt, A Michelsen (2012) High Arctic dry heath CO_2 exchange during the early cold season. *Ecosystems*, 15: 1083-1092.

Clark, D B, L M Mercado, S Sitch, C D Jones, N Gedney, M J Best, M Pryor, G G Rooney, R L H Essery, E Blyth, O Boucher, R J Harding, C Huntingford, P M Cox (2011) The Joint UK Land Environment Simulator (JULES), model description-part 2: carbon fluxes and vegetation dynamics. *Geosci. Model Dev.*, 4: 701-722.

Connolly, J, N T Roulet, J W Seaquist, N M Holden, P M Lafleur, E R Humphreys, B W Heumann, S M Ward (2009) Using MODIS derived *f*PAR with ground based flux tower measurements to derive the light use efficiency for two Canadian peatlands. *Biogeosciences*, 6: 225-234.

Corbett, J E, M M Tfaily, D J Burdige, W T Cooper, P H Glaser, J P Chanton (2013) Partitioning pathways of CO_2 production in peatlands with stable carbon isotopes. *Biogeochemistry*, 114: 327-340.

Davidson, E A, I A Janssens (2006) Temperature sensitivity of soil carbon decomposition and feedbacks to climate change. *Nature*, 440: 165-173.

Delbart, N, L Kergoat, T Le Toan, J Lhermitte, P Ghislain (2005) Determination of phenological dates in boreal regions using normalized difference water index. *Remote Sens. Environ.*, 97: 26–38.

Dijkstra, F A, S A Prior, G B Runion, H A Torbert, H Tian, C Lu, R T Venterea (2012) Effects of elevated carbon dioxide and increased temperature on methane and nitrous oxide fluxes: evidence from field experiments. *Front. Ecol. Environ.*, 10: 520-527.

Dlugokencky, E J, L Bruhwiler, J W C White, L K Emmons, P C Novelli, S A Montzka, K A Masarie, P M Lang, A M Crotwell, J B Miller, L V Gatti (2009) Observational constraints on recent increases in the atmospheric CH_4 burden. *Geophys. Res. Lett.*, 36: L18803.

Dolman, A J, G R van der Werf, M K van der Molen, G Ganssen, J W Erisman, B Strengers (2010) A carbon cycle science uptake since IPCC AR-4. *AMBIO*, 39: 402-412.

Dorrepaal, E, S Toet, R S P van Logtestijn, E Swart, M J van de Weg, T V Callaghan, R Aerts (2009) Carbon respiration from subsurface peat accelerated by climate warming in the subarctic. *Nature*, 460: 616-619.

Elberling, B, M P Tamstorf, A Michelsen, M F Arndal, C Sigsgaard, L Illeris, C Bay, B U Hansen, T R Christensen, E S Hansen, B H Jakobsen, L Beyens (2008) Soil and plant community-characteristics and dynamics at Zackenberg. *Adv. Ecol. Res.*, 40: 223-248.

Elberling, B, L Askaer, C J Jørgensen, H P Joensen, M Kühl, R N Glud, F R Lauritsen (2011) Linking Soil O_2, CO_2, and CH_4 concentrations in a wetland soil: implications for CO_2 and CH_4 fluxes. *Environ. Sci. Technol.*, 45: 3393-3399.

Elmendorf, S C, G H R Henry, R D Hollister, R G Björk, A D Bjorkman, T V Callaghan, L S Collier, E J Cooper, J H C Cornelissen, T A Day, A M Fosaa, W A Gould, et al. (2012) Global assessment of experimental climate warming on tundra vegetation: heterogeneity over space and time. *Ecol. Lett.*, 15: 164-175.

Entekhabi, D, E G Njoku, P E O'Neill, K H Kellogg, W T Crow, W N Edelstein, J K Entin, S D Goodman, T J Jackson, J Johnson, J S Kimball, et al. (2010) The Soil Moisture Active Passive (SMAP) mission. *Proc. IEEE*, 98: 704-716.

Forbrich, I, L Kutzbach, C Wille, T Becker, J Wu, M Wilmking (2011) Cross-evaluation of measurements of peatland methane emissions on microform and ecosystem scales using high-resolution landcover classification and source weight modeling. *Agri. Forest Meterol.*, 151: 864-874.

Frenzel, P, J Rudolph (1998) Methane emission from a wetland plant: the role of CH_4 oxidation in *Eriophorum*. *Plant Soil*, 202: 27-32.

Gedney, N, P M Cox (2003) The sensitivity of global climate model simulations to the representation of soil moisture heterogeneity. *J. Hydrometeorol.*, 4: 1265-1275.

Glanville, H C, P W Hill, L D Maccarone, P N Golyshin, D V Murphy, D L Jones (2012) Temperature and soil water controls on vegetation emergence, microbial dynamics, and soil carbon and nitrogen fluxes in a high Arctic tundra ecosystem. *Funct. Ecol.*, 26: 1366-1380.

Grosse, W, J Armstrong, W Armstrong (1996) A history of pressurized gas-flow studies in plants. *Aquat. Biol.*, 54: 57-100.

Hargreaves, K J, D Fowler, C E R Pitcairn, M Aurel (2001) Annual methane emission from Finnish mires estimated from eddy covariance campaign measurements. *Theor. Appl. Climatol.*, 70: 203-213.

Henderson, J M, J Eluszkiewicz, M E Mountain, T Nehrkorn, R Y-W Chang, A Karion, J B Miller, C Sweeney, N Steiner, S C Wofsy, C E Miller (2015) Atmospheric transport

simulations in support of the Carbon in Arctic Reservoirs Vulnerability Experiment (CARVE). *Atmos. Chem. Phys.,* 15: 4093-4116.

Hicks Pries, C E, E A G Schuur, K G Crummer (2013a) Thawing permafrost increases old soil and autotrophic respiration in tundra: partitioning ecosystem respiration using $\delta^{13}C$ and $\Delta^{14}C$. *Glob. Change Biol.,* 19: 649-661.

Hicks Pries, C E, E A G Schuur, J G Vogel, S M Natali (2013b) Moisture drives surface decomposition in thawing tundra. J. *Geophys. Res. Biogeo.,* 118: 1-11.

Högström, U (1988) Non-dimensional wind and temperature profiles in the atmospheric surface layer: a re-evaluation. *Boundary-Lay. Meteorol.,* 42: 55-78.

Hudson, J M G, G H R Henry, W K Cornwell (2011) Taller and larger: shifts in Arctic tundra leaf traits after 16 years of experimental warming. *Glob. Change Biol*., 17: 1013-1021.

Huemmrich, K F, J A Gamon, C E Tweedie, S F Oberbauer, G Kinoshita, S Houston, A Kuchy, R D Hollister, H Kwon, M Mano, Y Harazono, P J Webber, W C Oechel (2010a) Remote sensing of tundra gross ecosystem productivity and light use efficiency under varying temperature and moisture conditions. *Rem. Sens. Environ.,* 114: 481-489.

Huemmrich, K F, G Kinoshita, A Gamon, S Houston, H Kwon, W C Oechel (2010b) Tundra carbon balance under varying temperature and moisture regimes. *J. Geophys. Res.,* 115: G00102.

Hugelius, G, J Routh, P Kuhry, P Crill (2012) Mapping the degree of decomposition and thaw remobilization potential of soil organic matter in discontinuous permafrost terrain. *J. Geophys. Res.Biogeo.,* G00102: doi:10.1029/2011JG001873.

Hugelius, G, C Tarnocai, G Broll, J G Canadell, P Kuhry, K D Swanson (2013) The northern circumpolar soil carbon database: spatially distributed datasets of soil coverage and soil carbon storage in the northern permafrost regions. *Earth Syst. Sci. Data*, 5: 3-13.

Inglett, K S, P W Inglett, K R Reddy, T Z Osborne (2012) Temperature sensitivity of greenhouse gas production in wetland soils of different vegetation. *Biogeochemistry*, 108: 77-90.

Ise, T, P R Moorcroft (2006) The global-scale temperature and moisture dependencies of soil organic carbon decomposition: an analysis using a mechanistic decomposition model. *Biogeochemistry*, 80: 217-231.

Ise, T, A L Dunn, S C Wofsy, P R Moorcroft (2008) High sensitivity of peat decomposition to climate change through water-table feedback. *Nature Geosci*., 1: 763-766.

Jackowicz-Korczyński, M, T R Christensen, K Bäckstrand, P Crill, T Friborg, M Mastepanov, L Ström (2010) Annual cycle of methane emission from a subarctic peatland. J. *Geophys. Res. Biogeo.*, 115: G02009.

Joabsson, A, T R Christensen, B Wallén (1999) Vascular plant controls on methane emissions from northern peatforming wetlands. *TREE*, 14: 385-388.

Kane, E S (2012) Ecosystem carbon storage: squeezing the Arctic carbon balloon. *Nature Clim. Change*, 2: 841-842.

Kettridge, N, A Binley, S M Green, A J Baird (2011) Ebullition events monitored from northern peatlands using electrical imaging. *J. Geophys. Res.*, 116: G04004, doi:10.1029/2010JG001561.

Kim, Y, J S Kimball, K Zhang, K C McDonald (2012) Satellite detection of increasing Northern Hemisphere non-frozen seasons from 1979 to 2008: Implications for regional vegetation growth. *Rem. Sens. Environ.*, 121: 472-487.

Kimball, J S, L A Jones, K Zhang, F A Heinsch, K C McDonald, W C Oechel (2009) A satellite approach to estimate land-atmosphere CO_2 exchange for boreal and Arctic biomes using MODIS and AMSR-E. *IEEE T. Geosci. and Remote Sens.*, 47: 569-587.

Kimball, J S, R Reichle, K McDonald, E Njoku (2012) Soil Moisture Active Passive (SMAP) Algorithm Theoretical Basis Document (ATBD): SMAP Level 4 Carbon Data Product (L4_C), Initial Release v. 1, Jet Propulsion Laboratory, California Institute of Technology, (73 pp.).

King, D A, D P Turner, W D (2011) Parameterization of a diagnostic carbon cycle model for continental scale application. *Remote Sens. Environ.*, 115: 1653-1664.

Kip, N, J F van Winden, Y Pan, L Bodrossy, G J Reichart, A J P Smolders, M S M Jetten, J S S Damsté, H J M Op den Camp (2010) Global prevalence of methane oxidation by symbiotic bacteria in peat-moss ecosystems. *Nature Geosci.*, 3: 617-621.

Kutzbach, L, C Wille, E M Pfeiffer (2007) The exchange of carbon dioxide between wet arctic tundra and the atmosphere at the Lena River Delta, Northern Siberia, *Biogeosciences*, 4: 869-890.

Le Mer, J, P Roger (2001) Production, oxidation, emission and consumption of methane by soils: a review. *Eur. J. Soil Biol.*, 37: 25-50.

Levy, P E, A Burden, M D Cooper, K J Dinsmore, J Drewer, C Evans, D Fowler, J Gaiawyn, A Gray, S K Jones, et al. (2012) Methane emissions from soils: synthesis and analysis of a

large UK data set. *Glob. Change Biol.*, 18: 1657-1669.

Lloyd, J, J A Taylor (1994) On the temperature dependence of soil respiration. *Funct. Ecol.*, 8: 315-323

Lund, M, P M Lafleur, N T Roulet, A Lindroth, T R Christensen, M Aurela, B H Chojnicki, L B Flanagan, E R Humphreys, T Laurila, W C Oechel, J Olejnik, J Rinne, P Schubert, M B Nilsson (2010) Variability in exchange of CO_2 across 12 northern peatland and tundra sites. *Glob. Change Biol.*, 16: 2436-2448.

Marushchak, M E, I Kiepe, C Biasi, V Elsakov, T Friborg, T Johansson, T Virtanen, P Martikainen (2013) Carbon dioxide balance of subarctic tundra from plot to regional scales. *Biogeosciences*, 10: 437-452.

McCallum, I, O Franklin, E Moltchanova, L Merbold, C Schmullius, A Shvidenko, D Schepaschenko, S Fritz (2013) Improved light and temperature responses for light use efficiency based GPP models. *Biogeosciences*, 10: 6577-6590.

McGuire, A D, D J Hayes, D W Kicklighter, M Manizza, Q Zhuang, M Chen, M J Follows, K R Gurney, J W McClelland, J M Melillo (2010) An analysis of the carbon balance of the Arctic Basin from 1997 to 2006. *Tellus B*, 62: 455-474.

McGuire, A D, T R Christensen, D Hayes, A Heroult, E Euskirchen, J S Kimball, C Koven, P Lafleur, P A Miller, W Oechel, P Peylin, M Williams, Y Yi (2012) An assessment of the carbon balance of Arctic tundra: comparisons among observations, process models, and atmospheric inversions. *Biogeosciences*, 9: 3185-3204.

Meng, L, P G M Hess, N M Mahowald, J B Yavitt, W J Riley, Z M Subin, D M Lawrence, S C Swenson, J Jauhiainen, D R Fuka (2012) Sensitivity of wetland methane emissions to model assumptions: Application and model testing against site observations, *Biogeosciences*, 9: 2793-2819.

Merbold, L, Kutsch, W L, C Corradi, O Kolle, C Rebmann, P C Stoy, S A Zimov, E D Schulze (2009) Artificial drainage and associated carbon fluxes (CO_2/CH_4) in a tundra ecosystem. *Glob. Change Biol*., 15, 2599-2614.

Moosavi, S C, P M Crill (1997) Controls on CH_4 and CO_2 emissions along two moisture gradients in the Canadian boreal zone. *J. Geophys. Res. Atmos.*, 102: 261-277.

Natali, S M, E A Schuur, R L Rubin (2012) Increased plant productivity in Alaskan tundra as a result of experimental warming of soil and permafrost. *J. Ecol.*, 100: 488-498.

Oberbauer, S F, W Cheng, C T Gillespie, B Ostendorf, A Sala, G Gebauer, R A Virginia, J D Tenhunen (1996) Landscape patterns of carbon dioxide exchange in tundra ecosystems,

in: Ecological Studies, Vol. 120, edited by Reynolds, J. F. and Tenhunen, J. D., Springer-Verlag Berlin, Heidelberg, (pp. 223–256).

Olefeldt, D, N T Roulet, O Bergeron, P Crill, K Bäckstrand, T R Christensen (2012) Net carbon accumulation of a high-latitude permafrost palsa mire similar to permafrost-free peatlands. *Geophys. Res. Lett.*, 39 589-603.

Olefeldt, D, M R Turetsky, P M Crill, A D McGuire (2013) Environmental and physical controls on northern terrestrial methane emissions across permafrost zones. *Glob. Change Biol.*, 19: 589-603.

Olivas, P C, S F Oberbauer, C E Tweedie, W C Oechel, A Kuchy (2010) Responses of CO_2 flux components of Alaskan Coastal Plain tundra to shifts in water table. *J. Geophys. Res. Biogeo.*, 115: G00105, doi: 1029/2009JG001254.

Olsrud, M, T R Christensen (2011) Carbon partitioning in a wet and a semiwet subarctic mire ecosystem based on in situ ^{14}C pulse labeling. *Soil Biol. Biochem.*, 43: 231-239.

Parmentier, F J W, M K van der Molen, J van Huissteden, S A Karsanaev, A V Kononov, D A Suzdalov, T C Maximov, A J Dolman (2011a) Longer growing seasons do not increase net carbon uptake in the northeastern Siberian tundra. *J. Geophys. Res.Biogeo.*, 116: G04013, doi:10.1029/2011JG001653.

Parmentier, F J W, J van Huissteden, M K van der Molen, G Schaepman-Strub, S A Karsanaev, T C Maximov, A J Dolman (2011b) Spatial and temporal dynamics in eddy covariance observations of methane fluxes at a tundra site in northeastern Siberia. *J. Geophys. Res. Biogeo.*, 116, G03016: doi:10.1029/2010JG001637.

Parmentier, F J W, J van Huissteden, N Kip, H J M Op den Camp, M S M Jetten, T C Maximov, A J Dolman (2011c) The role of endophytic methane-oxidizing bacteria in submerged Sphagnum in determining methane emissions of Northeastern Siberia tundra. *Biogeosciences*, 8: 1267-1278.

Parmentier, F J W, T R Christensen, L L Sorensen, S Rysgaard, A D McGuire, P A Miller, D A Walker (2013) The impact of lower sea-ice extent on Arctic greenhouse-gas exchange. *Nature Clim. Change*, 3: 195-202.

Peng, D, B Zhang, L Liu (2012) Comparing spatiotemporal patterns in Eurasian FPAR derived from two NDVI-based methods. *Int. J. Digital Earth*, 5: 283-298.

Petrescu, A M R, L P H van Beek, J van Huissteden, C Prigent, T Sachs, C A R Corradi, F J W Parmentier, A J Dolman (2010) Modeling regional to global CH_4 emissions of boreal and arctic wetlands. *Global Biogeochem. Cy.*, 24: GB4009, doi:1029/2009GB003610.

Porter, C H, J W Jones, S Adiku, A J Gijsman, O Gargiulo, J B Naab (2010) Modeling organic carbon and carbon-mediated soil processes in DSSAT V4.5. *Oper. Res. Int. J.*, 10: 274-278.

Potter, C, S Klooster, S Hiatt, M Fladeland, V Genovese, P Gross (2006) Methane emissions from natural wetlands in the United States: Satellite-derived estimation based on ecosystem carbon cycling. *Earth Interact.*, 10: 1-12.

Preuss, I, C Knoblauch, J Gebert, E M Pfeiffer (2013) Improved quantification of microbial CH_4 oxidation efficiency in arctic wetland soils using carbon isotope fractionation, *Biogeosciences*, 10: 2539-2552.

Raupach, M R (1998) Influences of local feedbacks on land-air exchanges of energy and carbon. *Glob. Change Biol.*, 4: 477-494.

Reiche, M, G Gleixner, K Küsel (2010) Effect of peat quality on microbial greenhouse gas formation in an acidic fen. *Biogeosciences*, 7: 187-198.

Reichle, R H, R D Koster, G J M De Lannoy, B A Forman, Q Liu, S P P Mahanama, A Toure (2011) Assessment and enhancement of MERRA land surface hydrology estimates. *J. Climate*, 24: 6322-6338.

Rienecker, M M, M J Suarez, G Gelaro, R Todling, J Bacmeister, E Liu, M G Bosilovich, S D Schubert, L Takacs, G K Kim, S Bloom, J Chen, D Collins, A Conaty, A da Silva, et al. (2011) MERRA: NASA's Modern-Era Retrospective Analysis for Research and Applications. *J. Climate*, 24: 3624–3648.

Riley, W J, Z M Subin, D M Lawrence, S C Swenson, M S Torn, L Meng, N M Mahowald, P Hess (2011) Barriers to prediction changes in global terrestrial methane fluxes: analysis using CLM4Me, a methane biogeochemical model integrated in CESM. *Biogeosciences*, 8: 1925-1953.

Rinne, J, T Riutta, M Pihlatie, M Aurela, S Haapanala, J Tuovinen, E Tuittila, T Vesala (2007) Annual cycle of methane emission from a boreal fen measured by the eddy covariance technique. *Tellus B*, 59: 449-457.

Riutta, T, J Laine, M Aurela, J Rinne, T Vesala, T Laurila, S Haapanala, M Pihlatie, E S Tuittila (2007) Spatial variation in plant community functions regulates carbon gas dynamics in a boreal fen ecosystems. *Tellus B*, 59: 838-852.

Roberts, J (2000) The influence of physical and physiological characteristics of vegetation on their hydrological response. *Hydrol. Process.*, 14: 2885-2901.

Rosenberry, D O, P H Glaser, D I Siegel (2006) The hydrology of northern peatlands as affected

by biogenic gas: current developments and research needs. *Hydrol. Processes*, 20: 3601-3610.

Running, S W, R R Nemani, F A Heinsch, M Zhao, M Reeves, H Hashimoto (2004) A continuous satellite-derived measure of global terrestrial primary production. *BioScience*, 54: 547-560.

Sachs, T, C Wille, J Boike, L Kutzbach (2008) Environmental controls on ecosystem-scale CH_4 emission from polygonal tundra in the Lena River Delta, Siberia. *J. Geophys. Res.*, 113: 3096-3110.

Sachs, T, M Giebels, J Boike, L Kutzbach (2010) Environmental controls on CH_4 emission from polygonal tundra on the microsite scale in the Lena river delta, Siberia. *Glob. Change Biol.*, 16: 3096-3110.

Schneider von Deimling, T, M Meinshausen, A Levermann, V Huber, K Frieler, D M Lawrence, V Brovkin (2012) Estimating the near-surface permafrost-carbon feedback on global warming. *Biogeosciences*, 9: 649-665.

Schubert, P, L Eklundh, M Lund, M Nilsson (2010a) Estimating northern peatland CO_2 exchange from MODIS time series data. *Remote Sens. Environ.*, 114: 1178-1189.

Schubert, P, M Lund, L Ström, L Eklundh (2010b) Impact of nutrients on peatland GPP estimations using MODIS time series. *Remote Sens. Environ.*, 114: 2137-2145.

Schubert, P, F Lagergren, M Aurela, T Christensen, A Grelle, M Heliasz, L Klemedtsson, A Lindroth, K Pilegaard, T Vesala, L Eklundh (2012) Modeling GPP in the Nordic forest landscape with MODIS time series data-Comparison with the MODIS GPP product. *Remote Sens. Environ.*, 126: 136-147.

Schuur, E A G, J G Vogel, K G Crummer, H Lee, J O Sickman, T E Osterkamp (2009) The effect of permafrost thaw on old carbon release and net carbon exchange from Tundra. *Nature*, 459: 556-559.

Shiklomanov, N I, D A Streletskiy, F E Nelson, R D Hollister, V E Romanovsky, C E Tweedie, J G Bockheim, J Brown (2010) Decadal variations of active-layer thickness in moisture-controlled landscapes, Barrow, Alaska. *J. Geophys. Res.*, 115: G00104, doi:10.1029/2009JG001248.

Sigsgaard, C (2011) Guidelines and sampling procedures for the geographical monitoring programme of Zackenberg Basic. Zackenberg Ecological Research Operations, GeoBasis, (124 pp.).

Sitch, S, A D McGuire, J S Kimball, N Gedney, J Gamon, R Engstrom, A Wolf, Q Zhuang, J

Clein, K C McDonald (2007) Assessing the carbon balance of circumpolar Arctic tundra using remote sensing and process modeling. *Ecol. App.*, 17: 213-234.

Sjögersten, S, P A Wookey (2009) The impact of climate change on ecosystem carbon dynamics at the Scandinavian mountain birch forest-tundra heath ecotone. *AMBIO*, 38: 2-10.

Solano, R, D Didan, A Jacobson, A Huete (2010) MODIS Vegetation Index User's Guide (MOD13 Series), Version 2.0. Vegetation Index and Phenology Lab, The University of Arizona, (42 pp.).

Spahni, R, R Wania, L Neef, M van Weele, I Pison, P Bousquet, C Frankenberg, P N Foster, F Joos, I C Prentice, P van Velthoven (2011) Constraining global methane emissions and uptake by ecosystems. *Biogeosciences*, 8: 1643-1665.

Street, L E, P D Stoy, M Sommerkorn, B J Fletcher, V L Sloan, T C Hill, M Williams (2012) Seasonal bryophyte productivity in the sub-Arctic: a comparison with vascular plants. *Funct. Ecol.*, 26: 365-378.

Ström, L, A Ekberg, M Mastepanov, T R Christensen (2003) The effect of vascular plants on carbon turnover and methane emissions from a tundra wetland. *Glob. Change Biol.*, 9: 1185-1192.

Ström, L, M Mastepanov, T R Christensen (2005) Species-specific effects of vascular plants on carbon turnover and methane emissions from wetlands. *Biogeochemistry*, 75: 65-82.

Sturtevant, C S, W C Oechel (2013) Spatial variation in landscape-level CO_2 and CH_4 fluxes from arctic coastal tundra: influence from vegetation, wetness, and the thaw lake cycle. *Glob. Change Biol.*, 19: 2853-2866.

Sturtevant, C S, W C Oechel, D Zona, Y Kim, C E Emerson (2012) Soil moisture control over autumn season methane flux, Arctic Coastal Plain of Alaska. Biogeosciences, 9: 1423-440.

Sun, X, C Song, Y Guo, X Wang, G Yang, Y Li, R Mao, Y Lu (2012) Effect of plants on methane emissions from a temperate marsh in different seasons. *Atmos. Envion.*, 60: 277-282.

Tagesson, T, M Mastepanov, M P Tamstorf, L Eklundh, P Schubert, A Ekberg, C Sigsgaard, T R Christensen, L Ström (2012a) High-resolution satellite data reveal an increase in peak growing season gross primary production in a high-Arctic wet tundra ecosystem 1992-2008. *Int. J. Appl. Earth Obs.*, 18: 407-416.

Tagesson, T, M Mölder, M Mastepanov, C Sigsgaard, M P Tamstorf, M Lund, J M Falk, A

Lindroth, T R Christensen, L Ström, (2012b) Land-atmosphere exchange of methane from soil thawing to soil freezing in a high-Arctic wet tundra ecosystem. *Glob. Change Biol.*, 18: 1928-1940.

Tagesson, T, M Mastepanov, M Mölder, M P Tamstorf, L Eklundh, B Smith, C Sigsgaard, M Lund, A Ekberg, J M Falk, T Friborg, T R Christensen, L Ström (2013) Modelling of growing season methane fluxes in a high-Arctic wet tundra ecosystem 1997-2010 using in situ and high-resolution satellite data. *Tellus B*, 65: 1972.

Tian, H, X Xu, M Liu, W Ren, C Zhang, G Chen, C Lu (2008) Spatial and temporal patterns of CH_4 and N_2O fluxes in terrestrial ecosystems of North America during 1979-2008: application of a global biogeochemistry model. *Biogeosciences*, 7: 2673-2694.

Turetsky, M R, C C Treat, M P Waldrop, J M Waddington, J W Harden, D McGuire (2008) Short-term response of methane fluxes and methanogen activity to water table and soil warming manipulations in an Alaskan peatland. *J. Geophys. Res.*, 113: G00A10.

van Huissteden, J, R van den Bos, I Marticorena Alvarez (2006) Modelling the effect of water-table management on CO_2 and CH_4 fluxes from peat soils. *Neth. J. Geosci.*, 85: 3-18.

van Hulzen, J B, R Segers, P M van Bodegom, P A Leffelaar (1999) Temperature effects on soil methane production: an explanation for observed variability. *Soil Biol. Biochem.*, 31: 1919-1929.

Verry, E S, D H Boelter, J Paivanen, D S Nichols, T Malterer, A Gafni, A (2011). in: Peatland Biogeochemistry and Watershed Hydrology at the Marcell Experimental Forest, edited by Kolka, R., Sebestyen, S., Verry, E. S., and Brooks, K., CRC Press, Boca Raton, (pp. 135–176).

von Fischer, J C, L O Hedin (2007) Controls on soil methane fluxes: tests of biophysical mechanisms using stable isotope tracers. *Global Biogeochem. Cy.*, 21: GB2007, doi:10.1029/2006GB002687.

von Fischer, J C, R C Rhew, G M Ames, B K Fosdick, P E avon Fischer (2010) Vegetation height and other controls of spatial variability in methane emissions from the Arctic coastal tundra at Barrow, Alaska. J. *Geophys. Res.*, 115: G00103, doi:10.1029/2009JG001283.

Wagner, D, S Kobabe, S Liebner (2009) Bacterial community structure and carbon turnover in permafrost-affected soils of the Lena Delta, northeastern Siberia. *Can. J. Microbiol.*, 55: 73-83.

Walter, B P, M Heimann (2000) A process-based, climate-sensitive model to derive

methane emissions from natural wetlands: application to five wetland sites, sensitivity to model parameters, and climate. *Global Biogeochem. Cy.*, 14: 745-765.

Wania, R, I Ross, I C Prentice (2010) Implementation and evaluation of a new methane model within a dynamic global vegetation model: LPJ-WHyMe v1.3.1. *Geosci. Model Dev.*, 3: 565-584.

Wania, R, J R Melton, E L Hodson, B Poulter, B Ringeval, R Spahni, T Bohn, C Avis, G Chen, A V Eliseev, P O Hopcroft, W J Riley, Z M Subin, H Tian, P M van Bodegom, T Kleinen, Z C Yu, J S Singarayer, S Zürcher, D P Lettenmaier, D J Beerling, S N Denisov, C Prigent, F Papa, J O Kaplan (2013) Present state of global wetland extent and wetland methane modelling: methodology of a model inter-comparison project (WETCHIMP). *Geosci. Model Dev.*, 6: 617-641.

Watts, J D, J S Kimball, L A Jones, R Schroeder, K C McDonald (2012) Satellite microwave remote sensing of contrasting surface water inundation changes within the Arctic-Boreal Region. *Remote Sens. Environ.*, 127: 223-236.

Wegner, L H (2010) Oxygen transport in waterlogged plants. In: Waterlogging Signalling and Tolerance in Plants, edited by: Mancuso, S. and Shabala, S., Springer-Verlag Berlin Heidelberg, (294 pp.).

Wille, C, L Kutzbach, T Sachs, D Wagner, E M Pfeiffer (2008) Methane emission from Siberian arctic polygonal tundra: eddy covariance measurements and modeling. *Glob. Change Biol.*, 14: 1395-1408.

Wu, J, N T Roulet, J Sagerfors, M B Nilsson (2013) Simulation of six years of carbon fluxes for a sedge-dominated oligotrophic minerogenic peatland in Northern Sweden using the McGill wetland model (MWM). *J. Geophys. Res. Biogeo.*, 118: 795-807.

Yan, H, S Q Wang, D Billesbach, W Oechel, J H Zhang, T Meyers, T A Martin, R Matamala, D Baldocchi, G Bohrer, D Bragoni, R Scott (2012) Global estimation of evapotranspiration using a leaf area index-based surface energy and water balance model. *Remote Sens. Environ.*, 124: 581-595.

Yang, R, M A Friedl (2002) Determination of roughness lengths for heat and momentum over boreal forests. *Bound.-Lay. Meterol.*, 107: 581-603.

Yi, Y, J S Kimball, L A Jones, R H Reichle, K C McDonald (2011) Evaluation of MERRA land surface estimates in preparation for the soil moisture active passive mission. *J. Climate*, 24: 3797-3816.

Yi, Y, J S Kimball, L A Jones, R H Reichle, R Nemani, H A Margolis (2013) Recent climate and fire disturbance impacts on boreal and arctic ecosystem productivity

estimated using a satellite-based terrestrial carbon flux model. J. *Geophys. Res. Biogeo.*, 118: 1-17.

Yuan, W, Y Luo, X Li, S Liu, S Yu, T Zhou, M Bahn, A Black, A R Desai, A Cescatti, B Marcolla, C Jacobs, J Chen, M Aurela, C Bernhofer, B Gielen, G Bohrer, D R Cook, D Dragoni, A L Dunn, D Gianelle, T Grünwald, et al. (2011) Redefinition and global estimation of basal ecosystem respiration rate. *Global Biogeochem. Cy.*, 25: GB4002.

Zhang, X, J He, J Zhang, I Polyakov, R Gerdes, J Inoue, P Wu (2012a) Enhanced poleward moisture transport and amplified northern high-latitude wetting trend. *Nature Clim. Change*, 3: 47-51.

Zhang, Y, T Sachs, C Li, J Boike (2012b) Upscaling methane fluxes from closed chambers to eddy covariance based on a permafrost biogeochemistry integrated model. *Glob. Change Biol.*, 18: 1428-1440.

Zhao, M, F A Heinsch, R M Nemani, S W Running (2005) Improvements of the MODIS terrestrial gross and net primary production global data set. *Remote Sens. Environ.*, 95: 164-176.

Zhuang, Q, J M Melillo, D W Kicklighter, R G Prinn, A D McGuire, P A Steudler, B S Felzer, S Hu (2004) Methane fluxes between terrestrial ecosystems and the atmosphere at northern high latitudes during the past century: a retrospective analysis with a process-based biogeochemistry model. *Global Biogeochem. Cy.*, 18: GB3010.

Zona, D, W C Oechel, J Kochendorfer, K T Paw U, A N Salyuk, P C Olivas, S F Oberbauer, D A Lipson (2009) Methane fluxes during the initiation of a large-scale water table manipulation experiment in the Alaskan Arctic tundra. *Global Biogeochem. Cy.*, 23: GB2013, doi:10.1029/2009GB003487.

Zona, D, W C Oechel, J H Richards, S Hastings, I Kopetz, H Ikawa, S Oberbauer (2011) Light-stress avoidance mechanisms in a Sphagnum-dominated wet coastal Arctic tundra ecosystem in Alaska. *Ecology*, 92: 633-644.

Zona, D, D A Lipson, K T Paw U, S F Oberbauer, P Olivas, B Gioli, W C Oechel (2012) Increased CO_2 loss from vegetated drained lake tundra ecosystems due to flooding. *Global Biogeochem. Cy.*, 26: GB2004, doi:10.1029/2011GB004037.

Zubrzycki, S, L Kutzbach, G Grosse, A Desyatkin, E M Pfeiffer (2013) Organic carbon and total nitrogen stocks in soils of the Lena River Delta. *Biogeosci.*, 10: 3507-3524.

Zürcher, S, R Spahni, F Joos, M Steinacher, H Fischer (2013) Impact of an abrupt cooling event on interglacial methane emissions in northen peatlands. *Biogeosci.*, 10: 1963-1981.

Tables

Table 4.1 Description of flux tower locations and site characteristics including permafrost (PF) cover and climate. The length (days) of each tower site CO_2 and CH_4 record is provided in addition to the observation year.

Site Name	Location (Lat. Lon.)	Climate	Land Cover	Observation Period	In-Situ Data	Data Source
Siikaneva, Finland (SK)	61°50' N, 24°12' E	PF: N/A MAT 3.3°C MAP 713 mm	homogenous boreal oligotrophic fen with peat, sedges, graminoids	8 Mar - 14 Nov 2005 (273 days) CO_2 (165 days) CH_4	CO_2, CH_4 5, 10 cm T_s	Aurela et al. (2007) Rinne et al. (2007) Riutta et al. (2007)
Lena River, Russia (LR)	72°22' N, 126°30' E	PF: Continuous MAT -14.7 °C MSP 72-208 mm	wet polygonal tundra with sedges, dwarf shrubs, forbes, moss	19 Jul - 21 Oct 2003 (95 days) CO_2, CH_4 9 Jun - 17 Sep 2006 (101 days) CO_2, CH_4	CO_2, CH_4 5, 10 cm T_s $\leq$ 12 cm θ	Boike et al. (2008) Kutzbach et al. (2007) Sachs et al. (2008) Wille et al. (2008)
Zackenberg, Greenland (ZK)	74°28' N, 20°34' W	PF: Continuous MAT -9°C MAP 200 mm	heterogeneous wetland fen tundra with graminoids, heath, moss	24 Jun - 31 Oct 2008 (130 days) CO_2, CH_4 16 May - 25 Oct 2009 (163 days) CO_2, CH_4	CO_2, CH_4 2, 5, 10 cm T_s $\leq$ 20 cm θ	Sigsgaard (2011) Tagesson et al. (2012)
Stordalen, Sweden (SM)	68°20' N, 19°03' E	PF: Discontinuous MAT -0.9°C MAP 305 mm	palsa mire with graminoids, dwarf shrubs, birch, moss, lichen	1 Jan - 31 Dec 2006 (365 days) CH_4 1 Jan - 31 Dec 2007 (365 days) CH_4	CH_4 3 cm T_s	Jackowicz-Korczyński et al. (2010)
Kytalyk, Russia (KY)	70°49' N, 147°29' E	PF: Continuous MAT -10.5°C MAP 220 mm	polygonal tundra with mixed shrub, sedge, moss	8 Jun - 10 Aug 2009 (64 days) CO_2 5 Jul - 3 Aug 2009 (30 days) CH_4	CO_2, CH_4 4, 8 cm T_s	Parmentier et al. (2011a, b)

Barrow, Alaska (BA)	71°17’ N, 156°35’ W	PF: Continuous MAT -12°C MAP 106 mm	thaw lake basin with moss and sedge	12 Jun - 31 Aug 2007 North: (81 days) CO_2 North: (46 days) CH_4	CO_2, CH_4, 5, 10 cm T_s $\leq$ 10 cm θ	Zona et al. (2009, 2012)
				20 Aug - 21 Oct 2009 North: (30, 11 days) CO_2, CH_4, Central: (12, 23 days) CO_2, CH_4 South: (2, 10 days) CO_2, CH_4	CO_2, CH_4 5 cm T_s $\leq$ 10 cm θ	Sturtevant et al. (2012)

Table 4.2 Tower EC CO_2 records and TCF modeled gross primary production (GPP), ecosystem respiration (R_{eco}) and net ecosystem exchange (NEE) derived using in-situ information (in parentheses) or satellite remote sensing and reanalysis inputs. The Pearson correlation coefficients (r) are significant at a 0.05 probability level, excluding Kytalyk 2009 NEE ($r \leq 0.11$, $p \geq 0.17$) and Barrow 2007N GPP and NEE ($r < 0.1$, $p \geq 0.16$).

Site	Year	Flux	r	8 day r	RMSE	MRE	Site EC	TCF Model
					g C m^{-2} d^{-1}		Cumulative (g C m^{-2})	
Siikaneva	2005	GPP	0.84	0.94	0.8	-0.2	361.1	409.4
		R_{eco}	0.96 (0.96)	0.96 (0.98)	0.4 (0.3)	-0.3 (0.1)	289.9	365.6 (274.9)
		NEE	0.49 (0.91)	0.92 (0.92)	0.5 (0.3)	0.3 (-0.1)	-71.2	-43.8 (-86.2)
Lena River	2003	GPP	0.74	0.91	0.7	-0.1	72.3	131.5
		R_{eco}	0.77 (0.87)	0.83 (0.91)	1. (0.3)	-0.5 (-0.1)	56.3	103.3 (62.4)
		NEE	0.90 (0.94)	0.93 (0.97)	0.3 (0.3)	-0.1 (0.1)	-16.0	-28.2 (-9.9)
	2006	GPP	0.78	0.86	1.1	0.5	247.4	199.3
		R_{eco}	0.76 (0.84)	0.91 (0.91)	0.7 (0.6)	0.3 (0.2)	193.0	160 (176.4)
		NEE	0.57 (0.76)	0.62 (0.89)	0.7 (0.6)	0.2 (-0.2)	-54.4	-39.3 (-71.0)
Zackenberg	2008	GPP	0.75	0.76	1.8	< 0.1	218.2	215.4
		R_{eco}	0.67 (0.44)	0.80 (0.50)	1.1 (1.3)	0.3 (0.3)	215.9	175.5 (182.6)
		NEE	0.31 (0.83)	0.37 (0.85)	1.7 (1.3)	-0.3 (-0.3)	-2.3	-39.9 (-35.6)
	2009	GPP	0.91	0.96	1.3	0.6	305.0	234.6
		R_{eco}	0.86 (0.90)	0.93 (0.96)	0.8 (1)	0.4 (0.1)	250.3	183.7 (238.6)
		NEE	0.89 (0.89)	0.92 (0.92)	1.2 (1)	0.2 (-0.1)	-54.7	-50.9 (-66.4)
Kytalyk	2009	GPP	0.41	0.73	2.2	-1.5	143.2	224.9
		R_{eco}	0.49 (0.60)	0.80 (0.94)	1.6 (1.3)	-2.2 (-1.5)	60.8	200.2 (126.9)
		NEE	0.11 (0.92)	0.01 (0.95)	1.6 (1.3)	0.9 (1.5)	-82.4	-24.7 (-16.3)
Barrow	2007N	GPP	0.12	0.32	1.1	0.2	152.0	137.0
		R_{eco}	0.23 (0.61)	0.64 (0.82)	0.5 (0.4)	0.4 (-0.1)	117.4	104.3 (121.6)
		NEE	0.10 (0.79)	0.20 (0.79)	0.8 (0.4)	< 0.1 (0.1)	-34.6	-32.7 (-30.4)
	2009N	NEE	-	-	1.6	1.4	-62.1	-15.6
	2009C	NEE	-	-	0.5	0.4	-8.3	-3.6

Table 4.3 Tower EC CH_4 records and TCF model results using in-situ information (in parentheses) or satellite remote sensing and reanalysis inputs. The Pearson correlation coefficients (*r*) are significant at a 0.05 probability level, excluding Kytalyk 2009 ($r \leq 0.28$, $p \geq 0.07$).

Site	Year	*r*	8 day *r*	RMSE	MRE	Site EC	TCF Model
				mg C m^{-2} d^{-1}		Cumulative (g C m^{-2})	
Siikaneva	2005	0.72 (0.75)	0.90 (0.90)	21.8 (16.9)	-9.6 (-1.2)	5.9	7.6 (6.3)
Lena River	2003	0.59 (0.87)	0.88 (0.97)	9.1 (7.5)	4.7 (0.5)	1.4	0.9 (1.2)
	2006	0.53 (0.69)	0.81 (0.78)	6.9 (9.3)	-1.3 (-4.4)	1.4	1.6 (1.9)
Zackenberg	2008	0.78 (0.84)	0.91 (0.95)	35.7 (28.5)	11.6 (2.4)	7.6	6.1 (7.3)
	2009	0.75 (0.88)	0.84 (0.95)	28.7 (21.2)	-1.1 (-6.7)	6.3	6.5 (7.4)
Stordalen	2006	0.80 (0.80)	0.88 (0.89)	35 (33.4)	13.3 (0.9)	18.3	12.6 (17.9)
	2007	0.80 (0.79)	0.94 (0.89)	39.4 (42.5)	12.6 (-5.3)	22.1	17.5 (23.9)
Kytalyk	2009	0.28 (0.24)	0.66 (0.41)	20.1 (14.9)	-6.4 (0.7)	0.9	1.1 (0.8)
Barrow	2007N	0.51 (0.78)	0.94 (0.80)	5.8 (6.7)	-1.5 (-2.4)	0.7	0.8 (0.9)
	2009N	-	-	4.5 (15.9)	-0.5 (-12.6)	0.1	0.1 (0.2)
	2009C	-	-	4.2 (10.2)	0.4 (-4.7)	0.2	0.3 (0.3)
	2009S	-	-	7.2 (7.6)	-0.2 (6.3)	0.2	0.2 (0.2)

Figures

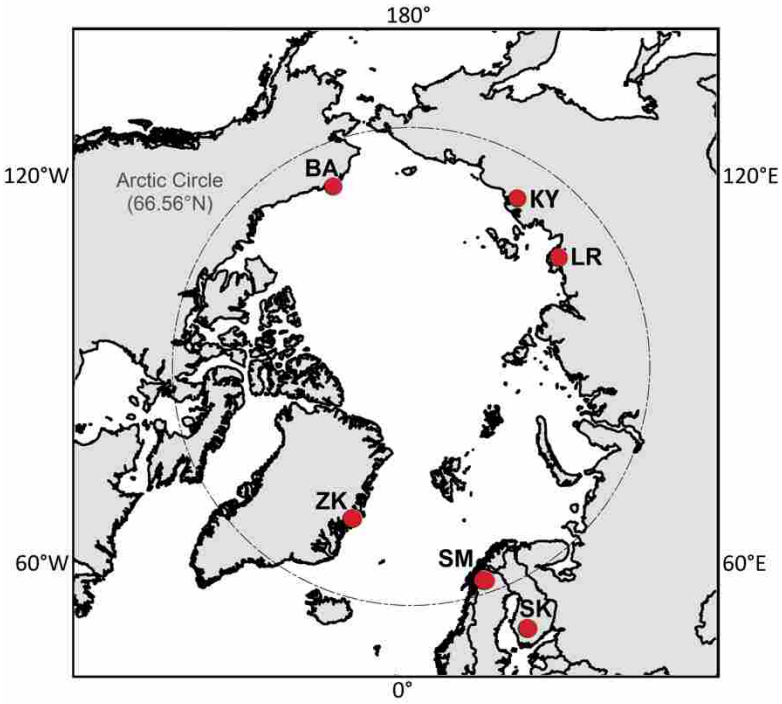

Figure 4.1 Locations of the flux tower sites (circles) used in this study, including Barrow (BA), Kytalyk (KY), Lena River (LR), Siikaneva (SK), Stordalen Mire (SM) and Zackenberg (ZK). The Arctic Circle is indicated by the dashed line.

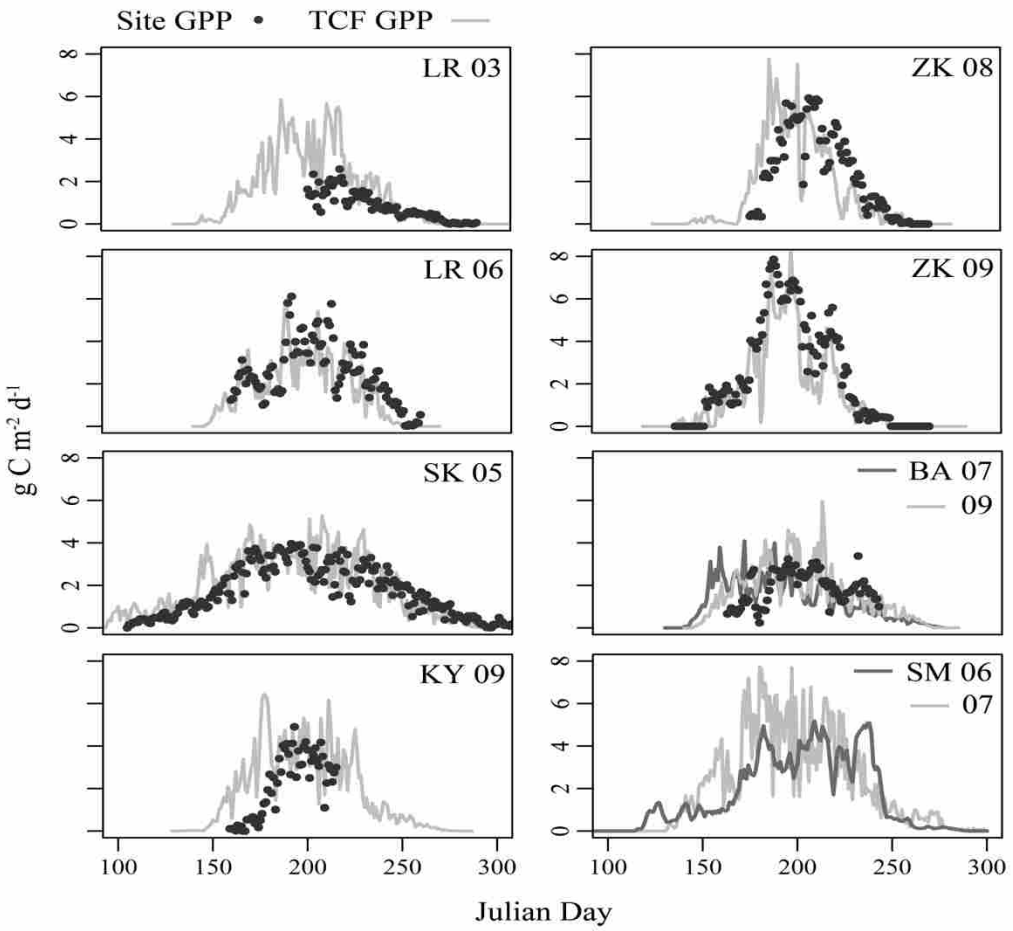

Figure 4.2 TCF model simulations for GPP (lines) using input remote sensing and reanalysis information as compared with flux tower EC records (circles). Site GPP records were not available for SM and BA 2009.

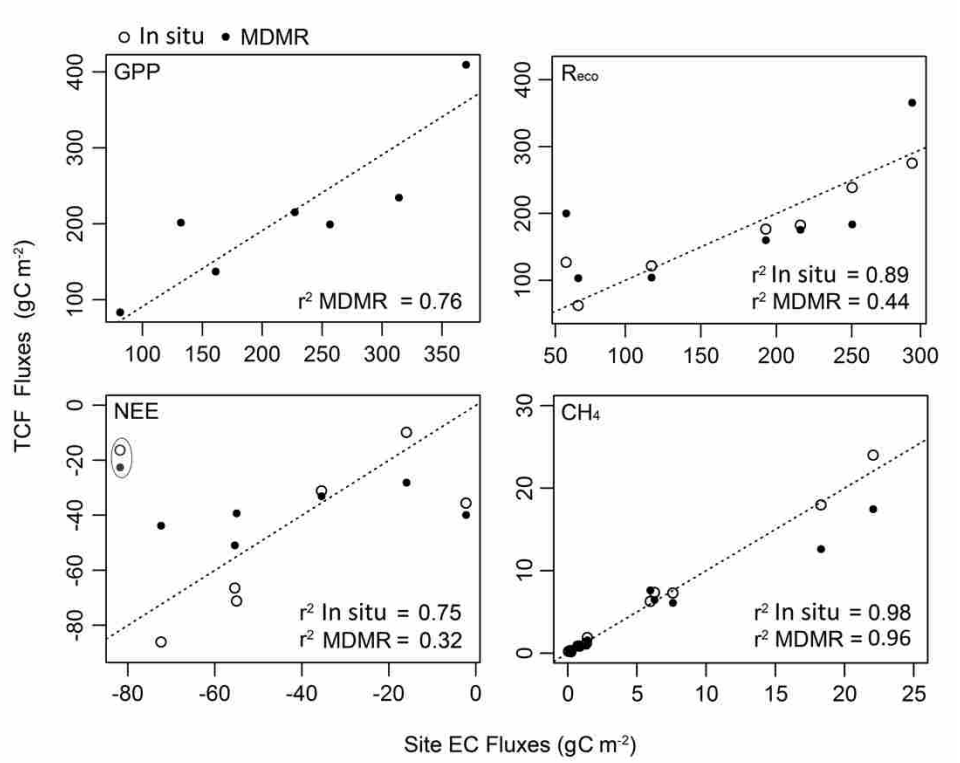

Figure 4.3 Correspondence between TCF model and tower EC records for cumulative (g C m^{-2}) GPP, R_{eco}, NEE, and CH_4 fluxes from six pan-Arctic tower locations. The TCF model simulations include those derived from in-situ measurements (open circles) or MODIS remote sensing and MERRA reanalysis inputs (MDMR; in black). A 1:1 relationship is indicated by the dashed line. The r^2 agreement is significant at a 0.05 probability level, except for MDMR based R_{eco} and NEE (p = 0.16 and 0.27), and excludes NEE fluxes for KY (circled) due to large differences in the CO_2 response relative to the other sites.

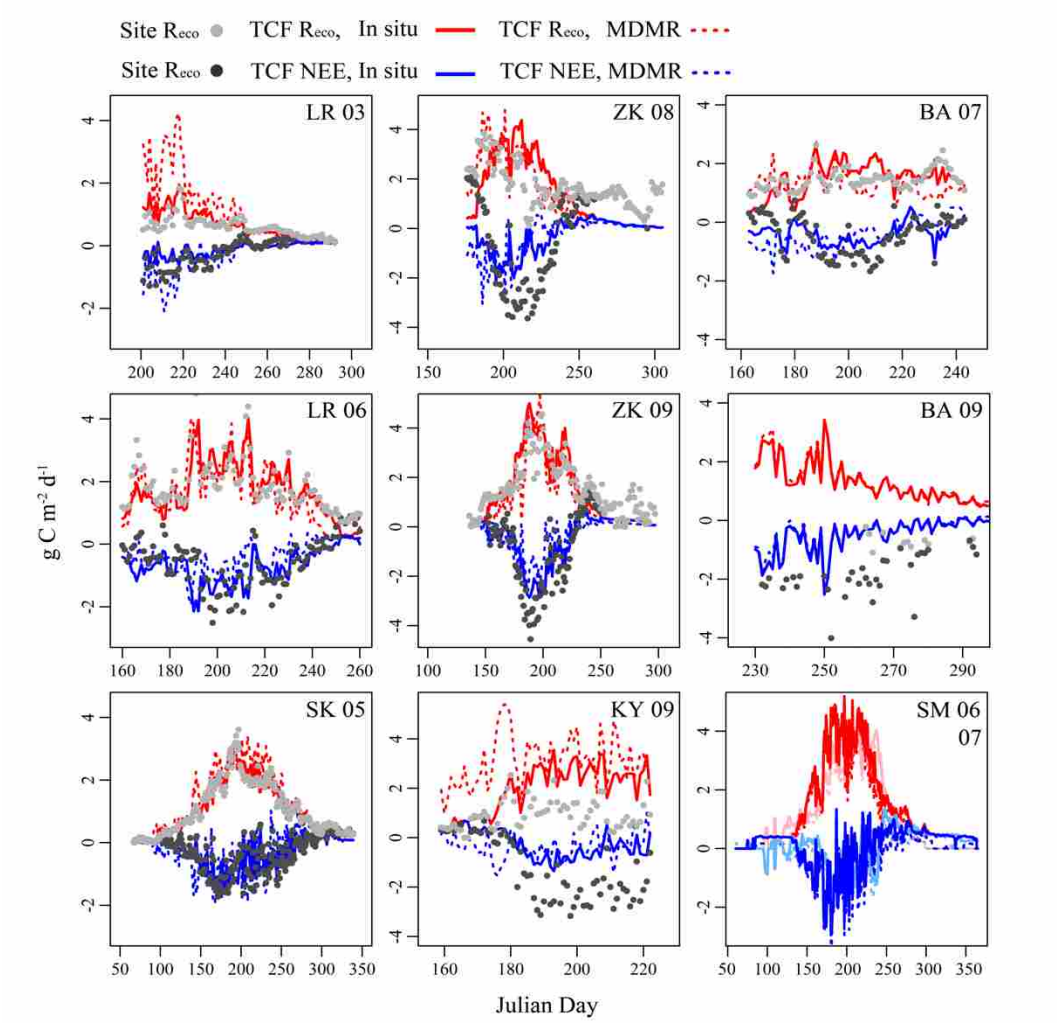

Figure 4.4 TCF model CO_2 simulations driven using in situ (solid lines) or remote sensing and reanalysis inputs (MDMR; dashed lines), as compared with tower EC records (circles) for R_{eco} and NEE. For BA 2009, in-situ R_{eco} was not available and NEE measurements from the northern (central) tower are shown in black (grey). The TCF model R_{eco} results for SM 2006 (2007) are displayed in light (dark) red and NEE is indicated in light (dark) blue.

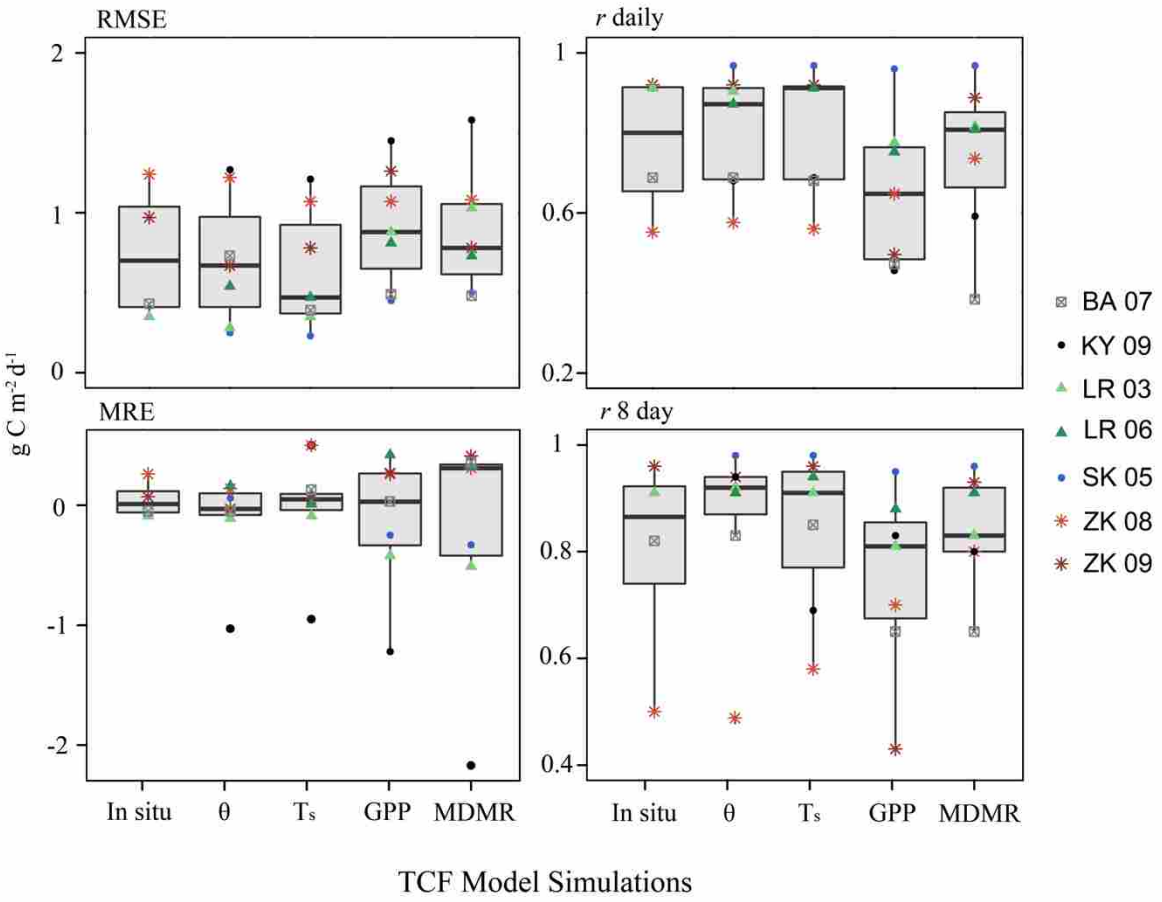

Figure 4.5 TCF model accuracy for R_{eco} relative to CO_2 records from five tower EC sites. The TCF model simulations include those determined from in-situ measurement inputs; reanalysis soil moisture (θ), soil temperature (T_s) or TCF LUE model simulated GPP inputs; TCF simulations derived entirely from remote sensing and reanalysis (MDMR) inputs. Measures of comparison include RMSE, MRE, *r*-values for daily and 8 day cumulative fluxes. The BA 2009 results represent the local spatial mean determined from north, central and southern Barrow tower locations.

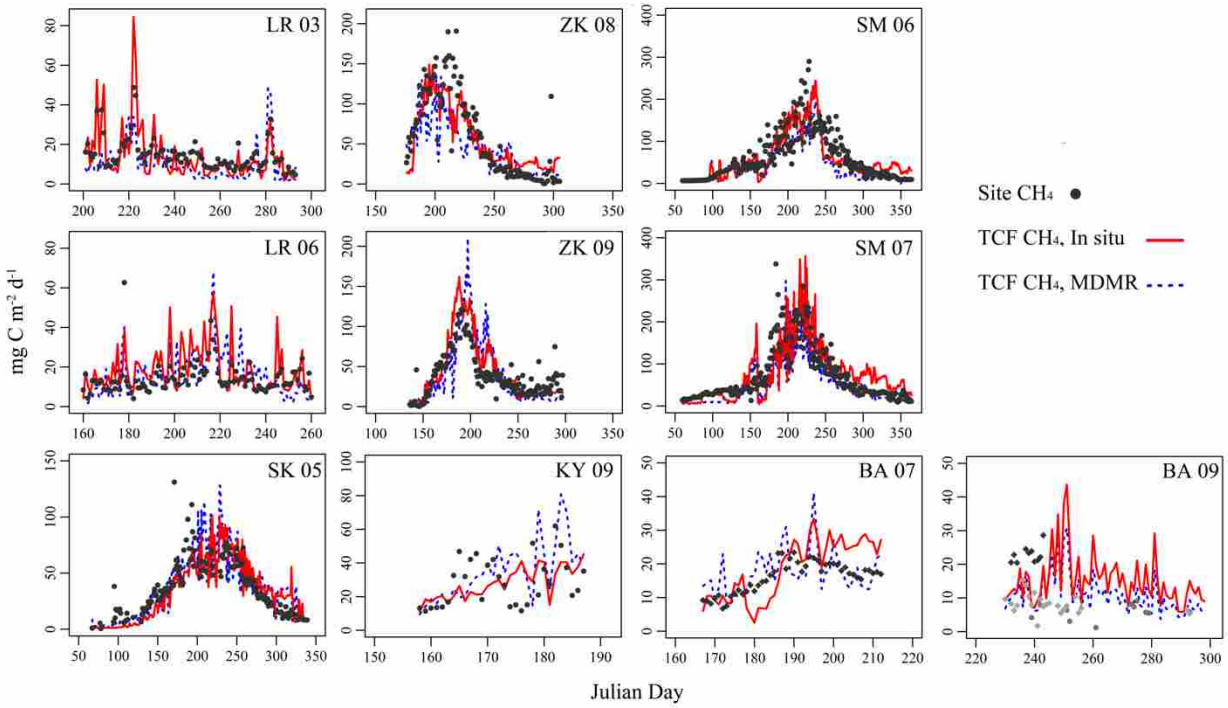

Figure 4.6 TCF model CH_4 simulations driven using in situ (solid lines) or input remote sensing and reanalysis (dashed lines) inputs, as compared with tower EC records (circles). For BA 2009, the TCF model results are simulation means for the three Barrow tower sites; diamond shapes indicate CH_4 flux observations from the northern (in dark gray) and central (in light gray) towers whereas grey circles indicate observations from the southern tower.

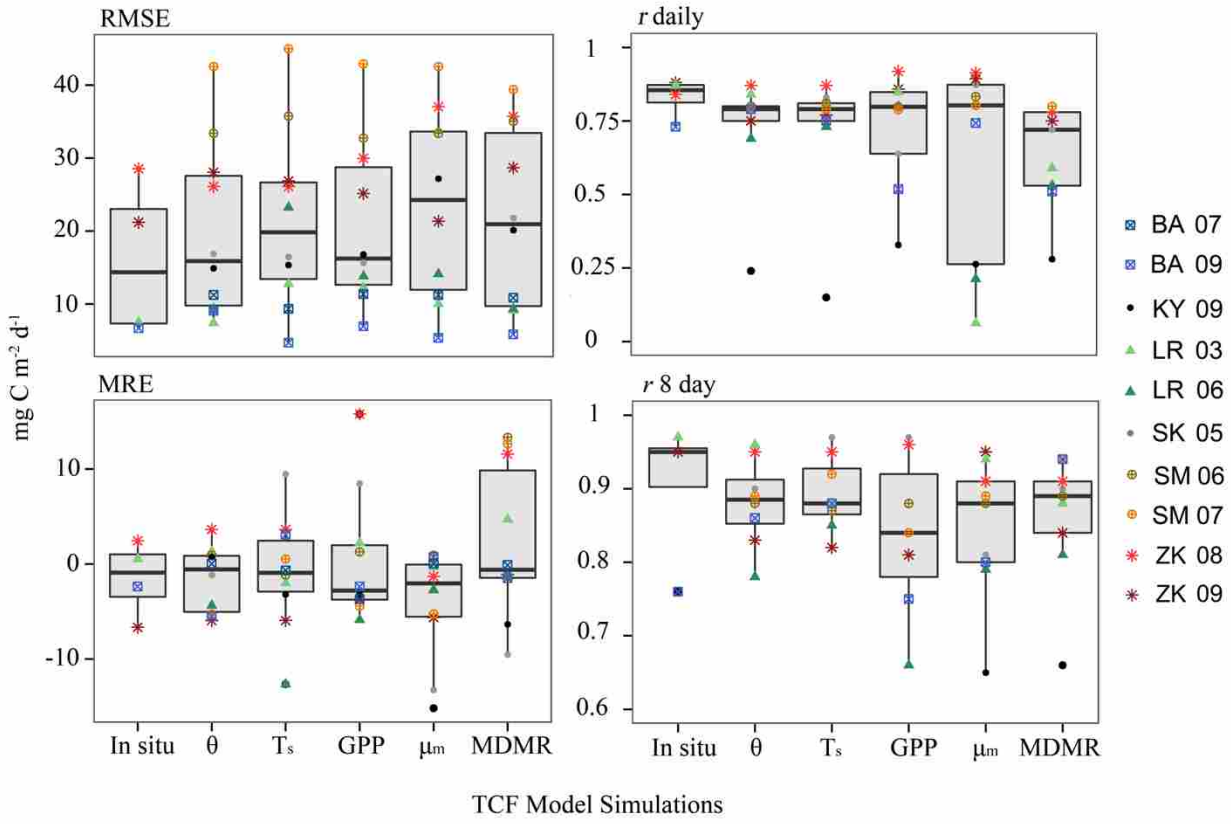

Figure 4.7 TCF model accuracy relative to CH_4 records from six tower EC sites. Model simulations include those derived from: in-situ measurements; reanalysis soil moisture (θ), soil temperature (T_s), surface wind velocity (μ_m) or TCF LUE model simulated GPP inputs; TCF simulations derived solely from remote sensing and reanalysis (MDMR) inputs. Measures of comparison include RMSE, MRE, *r*-values for daily and 8 day cumulative fluxes. Results for BA 2009 are means for north, central and southern Barrow tower locations.

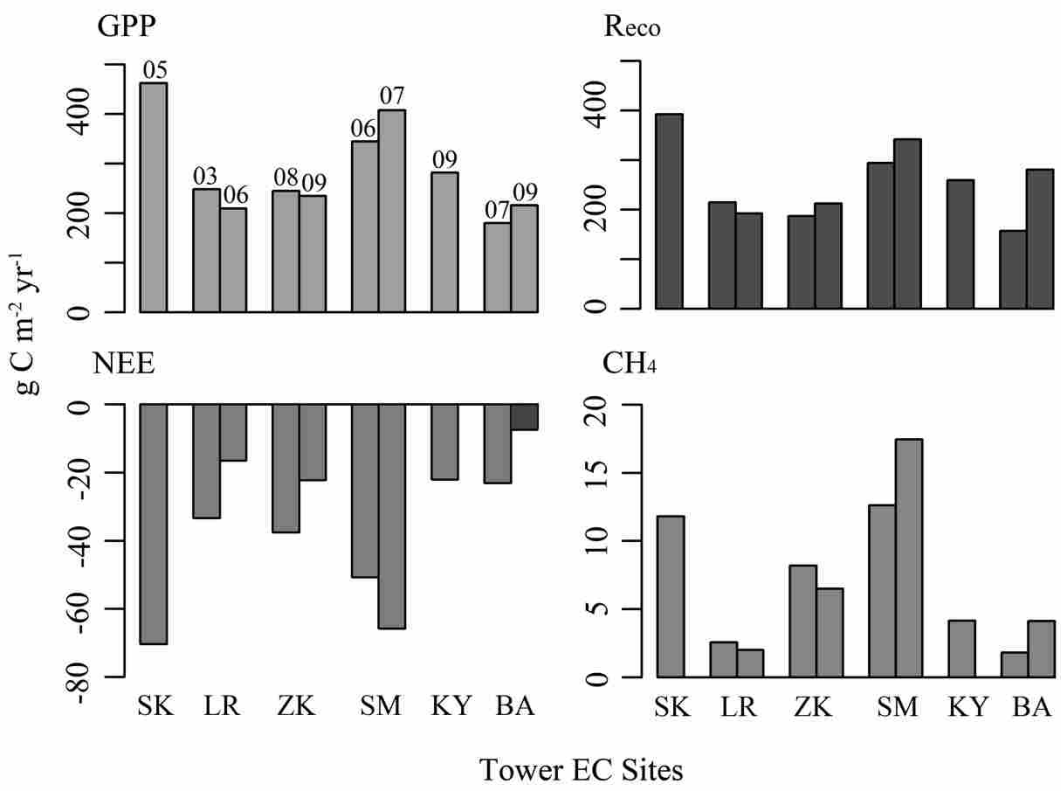

Figure 4.8 The TCF model simulation results for cumulative annual GPP, R_{eco}, NEE and CH_4 fluxes determined using satellite remote sensing and reanalysis inputs. For NEE, all sites are net CO_2 sinks except for BA 2009 which is a carbon source (in black).

Chapter 4 Supplement

Table S4.1 Definitions for the symbols and abbreviations used to describe the TCF model components and required input information.

Model Component	Symbols	Definition	Units
General	T_s	Soil temperature	K
	T_{min}	Daily minimum air temperature	K
	SW_{rad}	Incident shortwave radiation	W/m^2
	VPD	Vapor pressure deficit	Pa
	$APAR$	Absorbed photosynthetically active radiation	MJ m^{-2}
	$FPAR$	Fraction photosynthetically active radiation	[ ]
	ε_{max}	Maximum plant light use efficiency	mg C MJ^{-1}
	ε	Light use efficiency with environ. constraints	mg C MJ^{-1}
	θ	Volumetric water content	d^{-1}
	θ_{opt}	Soil moisture optimum	[ ]
	φ_s	Saturated pore volume	m^{-3} d^{-1}
	φ_a	Aerated pore volume	m^{-3} d^{-1}
CO_2 Model	CUE	Plant carbon use efficiency (NPP/GPP)	[ ]
	C_{met}	Metabolic carbon pool	g C m^{-2}
	C_{str}	Structural carbon pool	g C m^{-2}
	C_{rec}	Recalcitrant carbon pool	g C m^{-2}
	F_{met}	Fraction of NPP into C_{met}	[ ]
	F_{str}	Fraction of C_{met} allocated to C_{str}	[ ]
	F_{rec}	Fraction of C_{str} allocated to C_{rec}	[ ]
	R_a	Autotrophic respiration	g C m^{-2} d^{-1}
	R_h	Heterotrophic respiration	g C m^{-2} d^{-1}
	R_{eco}	Ecosystem respiration	g C m^{-2} d^{-1}
	K_p	Potential soil decomposition rate	d^{-1}
	K_{met}	Modified soil decomposition rate	d^{-1}
	T_{mult}	Temperature multiplier for K_p	[ ]
	T_{ref}	Reference temperature for T_{mult}	K
	W_{mult}	Soil moisture multiplier for K_p	[ ]

Table S4.1 continued.

Model Component	Symbols	Definition	Units
Soil CH_4 Production	R_{CH4}	Daily CH_4 production	mg C m^{-2} d^{-1}
	C_{CH4}	Total CH_4 storage	mg C m^{-2}
	R_o	CH_4 production rate	µM CH_4 d^{-1}
	Q_{10p}	Q_{10} temperature modifier, CH_4 production	K
	T_p	Reference temperature, CH_4 production	K
	F_{CH4}	Total CH_4 emission	mg C m^{-2} d^{-1}
	F_{plant}	Plant CH_4 transport	mg C m^{-2} d^{-2}
	F_{diff}	Diffusion CH_4 transport	mg C m^{-2} d^{-3}
	F_{ebull}	Ebullition CH_4 transport	mg C m^{-2} d^{-4}
Plant Transport	C_p	Plant CH_4 transport rate	d^{-1}
	P_{trans}	Transport modifier for C_p	[ ]
	f_{grow}	Plant growth scalar, based on GPP	d^{-1}
	μ_m	Mean daily wind velocity	m s^{-1}
	g_a	Aerodynamic conductance	m s^{-1}
	λ	Aerodynamic modifier	d^{-1}
	k	von Karman constant (for g_a)	[ ]
	z_m	Anemometer height	m
	d	Zero-plane displacement height (for g_a)	m
	z_{om}	Roughness length, momentum (for g_a)	m
	z_{ov}	Roughness length, heat/vapor transfer (for g_a)	m
	P_{ox}	Fraction oxidized during plant transport	[ ]
Diffusion And Ebullition	P_{diff}	Potential CH_4 diffusion	mg C m^{-2} d^{-1}
	R_{ox}	CH_4 oxidation	mg C m^{-2} d^{-1}
	A_{CH4}	Atmospheric CH_4	µM CH_4
	D_e	Effective soil diffusion rate	µM CH_4 d^{-1}
	D_{air}	CH_4 diffusion rate, aerated fraction	µM CH_4 d^{-1}
	D_{water}	CH_4 diffusion rate, saturated fraction	µM CH_4 d^{-1}
	τ	Soil tortuosity coefficient	[ ]
	L_s	Length of soil profile	m
	V_{max}	Maximum reaction rate,	µM CH_4 d^{-1}
	K_m	Substrate conc. at 1/2 V_{max}	µM CH_4
	Q_{10d}	Q_{10} temperature modifier, CH_4 diffusion	[ ]
	T_d	Reference temperature, CH_4 oxidation	K
	υ_e	CH_4 threshold for ebullition	µM
	C_e	CH_4 ebullition transport rate	µM d^{-1}

Table S4.2 Parameter values used for site-specific peatland (Biome 1) and wet tundra (Biome 2) TCF model CO_2 and CH_4 flux simulations.

TCF Component	Parameter		Tower Site:	SM	SK	LR	KY	ZK	BA
			Biome:	1	1	2	2	2	2
GPP	e_{max}	mg C MJ^{-1}		0.82	0.82	0.82	0.82	0.82	0.82
	θ_{min}	Fract.		0.15	0.15	0.15	0.15	0.15	0.15
	θ_{max}	Fract.		0.75	0.72	0.75	0.70	0.75	0.75
R_{eco}	CUE	Fract.		0.45	0.35	0.55	0.55	0.5	0.5
	K_p	d^{-1}		0.03	0.03	0.03	0.03	0.03	0.03
	F_{met}	Fract.		0.65	0.52	0.72	0.72	0.72	0.72
	T_{ref}	K		293	293	297	293	297	297
CH_4	ϕ	Fract.		0.75	0.75	0.70	0.70	0.70	0.70
	R_o	μM CH_4 d^{-1}		22.4	15.4	9.2	10.8	10.8	10.8*
	T_p	K		287	288	289	287	287	287
	Q_{10p}	[ ]		3.5	3.5	4	3.9	3.5	3.8
	P_{trans}	[ ]		8	9	7	7	7	7
	P_{ox}	Fract.		0.8	0.8	0.7	0.7	0.7	0.7
	A_{CH4}	μM CH_4		0.11	0.11	0.11	0.11	0.11	0.11
	V_{max}	μM CH_4 d^{-1}		120	120	120	120	120	120
	K_m	μM CH_4		1	1	1	1	1	1
	T_d	K		274	274	274	274	274	274
	Q_{10d}	[ ]		2	2	2	2	2	2
	v_e	μM		500	500	500	500	500	500
	C_e	μM d^{-1}		3	3	3	3	3	3

*A R_o value of 4.5 was used for BA 2007 to account for flooding disturbance impacts on substrate availability and methanogenesis.

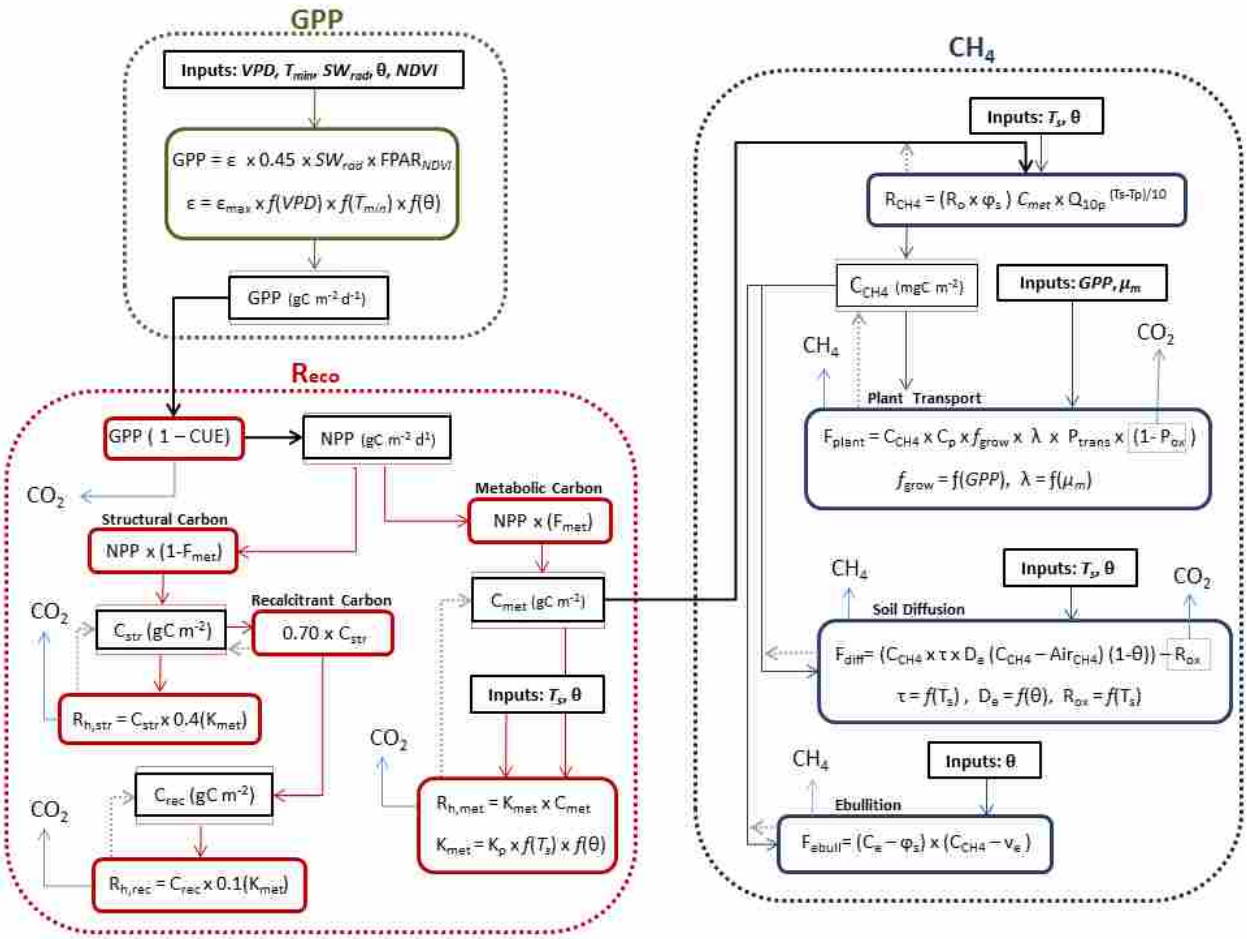

Figure S4.1 TCF model flow diagram for GPP (in green), R_{eco} (in red) and CH_4 (in blue) modules. Rectangular boxes denote primary environmental inputs (single border) or model derived stored carbon pools (double border) including C_{met}, C_{str}, C_{rec} and C_{CH4}. Rounded rectangles indicate major process calculations, and arrows show the direction of data flow. The dashed lines specify where pool updates occur at daily time steps to account for carbon losses.

Chapter 5: Regional and longer-term variability in northern high latitude wetland ecosystem carbon budgets

Corresponding publication:

Watts J D, J S Kimball, R Commane, D Zona, M Helbig, D Olefeldt, F J W Parmentier, T Sachs, L Bruhwiler, O Sonnentag, E Euskirchen, J Kochendorfer, E Humphreys, D Nadeau, J Rinne, M Lund, T Tagesson, M Jackowicz-Korczynski, W C Oechel, M Aurela, M Ueyama, et al. (In Prep.) Regional and longer-term variability in the northern high latitude wetland carbon budget. For submission to *Global Change Biol*.

5.1 Abstract

High latitude warming and changes in wetland hydrology is expected to substantially impact the northern terrestrial net ecosystem carbon balance, particularly in thawing permafrost affected landscapes. Changing environmental conditions may result in divergent responses observed in gross primary productivity (GPP), ecosystem respiration (Reco) of carbon dioxide (CO_2), net ecosystem CO_2 exchange (NEE; GPP – Reco) and methane (CH_4) emissions. Seasonal CH_4 losses are also expected to drastically shift net ecosystem carbon budgets (NECB) from net carbon sink to carbon source, unless terrestrial warming is mitigated by a coinciding decrease in landscape wetness. Here we examine recent (yrs. 2003-2015) wetland carbon budgets and corresponding changes in carbon flux components for the Arctic-boreal region. To do this, we compiled eddy covariance flux records from 36 high latitude tower sites. We also use an enhanced Terrestrial Carbon Flux (TCF) model developed for satellite remote sensing applications, with input MODIS remote sensing and reanalysis data. The resulting daily 1-km TCF model simulations had low RMSE uncertainties of 0.97 gC m^{-2} d^{-1} (NEE) and 21 mgC m^{-2} d^{-1} (CH_4) relative to the tower records. Model results indicate a net ecosystem carbon sink in tundra and boreal wetlands with respective average NEE values of -4 and -96 gC m^{-2} yr^{-1}. Accounting for NECB (NEE + CH_4) reduced the overall boreal wetland carbon sink by 20% and shifted tundra from carbon sink to carbon source (NECB = 1.6 gC m^{-2} yr^{-1}). Although the 13-yr TCF model flux records did not show significant ($\alpha = 0.05$) change in annual GPP, Reco, NEE and NECB across the tower sites, boreal wetlands experienced a significant increase in CH_4 flux (1.9 gC m^{-2} yr^{-1}; $p < 0.0001$) with higher increases occurring in non-forested boreal wetlands. This

study suggests that the continued monitoring of NECB in Arctic-boreal ecosystems through the integration of tower flux measurements, ecosystem models and satellite remote sensing is critical to determining the vulnerability of high latitude ecosystems to climate change.

5.2 Introduction

Northern permafrost landscapes store approximately 1 billion tonnes of carbon in the upper (1-3 m depth) soil layers, representing over a third of the global soil carbon pool (Schuur *et al*. 2015). Under a high warming scenario, soil thaw and subsequent decomposition of these stored organic materials could release carbon to the atmosphere at a magnitude comparable to current global deforestation rates (> 200 billion tonnes C-CO_2-eq by 2100), with a 2.5 times greater overall effect on climate if substantial methane (CH_4) release coincides with CO_2 (Zimov *et al*. 2006, Schuur & Abbott 2011). Warmer summers (Christensen *et al*. 2004, Åkerman *et al*. 2008) and a decreasing winter frozen period (Webb *et al*. 2016, Zona *et al*. 2016) in northern high latitudes will continue to increase the vulnerability of boreal and tundra ecosystems to changes in climate. However, these changes will likely vary geographically with divergent community response characteristics (Hinzman *et al*. 2005, Ernakovich *et al*. 2014, Bahn *et al*. 2015) influenced by plant species composition (Parmentier *et al*. 2011, Bjorkman *et al*. 2015, Davidson *et al*. 2016), local hydrology, snowpack and snowmelt (Bintanja & Selten 2014, Karlsson *et al*. 2015, Liljedahl *et al*. 2016, Wrona *et al*. 2016), fires and pest outbreaks (Helbig *et al*. 2016a, Loranty *et al*. 2016, Young *et al*. 2016), regional differences in warming patterns (Screen & Simmonds 2010, Serreze & Barry 2011, Walsh 2014) and active layer thaw depth (Pastick *et al*. 2015, Atchley *et al*. 2016).

High latitude warming might increase ecosystem carbon uptake by reducing cold-temperature constraints on plant carbon assimilation and growth (Elmendorf *et al*. 2012, Cahoon *et al*. 2016), yet recent studies show that earlier snowmelt and longer surface non-frozen seasons do not necessarily result in higher net plant productivity and carbon gain (Parmentier *et al*. 2011, Bjorkman *et al*. 2015) due to phenological constraints and frozen soil conditions that limit root growth. Plant response to warming is also species specific and can be influenced by environmental changes (e.g. wetting or drying, nutrient availability, species competition) that co-

occur with warming (Kremers *et al*. 2015). Boreal forest communities, carbon sinks in past decades, are increasingly shifting towards net carbon sources for atmospheric CO_2 following increases in autotrophic respiration under warmer summer temperatures (Hadden & Grelle 2016) and drought stress (Bond-Lamberty *et al*. 2013, Reichstein *et al*. 2013). Although regional wetting may increase boreal plant productivity, carbon uptake through photosynthesis may also decrease in regions experiencing increasing cloud cover and more limited light availability (Öquist *et al*. 2014). Boreal forest conversion to wetlands following permafrost thaw, and landscape waterlogging, can further increase ecosystem carbon (CO_2 + CH_4) source activity due to heightened CH_4 emissions (Helbig *et al*. 2016b, 2016c).

Soil respiration, and release of CO_2 to the atmosphere, in high latitude environments is regulated by the availability of carbon substrates from recent plant litter and organic materials stored in soil (Wagner *et al*. 2009, Olefeldt *et al*. 2013), soil temperature and frozen water conditions (Davidson & Janssens 2006, Zona *et al*. 2016), and shifts in soil wetness (Watts *et al*. 2014, Schuur *et al*. 2015). Warmer and wetter soil environments generally favor production of CH_4 (Turetsky *et al*. 2008, Treat *et al*. 2015), a greenhouse gas with an atmospheric warming potential 25 times more potent than CO_2 over a 100-yr time scale (Boucher *et al.* 2009). However, a recent synthesis of soil carbon incubation studies suggests that the form of carbon emitted from warming northern soils will be dominated by CO_2, resulting from more rapid soil decomposition under aerobic conditions (Schädel *et al*. 2016). Nonetheless, CH_4 emissions from northern wetlands are expected to significantly impact high latitude ecosystem carbon budgets, amplifying greenhouse gas contributions to atmospheric warming and shifting landscapes closer to net carbon source (Chang *et al*. 2014, Schuur *et al*. 2015, Natali *et al*. 2015).

Improvements in near surface trace gas sampling through portable and automatic flux chambers (Christensen *et al*. 2000, Elberling & Brandt 2003, Mastepanov *et al*. 2008), and eddy covariance flux towers (Baldocchi *et al*. 2001, Zona *et al*. 2016) provide systems capable of measuring landscape CO_2 and CH_4 exchange in often remote and rugged high latitude environments. Flux operations in northern Arctic and boreal environments remain challenged by harsh working conditions, high expenses for power supplies and transportation, and a lack of physical support needed for equipment maintenance (Baldocchi & Koteen 2012, Zona *et al*.

2016). Hence, chamber and flux measurements collected from remote environments often span only a summer season, and rarely extend through the winter (Zona *et al*. 2016); funding limitations often make it difficult to sample gas fluxes at a site for longer than a 2 to 3-year period. In consequence, the combined use of ecosystem models and eddy covariance observations is necessary to obtain more robust NECB estimates spanning larger regions and multi-year periods, and to improve understanding of the ecosystem controls that regulate vegetation and carbon cycling in vulnerable northern environments (Abbott *et al*. 2016).

Here we use a satellite data driven terrestrial carbon flux (TCF) model developed for northern wetland regions (Watts *et al*. 2014a), updated to include additional parametrizations of ecosystem functional type, and eddy covariance data collected from 36 towers across the northern high latitude (> 45 °N) region. Tower eddy covariance records are used in this study as the data represent a larger (>300-500 m^2) footprint relative to flux chambers (~1-m^2) (Davidson *et al*. 2016). We use the combined observations and TCF model outputs at a 1-km spatial resolution to assess carbon (CO_2 and CH_4) fluxes, underlying environmental controls, and recent changes in the net ecosystem carbon budget (CO_2 + CH_4; NECB) over a 13-yr period from 2003 to 2015. The NECB components include vegetation gross primary productivity (GPP), autotrophic respiration (Ra), soil heterotrophic respiration (Rh), and associated impacts on CO_2 and CH_4 emissions.

5.3 Methods

5.3.1 Flux tower CO_2 and CH_4 sites

Eddy covariance flux tower data were obtained for 36 tundra and boreal wetland sites (Figure 1) across the northern Arctic-boreal region, including Alaska, Canada, Greenland, Scandinavia and Russia. These data represent 52 individual flux records collected over years 2003-2015 (Table S5.1, Supplement) and regional gradients in permafrost conditions across the Arctic-boreal landscape. The records characterize the terrestrial carbon cycle for ecosystems having underlying continuous (14 sites), discontinuous (6 sites) and sporadic/isolated (2 sites) permafrost and seasonal surface active layer thaw depths varying from -20 cm below the surface (e.g. Greenland, Russia and North Slope Alaska) to > -70 cm (e.g. Scandinavia and boreal Alaska).

The remaining 14 tower sites are located outside the permafrost zone but experience seasonal freezing of the surface and root zone soil profile. Vegetation communities at the Arctic tundra tower sites include wet sedge, tussock, shrub-encroached tussock and dry heath. Vegetation at the non-tundra sites includes forested and non-forested boreal peatland and fen sites. Forest sites include black spruce (*Picea mariana*), larch (e.g *Larix sibirica*), birch and pine with a mixed understory that often includes moss. The dominant vegetation communities at the tower sites are listed in the Supplement (Tables S5.1, S5.2), along with corresponding publications that more fully describe site characteristics.

The eddy covariance flux records include ½ hourly NEE measurements partitioned into GPP and Reco components using methods deemed appropriate (e.g. Stoy *et al*. 2006, Lasslop *et al*. 2010, Reichstein *et al*. 2012) by the tower principal investigators. In addition to CO_2 flux, 15 of the sites also included ½ hourly CH_4 flux measurements. To correspond temporally with the mean daily TCF model estimates, the ½ hr fluxes were averaged per 24-hr period time step across the data records.

5.3.2 TCF model estimates for tower sites

5.3.2.1 TCF model description

The TCF model was developed as a precursor to the NASA Soil Moisture Active Passive (SMAP) mission Level 4 Carbon (L4_C) algorithms used to diagnose and reduce uncertainty in global terrestrial carbon budgets (Kimball *et al*. 2009, Kimball *et al*. 2016). The TCF model utilizes inputs from satellite optical-IR remote sensing (e.g. MODIS) to infer changes in surface vegetation cover and the fraction of photosynthetic active radiation (FPAR) absorbed during photosynthesis. The TCF model also readily incorporates microwave sensor data on surface soil thermal and moisture conditions, including water inundation, that affect carbon cycle processes. Ancillary meteorology inputs are used in the model to define daily incoming shortwave solar radiation (SW_{rad}; W/m^2), atmosphere vapor pressure deficit (VPD; Pa), near-surface (2 m) wind velocity (m/s; μ_m), air and soil temperature (°C), and root zone (up to 1m depth) soil moisture (m^3/m^3).

The TCF model is summarized here; a detailed description can be found in Watts *et al*. (2014a). Vegetation GPP is estimated in the model as the product of canopy absorbed photosynthetically active radiation (APAR, MJ m^{-2} d^{-1}) and a light use efficiency term (ε, g C MJ^{-1}) describing the conversion of APAR to vegetation biomass. Canopy FPAR is provided from MODIS (MOD15A2) inputs and can also be derived from lower-order vegetation indices (e.g. NDVI; Watts *et al*. 2014a). Photosynthetically Active Radiation (PAR) is defined as a fixed proportion of SW_{rad}, and multiplied by FPAR to derive APAR. Light use efficiency is determined from optimum ε rates specific to model plant functional types (PFT); these are reduced under sub-optimal environmental, thermal and moisture conditions. Controls on ε are defined using remote sensing and meteorology inputs, and include microwave derived landscape freeze-thaw status (FT; Kim *et al*. 2014), surface to root zone soil moisture (SM_{RZ}), soil or air temperature (T_s, T_a) and VPD (Watts *et al*. 2014a, Kimball *et al*. 2016). The start and end of the season for active vegetation growth (GPP) in the TCF model is constrained by microwave FT fields describing binary surface frozen (0) or non-frozen (1) states, in addition to inputs from T_a and T_s. For non-coniferous vegetation, the TCF model GPP remains inactive until at least six consecutive days of FT (1) is achieved; this step is taken to help reduce premature growing season onset in the modeled GPP fluxes (Watts *et al*. 2014a)

TCF daily CO_2 loss from R_{eco} under aerobic conditions is determined as the sum of autotrophic (R_a) and heterotrophic (R_h) respiration in near-surface litter and soil layers. A portion of daily net primary production (NPP; GPP-R_a) is allocated to metabolic (C_{met}), structural (C_{str}) and recalcitrant (C_{rec}) soil organic carbon (SOC) pools using a dynamic litterfall turnover scheme (Kimball *et al*. 2009, Watts *et al*. 2014a). The C_{met} pool represents easily decomposable plant residue and root exudates; C_{str} includes litter residues including hemi-cellulose and lignin; C_{rec} accounts for more slowly decomposing physically and chemically stabilized carbon and humified peat. Ecosystem R_h losses from soil decomposition of C_{met}, C_{str} and C_{rec} are regulated using dimensionless temperature and moisture multipliers (Watts *et al*. 2014a) that vary between 0 (fully constrained) and 1 (no constraint) as informed by daily input T_s and SM_{RZ}. Net ecosystem CO_2 exchange (NEE; gC m^{-2} d^{-1}) is determined as the residual difference between R_{eco} and GPP.

A CH_4 emissions algorithm was added to the TCF model to account for anaerobic carbon loss in northern wetland environments (Watts *et al*. 2014a, Zona *et al*. 2016). The model estimates daily CH_4 production according to T_s, SM_{RZ} and substrate availability from SOC pools within a one-dimensional soil profile for more direct implementation of remote sensing inputs and to simplify model parameterization for regional simulations (Watts *et al*. 2014a). Transfer of CH_4 from the soil to the atmosphere occurs through vegetation, soil diffusion and water ebullition pathways. Methanogenesis occurs within the saturated soil pore volume per a biome specific optimal production CH_4 rate, the availability of labile photosynthates (Ström *et al*. 2003, Olefeldt *et al*. 2013) and a soil Q_{10} modifier used to describe the temperature dependence of biological processes. Oxidation (conversion of CH_4 to CO_2) is accounted for during plant transport using a PFT specific scalar; for the soil diffusion pathway a Michaelis-Menten kinetics approach scaled by aerated pore space is used to regulate methantrophy (Watts *et al*. 2014a).

5.3.2.2 Updates to the TCF model for Arctic-boreal wetlands

The original TCF model (Kimball *et al*. 2009) and SMAP L4_C model parameter Look-Up-Table (LUT) logic (Kimball *et al*. 2016) is based on global MODIS Land Cover (MCD12Q1 Type 5) vegetation classes (e.g. Friedl *et al*. 2010). These LUT classes represent up to eight global plant functional type (PFT) classes, including evergreen and deciduous forests, shrubland, grassland, and cereal/ broadleaf cropland. The adjusted TCF wetlands model expands the PFT parameter table to better represent northern vegetation and wetland types. The initial LUT enhancement described in Watts *et al*. (2014a) included the addition of two general wetland classes: tundra and peatland. A new expanded TCF model LUT for the northern latitudes includes classes for shrub peatlands, forested peatlands, non-peatland permanent wetlands, barren tundra, shrub tundra, wet sedge tundra, and tussock tundra. The vegetation community types used to guide development of the updated TCF model LUT classes (Table S5.2) are derived from an expanded northern vegetation map (Figure 1) obtained from merged classifications using the 300-m resolution ESA CCI-LC 2010 Epoch land cover product (Kirches *et al*. 2014), the Circumpolar Arctic Vegetation Map (CAVM; Walker *et al*. 2005) and a high latitude peatland vegetation map (Watts *et al*. 2014b). The merged land cover map was re-

projected to a 1-km Equal Area Scalable Earth Grid Version 2 (EASE2) format with the WGS 84 ellipsoid (Brodzik *et al*. 2012). The land cover classes were assigned to each flux tower site based on the 1-km resolution grid cell overlying the central tower locations. An additional modification to the TCF model was the use of T_s to regulate carbon assimilation activity in the GPP module instead of T_a as had been used in prior TCF model simulations (Watts *et al*. 2014a). This step was taken as the high latitude GPP start-of-season is affected by the onset of spring thaw in frozen soil layers, which is correlated with bud break activity (Van Wijk *et al*. 2003, Euskirchen *et al*. 2006, Parmentier *et al*. 2011).

5.3.2.3 TCF model meteorology and remote sensing inputs

Daily input meteorology was obtained from the Goddard Earth Observing System Data Assimilation Version 5 (GEOS-5) MERRA archive (Rienecker *et al.* 2011) with 1/2 x 2/3° spatial resolution. In addition to near surface (≤ 10 cm) T_s and root zone θ information from the MERRA-Land reanalysis (Reichle *et al*. 2011) required for the R_{eco} and CH_4 simulations, daily MERRA SW_{rad}, T_{min} and VPD records were used to drive the internal GPP calculations. The MERRA near-surface (2 m) wind parameters were also used to obtain mean daily μ_m for the CH_4 simulations. The GEOS-5 data were re-projected from geographic lat./lon. to a 1-km EASE2 grid for input into the TCF model.

For the daily LUE-based GPP simulations, quality screened cloud-filtered 4-day 1-km FPAR values from MODIS MCD15A3 combined Terra and Aqua data records (Knyazikhin *et al.* 1999) were used as model inputs. The 4-day FPAR product is especially useful for monitoring high latitude environments due to rapid changes in vegetation growth occurring during the relatively short Arctic-boreal non-frozen season. The MCD15A3 records were converted from Sinusoidal grid to a 1-km EASE2 grid using Geospatial Data Abstraction Library for Python (GDAL 2.1.0). The resulting MCD15A3 data were gap-filled using a simple linear interpretation method. The spatially coarse 1-km FPAR values are used in this study rather than the 250-m FPAR derived from vegetation indices as described in Watts *et al*. (2014a) to more readily facilitate TCF model extrapolation from tower locations to the greater Arctic-boreal domain.

5.3.2.4 TCF model simulations

TCF model simulations were conducted for each tower site using reanalysis SW_{rad}, $T_{min,}$ VPD, SM_{RZ}, T_s, μ_m and input satellite FT (Kim *et al*. 2014) over the 2003-2015 period. The parameter values associated with TCF model GPP, Reco and CH_4 simulations are provided in the Supplement (Tables S5.3-5.5). Baseline carbon pools were initialized by continuously cycling ("spinning-up") the model using reanalysis inputs over a 14-yr period (1989 to 2002) to reach a dynamic steady-state between estimated NPP and surface SOC stocks (Kimball *et al*. 2009, Watts *et al*. 2014a). The resulting baseline SOC stocks were used as inputs in the 2003-2015 forward model simulations. The TCF model is designed to use reanalysis and satellite remote sensing input data representing the near-surface soil profile (> 30 cm) and more recent SOC accumulation in surface layers (~10 cm depth). This assumption is adequate for investigations of contemporary ecosystem flux variability, but may not be appropriate for multi-decadal analyses and studies of carbon loss from highly disturbed landscapes where deeper soils become exposed to near-surface processes.

5.3.2.5 TCF model assessment & site NECB trends

The temporal agreement between the tower EC records and TCF model simulations was assessed using mean residual error (MRE) between the tower eddy covariance records and TCF modeled CO_2 and CH_4 fluxes to identify potential positive (underestimation) and negative (overestimation) biases in the simulations; root-mean-square-error (RMSE) differences were used as a measure of model estimate uncertainty in relation to the tower EC records. Regression analysis was also used to ascertain which environmental predictor variables (e.g. land cover, mean annual precipitation and T_a, mean daily T_a and T_s, soil thaw depth) were significantly associated ($\alpha = 0.05$) with changes in mean daily tower eddy covariance flux estimates for NEE, Reco, GPP and CH_4 emissions. In situ soil moisture was not available for all tower sites and was not included in the multiple regression analysis. Finally, a Mann–Kendall trend test (Watts *et al*. 2012) was applied to the TCF model estimated annual totals for GPP, Reco, NEE, CH_4 emissions, and the NECB (NEE + CH_4) to determine trend direction and significance (here we use $\alpha = 0.1$) for ecosystem carbon fluxes over the 13-yr time period. The trend tests were applied

for the individual tower sites and TCF model records aggregated across tundra and boreal wetland vegetation communities.

5.4 Results

5.4.1 Site eddy covariance flux characteristics

Linear regression analysis indicates that thaw depth (cm), mean annual T_a (°C) and mean daily T_a and T_s (°C) contribute significantly ($p < 0.05$) to the regulation of mean daily NEE (gC m^{-2}) fluxes in Arctic-boreal environments (Table 5.1; Figure 5.2). Land cover, though not significant ($p = 0.09$), was also an important predictor in the model. Mean annual precipitation was not a significant predictor ($p = 0.7$) of daily NEE flux. All input environmental explanatory variables were significant for GPP when considering an α level of 0.1 (all variables sans thaw depth had p-values < 0.05). All explanatory variables were significant ($p < 0.01$) in explaining mean daily Reco. For model CH_4 emissions, land class, thaw depth, mean annual precipitation, mean annual T_a and mean daily T_s were significant at $p < 0.05$; daily T_a was not a significant predictor. For the GPP, Reco and CH_4 models, the predictor variables explained 50% ($R^2 = 0.5$) of the variability in carbon flux; however, for NEE the R^2 was substantially lower at 28%.

In general, the monthly summer (June-August) tower based GPP flux sums were larger (by a factor of 2.5) for boreal wetland landscapes (-143.6 $\pm$ 57 gC m^{-2} mon^{-1}; Figure 5.2) relative to the tundra land cover types included in this study (-57.7 $\pm$ 33 gC m^{-2} mon^{-1}), resulting from longer growing season length, warmer T_s and an absence of permafrost. Boreal GPP was larger in needleleaf/peatland and mixed forest/peatland (land classes 45, 47, 49) with monthly fluxes exceeding 300 gC m^{-2}. Monthly summer Reco flux sums for boreal wetlands (98 $\pm$ 35 vs. 41 $\pm$ 21 gC m^{-2} mon^{-1}) were more than twice as large relative to tundra. Reco was largest for the evergreen needleleaf forest/peatland and mixed needle/broadleaf/peatland landscapes (respective land classes = 45 & 49; Table S5.2).

Mean monthly NEE sink strength, however, was only slightly larger (by a factor of 1.4; -37 $\pm$ 12 gC m^{-2} mon^{-1}) for boreal wetland systems relative to tundra (-25 $\pm$ 20 gC m^{-2} mon^{-1}). Monthly CH_4 fluxes were also larger for boreal wetlands (1.8 $\pm$ 0.69 gC m^{-2} mon^{-1}) compared to

tundra (0.8 ± 0.41 gC m^{-2} mon^{-1}). The CH_4 emission magnitudes were highest for the Scandinavian shrub/herbaceous non-tundra wetlands (land class = 19) characterized by discontinuous or an absence of permafrost, and minimal forest cover in the flux tower footprint. Higher CH_4 fluxes were also observed for dwarf shrub/tussock tundra (land class = 28) found at Ivotuk, Alaska and Zackenberg, Greenland, although the temporal period of release at these sites was limited over a short time span (weeks to ~2 months) due to extended frozen soil conditions.

5.4.2 Comparison of TCF model simulations with flux measurements

The resulting TCF model simulations agree well with the tower observed GPP, Reco, NEE and CH_4 eddy covariance fluxes (Figures 5.3, 5.4). The TCF daily fluxes replicate the carbon sink/source patterns observed over Arctic-boreal wetland tower sites (Figure 5.5), with peak CO_2 and CH_4 emissions occurring in July and August and persisting throughout the winter at trace levels (~ 0.02-0.4 gC for Reco and 10-20 mgC for CH_4). The TCF model estimates, however, do not capture occasional episodic CO_2 and CH_4 loss from soils to the atmosphere that can occur following spring ice-off and autumn re-freeze events (e.g. Ivotuk tundra and Tanana Flats Bog, Alaska; Figure 5.2). The TCF model also estimates a GPP start-of-season occurring 3 to 6 days prior to GPP records obtained from tower eddy covariance data (e.g. Figure 5.2) even with the input satellite FT surface observations, and could reflect the coarse 4-day MODIS FPAR compositing. The premature GPP estimates are more prevalent for colder boreal and tundra ecosystems where cold surface soil conditions and residual snow cover constrain the timing of annual vegetation leaf-out activity.

A TCF algorithm error (RMSE) analysis for the Arctic-boreal flux tower sites, relative to the eddy covariance record observations, demonstrates carbon flux retrieval accuracy within targets specified by global satellite based carbon model guidelines (Kimball *et al*. 2016) and prior Arctic model investigations (Watts *et al*. 2014a). The RMSE uncertainty (Table 5.2) for NEE at the flux tower sites are 0.97 ± 0.46 gC m^{-2} d^{-1}, and is similar to that reported in Watts *et al*. (2014a) for model simulations using MERRA reanalysis and 250-m MODIS vegetation index inputs. The corresponding RMSE values for GPP and Reco are 1.08 ± 0.44 and 0.85 ± 0.49 gC m^{-2} d^{-1}, respectively. For CH_4, TCF model RMSE uncertainty values of 21 ± 12 mgC m^{-2} d^{-1} are also similar to those reported in prior studies (Watts *et al*. 2014a, 2014b). Corresponding MRE values

for the tower sites are 0.04 ± 0.43, 0.01 ± 0.27 and 0.13 ± 0.39 gC m^{-2} d^{-1} for respective NEE, GPP and Reco fluxes indicating that, on average, the model is slightly underestimating CO_2 fluxes relative to the eddy covariance data. For CH_4 the MRE is -0.65 ± 5.93 mgC m^{-2} d^{-1}.

5.4.3 Annual TCF model flux budgets

The 13-yr (2003-2015) TCF model flux record indicates that boreal wetlands had the largest total annual NEE (-96 ± 86 gC m^{-2} yr^{-1}) which results from a longer non-frozen period, increasing the GPP CO_2 sink (-618 ± 246 gC m-^{2} yr^{-1}). Forested wetlands, on average, had larger NEE sink strength (-122 ± 99 gC m^{-2} yr^{-1}) relative to non-forested boreal wetlands (-72 ± 65 gC m^{-2} yr^{-1}), attributed to the longer growing season for conifers (boreal wetland GPP = -493 ± 194 vs. 757 ± 222 gC m^{-2} yr^{-1} for forested wetlands). Boreal Reco averaged 554 ± 245 gC m^{-2} yr^{-1}, with 435 ± 202 gC m^{-2} $yr^{-1}$for non-forested wetlands and 690 ± 223 gC m^{-2} $yr^{-1}$for forested wetlands.

The tundra sites experienced a small annual NEE sink (-4 ± 37 gC m^{-2} yr^{-1}). Although the extended frozen season and relatively short (2-4 month) summer period at the tundra sites limited soil decomposition (Reco = 222 ± 92 gC m^{-2} yr^{-1}), the cold climate also greatly constrained vegetation GPP (-226 ± 96 gC m^{-2} yr^{-1}), thereby reducing the annual CO_2 sink.

Annual release of CH_4 from the boreal sites averaged 23 ± 26 gC m^{-2} yr^{-1}. The CH_4 emissions from non-forested wetlands were 25 ± 32 gC m^{-2} yr^{-1}, slightly higher than the forested wetland sites (18 ± 13 gC m^{-2} yr^{-1}). Tundra CH_4 emissions were substantially less, at 7 ± 4 gC m^{-2} yr^{-1}. When considering NEE + CH_4 loss, boreal wetland NECB was -79 ± 90 gC m^{-2} yr^{-1}; this reduced net ecosystem carbon sink strength by 19% relative to NEE. Partitioning boreal non-forest wetlands and forested wetlands, NECB values were -51 ± 68 gC m^{-2} yr^{-1} and -105 ± 101 gC m^{-2} yr^{-1}, respectively. The tundra NECB was 1.6 ± 31 gC m^{-2} yr^{-1}, resulting in net ecosystem carbon loss as opposed to being a small carbon sink when considering only NEE. Factoring in an enhanced atmospheric forcing potential for CH_4, at least 25 times that of CO_2 over a 100-year time period, the boreal wetlands had an average global warming potential (GWP) of 472 ± 640 g CO_2eq m^{-2} yr^{-1} (607 ± 815 g CO_2eq m^{-2} yr^{-1} for non-forested and 336 ± 348 CO_2eq m^{-2} $yr^{-1}$for forested wetlands). For tundra the GWP was 156 ± 93 g CO_2eq m^{-2} yr^{-1}.

5.4.4 Trends in NECB and component fluxes

A generalized grouping of ecosystem types (e.g. boreal wetland; boreal forested wetland; boreal non-forest wetland; tundra) shows a slight decline in boreal GPP from 2005-2013, followed by an increase in yrs. 2014-2015 (Figure 5.6). Boreal Reco was relatively stable during this period, but increased considerably in 2014-2015 (~ 100 gC m^{-2}) in the forested wetlands following a short decline in 2013. The tundra wetlands had substantial year-to-year variability in GPP and Reco, with a decrease in GPP occurring from 2008-2009 and 2010-2014, followed by an increase in 2015. The combined GPP and Reco response over the 13-yr period in boreal wetlands shows a decrease in NEE (less carbon sink) from 2003-2009, followed by a stabilization in 2010-2013, and then an increase in NEE from 2014-2015. The tundra wetlands show something similar, with NEE decreasing from 2003-2013, followed by an increase from 2014-2015. Wetland CH_4 emissions from boreal sites increased steadily over yrs. 2003-2015. In tundra, CH_4 was relatively stable with a small increase in 2007.

The Mann Kendall trend results for TCF model annual flux sums, averaged according to general ecosystem type, indicate a lack of trend significance ($\alpha = 0.1$) for NEE and Reco when considering the 36 Arctic-boreal sites (Table 5.3). However, the boreal wetlands did show a significant increase in CH_4 flux during the 13-yr period with higher increases and greater trend significance occurring for the non-forested boreal wetland sites (1.9 gC m^{-2} yr^{-1}; $p < 0.0001$). The boreal forested wetlands also showed a significant decrease in GPP flux (9.9 gC m^{-2} yr^{-1}; $p = 0.08$). Increasing annual CH_4 emissions in the non-forested boreal wetlands decreased the NECB (7.1 gC m^{-2} yr^{-1}; $p = 0.08$) during the observation period.

Mann Kendall trend tests for the individual tower sites reveal contrasting flux response over the 13-yr period based on geographic location and land cover type (Figure 5.7). Ten of the 36 tower sites had a significant ($p < 0.1$) increase in annual Reco from 2003-2015 (i.e. site numbers 1, 2, 8, 9, 13, 20, 28, 30, 31, 32; see Table S5.1). Five towers had significant increases in annual GPP (site numbers 17, 28, 29, 33, 34) whereas two sites showed a decrease in GPP (3, 18). Only four sites revealed an overall decrease in annual NEE CO_2 sink (i.e. sites 6, 10, 19, 36) and included two Alaska North Slope tussock and sedge sites, a sedge fen in Finland, and a boreal peat site in

Manitoba, Canada. For CH_4, eight sites showed an increase in annual emissions (i.e. 13, 18, 20, 21, 23, 25, 28, 32); one site showed a decrease (i.e. 9).

5.5 Discussion & conclusion

This study investigates recent (yrs. 2003-2015) changes in Arctic-boreal carbon fluxes and NECB using flux observations obtained from 36 high latitude eddy covariance tower sites and 13-yr records of daily 1-km resolution NEE, GPP, Reco, CH_4 and NECB simulations from an enhanced satellite data driven TCF model developed for northern wetland regions.

The TCF model estimates are in close agreement with the tower observed NEE and CH_4 eddy covariance fluxes, and replicate the carbon sink/source patterns observed over Arctic-boreal wetland tower sites. The RMSE uncertainty for NEE at the flux tower sites (0.97 ± 0.46 gC m^{-2} d^{-1}) is comparable to other model simulations using MERRA reanalysis and MODIS inputs (Watts *et al*. (2014a). The RMSE uncertainty for CH_4 (21 ± 12 mgC m^{-2} d^{-1}) is also similar to those reported in prior studies (Watts *et al*. 2014a, 2014b). The higher RMSE values for NEE (> 1.2 gC m^{-2} d^{-1}) observed for some Arctic sites result from a seasonal mismatch between reanalysis and site T_s (e.g. Imnavait hillslope tussock in Alaska and Zackenberg wet fen tundra in Greenland). High RMSE values for NEE also occur for a NOAA North Slope (Deadhorse area) tower site in Alaska, resulting from recent large, localized increases in active layer depth (and T_s) that are not reflected in the coarse 0.5° resolution MERRA reanalysis records. Similar temperature mismatch may also contribute to the higher RMSE values observed at the Scotty Creek boreal bog in the Canadian NWT where permafrost thaw and thermokarst activity has resulted in warmer soil conditions and waterlogging relative to adjacent landscapes (Helbig *et al*. 2016b). However, the higher model estimate uncertainty for these ecosystems is still within the range of acceptable error for northern high latitude systems (Marushchak *et al*. 2013, Kimball *et al*. 2016).

Although the TCF model performs well in simulating the seasonal NEE patterns at these sites, the model does not capture episodic CO_2 emission events occurring during spring thaw when CO_2 trapped in frozen soils is released following surface ice and snow melt (e.g. as observed at Tanana Flats). This episodic release can also occur during the autumn freeze, when contracting soils push CO_2 (and CH_4) stored at depth towards the surface (Mastepanov *et al*.

2008). Representing these episodic processes would require an increase in model complexity and the addition of multiple soil layers and a heat transfer model, and is beyond the intended scope of the satellite data driven TCF model framework.

The regulating effect of environmental conditions on carbon flux is evident in the Arctic-boreal tower site records and the TCF model simulations. Higher monthly NEE loss occurred at permafrost sites where thaw depths ranged between -40 and -50 cm below the surface, reflecting a priming effect on respiration as deeper stored SOC became available for microbial activity, offsetting vegetation GPP (Schuur *et al*. 2015, Schädel *et al*. 2016). Continuing permafrost thaw also facilitates sub-surface drainage and drying of the surface soil layers. The drier surface soils support warmer, aerobic conditions which accelerate microbial decomposition rates and CO_2 loss (Watts *et al*. 2014a). This priming effect at summer thaw depths near -40 cm was also observed in the tower records for CH_4 but began to decrease with further active layer deepening if soil drainage occurred. Overall, a decrease in CO_2 sink (more positive NEE) resulted when cooler T_s and T_a temperatures limited GPP and the offset of CO_2 loss from Reco, or warmer conditions (monthly average air temperatures > 17°C) resulted in drier soil conditions which heightened Reco and reduced GPP. These response characteristics have been reported elsewhere (Parmentier *et al*. 2011, Sturtevant & Oechel 2013). Ecosystem CH_4 emissions from the observed Arctic-boreal landscapes were relatively minimal at temperatures below 0°C but increased substantially at or above 0°C, reflecting the strong temperature sensitivity of methanogens (Watts *et al*. 2014a, 2014b; Zona *et al*. 2016).

This investigation indicates that tundra landscapes are particularly vulnerable to shifts from classification as net carbon (NECB) sink to net carbon source when accounting for annual CH_4 emissions in addition to NEE. Tundra NEE showed a very minimal average carbon sink (-4 ± 37 gC m^{-2} yr^{-1}) during yrs. 2003-2015. The corresponding NECB was 1.6 ± 31 gC m^{-2} yr^{-1}, shifting tundra to a net carbon source. At some tundra tower sites, CH_4 emissions in the wet and warm years of 2008 and 2012 offset the already minimal NEE sink by 200-500%. With continued climate warming the relatively low annual CO_2 uptake through GPP in tundra environments is less likely to offset microbial decomposition of SOC, especially given the lessening cold temperature protection of stored labile carbon substrates (Watts *et al*. 2014a,

2014b, Zona *et al*. 2016). In contrast, the boreal wetland sites have much higher magnitudes of annual GPP and stronger (more negative) NEE sink (-96 $\pm$ 86 gC m^{-2} yr^{-1}). Yet, a 20% reduction in carbon sink (NECB -76 $\pm$ 90 gC m^{-2} yr^{-1}) was evident at the boreal sites when accounting for carbon loss as CH_4. When considering the 25-times higher atmospheric warming potential for CH_4 (Boucher *et al.* 2009), all ecosystems showed an average positive GWP (472 $\pm$ 640 g CO_2eq m^{-2} yr^{-1} for boreal forests and 156 $\pm$ 93 g CO_2eq m^{-2} yr^{-1} for tundra).

Change in NEE sink activity for the Arctic-boreal tundra was not significant ($p > 0.19$) during the 2003-2015 yr. period, nor were the observed changes in Reco ($p > 0.45$), GPP ($p > 0.08$) and the NECB ($p > 0.08$). However, boreal wetlands did show significant increase in CH_4 ($p < 0.05$) resulting from warming T_s and CH_4 sensitivity to changing thermal conditions, an increasing annual non-frozen season, and sufficient soil wetness and landscape inundation to support anaerobic conditions. These results indicate that a lengthening of the surface non-frozen season in Arctic-boreal communities does not necessarily lead to higher net annual CO_2 sink activity due to moisture and vegetation phenology controls on GPP and carbon loss contribution from Reco and CH_4 (Watts *et al*. 2014a). Other studies have reported a similar lack of overall change in ecosystem carbon balance (Marchand *et al*. 2004, Sistla *et al*. 2013) and tundra CH_4 emissions (Miller *et al*. 2016, Sweeney *et al*. 2016) despite northern high latitude warming. Although the trends in regional Reco were not significant, the TCF modeled CO_2 emissions show a steep rise in yrs. 2014 and 2015 that reflect warmer summer temperatures. This reveals a need for further long-term monitoring of these ecosystems to ascertain changes in longer-term soil respiration rates (Watts *et al.* 2014a), especially considering ecosystem surface drying trends that have been observed in localized Arctic-boreal systems (Watts *et al*. 2014b). The indication of trend in CO_2 and CH_4 exchange at individual tower sites, but not in the regional grouping of tundra and boreal wetlands, shows a need for more localized landscape monitoring, in compliment to regional analyses, to understand contrasting ecosystem response to shifting climate and interannual wetting/drying effects.

On-going efforts are needed to better quantify the NECB in Arctic-boreal ecosystems, and to detect contrasting patterns and regional trends in carbon uptake through GPP and carbon loss through CO_2 respiration and wetland CH_4 emissions. Given the limited network of eddy

covariance flux towers in northern high latitude environments, and lack of temporal permanence in flux tower observations, the on-going integration of in situ gas sampling with satellite and airborne remote sensing and ecosystem flux models will be crucial to track changes in carbon balance (Fisher *et al*. 2014, Miller *et al*. 2016, Parazoo *et al*. 2016) and shifts from ecosystem carbon sink to carbon source in tundra and boreal wetlands.

5.6 References

Abbott, B W, J B Jones, E A G Schuur, F S Chapin III, W B Bowden, et al. (2016) Biomass offsets little or none of permafrost carbon release from soils, streams, and wildfire: an expert assessment. *Environ. Res. Lett*., 11: 034014.

Atchley, A L, E T Coon, S L Painter, D R Harp, C J Wilson (2016) Influences and interactions of inundation, peat, and snow on active layer thickness. *Geophys. Res. Lett.*, 43: 5116-5123.

Bahn, M, M Reichstein, K Guan, J M Moreno, C Williams (2015) Preface: climate extremes and biogeochemical cycles in the terrestrial biosphere: impacts and feedbacks across scales. *Biogeosci.*, 12: 4827-4830.

Baldocchi, D, E Falge, L Gu, R Olson, D Hollinger, S Running, P Anthoni, C Bernhofer, K Davis, R Evans, et al. (2001). FLUXNET: A new tool to study the temporal and spatial variability of ecosystem-scale carbon dioxide, water vapor, and energy flux densities. *Bull. Amer. Met. Soc.*, 82: 2415-2434.

Baldocchi, D, L Koteen (2012) Methane flux measurements, new opportunities for FLUXNET. *FluxLetter*, 4: 1-15.

Bergh, J, R E McMurtrie, S Linder (1998) Climatic factors controlling the productivity of Norway spruce: A model-based analysis. *Forest Ecol. Management*, 110: 127-139.

Bintanja, R, F M Selten (2014) Future increases in Arctic precipitation linked to local evaporation and sea-ice retreat. *Nature*, 509: 479-482.

Bjorkman, A D, S C Elmendorf, A L Beamish, M Vellend, G H R Henry (2015) Contrasting effects of warming and increased snowfall on Arctic tundra plant phenology over the past two decades. *Global Change Biol.*, 21: 4651-4661.

Boucher, O, P Friedlingstein, B Collins, K P Shine (2009) The indirect global warming potential and global temperature change potential due to methane oxidation. *Environ. Res. Lett.*, 4: 044007.

Bond-Lamberty, B, A V Rocha, K Calvin, B Holmes, C Wang, M L Goulden (2013) Disturbance legacies and climate jointly drive tree growth and mortality in an intensively studied boreal forest. *Global Change Biol.*, 20: 216-227.

Brodzik, M J, B Billingsley, T Haran, B Raup, M H Savoie (2012) EASE-Grid 2.0: Incremental but Significant Improvements for Earth-Gridded Data Sets. *ISPRS Int. J. Geo-Information*, 1:32-45.

Cahoon, M P, P F Sullivan, E Post (2016) Greater abundance of *Betula nana* and early onset of the growing season increase ecosystem CO_2 uptake in West Greenland. *Ecosystems*, 19: 1149-1163.

Chang, R Y-W, C E Miller, S J Dinardo, A Karion, C Sweeney, B C Daube, J M Henderson, et al. (2014) Methane emissions from Alaska in 2012 from CARVE airborne observations. *PNAS*, 111: 16694-16699.

Christensen, T Friborg, M Sommerkorn, J Kaplan, L Illeris, H Soegaard, C Nordstroem, S Jonasson (2000) Trace gas exchange in a high-Arctic valley: 1. Variation in CO_2 and CH_4 flux between tundra vegetation types. *Global Biogeochem. Cy.*, 14: 701-713.

Christensen, T R, T Johansson, H J Akerman, M Mastepanov, N Malmer, T Friborg, P Crill, Bo H Svensson (2004) Thawing sub-arctic permafrost: effects on vegetation and methane emissions. *Geophys. Res. Lett.*, 31: L04501

Davidson, E A, I A Janssens (2006) Temperature sensitivity of soil carbon decomposition and feedbacks to climate change. *Nature*, 440: 165-173.

Davidson, S J, M J Santos, V L Sloan, J D Watts, G K Phoenix, W C Oechel, D Zona (2016) Upscaling arctic tundra vegetation communities using field spectroscopy and multispectral satellite data in North Alaska, U.S.A. *Remote Sens,* 8: 978-1002.

Elberling, B, K K Brandt (2003) Uncoupling of microbial CO_2 production and release in frozen soil and its implications for field studies of arctic C cycling. *Soil Biol. Biochem.*, 35: 263-272.

Ernakovich, J G, K A Hopping, A B Berdanier, R T Simpson, E J Kachergis, H Steltzer, M D Wallenstein (2014) Predicted responses of arctic and alpine ecosystems to altered seasonality under climate change. *Global Change Biol.*, 20: 3256-3269.

Euskirchen, E S, A D McGuire, D W Kicklighter, Q Zhuang, J S Clein, R J Dargaville, D G Dye, J S Kimball, K C McDonald, J M Melillo, V E Romanovsky, N V Smith (2006) Importance of recent shifts in soil thermal dynamics on growing season length, productivity, and carbon sequestration in terrestrial high-latitude ecosystems. *Global Change Biol*., 12: 731-750.

Fisher, J B, M Sikka, W C Oechel, W C Huntzinger, D N Melton, C D Koven, et al. (2014) Carbon cycle uncertainty in the Alaskan Arctic. *Biogeosciences*, 11: 4271-4288.

Friedl M A, D Sulla-Menashe, B Tan, A Schneider, N Ramankutty, A Sibley, X Huang (2010) MODIS Collection 5 global land cover: Algorithm refinements and characterization of new datasets, 2001-2012, Collection 5.1 IGBP Land Cover, Boston University, Boston, MA, USA.

Hadden, D, A Grelle (2016) Changing temperature response of respiration turns boreal forest from carbon sink to carbon source. *Ag. Forest Met.*, 223: 30-38.

Helbig, M, C Pappas, O Sonnentag (2016a) Permafrost thaw and wildfire: equally important drivers of boreal tree cover changes in the Taiga Plains, Canada. *Geophys. Res. Lett.*, 43: 1598-1606.

Helbig, M, K Wischnewski, N Kljun, L E Chasmer, W L Quinton, et al. (2016b) Regional atmospheric cooling and wetting effect of permafrost thaw-induced boreal forest loss. *Global Change Biol*., 22: 4048-4066.

Helbig, M, L E Chasmer, N Kljun, W L Quinton, C C Treat, O Sonnentag (2016c) The positive net radiative greenhouse gas forcing of increasing methane emissions from a thawing boreal forest-wetland landscape. *Global Change Biol.*, doi:10.1111/gcb.13520.

Hinzman, L, N D Bettez, W R Bolton, F S Chapin, M B Dyurgerov, C L Fastie, B Griffith, et al. (2005) Evidence and implications of recent climate change in northern Alaska and other Arctic regions. *Climatic Change*, 72: 251-298.

Jackowicz-Korczyński, M, T R Christensen, K Bäckstrand, P Crill, T Friborg, M Mastepanov, L Ström (2010) Annual cycle of methane emission from a subarctic peatland. *J. Geophys. Res. Biogeo.*, 115: G02009.

Karlsson, J M, F Jaramillo, G Destouni (2015) Hydro-climatic and lake change patterns in Arctic permafrost and non-permafrost areas. J. *Hydrol*., 529: 134-145.

Kim Y, J S Kimball, K Zhang, K Didan, I Velicongna, K C McDonald (2014) Attribution of divergent northern vegetation growth responses to lengthening non-frozen season optical-NIR and microwave remote sensing. *Int. J. Remote Sens.* 35:3700-3721.

Kimball J S, L A Jones, J Glassy, R Reichle (2016a) SMAP L4 Global Daily 9 km Carbon Net Ecosystem Exchange, Version 2. Boulder, Colorado, USA. NASA National Snow and Ice Data Center Distributed Active Archive Center. doi: http://dx.doi.org/10.5067/UBKO5ZUI7I5V.

Kimball J S, L A Jones, K Zhang, F A Heinsch, et al. (2009) A satellite approach to estimate land-atmosphere CO_2 exchange for Boreal and Arctic biomes using MODIS and AMSR-E. *IEEE Trans. Geosci. Remote Sens.* 47: 569-587.

Kirches G, Brockmann, M Boettcher, M Peters, S Bontemps, C Lamarche, M Schlerf, M Santoro, P Defourny (2014) CCI-LC Product User Guide. ESA. 87 pp.

Knyazikhin, Y, J Glassy, J L Privette, Y Tian, A Lotsch, Y Zhang, Y Wang, J T Morisette, P Votava, R B Myneni, R Nemani, S W Running (1999) MODIS Leaf Area Index (LAI) And fraction of Photosynthetically Active Radiation Absorbed by Vegetation (FPAR) Product (MOD15). Algorithm Theoretical Basis Document. V.4. https://lpdaac.usgs.gov/dataset_discovery/modis/modis_products_table/mcd15a3.

Kremers, K, R D Hollister, S F Oberbauer (2015) Diminished response of Arctic plants to warming over time. *PLoS ONE,* 10: e0116586.

Lasslop G, M Geichstein, D Papale, A D Richardon, A Arneth, A Barr, P Stoy, G Wohlfahrt (2010) Separation of net ecosystem exchange into assimilation and respiration using a light response curve approach: critical issues and global evaluation. *Global Change Biol.,* 16: 187-208.

Liljedahl, A K, J Boike, R P Daanen, A N Fedorov, G V Frost, G Grosse, L D Hinzman, et al. (2016) Pan-Arctic ice-wedge degradation in warming permafrost and its influence on tundra hydrology. *Nature Geosci.,* 9: 312-318.

Loranty, M M, W Lieberman-Cribbin, L T Berner, S M Natali, S J Goetz, H D Alexander, A L Kholodov (2016) Spatial variation in vegetation productivity trends, fire disturbance, and soil carbon across arctic-boreal permafrost ecosystems. *Environ. Res. Lett.*, 11: 095008

Marchand, F L, I Nijs, H J de Boeck, F Kockelbergh, S Mertens, L Beyens (2004) Increased turnover but little change in the carbon balance of high-Arctic tundra exposed to whole growing season warming. *Arctic Antarctic Alpine Res.*, 36: 298-307.

Marushchak, M E, I Kiepe, C Biasi, V Elsakov, T Friborg, T Johansson, T Virtanen, P Martikainen (2013) Carbon dioxide balance of subarctic tundra from plot to regional scales. *Biogeosciences*, 10: 437-452.

Mastepanov, M, C Sigsgaard, E J Dlugokencky, S Houweling, L Strom, M P Tamstorf, T R Christensen (2008) Large tundra methane burst during onset of freezing. *Nature*, 456: 628-630.

Natali, S M, E A G Schuur, M Mauritz, J D Schade, G Celis, K G Crummer, et al. (2015) Permafrost thaw and soil moisture driving CO_2 and CH_4 release from upland tundra. *J.*

Geophys. Res. Biogeosci., 120: 525-537.

Olefeldt, D, M R Turetsky, P M Crill, A D McGuire (2013) Environmental and physical controls on northern terrestrial methane emissions across permafrost zones. *Glob. Change Biol.*, 19: 589-603.

Osterkamp, T E, L Viereck, Y Shur, M T Jorgenson, C Racine, et al. (2000) Observations of thermokarst and its impact on boreal forests in Alaska, USA. *Arctic, Antarctic, and Alpine Res.*, 32: 303-315.

Öquist, M G, K Bishop, A Grelle, L Klemedtsson, S J Kohler, H Laudon, A Lindroth, et al. (2014) The full annual carbon balance of boreal forests is highly sensitive to precipitation. *Environ. Sci. Technol. Lett.*, 1: 315-319.

Parazoo, N C, R Commane, S C Wofsy, C D Koven, C Sweeney, D M Lawrence, J Lindaas, R Y-W Chang, C E Miller (2016) Detecting regional patterns of changing CO_2 flux in Alaska. *PNAS*, 113: 7733-7738.

Parmentier, F J W, M K van der Molen, J van Huissteden, S A Karsanaev, A V Kononov, D A Suzdalov, T C Maximov, A J Dolman (2011) Longer growing seasons do not increase net carbon uptake in the northeastern Siberian tundra. *J. Geophys. Res.Biogeo.*, 116: G04013, doi:10.1029/2011JG001653.

Pastick, N J, M T Jorgenson, B K Wylie, S J Nield, K D Johnson, A O Finley (2015) Distribution of near-surface permafrost in Alaska: estimates of present and future conditions. *Remote Sens. Environ*., 168: 301-315.

Reichle, R H, R D Koster, G J M De Lannoy, B A Forman, Q Liu, S P P Mahanama, A Toure (2011) Assessment and enhancement of MERRA land surface hydrology estimates. *J. Climate*, 24: 6322-6338.

Reichstein, M, P C Stoy, A R Desai, G Lasslop, A R Richardson. Partitioning of net fluxes. In: M. Aubinet et al. (eds.), *Eddy Covariance: A Practical Guide to Measurement and Data Analysis*, Springer Atmospheric Sciences. Doi:10.1007/978-94-007-2351-1_9, (pp. 263-298).

Reichstein, M, M Bahn, P Ciais, D Frank, M D Mahecha, S I Seneviratne, J Zscheischler, C Beer, et al. (2013) Climate extremes and the carbon cycle. *Nature*, 287. Doi:10.1038/nature12350

Rienecker M M, M J Suarez, R Gelaro, R Todling, J Bacmeister, E Liu, M Bosilovich. S D Schubert, L Takacs, et al. (2011) MERRA: NASA's Modern-Era Retrospective Analysis for Research and Applications. *J. Climate* 24: 3624–3648.

Schädel, C, M K F Bader, E A G Schuur, C Biasi, R Brancho, et al. (2016) Potential carbon emissions dominated by carbon dioxide from thawed soils. *Nature Clim. Change*, 6: 950-953.

Schuur, E A G, B Abbott (2011) Climate change: high risk of permafrost thaw. *Nature*, 480: 32-33.

Schuur, E A G, A D McGuire, C Schadel, G Grosse, J W Harden, D J Hayes, G Hugelius, C D Koven, P Kuhry, D M Lawrence, S M Natali, et al. (2015) Climate change and the permafrost carbon feedback. *Nature*, 520: 171-179.

Screen, J A, I Simmonds (2010) The central role of diminishing sea ice in recent Arctic temperature amplification. *Nature*, 464: 1334-1337.

Serreze, M C, R G Barry (2011) Processes and impacts of Arctic amplification: a research synthesis. *Global Planet. Change*, 77:85-96.

Sistla, S A, J C Moore, R T Simpson, L Gough, G R Shaver, J P Schimel (2013) Long-term warming restructures Arctic tundra without changing net soil carbon storage. *Nature*, 497: 615-618.

Stoy, P C, G G Katul, M B S Siqueira, J-Y Juang, K A Novick, J M Uebelherr, R Oren (2006) An evaluation of models for partitioning eddy covariance-measured net ecosystem exchange into photosynthesis and respiration. *Ag. Forest Met*., 141: 2-18.

Ström, L, M Mastepanov, T R Christensen (2005) Species-specific effects of vascular plants on carbon turnover and methane emissions from wetlands. *Biogeochemistry*, 75: 65-82.

Sturtevant, C S, W C Oechel (2013) Spatial variation in landscape-level CO_2 and CH_4 fluxes from arctic coastal tundra: influence from vegetation, wetness, and the thaw lake cycle. *Glob. Change Biol.*, 19: 2853-2866.

Sweeney, C, E Dlugokencky, C E Miller, S Wofsy, A Karion, S Dinardo, R Y-W Chang, J B Miller, L Bruhwiler, A M Crotwell, et al. (2016) No significant increase in long-term CH_4 emissions on North Slope of Alaska despite significant increases in air temperature. *Geophys. Res. Lett.*, 43: 6604-6611.

Treat, C C, S M Natali, J Ernakovich, C M Iversen, M Lupascu, A D McGuire et al. (2015) A pan-Arctic synthesis of CH_4 and CO_2 production from anoxic soil incubations. *Global Change Biol*., 21: 2787-2803.

Turetsky, M R, C C Treat, M P Waldrop, J M Waddington, J W Harden, A D McGuire (2008) Short-term response of methane fluxes and methanogen activity to water table and soil warming manipulations in an Alaskan peatland. *J. Geophys. Res. Biogeosci.* 113:

G00A10.

Van Wijk, M T, M Williams, J A Laundre, G R Shaver (2003) Internanual variability of plant phenology in tussock tundra: modelling interactions of plant productivvity, plant phenology, snowmelt and soil thaw. Global Change Biol., 9: 743-758.

Wagner, D, S Kobabe, S Liebner (2009) Bacterial community structure and carbon turnover in permafrost-affected soils of the Lena Delta, northeastern Siberia. *Can. J. Microbiol.*, 55: 73-83.

Walker D A, M K Raynolds, F J A Daniels, E Einarsson, et al. (2005) The Circumpolar Arctic vegetation map. *J. Veg. Sci.,* 16: 267-282.

Walsh, J (2014) Intensified warming of the Arctic: causes and impacts on middle latitudes. *Global Planet. Change*, 117: 52-63.

Watts J D, J S. Kimball, L A Jones, et al. (2012) Satellite microwave remote sensing of contrasting surface water inundation changes within Arctic-Boreal region. *Remote Sens. Environ*., 127: 223-236.

Watts J D, J S Kimball, F-J W Parmentier, T Sachs, J Rinne, D Zona, W Oechel, T Tagesson, M Jackowicz-Korczyński, M Aurela (2014a) A satellite data driven biophysical modeling approach for estimating northern peatland and tundra CO_2 and CH_4 fluxes. *Biogeosciences* 11: 1961-1980.

Watts J D, J S Kimball, A Bartsch, K C McDonald (2014b) Surface water inundation in the boreal-Arctic: potential impacts on regional methane emissions. *Environ. Res. Lett.* 9: 1-13.

Webb, E E, E A G Schuur, S M Natali, K L Oken, R Bracho, J P Krapek, D Risk, N R Nickerson (2016) Increased wintertime CO_2 loss as a result of sustained tundra warming. *J. Geo. Res. Lett. Biogeosci.*, 121: 249-265.

Wrona, F J, M Johansson, J M Culp, A Jenkins, J Mard, I H Myers-Smith, T D Prowse, W F Vincent, P A Wookey (2016) Transitions in Arctic ecosystems: ecological implications of a changing hydrological regime. *J. Geophys. Res. Biogeosci.*, 121: 650-674.

Young, A M, P E Higuera, P A Duffy, F S Hu (2016) Climatic thresholds shape northern high latitude fire regimes and imply vulnerability to future climate change. *Ecography*, 39: 001-012.

Zimov, S A, S P Davydov, G M Zimova, A I Davydova, E A G Schuur, K Dutta, F S Chapin III (2006) Permafrost carbon: stock and decomposability of a globally significant carbon pool. *Geophys. Res. Lett.*, 33: L20502.

Zona D, B Gioli, R Commane, J Lindaas, S C Wofsy, C E Miller, S J Dinardo, S Dengel, C Sweeney, A Karion, R Y-W Chang, J M Henderson, P C Murphy, J P Goodrich, V Moreaux, A Liljedahl, J D Watts, J S Kimball, D A Lipson, W C Oechel (2016) Cold season emissions dominate the Arctic tundra methane budget. *Proc. Nat. Acad. Sci.*, 113: 40-45.

Tables

Table 5.1 Multiple linear regression results for flux tower NEE, GPP, Reco (gC m^{-2} d^{-1}) and CH_4 records (mgC m^{-2} d^{-1}) from the 35 Arctic-boreal wetland sites. Explanatory variables include land cover class, permafrost thaw depth, mean annual precipitation (MAP; mm), mean annual air temperature (°C), mean daily air and soil temperature (Ta, Ts; °C). The parameter estimates are shown, along with model standard error, t-values, p-values, root square error (RSE), F-statistic, the degrees of freedom, and the coefficient of determination (R^2). Parameter significance is denoted as * where $p < 0.1$, ** where $p < 0.05$, and *** where $p < 0.01$.

NEE	**Estimate**	**Std.Error**	**t-value**	**p-value**	**Significance**
Intercept	5.24	6.24	0.84	4.00E-01	
Land Class	-0.18	0.11	-1.72	9.00E-02	*
ThawDepth	-0.14	0.06	-2.18	3.00E-02	**
MAP	0.002	0.01	0.38	7.10E-01	
MAT	1.61	0.33	4.83	1.64E-06	***
Ta	-0.61	0.13	-4.76	2.33E-06	***
Ts	-1.26	0.23	-5.54	4.23E-08	***
RSE	26	Deg. Freedom	722		
F-stat	46	R^2	0.28	p-value	< 2.2e-16

Reco	**Estimate**	**Std.Error**	**t-value**	**p-value**	**Significance**
Intercept	35.77	10.28	3.48	5.30E-04	***
Land Class	0.66	0.17	3.77	1.78E-04	***
ThawDepth	-0.27	0.11	-2.59	9.92E-03	***
MAP	-0.03	0.01	-2.59	3.14E-03	***
MAT	4.03	0.55	7.29	8.523-13	***
Ta	1.29	0.22	5.95	4.27E-09	***
Ts	3.59	0.4	9.08	2.00E-16	***
RSE	42	Deg. Freedom	682		
F-stat	110	R^2	0.49	p-value	< 2.2e-16

GPP	**Estimate**	**Std.Error**	**t-value**	**p-value**	**Significance**
Intercept	-25.27	12.25	-2.06	4.00E-02	**
Land Class	-0.91	0.21	-4.38	1.39E-05	***
ThawDepth	0.22	0.12	1.74	8.00E-02	*
MAP	0.03	0.01	2.31	2.00E-02	**
MAT	-2.57	0.66	-3.89	1.09E-04	***
Ta	-1.64	0.26	-6.32	4.80E-10	***
Ts	-4.55	0.47	-9.63	2.00E-16	***
RSE	50	Deg. Freedom	682		
F-stat	114	R2	0.5	p-value	< 2.2e-16

CH_4	**Estimate**	**Std.Error**	**t-value**	**p-value**	**Significance**
Intercept	4792	679	7.06	4.09E-11	***
Land Class	-50.55	10.51	-4.81	3.32E-06	***
ThawDepth	13.3	6.73	1.98	4.00E-02	**
MAP	-5.59	1.32	-4.23	3.75E-05	***
MAT	80.96	39.82	2.03	4.00E-02	***
Ta	-22.37	17.05	-1.31	1.90E-01	
Ts	209.47	25.34	8.27	3.71E-14	***
RSE	1087	Deg. Freedom	171		
F-stat	31	R^2	0.52	p-value	< 2.2e-16

Table 5.2 TCF model results for tower sites relative to fluxes derived from eddy covariance methods. Measures of model estimate disagreement include the root mean square error (RMSE) and mean residual error (MRE). RMSE and MSE are provided for NEE, GPP, Reco (units are gC m^{-2} d^{-1}) and CH_4 (mgC m^{-2} d^{-1}) flux estimates.

SITE	RMSE.NEE	MRE.NEE	RMSE.GPP	MRE.GPP	RMSE.Reco	MRE.Reco	RMSE.CH4	MRE.CH4
			gC m^{-2} d^{-1}				mgC m^{-2} d^{-1}	
1	0.69	-0.03	0.84	-0.04	0.85	0.09	14	-6.01
2	0.86	-0.05	0.98	-0.11	0.91	0.27		
3	1.21	0.26	0.97	-0.11	1.01	-0.13		
4	0.96	-0.1	1.66	0	0.77	0.26		
5	0.73	0.09	0.89	0.01	0.81	-0.08	4.94	-0.44
6	1.3	-0.22	1.15	0.42	3.19	2.02		
7	0.6	0.12	0.63	-0.02	0.66	0.24		
8	0.34	0.06	0.28	-0.1	0.43	-0.11	14.35	-0.78
9	0.84	-0.21	0.99	-0.12	1.22	-0.03	22.42	2.5
10	0.63	0.05	0.92	-0.41	0.5	0.36	4.52	0.04
11	0.48	-0.12	0.54	-0.11	0.45	-0.13	10.86	-6.12
12	0.33	0.05	0.34	-0.04	0.36	0.04	9.06	6.48
13	1.27	-0.94	1.29	-0.75	0.63	0.09	23.34	11.37
14	0.79	-0.07	1.05	0.13	0.78	-0.21	12.8	-1.09
15	0.84	0.2	0.98	-0.03	0.81	0.17	25.38	-1.72
16	1.29	-0.23	1.22	0.29	0.86	-0.14	19.63	0.87
17	0.53	0.12	0.67	0.13	0.35	0.1	31.35	4.1
18	0.95	0.07	1.17	0.01	0.76	-0.04		
19	0.84	0.23	0.99	-0.03	0.8	0.03		
20	0.77	0.12	1.17	0.31	0.73	-0.23		
21	0.8	0.36	1.08	0.51	0.62	-0.26		
22	1.84	0.9	1.84	0.17	1.26	0.47		
23	2.02	0.71	2.38	0.07	1.29	0.57		
24	0.76	0.36	0.9	0	0.88	0.21		
25	0.81	0.24	0.99	0	0.95	0.22		
26	0.51	0.05	0.67	-0.06	0.64	0.23		
27	1.42	0.59	1.52	0.44	0.87	0.13	35.6	4.42
28	1.42	0.59	1.52	0.44	0.87	0.13	35.6	4.42
29	1.15	0.16	1.42	-0.18	1.33	0.05	35.43	-15.2
30	1.22	-0.73	0.96	-0.07	0.62	0.14	12.06	1.75
31			1.9	-0.72				
32	2.31	-1.33	1.38	0.02	1.01	-0.14		
34	0.54	-0.13	0.64	-0.03	0.42	-0.12	24	-6.28
35							46.98	-5.47
36	0.85	-0.01	0.81	-0.04	0.45	0	34.09	-5.1
Mean	0.96	0.01	1.07	-0.01	0.85	0.13	21.16	-0.93
Stdev	0.47	0.43	0.45	0.27	0.51	0.41	11.95	5.98

Table 5.3 Mann Kendall trend results for TCF model simulated annual NEE, GPP, Reco, CH_4 and NECB (gC m^{-2} yr^{-1}) for years 2003-2015. The intercept and trend indicate the linear model component. Tau indicates the rank correlation between the carbon fluxes and time. The * denotes trend significance at $\alpha = 0.05$.

	Intercept	Trend	Tau	P-value
NEE				
Boreal Wetland	-141.7	8.17	0.12	0.63
Boreal Forested Wetland	-183.2	11.59	0.18	0.45
Boreal Non-forested Wetland	-94.7	4.44	0.21	0.37
Tundra	-15.7	1.51	0.3	0.19
GPP				
Boreal Wetland	635.5	-7.22	-0.33	0.15
Boreal Forested Wetland	788	-9.89	-0.39	0.08
Boreal Non-forested Wetland	556.9	-7.71	-0.18	0.45
Tundra	225.76	-0.33	-0.15	0.54
Reco				
Boreal Wetland	525.7	3.5	0.09	0.74
Boreal Forested Wetland	650.3	4.24	0.09	0.73
Boreal Non-forested Wetland	394.4	3.4	0.15	0.53
Tundra	209.9	1.23	0.18	0.45
CH4				
Boreal Wetland	11.76	1.6	0.73	0.001*
Boreal Forested Wetland	11.16	1.1	0.45	0.05*
Boreal Non-forested Wetland	13.9	1.99	0.82	<0.0001*
Tundra	6.3	0.01	0.12	0.63
NECB				
Boreal Wetland	-142.2	10.11	0.33	0.15
Boreal Forested Wetland	-185.9	13.39	0.3	0.19
Boreal Non-forested Wetland	-96.6	7.13	0.39	0.08
Tundra	6.3	0.01	0.12	0.63

Figures

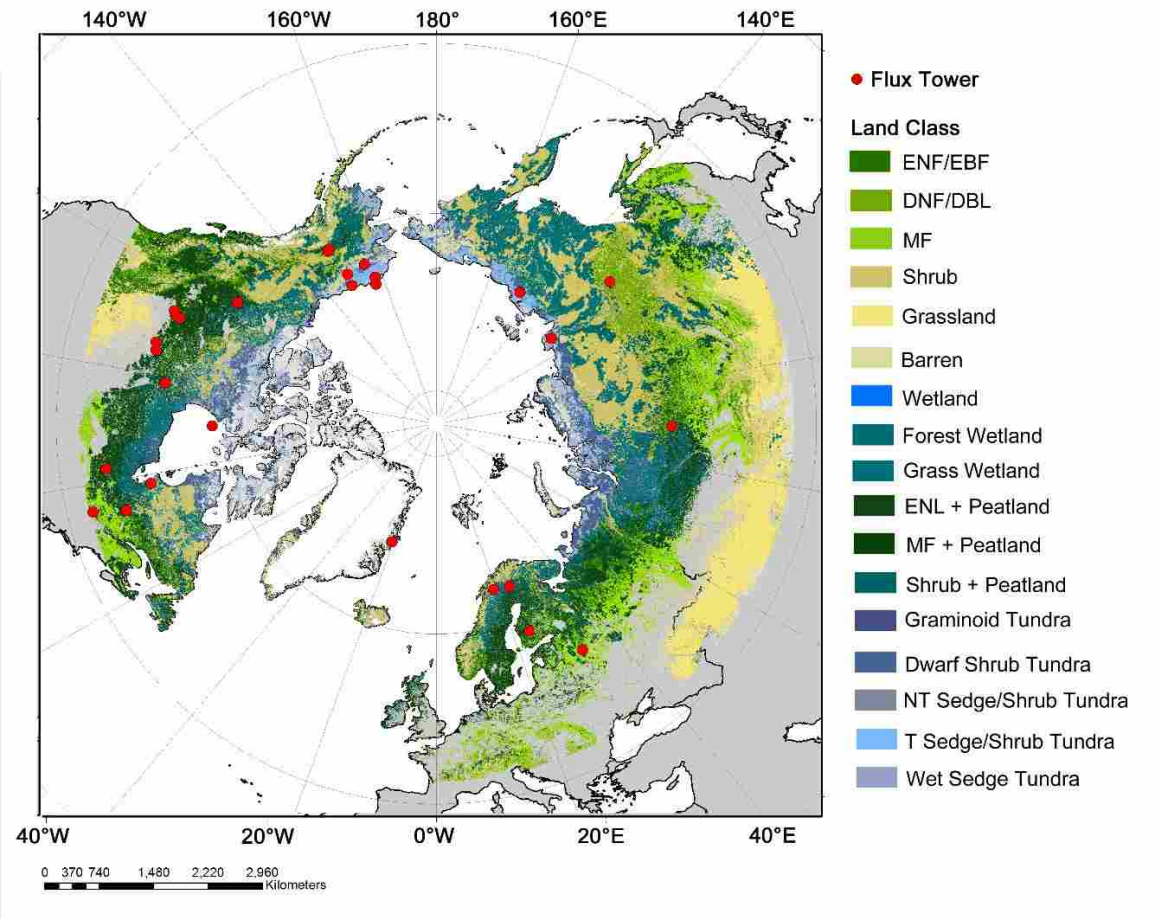

Figure 5.1 Land cover for high latitude regions > 45°N as derived from merged ESA CCI-LC 2010 (Kirches *et al*. 2014), Circumpolar Arctic Vegetation Map (CAVM; Walker *et al*. 2005) and peatland (Watts *et al*. 2014b) classification fields. Filled red circles denote flux tower validation sites. Land cover classes include Evergreen Needleleaf and Broadleaf Forest (ENF/EBF), Deciduous Needleleaf and Broadleaf Forest (DNF/DBL), Mixed Forest (MF), Tussock (T) and Non-Tussock (NT) sedge/shrub tundra and other tundra, peatland, and wetland shrub and grassland vegetation.

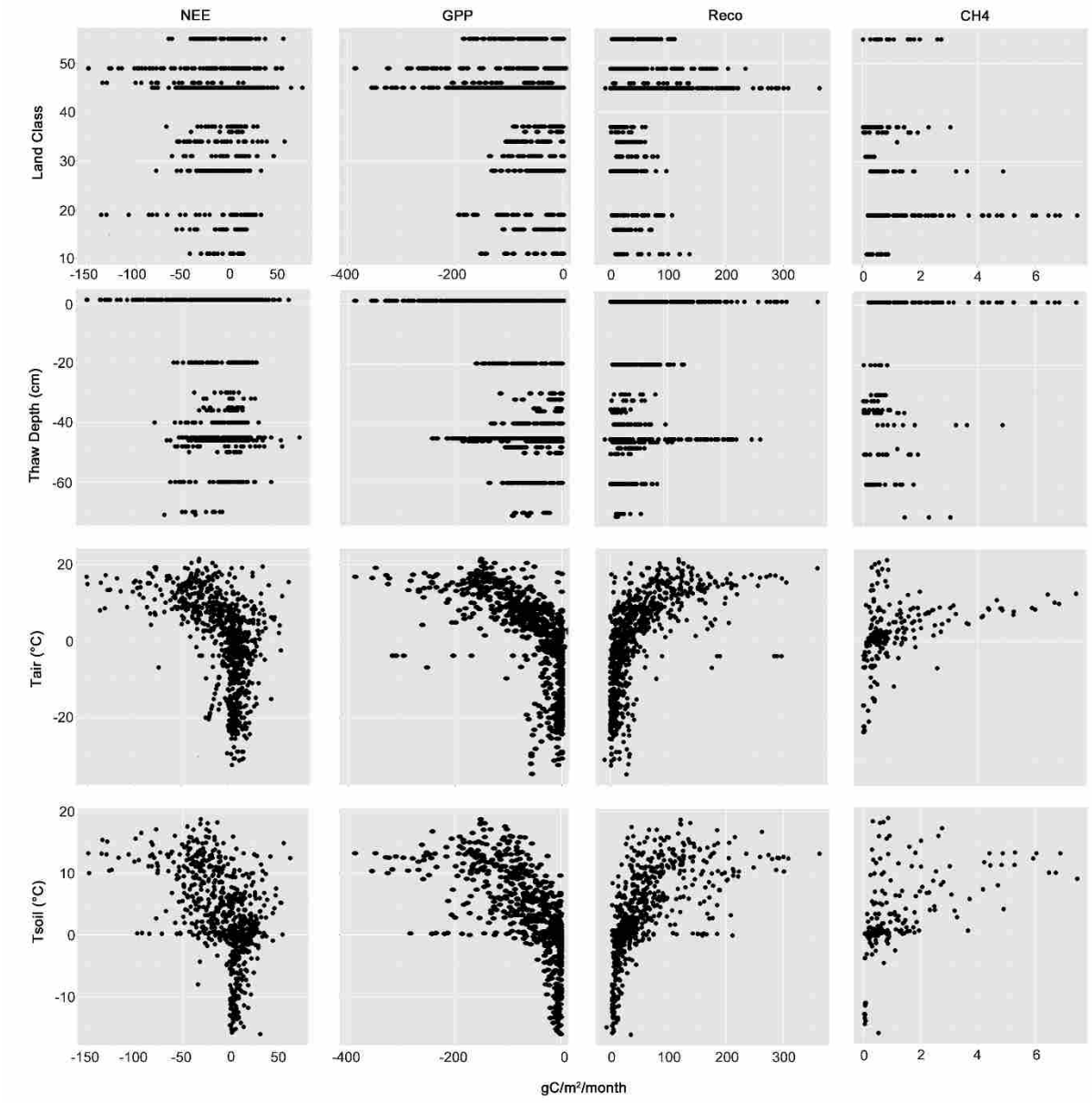

Figure 5.2 Ecosystem characteristics observed in eddy covariance tower records for net ecosystem CO_2 exchange (NEE) and CH_4 emissions (gC/m^2/month) from northern high latitude wetland sites. Key environmental regulators influencing seasonal flux magnitudes include vegetation community type (e.g. boreal or tundra wetlands), the thaw depth (cm) of soils overlaying permafrost, and air/soil temperature (°C). Landscape wetness (not shown) is also a key factor, with carbon emissions shifting towards anaerobic CH_4 pathways under very wet or saturated soil conditions. Thaw depths of '0' indicate an absence of permafrost in the landscape immediate to the tower sites.

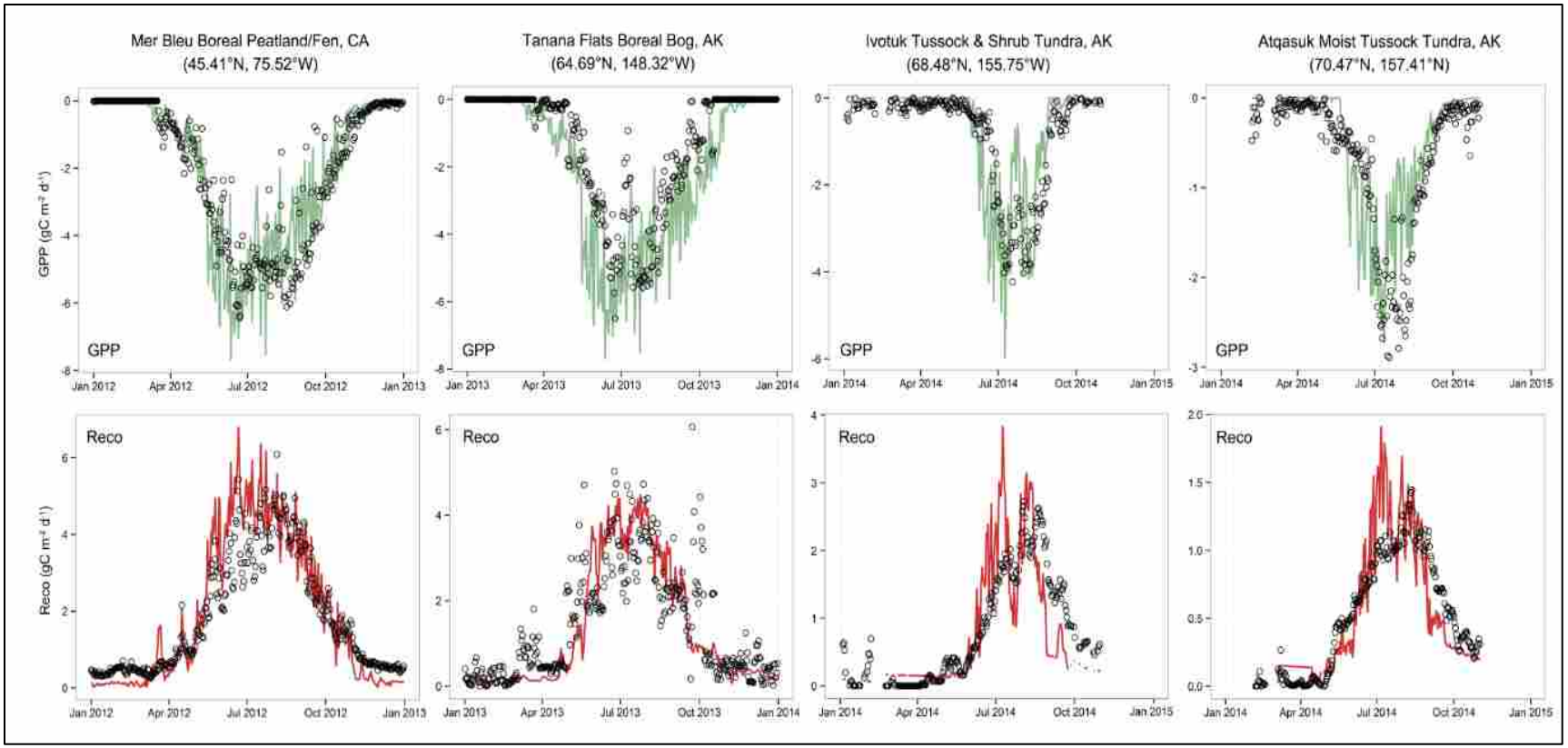

Figure 5.3 Example TCF model simulation results shown for four of the 36 Arctic-boreal flux tower sites, using 1-km MODIS FPAR (MCD15A3) and 0.5° NASA GMAO MERRA reanalysis inputs. Model estimated gross primary productivity (GPP; gC m^{-2} d^{-1}) is indicated by the green lines, whereas model estimated ecosystem CO_2 respiration (Reco; gC m^{-2} d^{-1}) is shown in green. The open circles denote daily flux averages obtained through tower eddy covariance observations. The four ecosystems included here represent two boreal sites (Mer Bleu and Tanana Flats) and two tundra sites (Ivotuk and Atqasuk).

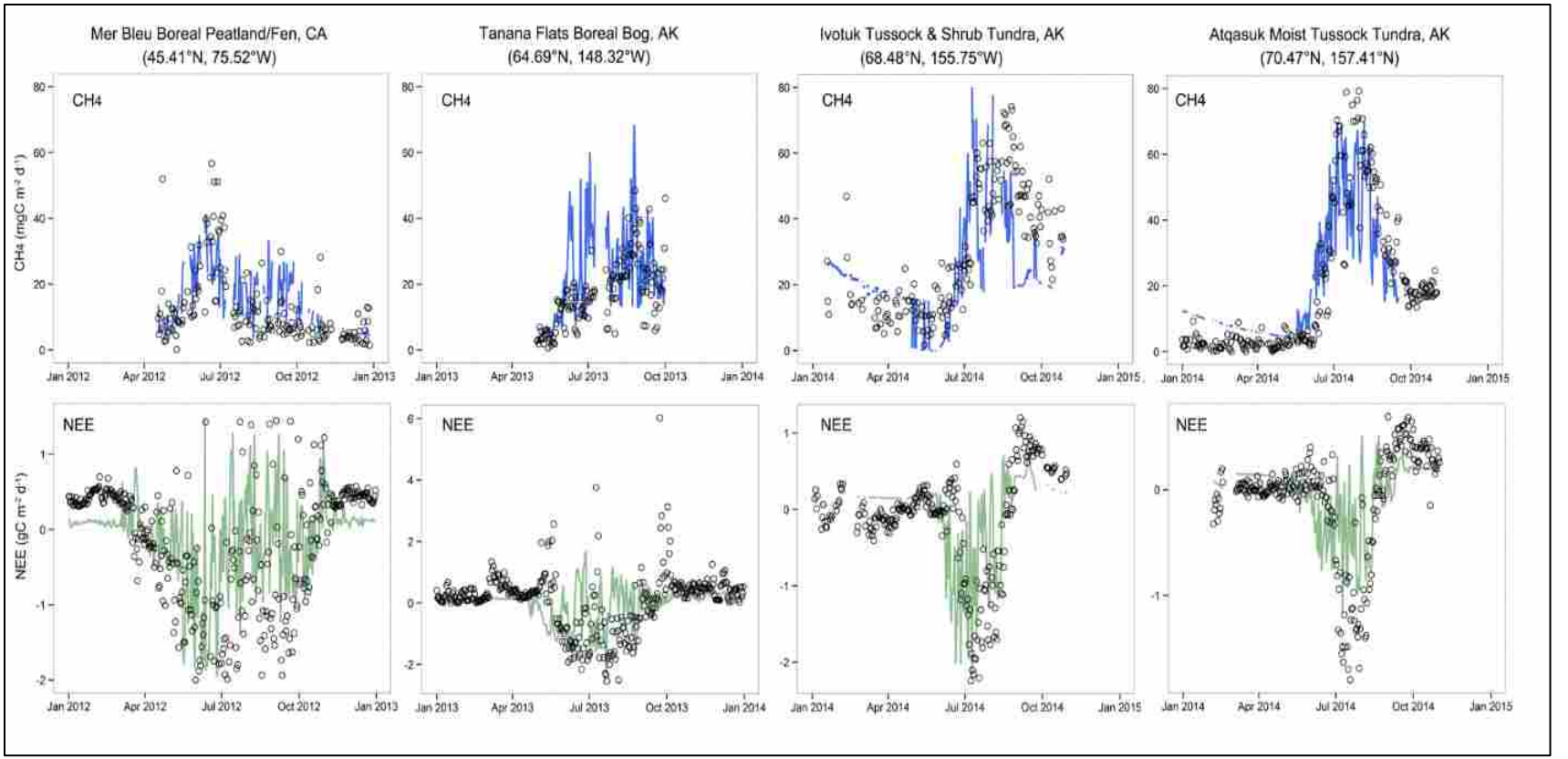

Figure 5.4 Example TCF model simulation results shown for four of the 36 Arctic-boreal flux tower sites, using 1-km MODIS FPAR (MCD15A3) and 0.5° NASA GMAO MERRA reanalysis inputs. Model estimated CH_4 emissions (mgC m^{-2} d^{-1}) are indicated by the blue lines, whereas model estimated net ecosystem CO_2 exchange (NEE; gC m^{-2} d^{-1}) is shown in green. The open circles denote daily flux averages obtained through tower eddy covariance observations. The four ecosystems included here represent two boreal sites and two tundra sites. The boreal sites are: (1) a Canadian non-permafrost boreal peat and fen wetland (Mer Bleu; site number 14); and (2) a boreal bog in Alaska with discontinuous permafrost (Tanana Flats; site number 1). The tundra sites are: (1) upland mixed tussock and shrub tundra in Alaska having underlying continuous permafrost (Ivotuk; site number 9); and (2) lowland moist tussock tundra having underlying continuous permafrost (Atqasuk; site number 8).

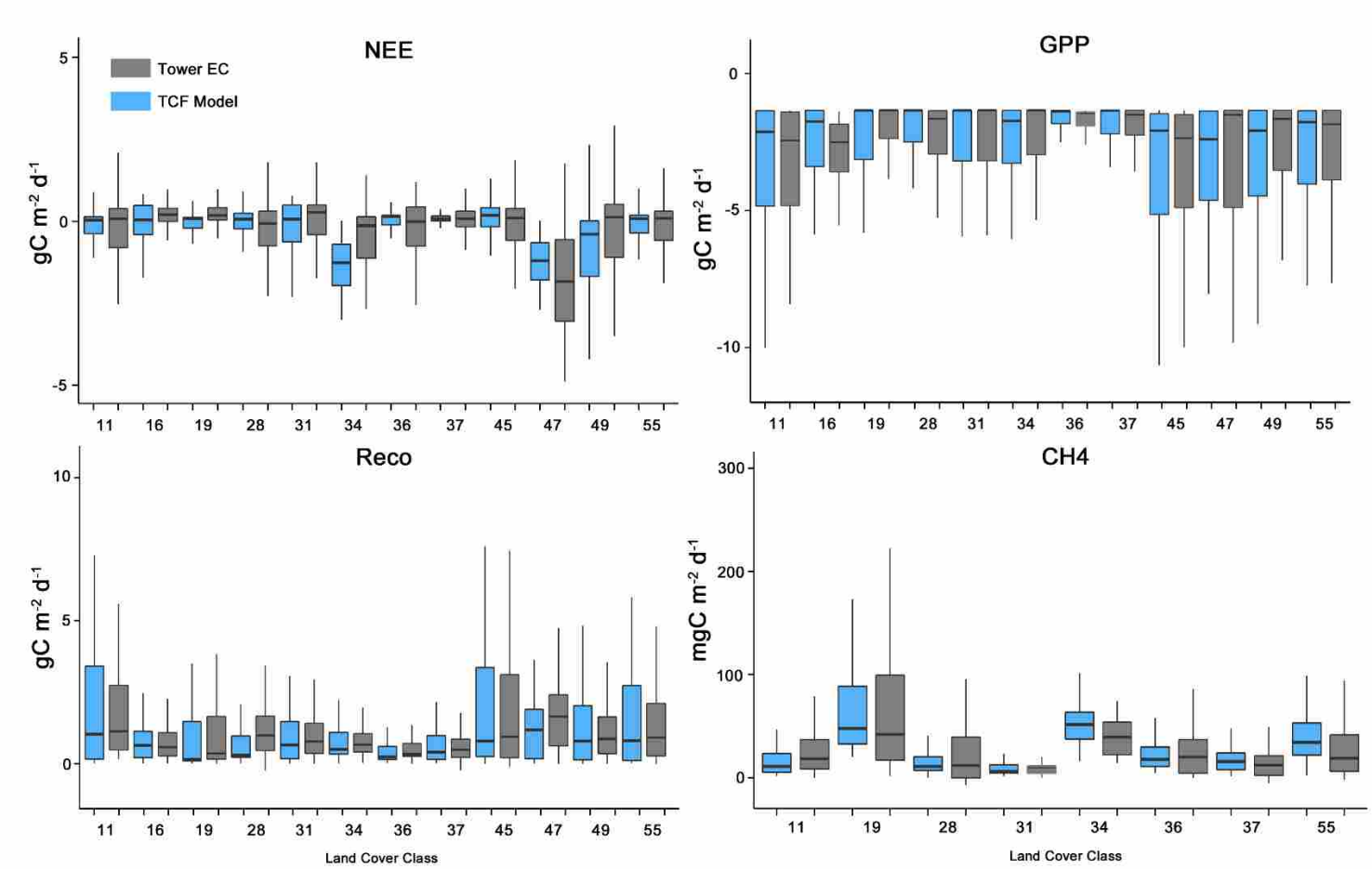

Figure 5.5 Distributions of daily mean fluxes for NEE, GPP, Reco (gC m^{-2} d^{-1}) and CH_4 (mgC m^{-2} d^{-1}) obtained from the 1-km res. TCF model simulations (in blue) and tower eddy covariance datasets (in grey) by land cover class. The boxplot median values are indicated by black horizontal lines; vertical tails indicate the flux range.

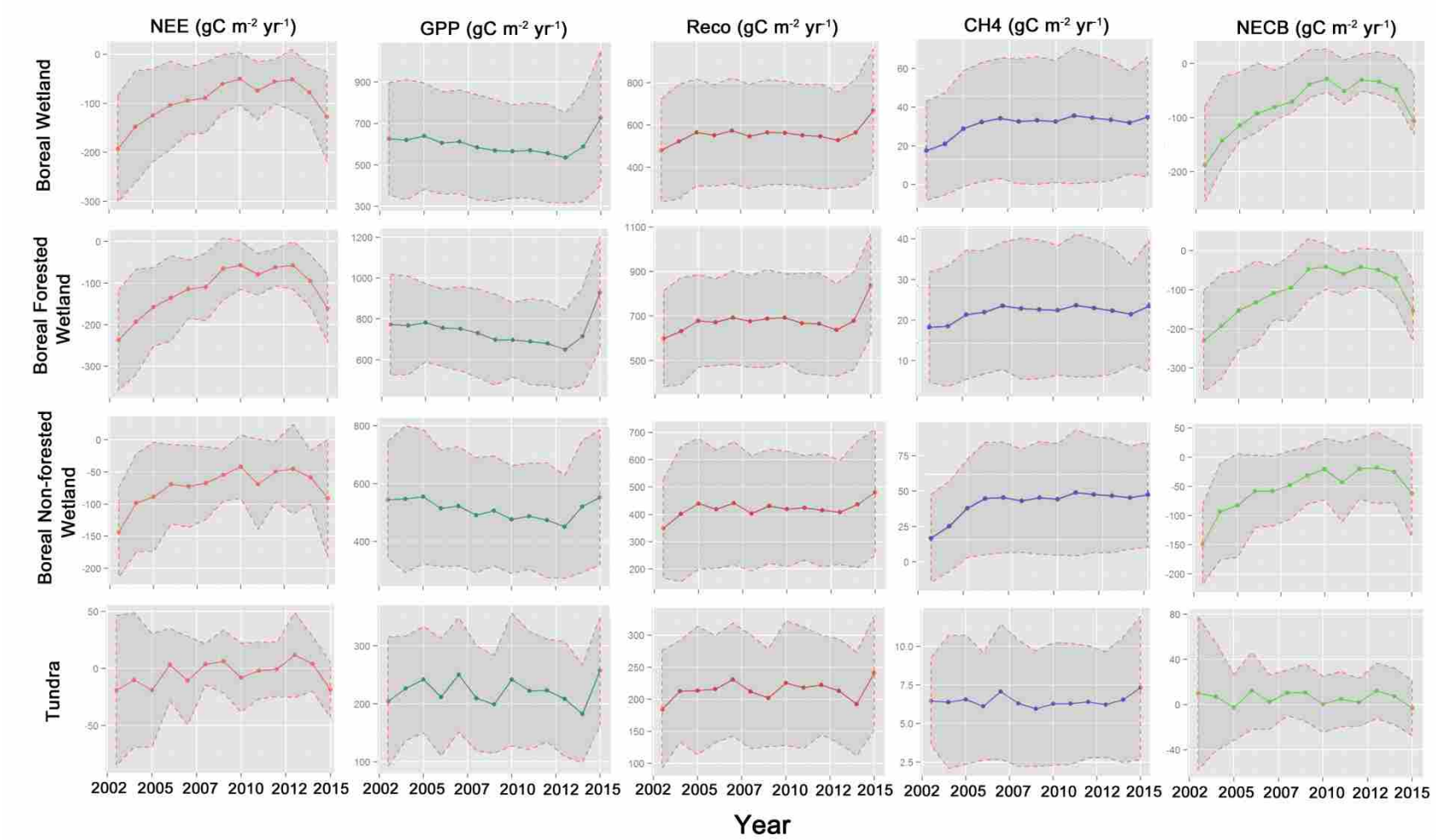

Figure 5.6 Annual variability in NEE, GPP, Reco, CH_4 and NECB (gC m^{-2} yr^{-1}) for Arctic-boreal flux tower locations according to aggregated ecosystem type (i.e. Boreal wetland; Boreal forested wetland; Boreal non-forested wetland; Tundra). The solid lines indicate across-site flux means and the shaded regions denote +/- 1 standard deviation around the mean.

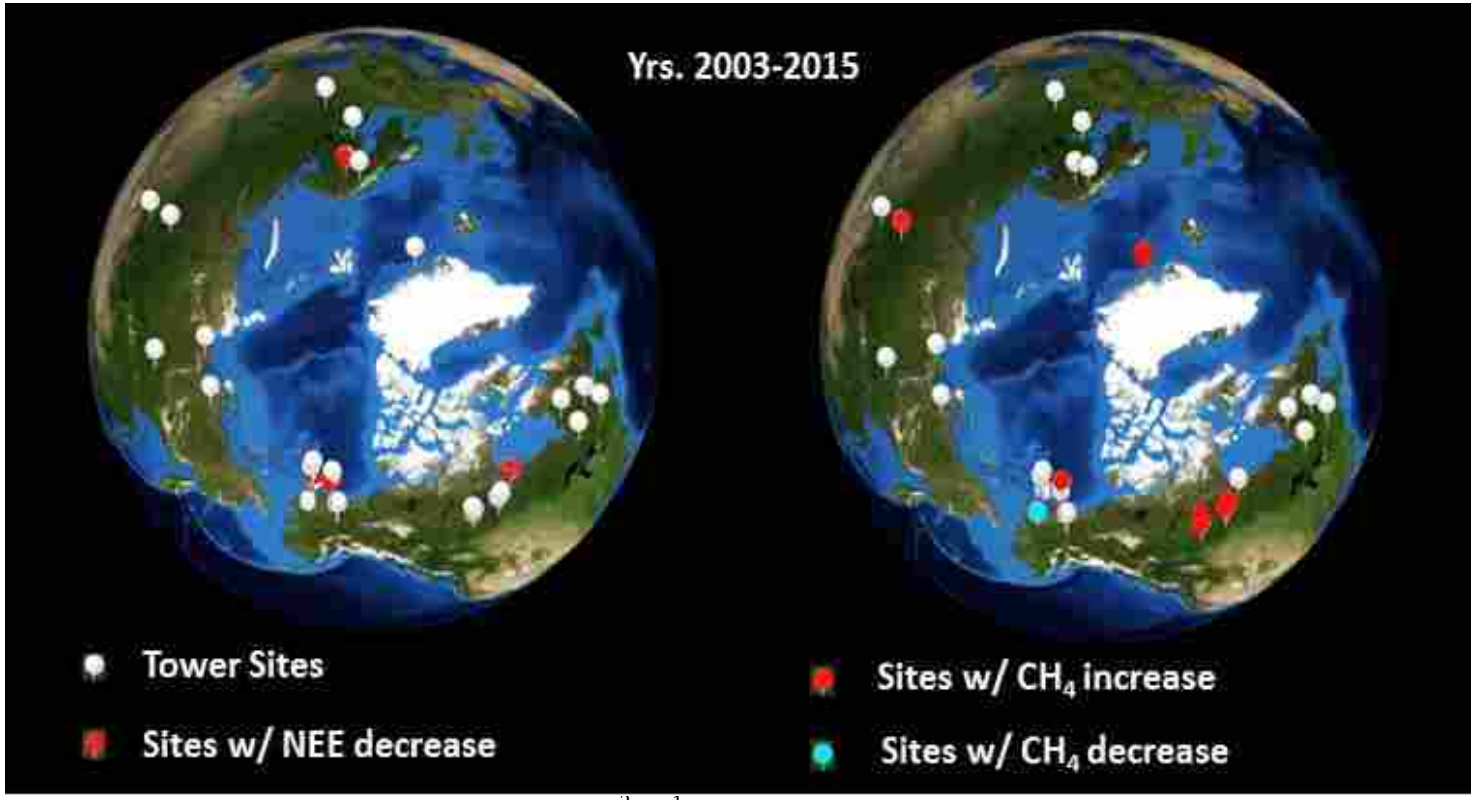

Figure 5.7 Site trends in NEE and CH_4 (gC m^{-2} yr^{-1}) for Arctic-boreal flux tower locations, from 2003 through 2015. Locations of the 36 towers are shown by the white circles. Red circles denote sites having significant trends ($p < 0.1$) in annual net CO_2 or CH_4 flux. The blue circle indicates a significant decrease in annual site CH_4 emissions over the 13-yr period.

Chapter 5 Supplement

Table S5.1 Flux tower site information, including associated 1-km land cover class type, permafrost (PF) class, active layer thaw depth, elevation, mean annual precipitation and temperature (MAP, MAT), the measured gas species, years of available flux record, and associated publications.

Site Number	Region	Tower Coordinates	Site Location	Site Description	Land Class	PF	Thaw Depth (cm)	Elev (m)	MAP (mm)	MAT (°C)	Species	Year(s) of Record	Publications or Contact Info
1	AK	64.696°N, 148.320°W	Tanana Flats (TF BB)	Boreal Thermokarst Collapse Scar Bog	55	Discont.	0.62	100	287	-3.1	CH4 CO2	2013 2011-2013	Euskirchen et al. 2014
2	AK	64.696°N, 148.323°W	Tanana Flats (TF Bs)	Sparsely Treed Black Spruce	45	Discont.	0.53	100	287	-3.1	CO2	2011-2013	Euskirchen et al. 2014
3	AK	64.704°N, 148.313°W	Tanana Flats (TF Rf)	Rich Fen (No Trees)	45	Discont.	> 2.5 m	100	287	-3.1	CO2	2011-2013	Euskirchen et al. 2014
4	AK	64.8663°N, 147.856°W	University of Alaska Fairbanks	Open Canopy Black Spruce	45	Discont.	-45	158	263	-2.9	CO2	2003-2011	Ueyama et al. 2014; Iwata et al. 2012
5	AK	68.606°N, 149.311°W	Imnavait	Wet Sedge Fen (Riparian)	16	Cont.	60	930	318	-7.4	CH4 CO2	2012-2013 2008-2010; 2012-2013	Euskirchen et al. 2012
6	AK	68.608°N, 149.304°W	Imnavait	Tussock (Hillslope)	55	Cont.	70	930	318	-7.4	CO2	2008-2010	Euskirchen et al. 2012
7	AK	68.607°N, 149.296°W	Imnavait	Dry Heath (Ridge)	33	Cont.	40	930	318	-7.4	CO2	2008-2010; 2012-2013	Euskirchen et al. 2012
8	AK	70.469° N, 157.408°W	Atqasuk	Moist Tussock	36	Cont.	-50	15	102.7	-9.7	CH4 CO2	2013-2014 2013-2014	Donatella Zona d.zona@sheffield.ac.uk
9	AK	68.486°N, 155.750°W	Ivotuk	Moist Tussock & Shrub/Moss/Lichen	28	Cont.	-60	568	MSP: 210	-7.9	CH4 CO2	2013-2014 2013-2014	Donatella Zona d.zona@sheffield.ac.uk
10	AK	71.323°N, 156.609°W	Barrow; CMDL	Wet Sedge & Grass Tundra	37	Cont.	-32	6	MAP 110	-12.6	CH4 CO2	2014 2013-2014	Donatella Zona d.zona@sheffield.ac.uk
11	AK	71.280°N, 156.596°W	Barrow; BES	Wet Inundated Sedge/Grass/Moss	37	Cont.	-36	6	MSP: 72	-12.6	CH4 CO2	2013-2014 2013-2014	Donatella Zona d.zona@sheffield.ac.uk

Site Number	Region	Tower Coordinates	Site Location	Site Description	Land Class	PF	Thaw Depth (cm)	Elev (m)	MAP (mm)	MAT (°C)	Species	Year(s) of Record	Publications or Contact Info
12	AK	71.281°N, 156.612°W	Barrow; BEO	Med Dry Poly. Tundra; (Grass/Sedge/Moss/ Dwarf Shrub)	37	Cont.	-35	7	MSP: 72	-12.6	CH4 CO2	2013-2014 2013-2014	Donatella Zona d.zona@sheffield.ac.uk
13	AK	70.1°N, 148.6°W	Prudhoe Bay; NOAA/ATDD	Wet Sedge	37	Cont.	-71	30	103	-11.8	CH4 CO2	2013-2014 2013-2014	John Kochendorfer john.kochendorfer@noaa.gov
14	CA	45.41°N, 75.51°W	Ottawa	Bog Peatland & Fen	11	None	NA	65	943	6.4	CH4 CO2	2011-2012 2011-2012	Brown et al. 2014
15	CA	53.674°N, 78.170°W	Quebec; St. James Bay Lowlands	Boreal Sphagnum Bog	11	None	NA	71	697	-2.4	CH4	2012	Nadeau et al. 2013
16	CA	61.18°N, 121.3°W	Scotty Creek, NWT	Boreal Forest; 3-4 m peat	11	Spor.	1000	283	369	-3.2	CO2	2015-2016	Helbig et al. 2016a; Helbig et al. 2016b
17	CA	61.18°N, 121.3°W	Scotty Creek, NWT	Boreal Forest + Thermokarst Bog; 3-4 m peat	11	Spor.	1000	283	369	-3.2	CO2	2015-2016	Helbig et al. 2016a; Helbig et al. 2016b
18	CA	54.953°N, 112.467°W	Western Peatland Lac LaBiche	Peatland; stunted trees, shrubs, herbs, moss	49	None	NA	540	324	-1.84	CO2	2003-2005; 2008-2009	Larry Flanagan; larry.flanagan@uleth.ca
19	CA	55.88°N, 98.48°W	Manitoba; BOREAS NSA- Old Black Spruce	Boreal Black Spruce; moss understory	45	None	NA	253	509	-2.9	CO2	2003; 2007-2008	Brian Amiro; brian_amiro@umanitoba.ca
20	CA	55.537°N, 112.335°W	Alberta Western Peatland	Poor Fen (No Trees)	49	None	NA	732	504	2.1	CO2	2004	Adkinson et al. 2011
21	CA	55.537°N, 112.335°W	Alberta Western Peatland	Rich Fen (No Trees)	49	None	NA	732	504	2.1	CO2	2004	Adkinson et al. 2011
22	CA	48.217°N, 82.155°W	Ontario, Groundhog River	Old (70+ years) Mixed Forest; aspen, birch, spruce, moss	49	None	NA	355	835	1.3	CO2	2003-2005	Pejam et al. 2006

Site Number	Region	Tower Coordinates	Site Location	Site Description	Land Class	PF	Thaw Depth (cm)	Elev (m)	MAP (mm)	MAT (°C)	Species	Year(s) of Record	Publications or Contact Info
23	CA	53.6289°N, 106.198°W	Saskatchewan; Old Aspen	Old (70+ years) Aspen; + 10% balsam poplar, moss	45	None	NA	580	406	0.5	CO2	2003-2010	Andy Black; (andrew.black@ubc.ca)
24	CA	49.6925°N, 74.342°W	Quebec; Eastern Old Black Spruce (EOBS)	90-100 yr old Black Spruce and Jack Pine; moss	45	None	NA	390	962	-0.36	CO2	2003-2006	Bergeron et al. 2006
25	CA	53.916°N, 104.692°W	Saskatchewan; Old Jack Pine (SOJP)	Jackpine and lichen	45	None	NA	518	390-542	0.1	CO2	2003-2005	Warren Helgason; warren.helgason@usask.ca
26	GL	74.4732°N, 20.5503°W	Zackenberg	Well Drained Cassiope Heath	28	Cont.	-46	40	200	-9	CO2	2004-2014	Magnus Lund ml@bios.au.dk
27	GL	74.4791°N, 20.5557°W	Zackenberg	Wet Fen	28	Cont.	-40	40	200	-9	CO2	2007-2014	Magnus Lund ml@bios.au.dk
28	GL	74.4791°N, 20.5557°W	Zackenberg	Wet Fen	28	Cont.	-40	38	200	-9.2	CH4	2008-2009	Tagesson et al. 2012
											CO2	2008-2009	Tagesson et al. 2012
29	RU	70.829°N, 147.494°E	Chokurdakh/ Kytalyk	Moist Tussock; wedge polygon	34	Cont.	-35	48	220	-10.5	CH4	2008-2009	Parmentier et al. 2011a Parmentier et al. 2011b
											CO2	2003-2010	
30	RU	72.3733°N, 126.4979°E	Samoylov Island-Lena Delta	Moist Tundra	34	Cont.	-30	16	MSP: 72-208	-14.7	CH4	2003-2004	Wille et al. 2008
											CO2	2003-2004	Kutzbach et al. 2007
											CH4	2006	Sachs et al. 2008; Sachs et al. 2010
											CO2	2006	Sachs et al. 2008; Sachs et al. 2011
31	RU	56.4615°N, 32.9221°E	Fedorovskoje, near Nelidovo.	Old Drained Spruce	45	None	NA	265	584	3.73	CO2	2003-2006	McCallum et al. 2013
32	RU	60.8001°N, 89.3508°E	Zotino; West side of Yenisei River	Old Pine Forest; surrounded by sphagnum peat bogs	45	None	NA	90	943	-3.27	CO2	2003-2004	Corinna Rebmann corinna.rebmann@ufz.de
33	RU	62.255°N, 129.241389°	Yakutsk Spasskaya Pad	Larch Forest	47	Discont.	-200	220	111-347	-8.8	CO2	2004-2007	Ohta et al. 2008

Site Number	Region	Tower Coordinates	Site Location	Site description	Land Class	PF	Thaw Depth (cm)	Elev (m)	MAP (mm)	MAT (°C	Species	Year(s) of Record	Publications or Contact Info
34	FI	61.8327°N, 24.1928°E	Siikaneva	Boreal Open Fen Wetland; moss & sedge dominated	55	None	NA	170	713	3.3	CH4 CO2	2005 2004-2005	Aurela et al. 2007; Rinne et al. 2007
35	SE	68.3542°N, 19.0471°E	Stordalen Grassland (Mire)	Boreal Birch; wet & tall graminoid wetland & open water	19	Discont.	NA	347	364.5	-0.21	CH4	2006-2007	Jackowicz-Korczynski et al. 2010
36	FI	67.9972°N, 24.2092°E	Lompolojänkkä	Sedge Fen; with deep peat	19	None	NA	274	484	-1.4	CO2	2006-2010	Aurela et al. 2009

Table S5.2 Vegetation land cover classes from a merged 1-km resolution land cover map (See section *5.3.2.2*) as represented by the flux tower sites used in this study. The land cover classification number (Land Class) is provided, along with a description of the associated general vegetation community types.

Land Class	Vegetation Community Type
11	Permanent wetland
16	Barren or sparsely vegetated
19	Shrub and herbaceous non-tundra wetland
28	Dwarf-shrub tundra
33	Non-tussock sedge-shrub-moss tundra
34	Tussock sedge-shrub-moss tundra (shrub land characteristics)
36	Tussock sedge-shrub-moss tundra (savanna characteristics)
37	Wet sedge-moss tundra
45	Evergreen needle leaf forest + peatland
47	Deciduous needle leaf forest + peatland
49	Mixed forest (evergreen, deciduous) needle and broad leaf forest + peatland
55	Shrub wetland + peatland

Table S5.3 TCF model parameter values for GPP specific to tundra and forested wetland land class types. Parameters include maximum light use efficiency (LUE_max), soil temperature minimum and maximum (Ts_max, Ts_min), vapor pressure deficit minimum and maximums (VPD_min, VPD_max) and root zone soil moisture minimum and maximum (SM_min, SM_max). Further description of these parameters can be found in Watts *et al*. (2014a).

Sites	Land Class	LUE_max	Ts_max	Ts_min	VPD_min	VPD_max	SM_min	SM_max
14, 15, 16, 17	11	1.01	8.75	-0.25	600	4250	0.14	0.55
5	16	0.97	8.00	0.50	300	2500	0.45	0.85
35, 36	19	0.87	12.50	-0.25	450	2500	0.15	0.55
9,25,26,27,28	28	1.67	6.00	-4.70	600	3900	0.15	0.49
7	33	0.96	10.50	-2.00	300	3000	0.35	0.90
29, 30	34	0.98	5.00	-2.00	600	3500	0.15	0.45
8	36	1.30	6.00	-3.50	500	4500	0.15	0.45
10,11, 12, 13	37	1.15	4.75	-4.25	575	3500	0.15	0.50
2,3,4,19,23,24,31,32	45	1.19	9.88	-9.38	625	4100	0.13	0.46
33	47	1.35	8.00	-15.00	600	5500	0.10	0.35
18,20,21,22	49	0.90	11.75	0.88	600	3750	0.15	0.50
1,6,34	55	1.05	9.00	-3.50	500	3333	0.25	0.62

Table S5.4 TCF model parameter values for Reco specific to tundra and forested wetland land class types. These include Rhet scaling parameters for the soil moisture curve (SM1, SM2), the soil temperature curve (PTM1-PTM3), the metabolic fraction of NPP (FMET), the proportional rate allocation for respective structural and slow soil organic carbon pool decomposition (KSTR; KSLW). KOPT is the proportion of GPP lost through Ra. Further description of these parameters can be found in Watts *et al*. (2014a).

Sites	Land Class	SM1	SM2	PTM1	PTM2	PTM3	FMET	FSTR	KSTR	KSLW	FRAUT	KOPT
14, 15, 16, 17	11	2.1	1	244.81	0.017	240.63	0.71	0.7	0.4	0.009	0.40	0.03
5	16	2.1	1	249.56	0.017	240.13	0.71	0.7	0.4	0.009	0.40	0.03
35, 36	19	2.1	1	250.56	0.016	240.13	0.71	0.7	0.4	0.009	0.47	0.02
9,25,26,27,28	28	2.1	1	249.31	0.061	236.88	0.71	0.7	0.4	0.009	0.43	0.03
7	33	2.2	1	240.56	0.016	240.13	0.70	0.7	0.4	0.009	0.36	0.03
29, 30	34	2.1	1	249.56	0.017	240.13	0.71	0.7	0.4	0.009	0.46	0.03
8	36	2.2	1	251.56	0.191	235.13	0.71	0.7	0.4	0.009	0.35	0.03
10,11, 12, 13	37	2.1	1	247.81	0.145	237.38	0.71	0.7	0.4	0.009	0.46	0.03
2,3,4,19,23,24,31,32	45	2.1	1	248.31	0.032	235.13	0.71	0.7	0.4	0.009	0.48	0.03
33	47	2.1	1	249.56	0.005	235.13	0.71	0.7	0.4	0.009	0.55	0.03
18,20,21,22	49	2.1	1	244.96	0.009	240.73	0.71	0.7	0.4	0.009	0.50	0.02
1,6,34	55	2.1	1	247.56	0.074	241.46	0.71	0.7	0.4	0.009	0.41	0.02

Table S5.5 TCF model parameter values for CH_4 production and emission through vegetation, soil diffusion and ebullition pathways specific to tundra and forested wetland land class types. These include a volumetric scalar for CH_4 storage (LT), CH_4 production rate (g C per liter H_2O/day), reference soil temperature for the Q10 CH_4 production curve (QTREF), the Q10 coefficient for CH_4 production, a baseline constant for plant CH_4 transport (Cp), the fraction of CH_4 oxidized during plant transport (Pox), and an annual maximum GPP value used in the vegetation transport functions to indicate peak biomass potential (Fgrow_max). Further description of these parameters can be found in Watts *et al*. (2014a).

Sites	Land Class	LT	Ro	QTREF	Q10p	Cp	Pox	Fgrow_max
14,15,17	11	13.0	1.25E-05	288	3.7	0.18	0.62	6.67
35,36	19	15.5	3.40E-05	287	3.0	0.19	0.60	5.50
9,25,26,27	28	12.8	3.17E-05	289	3.8	0.18	0.64	7.13
29,30	34	15.0	2.50E-05	287	2.5	0.19	0.55	6.50
10,11,12,13	37	15.8	7.63E-05	287	3.3	0.20	0.63	4.00
19,23,24,31,32,46,47	45	11.0	2.00E-05	287	2.8	0.31	0.60	6.79
18,20,21,22	49	10.0	6.80E-06	287	3.3	0.19	0.54	7.50
1,34	55	13.5	3.00E-05	287	2.9	0.40	0.65	5.75

S5 References

Adkinson, A C, K H Syed, L B Flanagan (2011) Contrasting responses of growing season ecosystem CO2 exchange to variation in temperature and water table depth in two peatlands in northern Alberta, Canada. *J. Geophys. Res.*, 116.

Aurela, M., A. Lohila, J-P. Tuovinen, H. Hatakka, T. Ruitta, T. Laurila. 2009. Carbon dioxide exchange on a northern boreal fen. *Boreal Env. Res*. 14: 699-710.

Bergeron, O, H A Margolis, T A Black, C Coursolle, A L Dunn, A G Barr, S C Wofsy (2006) Comparison of carbon fluxes over three boreal black spruce forests in Canada. *Global Change Biol*., 12: 1-19.

Brown M G, E R Humphreys, T R Moore, N T Roulet, P M Lafleur (2014) Evidence for a nonmonotonic relationship between ecosystem-scale peatland methane emissions and water table depth. *J. Geophys. Res. Biogeosciences*, 119: 826-835.

Euskirchen E S, M S Bret-Harte, G J Scott, C Edgar, G R Shaver (2012) Seasonal patterns of carbon dioxide and water fluxes in three representative tundra ecosystems in northern Alaska. *Ecosphere* 3: 1-19.

Euskirchen E S, C W Edgar, M R Turetsky, M P Waldrop, J W Harden (2014) Differential response of carbon fluxes to climate in three peatland ecosystems that vary in the presence and stability of permafrost. *J. Geophys. Res. Biogeosci.*, 119: 1576-1595.

Helbig, M, C Pappas, O Sonnentag (2016a) Permafrost thaw and wildfire: equally important drivers of boreal tree cover changes in the Taiga Plains, Canada. *Geophys. Res. Lett.*, 43: 1598-1606.

Helbig, M, K Wischnewski, N Kljun, L E Chasmer, W L Quinton, et al. (2016b) Regional atmospheric cooling and wetting effect of permafrost thaw-induced boreal forest loss. *Global Change Biol*., 22: 4048-4066.

Helbig, M, L E Chasmer, N Kljun, W L Quinton, C C Treat, O Sonnentag (2016c) The positive net radiative greenhouse gas forcing of increasing methane emissions from a thawing boreal forest-wetland landscape. *Global Change Biol.*, doi:10.1111/gcb.13520.

Iwata, H, Y Harazono, M Ueyama (2012) The role of permafrost on water exchange of a black spruce forest in Interior Alaska. *Agri. Forest Meteorol.*, 161: 107-115.

Kutzbach L, C Wille, E-M Pfeiffer. (2007) The exchange of carbon dioxide between wet

arctic tundra and the atmosphere at the Lena River Delta, Northern Siberia. *Biogeosciences*, 4: 869-890.

McCallum, I, O Franklin, E Moltchanova, L Merbold, et al. (2013) Improved light and temperature responses for light-use-efficiency-based GPP models. *Biogeosciences*, 10: 6577-6590.

Nadeau, D F, A N Rousseau, C Coursolle, H A Margolis, M B Parlange (2013) Summer methane fluxes from a boreal bog in northern Quebec, Canada, using eddy covariance measurements. *Atmos. Environ.*, 81: 464-474.

Ohta, T, T C Maximov, A Dolman, T Nakai, M K van der Molen, A V Kononov, A P Maximov, T Hiyama, et al. (2008) Interannual variation of water balance and summer evapotranspiration in an eastern Siberian larch forest over a 7-year period (1998-2006). *Agri. For. Meteorol.*, 140: 1941-1953.

Parmentier, F J W, J van Huissteden, M K van der Molen, A J Dolman, G Schaepman-Strub, S A Karsanaev, T C Maximov (2011a) Spatial and temporal dynamics in eddy covariance observations of methane fluxes at a tundra site in northeastern Siberia. *J. Geophys. Res.*, 116, G03016.

Parmentier F J W, M K van der Molen, J van Huissteden, S A Karsanaev, A V Kononov, D A Suzdalov, T C Maximov, A J Dolman (2011b) Longer growing seasons do not increase net carbon uptake in the northeastern Siberian tundra. *J. Geophys. Res.*, 116, G04013.

Pejam, M R, M A Arain, J H McCaughey (2006) Energy and water vapour exchanges over a mixedwood boreal forest in Ontario, Canada. *Hydrol. Process*., 20: 3709-3724.

Sachs, T, C Wille, J Boike, L Kutzbach (2008) Environmental controls on the ecosystem-scale CH_4 emission from polygonal tundra in the Lena River Delta, Siberia. *J. Geophys. Res.*, 113, doi:10.1029/2007JG000505.

Sachs, T, M Giebels, J Boike, L Kutzbach (2010) Environmental controls on CH_4 emission from polygonal tundra on the microsite scale in the Lena river delta, Siberia. *Glob. Change Biol.*, 16: 3096-3110.

Tanja, S, F Berninger, T Vesala, T Markkanen, P Hari, et al. (2003). Air temperature triggers the recovery of evergreen boreal forest photosynthesis in spring. *Global Change Biol.*, 9:1410-1426.

Tagesson T, M Molder, M Mastepanov, C Sigsgaard, M P Tamstorf, M Lund, J M Falk, A Lindroth, T R Christensen, L Strom (2012) Land-atmosphere exchange of methane from soil thawing to soil freezing in a high-Arctic wet tundra ecosystem. *Global Change Biol.*, 18: 1928-1940.

Ueyama, M, H Iwata, Y Harazono (2014) Autumn warming reduces the CO_2 sink of a black spruce forest in interior Alaska based on a nine-year eddy covariance measurement. *Global Change Biol.*, 20: 1161-1173.

Watts J D, J S Kimball, F-J W Parmentier, T Sachs, J Rinne, D Zona, W Oechel, T Tagesson, M Jackowicz-Korczyński, M Aurela (2014a) A satellite data driven biophysical modeling approach for estimating northern peatland and tundra CO_2 and CH_4 fluxes. *Biogeosciences* 11: 1961-1980.

Watts J D, J S Kimball, F J W Parmentier, T Sachs, J Rinne, D Zona, W Oechel, T Tagesson, M Jackowicz-Korczyński, A Aurela (2014b) A satellite data driven biophysical modeling approach for estimating northern peatland and tundra CO_2 and CH_4 fluxes. *Biogeosciences,*11: 1961-1980

Wille C, L Kutzbach, T Sachs, D Wagner, E-M Pfeiffer (2008) Methane emission from Siberian arctic polygonal tundra: eddy covariance measurements and modeling. *Global Change Biol.*, 14:1395-1409.

Chapter 6: Chapter summaries and recommendations for future research

This chapter summarizes the research presented in Chapters 2-5, identifies information gaps and high-priority data needs, and provides recommendations for future investigations.

6.1 Fractional water inundation

A global land fractional open water (Fw) database using AMSR-E satellite passive microwave remote sensing 18.7 and 23.3 observations (Chapter 2) was assessed to determine the sensitivity of daily 25-km Fw retrievals to changes in northern high latitude surface hydrology, and the ability of the Fw retrievals to detect regional wetting and drying trends occurring in warming permafrost landscapes (Watts *et al*. 2012). Validation of this product was accomplished using finer resolution (30-m to 250-m resolution) static Fw maps derived from Landsat, MODIS and SRTM radar (MOD44W) data. Additional validation was achieved for major Arctic river basins (i.e. Yukon, Mackenzie, Ob, Yenisei, Lena) by comparing basin averaged Fw with monthly mean river discharge ($m^3 s^{-1}$). The Fw comparison results showed favorable agreement (R^2 = 71-84%) with the static surface water maps, with an improved ability to account for standing water in vegetated wetland areas that are not characterized by dense overlaying canopy cover (Watts *et al*. 2012). The Fw analysis for the five Arctic river basins also showed relatively strong retrieval correlations ($R > 0.70$) with the discharge records, despite other hydrological influences on river drainage, including contributions from snowmelt and groundwater, and a local decoupling of lakes and wetlands from whole basin water flow (Vörösmarty *et al*. 2001, Syed *et al*. 2007).

The AMSR-E record indicates that approximately 7% of the Arctic-boreal domain (1.4×10^6 km^2) is inundated with surface water during the non-frozen summer months (Watts *et al*. 2014a). Results from an initial Arctic-boreal Fw trend analyses (yrs. 2001-2010 and 2001-2011) indicated that 9% of the permafrost affected region experienced a significant increase ($p < 0.1$) in surface water inundation (Watts *et al*. 2011, Watts *et al*. 2014a) in recent years, whereas 2.2% of the region experienced significant surface water

drying. Wetting was widespread in the continuous permafrost zone, where soils remain frozen for much of the year with only a shallow (~ 30-70 cm depth) seasonal non-frozen active layer. Drying was more prevalent in southern discontinuous and sporadic/isolated permafrost zones having a much deeper active layer (70 to > 100 cm depth) and increased sub-surface soil water drainage.

Wetting and drying patterns in permafrost affected landscapes have also been documented in studies using higher resolution ($\leq$ 60 m) optical-IR satellite remote sensing data (e.g. Smith *et al.* 2005, Walter *et al.* 2006, Carroll *et al*. 2011, Andresen & Lougheed 2015), yet Watts *et al*. (2012, 2014a) is the first to demonstrate that these changes can be assessed for the larger Arctic-boreal region using a continuous (daily) AMSR-E microwave data record having minimal temporal gaps due to insensitivity to cloud cover and changing solar illumination effects that often limit data quality in optical records. This record has now been extended through 2015 by integrating the AMSR-E record with similar observations from the Advanced Microwave Scanning Radiometer 2 (AMSR2) sensor on the JAXA GCOM-W1 satellite (Du *et al*. 2014). The AMSR-E/2 record provides for continued Fw monitoring over the Arctic-boreal zone and 13+ year period.

6.2 Fractional water inundation and wetland methane budgets

The impact of applying satellite microwave Fw inundation records for Arctic-boreal wetland CH_4 monitoring applications was assessed in Chapter 3. This study used a JULES based satellite data driven model to investigate the combined effect of surface warming and moisture variability on high northern latitude ($\geq$ 45° N) wetland CH_4 emissions, by considering sub-grid scale changes in Fw at 15-day, monthly and annual intervals, and the potential influence of recent (2003-2011) wetting/drying trends on northern CH_4 emissions (Watts *et al*. 2014a). The JULES model is relatively simple and estimates per 25-km grid cell wetland CH_4 emissions through a production rate constant modified by a soil temperature (Q10) factor, input soil carbon quantity (kg C), satellite microwave surface freeze/thaw indices (0 = frozen surface, 1 = thawed surface), surface Fw inundation and volumetric soil moisture for non-inundated surface areas.

The modeled CH_4 fluxes were within the 5-180 mg CH_4 m^{-2} d^{-1} range observed in the lake and wetland measurements (see the Chapter 3 Supplement, Table S3.1) and estimate mean summer emissions of 55 Tg CH_4 yr^{-1} from Arctic-boreal wetlands. Arctic wetting and summer warming in the 9-yr. (2003-2011) record increased wetland emissions by 0.48 Tg CH_4 yr^{-1}, but this was mainly offset by decreasing emissions (-0.32 Tg CH_4 yr^{-1}) in sub-Arctic areas experiencing surface drying or cooling. The combined influence of warming and wetting in the Fw and reanalysis surface meteorology records contributed to an increase in methane emissions across 16% of the Arctic-boreal domain at a mean rate of 43 tonne CH_4 yr^{-1} from 2003 to 2011. These increases occurred primarily in Canada and eastern Siberia, where summer warming has been observed in both in-situ measurements and reanalysis records. These findings agree with a projected 15% increase in CH_4 emitting area that might occur with continued climate change in the northern wetland regions (Gao *et al.* 2013).

In global and regional wetland CH_4 studies, the largest budget uncertainties continue to result from a lack of information to adequately define wetland area extent (Melton *et al*. 2013, Kirschke *et al*. 2013, Watts *et al*. 2014a). Furthermore, CH_4 transport from soil-to-atmosphere is strongly regulated by vegetation community types and species (Davidson *et al*. 2016). Ongoing improvements to vegetation maps suitable for Arctic-boreal CH_4 emission budget mapping are still required (Davidson *et al*. 2016, Watts *et al*. In Prep), although regional efforts using satellite radar data have made considerable progress in mapping vegetated wetlands in Alaska (Whitcomb *et al*. 2014). Additional efforts have used radar remote sensing to delineate peatlands in permafrost regions using time series of soil moisture and inundation dynamics (Bartsch *et al*. 2009). Methods developed for downscaling high temporal but coarser (e.g. 25-km) spatial resolution passive microwave Fw data to the landscape level show additional promise for informing regional CH_4 models (Fluet-Chouinard *et al*. 2015). New 5-km passive microwave Fw datasets with 10-day sampling intervals are also now available for the Arctic-boreal region from yrs. 2003-2015 (Du *et al*. 2016). The 5-km Fw records incorporate information from higher frequency (89 GHz) AMSR brightness temperature

retrievals and show greater sensitivity to surface water changes from open water lake and pond bodies, relative to vegetated wetlands (Figure 1; Du *et al*. 2016).

Combined information from 25-km and 5-km AMSR-E/AMSR2 records, in conjunction with available radar-based static lake maps for the pan-Arctic region, new soil moisture data records (e.g. from SMAP; Kimball *et al*. 2012), radar derived soil organic carbon records (Bartsch *et al*. 2016a) and spatial downscaling (Fluet-Chouinard *et al*. 2015), could provide enough information to spatially partition seasonal changes in lake area extent, expansion and contraction of high CH_4 emitting littoral zones (Juutinen *et al*. 2003) and wetting/drying in vegetated wetlands. These efforts, and the development of a new high resolution (30 m) Arctic-boreal wetland vegetation map using input data from Landsat, MODIS, and Sentinel (Bartsch *et al*. 2016b) will be necessary to reduce uncertainty in northern CH_4 wetland budgets.

An improved understanding of lateral transport of terrestrial-originating CH_4 by stream and river channels (Benoy *et al*. 2007, van Huissteden *et al*. 2009) and CH_4 emission response in wetlands under water inundated conditions is also necessary. For example, regional modeling studies (Watts *et al*. 2014a) show temporal agreement with changes in atmospheric CH_4 concentrations and CH_4 emission estimates resulting from expansion or contraction of regional inundation area. However, field studies show a substantial decrease in landscape CH_4 emissions when water begins to submerge venting structures in wetland vegetation (Juutinen *et al*. 2003, Zona *et al*. 2009) suggesting the need to monitor vegetation and water level height in addition to landscape inundation. Perhaps more effective than inundation monitoring would be improvement of surface and rootzone volumetric soil moisture records for organic and mineral soils in the Arctic-boreal region, especially since a recent regional analysis reveals higher CH_4 emissions occurring in upland tussock tundra communities having wet soils but minimal surface inundation (Zona *et al*. 2016).

6.3 TCF model development for northern wetlands

The enhancement of a Terrestrial Carbon Flux (TCF) model (Kimball *et al*. 2009; 2016) to include tundra and peatland land cover functional types and a wetland CH_4 emission module (Watts *et al*. 2014b) was presented in Chapter 4. The TCF model allows for in situ, satellite remote sensing and reanalysis information to be used as primary environmental inputs and provides a framework to monitor the terrestrial net ecosystem carbon budget (NECB; $CO_2 + CH_4$). The TCF model estimates mean daily fluxes (gC m^{-2}) of vegetation gross primary productivity (GPP), ecosystem CO_2 respiration (Reco; with autotrophic and heterotrophic components), and net ecosystem exchange (NEE; GPP – Reco). The TCF model CH_4 emissions algorithm simulates gas production using near-surface soil temperature, soil volumetric water content and labile organic carbon as inputs. Plant CH_4 transport (mgC m^{-2} d^{-1}) is determined by vegetation growth characteristics derived from GPP, plant functional traits and canopy/surface turbulence. Methane diffusion is determined based on temperature and soil moisture constraints to gas movement through the soil column, and column oxidation potential. Ebullition (bubble transport) of CH_4 is assessed using a simple gradient method.

The TCF model simulations using in-situ data from six Arctic-boreal flux tower sites (see Section 4.3.2) explained > 70% of the R^2 variability in the 8 day cumulative eddy covariance measured fluxes. Model simulations using coarser satellite (250-m MODIS) and reanalysis (0.5° MERRA) records accounted for approximately 69% and 75% of the respective r^2 variability in the tower CO_2 and CH_4 records, with RMSE uncertainties of $\leq$ 1.3 gC m^{-2} d^{-1} (CO_2) and 18.2 mgC m^{-2} d^{-1} (CH_4). This study found the estimated annual wetland CH_4 emissions to be relatively small (< 18 g C m^{-2} yr^{-1}) compared to R_{eco} (> 180 g C m^{-2} yr^{-1}). However, CH_4 fluxes reduced the across-site NECB by 23% and contributed to a global warming potential of approximately 165 $\pm$ 128 g CO_2 eq m^{-2} yr^{-1} when considered over a 100-year time span.

This initial TCF model evaluation indicated a strong potential for using the model to document landscape scale variability in CO_2 and CH_4 fluxes, and to estimate the NECB for northern peatland and tundra ecosystems. However, opportunities remain for

model improvement. For example, in some cases the TCF model GPP (informed using air temperature constraints and microwave based surface freeze/thaw indices) start-of-season was premature relative to GPP estimates obtained from site tower eddy covariance records. The delayed site GPP response likely resulted from a shallow (< 14 cm) early season thaw depth that limited bud break activity in deeper rooted shrubs (e.g. *Betula nana* and *Salix pulchra*). Experimental TCF model simulations using a temperature driven phenology model (Parmentier *et al*. 2011) reduced the corresponding RMSE difference for Kytalyk by 56% (to 1 g C m^{-2} d^{-1}).

Alternatives to using a temperature driven phenology model may include coupling the TCF model to a multi-layer permafrost and hydrology soil model for finer temperature regulation of carbon dynamics by depth (Yi *et al*. 2015). A coupled TCF-permafrost model would also be able to regulate soil metabolic activities and carbon loss from deeper soil layers following seasonal and annual changes in the active layer, making the model more compatible with field study warming experiments. It may also be possible to regulate TCF model GPP start-of-season through seasonal input estimates of permafrost active layer depth obtained using combined satellite microwave remote sensing and process model simulations (Park *et al*. 2016). Further improvements to the TCF GPP model could include the experimental use of solar-induced chlorophyll fluorescence (Zhang *et al*. 2016) in addition to input MODIS FPAR (fraction of daily photosynthetically active solar radiation) products or FPAR derived from MODIS optical-IR vegetation indices.

6.4 Assessment of longer-term NECB response in TCF model simulations across Arctic-boreal flux tower sites

Recent (yrs. 2003-2015) wetland carbon budgets and corresponding changes in carbon flux components for the Arctic-boreal region were investigated in Chapter 5 (Watts *et al*. In Prep.). The TCF model presented in Chapter 4 (Watts *et al*. 2014b) was further developed to include 12 wetland functional types representative of Arctic-boreal tundra and boreal vegetation (Table S5.2). The GPP module was also modified to use

input near-surface (> 20 cm) soil temperatures for tundra landscapes, instead of air temperature. This step was taken to mitigate issues with premature GPP start-of-season (see Section 6.4; Chapter 4).

The original eddy covariance database (presented in Watts *et al*. 2014b) was expanded from six tower sites to include data from 36 tower locations (Table S5.1). This enhanced tower eddy covariance database was essential to further evaluate the ability of the TCF model to accurately estimate CO_2 and CH_4 fluxes from Arctic-boreal environments prior to using the model to generate 1-km res. carbon flux estimates for high latitude (> 45°N) wetland regions (an example is provided in Figure 2). This investigation also resulted in 1-km res. northern wetland vegetation map resulting from the merging of the 300-m resolution ESA CCI-LC 2010 Epoch land cover product (Kirches *et al*. 2014), the Circumpolar Arctic Vegetation Map (Walker *et al*. 2005) and a peatland vegetation map (Watts *et al*. 2014a). This step was necessary to remedy the lack of an Arctic-boreal wetland vegetation map suitable for CH_4 mapping purposes (see the discussion in Section 6.3).

The resulting daily 1-km TCF model simulations had low RMSE uncertainties of 0.97 gC m^{-2} d^{-1} (NEE) and 21 mgC m^{-2} d^{-1} (CH_4) relative to the tower records, and are similar to those reported elsewhere (Watts *et al*. 2014b). The model results indicated a net ecosystem carbon sink for the 36 tower tundra and boreal wetland sites with respective average NEE values of -4 and -96 gC m^{-2} yr^{-1}. Accounting for NECB (NEE $\pm$ CH_4) reduced the overall boreal wetland carbon sink by 20% and shifted tundra from carbon sink to carbon source (NECB = 1.6 gC m^{-2} yr^{-1}). Significant ($\alpha = 0.1$) change in annual Reco and NEE were not observed in the 13-yr TCF model records for boreal and tundra wetland groups. However, this analysis indicated a significant increase in CH_4 flux (1.9 gC m^{-2} yr^{-1}) from boreal wetlands (forested and non-forested) and a significant decrease (9.9 gC m^{-2} yr^{-1}) in GPP in boreal forested wetlands.

The TCF model simulations also show contrasts in carbon flux response relative to geographic location and land cover type, with mixed trends observed at individual flux

sites. The 13-yr trend analysis showed that 28% of the tower sites had an increase in annual CO_2 loss through Reco, distributed across boreal and tundra wetlands. For GPP flux, 14% of the tower sites showed an increase in annual CO_2 assimilation and 5% of the sites showed a decrease (both were boreal wetlands). Only 11% of the sites (two tundra and two boreal) showed a decrease in annual NEE. However, 22% of the sites had increasing annual CH_4 emissions (three tundra, five boreal), further decreasing NECB.

The results from this study emphasize the need for continued NECB monitoring in Arctic-boreal ecosystems through the integration of tower flux measurements, ecosystem models and satellite remote sensing. Next steps for this analysis will be the expansion of TCF model simulations to include all 1-km wetland grid cells for the Arctic-boreal region (Figure 2) and an assessment of NECB change from 2003-2015 according to the 12 functional land cover types presented in this study (Watts *et al*. In Prep). Modification of wetland area in the tundra and boreal zones using AMSR-E/2 derived 5-25 km resolution Fw inputs, and associated impacts on seasonal CH_4 emission totals, will also be assessed. Finally, the ability of TCF model simulated fluxes to account for recent variability and trends in northern high atmospheric CO_2 and CH_4 fluxes will be investigated using inverse modeling (e.g. Alexe *et al*. 2014, Bruhwiler *et al*. 2014).

References

Alexe, M, P Bergamaschi, A Segers, R Detmers, A Butz, O Hasekamp, R A Scheepmaker (2014) Inverse modeling of CH4 emissions for 2010–2011 using different satellite retrieval products from GOSAT and SCIAMACHY. *Atmos. Chem. Phys. Discuss*., 14: 11493-11539.

Andresen, C G, V L Lougheed (2015) Disappearing Arctic tundra ponds: Fine-scale analysis of surface hydrology in drained thaw lake basins over a 65 year period (1948–2013). *J. Geophys. Res.: Biogeosciences*, 120: 466-479.

Bartsch, A, W Wagner, K Scipal, C Pathe, D Sabel, P Wolski (2009) Global monitoring of wetlands–the value of ENVISAT ASAR global mode. *J. Environ. Management*, 90: 2226-2233.

Bartsch, A, A Höfler, C Kroisleitner, A M Trofaier (2016a). Land Cover Mapping in

Northern High Latitude Permafrost Regions with Satellite Data: Achievements and Remaining Challenges. *Remote Sensing*, 8: 979.

Bartsch, A, B Widhalm, P Kuhry, G Hugelius, J Palmtag, M B Siewert (2016b) Can C-band synthetic aperture radar be used to estimate soil organic carbon storage in tundra? *Biogeosciences*, 13: 5453.

Benoy, G, K Cash, E McCauley, F Wrona (2007) Carbon dynamics in lakes of the boreal forest under a changing climate. *Environ. Reviews*, 15: 175-189.

Bruhwiler, L, E Dlugokencky, K Masarie, M Ishizawa, A Andrews, J Miller, D Worthy (2014) CarbonTracker-CH 4: an assimilation system for estimating emissions of atmospheric methane. *Atmospheric Chem. Phys.*, 14: 8269-8293.

Carroll, M L, J R G Townshend, C M DiMiceli, T Loboda, R A Sohlberg (2011) Shrinking lakes of the Arctic: Spatial relationships and trajectory of change. *Geophys. Res. Lett., 38*.

Davidson S J, M J Santos, V L Sloan, J D Watts, G K Phoenix, W C Oechel, D Zona (2016) Upscaling arctic tundra vegetation communities using field spectroscopy and multispectral satellite data in North Alaska, U.S.A. *Remote Sens,* 8: 978-1002.

Du, J., J S Kimball, J C Shi, L A Jones, S Wu, R Sun, H Yang (2014) Inter-calibration of satellite passive microwave land observations from AMSR-E and AMSR2 using overlapping FY3B-MWRI sensor measurements. *Rem. Sens.*, 6: 8594-8616.

Du, J, J S Kimball, L A.Jones, J D Watts (2016) Implementation of satellite based fractional water cover indices in the pan-Arctic region using AMSR-E and MODIS. *Rem. Sens. Environ.*, 184: 469-481.

Fluet-Chouinard, E, B Lehner, L M Rebelo, F Papa, S K Hamilton (2015) Development of a global inundation map at high spatial resolution from topographic downscaling of coarse-scale remote sensing data. *Remote Sens. Environ.*, 158: 348-361.

Gao, X, C A Schlosser, A Sokolov, K W Anthony, Q Zhuang, D Kicklighter (2013) Permafrost degradation and methane: low risk of biogeochemical climate-warming feedback. *Environ. Res. Lett.*, 8: 035014 doi:10.1088/1748-9326/8/3/035014.

Juutinen, S, J Alm, T Larmola, J T Huttunen, M Morero, S Saarnio, J Silvola (2003) Methane (CH_4) release from littoral wetlands of boreal lakes during an extended flooding period. *Global Change Biol.*, 9: 413-424.

Kimball J S, L A Jones, K Zhang, F A Heinsch, et al. (2009) A satellite approach to estimate land-atmosphere CO_2 exchange for Boreal and Arctic biomes using MODIS and AMSR-E. *IEEE Trans. Geosci. Remote Sens.*, 47: 569-587.

Kimball, J S, R Reichle, K McDonald, E Njoku (2012) Soil Moisture Active Passive (SMAP) Algorithm Theoretical Basis Document (ATBD): SMAP Level 4 Carbon Data Product (L4_C), Initial Release v. 1, Jet Propulsion Laboratory, California Institute of Technology, (73 pp.).

Kimball J S, L A Jones, J Glassy, R Reichle (2016a) SMAP L4 Global Daily 9 km Carbon Net Ecosystem Exchange, Version 2. Boulder, Colorado, USA. NASA National Snow and Ice Data Center Distributed Active Archive Center. doi: http://dx.doi.org/10.5067/UBKO5ZUI7I5V.

Kirschke, S, P Bousquet, P Ciais, M Saunois, J G Canadell, E J Dlugokencky, P Cameron-Smith (2013) Three decades of global methane sources and sinks. *Nature Geosci.*, 6: 813-823.

Park, H, Y Kim, J S Kimball (2016). Widespread permafrost vulnerability and soil active layer increases over the high northern latitudes inferred from satellite remote sensing and process model assessments. *Remote Sens. Environ.*, 175: 349-358.

Parmentier, F J W, M K van der Molen, J van Huissteden, S A Karsanaev, A V Kononov, D A Suzdalov, T C Maximov, A J Dolman (2011) Longer growing seasons do not increase net carbon uptake in the northeastern Siberian tundra. *J. Geophys. Res. Biogeo.*, 116: G04013, doi:10.1029/2011JG001653.

Smith, L C, Y Sheng, G M MacDonald, L D Hinzman (2005) Disappearing Arctic lakes. *Science*, 308: 1429.

Syed, T H, J S Famiglietti, V Zlotnicki, M Rodell (2007) Contemporary estimates of Pan-Arctic freshwater discharge from GRACE and reanalysis. *Geophys. Res. Lett.*, 34 (6 pp.).

Van Huissteden, J, T C Maximov, A J Dolman (2005). High methane flux from an arctic floodplain (Indigirka lowlands, eastern Siberia). *J. Geophys. Res.: Biogeosciences*, *110*(G2).

Vörösmarty, C, L Hinzman, B Peterson, D Bromwich, L Hamilton, J Morison, R Webb (2001). *The Hydrologic Cycle and its Role in Arctic and Global Environmental Change*. Fairbanks, AK: ARCUS.

Walter, K M, S A Zimov, J P Chanton, D Verbyla, F S Chapin, F. S., III (2006) Methane bubbling from Siberian thaw lakes as a positive feedback to climate warming. *Nature*, 443: 71–75.

Watts J D, J S Kimball, L A Jones, R Schroeder, K C McDonald (2012) Satellite microwave remote sensing of contrasting surface water inundation changes within the Arctic-Boreal Region. *Rem. Sens. Environ.*, 127: 223-236.

Watts J D, J S Kimball, F-J W Parmentier, T Sachs, J Rinne, D Zona, W Oechel, T Tagesson, M Jackowicz-Korczyński, M Aurela (2014a) A satellite data driven biophysical modeling approach for estimating northern peatland and tundra CO_2 and CH_4 fluxes. *Biogeosciences,* 11: 1961-1980.

Watts J D, J S Kimball, F J W Parmentier, T Sachs, J Rinne, D Zona, W Oechel, T Tagesson, M Jackowicz-Korczyński, A Aurela (2014b) A satellite data driven biophysical modeling approach for estimating northern peatland and tundra CO_2 and CH_4 fluxes. *Biogeosciences,*11: 1961-1980

Watts J D, J S Kimball, R Commane, D Zona, M Helbig, D Olefeldt, F J W Parmentier, T Sachs, L Bruhwiler, O Sonnentag, E Euskirchen, J Kochendorfer, E Humphreys, D Nadeau, J Rinne, M Lund, T Tagesson, M Jackowicz-Korczynski, W C Oechel, M Aurela, M Ueyama, et al. (In Prep.) Regional and longer-term variabilityin the northern high latitude wetland carbon budget. For submission to *Global Change Biol*.

Whitcomb, J, M Moghaddam, K C McDonald, J Kellndorfer, E Podest (2009) Mapping vegetated wetlands of Alaska using L-band radar satellite imagery. *Canadian Journal of Remote Sensing*, 35: 54-72.

Yi, Y, J S Kimball, M A Rawlins, M Moghaddam, E S Euskirchen (2015) The role of snow cover affecting boreal-arctic soil freeze-thaw and carbon dynamics. *Biogeosciences*, 12: 5811-5829.

Zhang, Y, X Xiao, C Jin, J Dong, S Zhou, P Wagle, Y Qin (2016) Consistency between sun-induced chlorophyll fluorescence and gross primary production of vegetation in North America. *Remote Sens. Environ.*, 183: 154-169.

Zona, D, W C Oechel, J Kochendorfer, K T Paw U, A N Salyuk, P C Olivas, D A Lipson, (2009) Methane fluxes during the initiation of a large-scale water table manipulation experiment in the Alaskan Arctic tundra. *Global Biogeochem. Cycles*, *23*(2).

Zona D, B Gioli, R Commane, J Lindaas, S C Wofsy, C E Miller, S J Dinardo, S Dengel, C Sweeney, A Karion, R Y-W Chang, J M Henderson, P C Murphy, J P Goodrich, V Moreaux, A Liljedahl, J W Watts, J S Kimball, D A Lipson, W C

Oechel (2016) Cold season emissions dominate the Arctic tundra methane budget. *Proc. Nat. Acad. Sci.*, 113: 40-45.

Figures

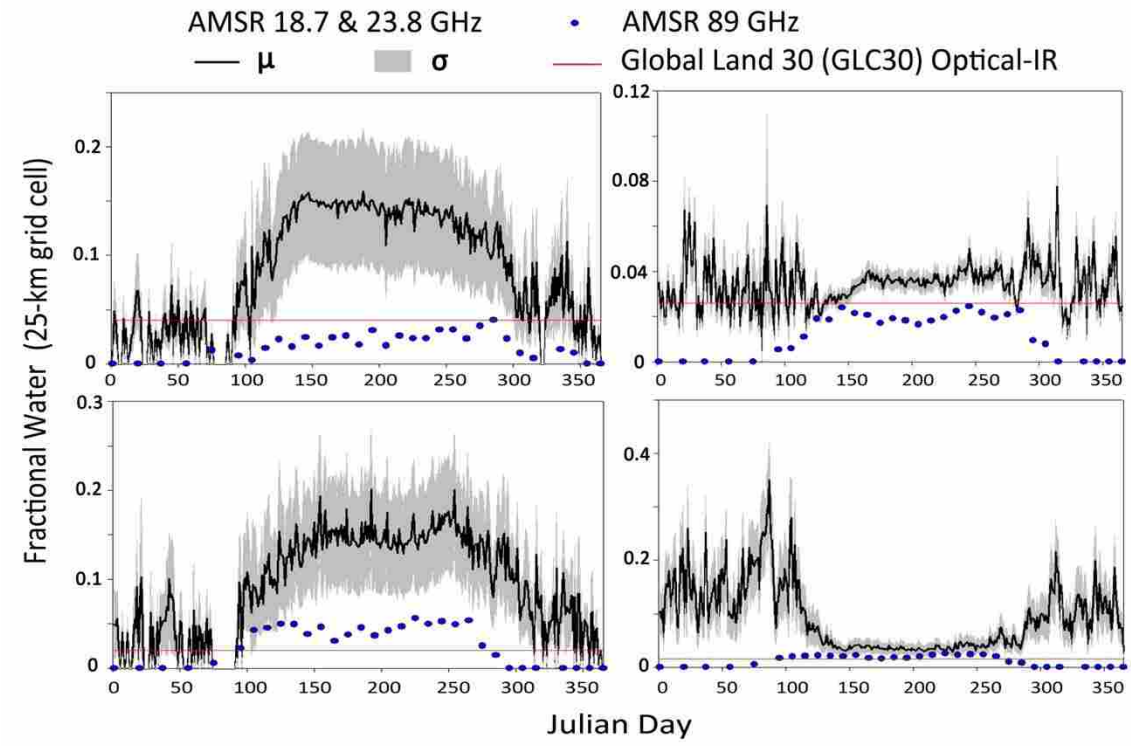

Figure 1 The AMSR 18.7 and 23.8 GHz Fw retrievals capture dynamic wetland inundation and seasonal variability in surface water area (black lines) for Alaska ecosystems, in contrast to static surface water products (e.g. 30-m optical-IR). The 25-km Fw observations (Watts *et al*. 2012) are complimented by finer (5-km) resolution Fw retrievals from the AMSR 89 GHz record (Du *et al*. 2016) with less sensitivity to flooded vegetation relative to lake bodies (blue circles). The upper left plot shows inundation response in open (flooded) tundra wetlands relative to tundra wetlands having lower water tables and less landscape standing water (upper right). The bottom plots show inundation response in boreal wetlands prone to summer flooding (left) and those characterized by spring flooding transitioning to saturated soils in summer (right).

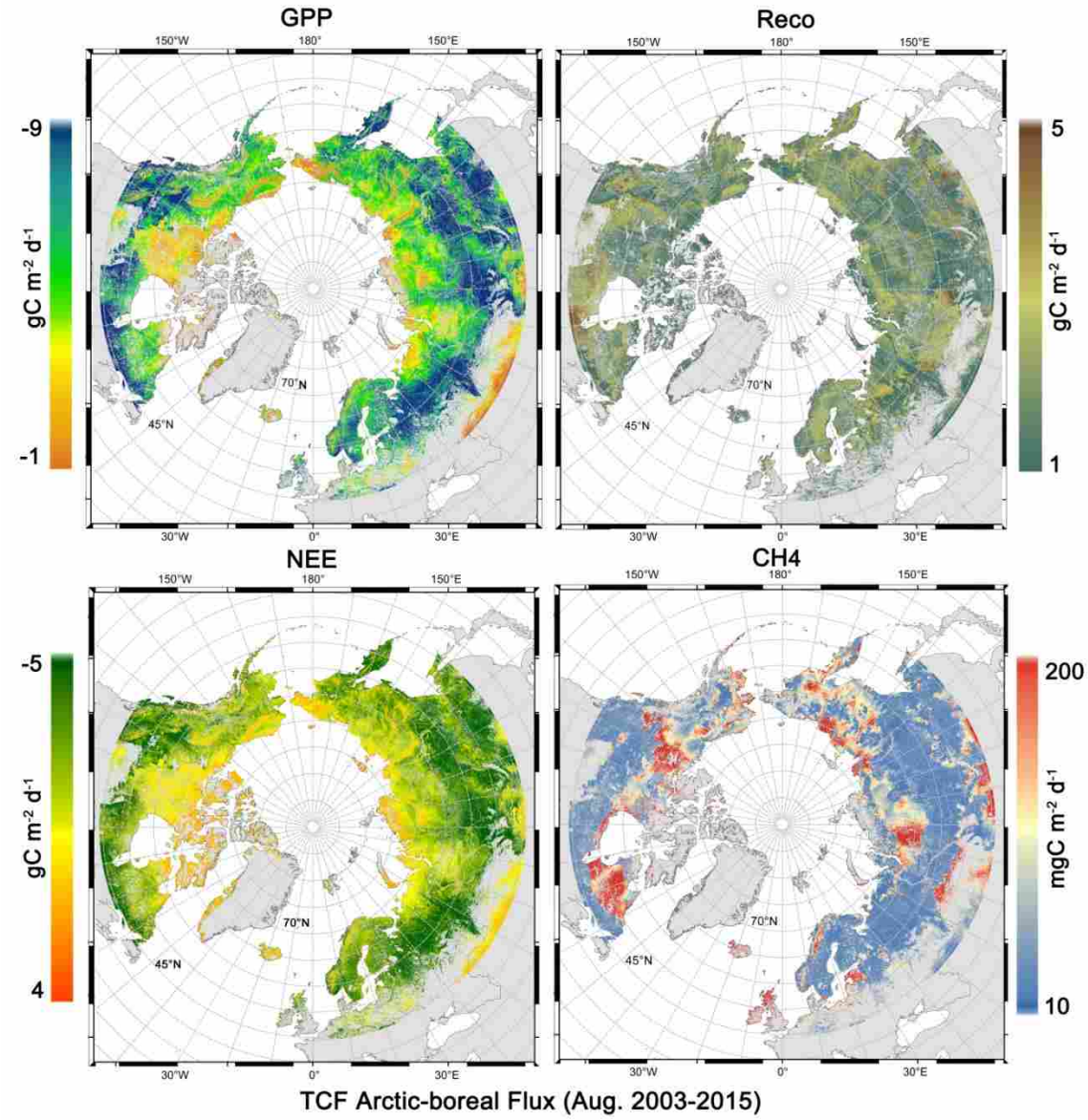

Figure 2 Example TCF wetland model estimates for average August vegetation gross primary productivity (GPP; gC m^{-2} d^{-1}), ecosystem CO_2 respiration (Reco; gC m^{-2} d^{-1}), net ecosystem CO_2 exchange (NEE) and CH_4 emissions over the 13-yr (2003-2015) study period. Model simulations are daily at a 1-km spatial resolution using MODIS (MCD15A3) and MERRA reanalysis inputs, in addition to landscape freeze/thaw records and inundation area extent provided through AMSR-E/2 fractional water records (Watts *et al*. 2012, 2014b; Watts *et al*. In Prep).